Dielectric Effects in Complex Fluids

Von der Fakultät Mathematik und Physik der Universität Stuttgart
und dem Stuttgarter Zentrum für Simulationswissenschaft
(SC SimTech) zur Erlangung der Würde eines Doktors der
Naturwissenschaften (Dr. rer. nat.) genehmigte Abhandlung

vorgelegt von

Johannes Zeman

aus Backnang

Hauptberichter: Prof. Dr. Christian Holm
Mitberichter: Prof. Dr. Johannes Kästner
Drittgutachter: Prof. Dr. Joachim Dzubiella

Tag der mündlichen Prüfung: 2021-12-21

Institut für Computerphysik der Universität Stuttgart

2022

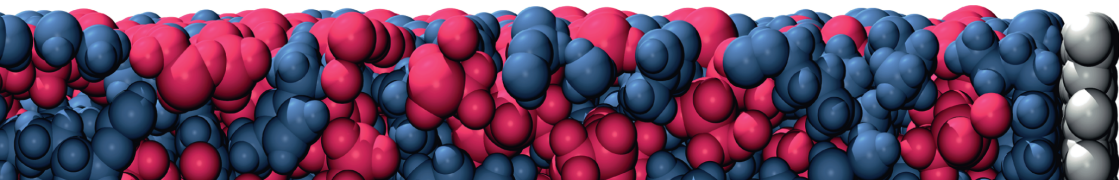

Erklärung über die Eigenständigkeit der Dissertation

Die vorliegende Dissertation zum Thema *Dielectric Effects in Complex Fluids* stellt meine eigenständig erbrachte Leistung dar.

Ich habe ausschließlich die angegebenen Quellen und Hilfsmittel benutzt. Wörtlich oder inhaltlich aus anderen Werken übernommene Angaben habe ich als solche kenntlich gemacht.

Die Richtigkeit der hier getätigten Angaben bestätige ich und versichere, nach bestem Wissen die Wahrheit erklärt zu haben.

Stuttgart, 7. Februar 2022

Johannes Zeman

Acknowledgments

This work would not have been possible without the tremendous support I received from other people. First of all, I want to thank my supervisor Christian Holm for all the ideas, guidance, and encouragement he provided, and also for the patience he showed for me. Likewise, I want to thank my former supervisor Axel Arnold, who gave me the possibility to work in the field of Computational Physics in the first place. I would also like to express my gratitude to Johannes Kästner and Joachim Dzubiella for their efforts and time taken to assess this work.

I thank my family, especially my parents, for their love and encouragement they gave me throughout my life. Without their support, I could have never gotten this far. Of course, the same applies to all my friends, who always helped me in my choices with both the necessary criticism and support. One among them who sticks out in particular with respect to my scientific journey is Michael Schlaile, who gave me the possibility to broaden my horizon towards scientific fields beyond Physics.

Since research can only thrive in the right environment, I am very grateful to all my colleagues at the Institute for Computational Physics. They helped me tremendously in developing new ideas and made my time at the institute so very enjoyable. In that respect, I am especially grateful to Jens Smiatek and Frank Uhlig for their inspiring ideas and motivating discussions, and to Tillmann Kleiner for his mathematical expertise. Likewise, I would like to thank Rudolf Hilfer for the many scientific and political discussions we had.

Last but most importantly, I want to thank Martina Gassenmeier for her unwavering love, her understanding and patience, and for all the sacrifices she has made for me during the past years.

Contents

1 Zusammenfassung

Während die ersten theoretischen Modelle zur Beschreibung dielektrischer Relaxationsprozesse vor allem auf die Arbeiten von Peter Debye[1] im frühen zwanzigsten Jahrhundert zurückgehen, wird der Begriff *dielektrische Spektroskopie* heutzutage in erster Linie als ein Sammelbegriff für mehrere experimentelle Messverfahren verstanden, die in der Lage sind, den frequenz- und materialabhängigen Antwortkoeffizienten $\varepsilon_r(\omega)$ in Bezug auf ein von außen angelegtes elektrisches Wechselfeld $\boldsymbol{E}(\omega)$, welches mit der Kreisfrequenz ω schwingt, bis in den Terahertzbereich hinein zu messen. Dieser Antwortkoeffizient setzt die induzierte Polarisation (d.h. die Antwort) des Materials ins Verhältnis zum angelegten elektrischen Feld $\boldsymbol{E}$. Unter der Annahme eines schwachen angelegten äußeren Feldes gilt für ein homogenes und isotropes dielektrisches Medium die Beziehung

$$\boldsymbol{P} = \varepsilon_0 \chi_e \boldsymbol{E} = \varepsilon_0(\varepsilon_r - 1)\boldsymbol{E}\,, \tag{1.1}$$

wobei die Konstante ε_0 die Vakuumpermittivität beschreibt. Der Antwortkoeffizient $\chi_e = \varepsilon_r - 1$ wird als (dimensionslose) *elektrische Suszeptibilität* bezeichnet und ε_r als die *relative Permittivität*, wobei beide allgemein komplexwertige Größen sind. Die Permittivität ist hierbei definiert als

$$\varepsilon_r(\omega) = \varepsilon_r'(\omega) - i\varepsilon_r''(\omega) \tag{1.2}$$

mit der imaginären Zahl i, welche ihrerseits als $i^2 = -1$ definiert ist. Der Realteil von $\varepsilon_r'(\omega)$, welcher üblicherweise als *Dispersion* bezeichnet wird[a], verhält sich proportional zur vom Medium *reversibel* aufgenommenen Feldenergie. Mit steigender Frequenz sind die molekularen

[a] Der Ausdruck „Dispersion“ bezeichnet auch das allgemeine Phänomen, dass die dielektrische Permittivität insgesamt frequenzabhängig ist. Hier wird der Begriff allerdings ausschließlich für die Benennung des Realteils $\varepsilon_r'(\omega)$ verwendet.

Bestandteile des Materials zunehmend weniger in der Lage, in ihrer Bewegung den Schwingungen des angelegten Feldes zu folgen, was zu einer Phasenverschiebung zwischen dem externen Feld und der Antwort des Systems führt und somit einen größerwerdenden Imaginärteil ε_r'' der Permittivität zur Folge hat. Da diese Verzögerung im Allgemeinen mit materialabhängigen dissipativen Effekten einhergeht, ist die Amplitude von ε_r'' ein Maß für die *dielektrische Absorption*, welche dementsprechend das Verhältnis zur innerhalb des Mediums *irreversibel* aufgenommenen Feldenergie beschreibt. Aufgrund der Tatsache, dass dem frequenzabhängigen Verhalten sowohl des Real- als auch des Imaginärteils der dielektrischen Permittivität dieselben physikalischen Prozesse zugrundeliegen, besteht ein kausaler – und somit analytischer – Zusammenhang zwischen ε_r' und ε_r'',[2] weshalb beide dieser Größen aus der jeweils anderen mit Hilfe der Kramers-Kronig-Relationen berechnet werden können.[3]

Experimentell wird die komplexe Permittivität üblicherweise aus Messungen der frequenzabhängigen Leitfähigkeit anhand der Beziehung[4]

$$\varepsilon_r(\omega) = \varepsilon_r^{\infty} + \frac{i\sigma_e(\omega)}{\varepsilon_0 \omega} \tag{1.3}$$

berechnet. Dabei bezeichnet ε_r^{∞} die sogenannte „instantane“ Antwort des physikalischen Systems, welche die Gesamtheit aller Relaxationsprozesse beinhaltet, die zu schnell sind um durch eine (generell bandbegrenzte) Messung erfasst werden zu können (z. B. elektronische Polarisation oder Kernpolarisation).

Im Verlauf des vergangenen Jahrhunderts entwickelte sich die dielektrische Spektroskopie zu einem wichtigen wissenschaftlichen und industriellen Werkzeug, das es ermöglicht, Erkenntnisse über dynamische Prozesse innerhalb unterschiedlichster Materialien zu erhalten. Die blaue Kurve in Abbildung 1.1, welche die Anzahl der Publikationen pro Jahr beschreibt (durch die Suchmaschine Google Scholar[5] ermittelt), die die Schlagworte “dielectric relaxation” oder “dielectric spectroscopy” beinhalten, zeigt anschaulich, dass dieser Forschungsbereich

immer noch stetig wächst. Die Methode der dielektrischen Spektroskopie findet heutzutage in vielen wissenschaftlichen und industriellen Bereichen Anwendung, wie zum Beispiel in der Biotechnologie,[6–8] in der Qualitätssicherung der chemischen[9–11] und der Lebensmittelindustrie[12–14] sowie in der Batterieentwicklung.[15]

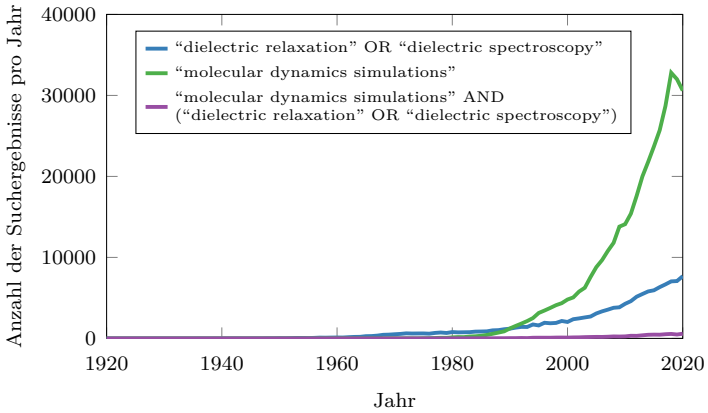

Abbildung 1.1: Anzahl der Google Scholar-Suchergebnisse[5] pro Jahr von 1920 bis 2020, welche die Begriffe *"dielectric relaxation" OR "dielectric spectroscopy"* (blaue Linie), *"molecular dynamics simulations"* (grüne Linie), oder *"molecular dynamics simulations" AND ("dielectric relaxation" OR "dielectric spectroscopy")* (violette Linie) enthalten. Die Anzahl der Publikationen, welche sowohl die Begriffe "dielectric relaxation / spectroscopy" als auch "molecular dynamics" enthalten, ist relativ gering.

Obwohl ein überaus gutes Verständnis der in der experimentellen dielektrischen Spektroskopie eingesetzten Messtechniken besteht, erweist sich die Interpretation der Messergebnisse und deren Deutung in Bezug auf die zugrundeliegenden mikroskopischen Mechanismen oft als schwierig und kann mitunter uneindeutig sein. Im Gegensatz dazu kann man erwarten, dass dies ein viel geringeres Problem darstellt, wenn die Spektren aus Molekulardynamiksimulationen (MD-Simulationen, siehe Abschnitt 3.3) berechnet werden, da diese Simulationsmethode räumliche und zeitliche Auflösungen im Subnanometer- und Femtosekundenbereich ermöglicht und somit alle mikroskopischen Prozesse direkt beobachtbar macht. Obwohl sich MD-Simulationen mittlerweile zu ei-

nem extrem häufig eingesetzten wissenschaftlichen Werkzeug entwickelt haben (man beachte die grüne Linie in Abbildung 1.1), so scheint die Vorhersage dielektrischer Materialeigenschaften mit dieser Simulationsmethode (siehe violette Linie in Abbildung 1.1) bisher dennoch eher ein Nischendasein zu fristen. Ein Grund für diese Tatsache ist sicherlich der hohe Rechenaufwand, den solche Simulationen mit sich bringen, zumal die Berechnung dielektrischer Spektren sehr lange Simulationszeiten im Bereich von Mikrosekunden erfordern. Nichtsdestotrotz ist es heutzutage durch die Verfügbarkeit zunehmend leistungsfähigerer Rechenbeschleuniger (wie z. B. Grafikprozessoren) möglich, derartig lange Simulationszeiten innerhalb vertretbarer Rechenzeit zu erreichen.

Im Prinzip könnte man bei der Berechnung dielektrischer Spektren mit Hilfe rechnergestützter Simulationen analog zum experimentellen Messprinzip vorgehen, indem man ein externes elektrisches Feld vorgibt. Dies würde allerdings bedeuten, dass man für jede Frequenz des angelegten Feldes eine unabhängige Simulation durchführen müsste, was je nach gewünschter Bandbreite und Auflösung des zu berechnenden Spektrums einen nicht zu vertretenden Rechenaufwand mit sich brächte.

In einem physikalischen System, welches sich im thermischen Gleichgewicht befindet, bewegen sich die enthaltenen Teilchen ständig um ihre Gleichgewichtslage, und zwar auch dann, wenn kein externes elektrisches Feld angelegt ist. Zumal die Teilchen in einem dielektrischen Medium elektrische Ladungen tragen, führt dies zu einem ständigen Auf- und Wiederabbau von materialinternen elektrischen Feldern. Da die räumliche Anordung und die Geschwindigkeiten aller Teilchen eines Systems in einer entsprechenden Simulation zu jedem Zeitpunkt bekannt sind, kann die Reaktion des Systems auf seine eigenen internen elektrischen Felder gemessen werden um daraus mit Hilfe eines fluktuationsbasierten Ansatzes, welcher erstmals von Kubo beschrieben wurde,[16] das entsprechende dielekrische Spektrum zu berechnen. Diese Methode wird in Kapitel 3 aus Prinzipien der statistischen Mechanik hergeleitet. Daraus ergibt sich die Möglichkeit, die frequenzabhängige

elektrische Leitfähigkeit $\sigma_e(\omega)$ aus dem Gesamtstrom $\boldsymbol{j}(t)$ anhand der Formel

$$\sigma_e(\omega) = \frac{1}{3Vk_\mathrm{B}T} \int_0^\infty \langle \boldsymbol{j}(0)\, \boldsymbol{j}(\tau) \rangle\, e^{i\omega\tau}\, \mathrm{d}\tau \tag{1.4}$$

zu berechnen. Dabei bezeichnet V das Volumen des Systems, T seine Temperatur, k_B die Boltzmann-Konstante, der Operator $\langle\cdot\rangle$ steht für das kanonische Mittel und der Strom $\boldsymbol{j}(t)$ wird durch die Ladung q und Geschwindigkeit $\boldsymbol{v}(t)$ eines jeden Teilchens gemäß

$$\boldsymbol{j}(t) = \sum_i q_i\, \boldsymbol{v}_i(t) \tag{1.5}$$

berechnet. Die frequenzabhängige dielektrische Permittivität $\varepsilon_r(\omega)$ wird anschließend über Gleichung (1.3) berechnet.

Ursprünglich sollte der Titel dieser Arbeit lediglich „Vorhersage dielektrischer Spektren mit Hilfe von Computersimulationen“ lauten. Schon während der Entwicklung der für die Berechnung dielektrischer Spektren aus MD-Simulationen benötigten Programme (siehe Kapitel 4) wurde schnell kar, dass es diese Werkzeuge ermöglichen würden, eine Vielzahl unterschiedlicher Themenbereiche zu bearbeiten, bei welchen die Kenntnis dielektrischer Materialeigenschaften vonnöten ist.

Im Folgenden sind diese Themen im Hinblick sowohl auf unsere Beiträge zu Gemeinschaftsprojekten mit anderen Forschungsgruppen als auch unsere eigenen wissenschaftlichen Arbeiten zusammengefasst.

1.1 Die Nichtidealität mehrkomponentiger Lösungen

Wie bereits erwähnt wurde, bringen MD-Simulationen gegenüber experimentellen Messungen den Vorteil mit sich, dass die mikroskopischen Zustände und die dynamische Entwicklung des betrachteten

Systems stets bekannt sind. Insbesondere für die Berechnung dielektrischer Spektren bedeutet dies, dass die Beiträge unterschiedlicher molekularer Spezies getrennt voneinender betrachtet werden können, was gleichermaßen für deren gegenseitige Beeinflussung gilt. Zumal sich der Gesamtstrom $\boldsymbol{j}(t)$ diesbezüglich additiv verhält und es sich bei der Fourier-Laplace-Transformation in Gleichung (1.4) um eine lineare Transformation handelt, können die Anteile der in einer binären Mischung enthaltenen Molekülsorten A, B am Gesamtspektrum durch getrennte Summation über die entsprechenden Moleküle $\{n \in A\}$, $\{m \in B\}$ berechnet werden:

$$\boldsymbol{j}(t) = \boldsymbol{j}_{\mathrm{A}}(t) + \boldsymbol{j}_{\mathrm{B}}(t) = \sum_{n \in A} q_n \boldsymbol{v}_n(t) + \sum_{m \in B} q_m \boldsymbol{v}_m(t) \tag{1.6}$$

Daraus folgt, dass die Gleichung (1.4) in der Form

$$\begin{aligned} \sigma_e(\omega) &= \frac{1}{3Vk_{\mathrm{B}}T} \left(\langle \boldsymbol{j}_{\mathrm{A}}(0)\boldsymbol{j}_{\mathrm{A}}(t) \rangle_\omega + \langle \boldsymbol{j}_{\mathrm{B}}(0)\boldsymbol{j}_{\mathrm{B}}(t) \rangle_\omega + 2\langle \boldsymbol{j}_{\mathrm{A}}(0)\boldsymbol{j}_{\mathrm{B}}(t) \rangle_\omega \right) \\ &=: \sigma_{\mathrm{A}}(\omega) + \sigma_{\mathrm{B}}(\omega) + \sigma_{\mathrm{AB}}(\omega) \end{aligned} \tag{1.7}$$

ausgedrückt werden kann, wobei das Subskript ω als Kurzschreibweise für die Fourier-Laplace-Transformation verwendet wurde. Die Formel (1.3) für das dielektrische Spektrum kann gleichermaßen umgeformt werden:

$$\begin{aligned} \varepsilon_r(\omega) &= \varepsilon_r^\infty + \frac{i}{\varepsilon_0 \omega} \left(\sigma_{\mathrm{A}}(\omega) + \sigma_{\mathrm{B}}(\omega) + \sigma_{\mathrm{AB}}(\omega) \right) \\ &=: \varepsilon_r^\infty + \varepsilon_{\mathrm{A}}(\omega) + \varepsilon_{\mathrm{B}}(\omega) + \varepsilon_{\mathrm{AB}}(\omega) \end{aligned} \tag{1.8}$$

Die direkte Berechnung des spektralen Interaktionsanteils $\varepsilon_{\mathrm{AB}}(\omega)$ birgt die Möglichkeit, Korrelationseffekte in der Dynamik binärer Mischungen zu untersuchen.[b] Dementsprechend liegt es nicht fern, diese Möglichkeit zu nutzen, um die Eigenschaften von Systemen zu ergründen, in welchen zu erwarten ist, dass Korrelationseffekte eine nicht zu vernachlässigende Rolle spielen, was auf nichtideale Lösungen zutrifft. Mit dieser Zielsetzung untersuchten wir in Zusammenarbeit mit dem SimTech-Projekt 1-2 die Eigenschaften von wässrigen Dimethylsulfoxidlösungen

[b] Die Gleichungen (1.7) und (1.8) beschränken sich nicht auf binäre Lösungen; sie sind leicht auf mehrkomponentige Mischungen erweiterbar.

($DMSO_{aq}$).[17] Unsere Ergebnisse legen dar, dass es in der Tat der Kreuzterm $\varepsilon_{H_2O/DMSO}(\omega)$ ist, in welchem sich das nichtideale Verhalten des Systems manifestiert. Abbildung 1.2 stellt den konzentrationsabhängigen Verlauf der unterschiedlichen Beiträge $\varepsilon_{H_2O}(\omega)$, $\varepsilon_{DMSO}(\omega)$ und $\varepsilon_{H_2O/DMSO}(\omega)$ am Gesamtspektrum dar.

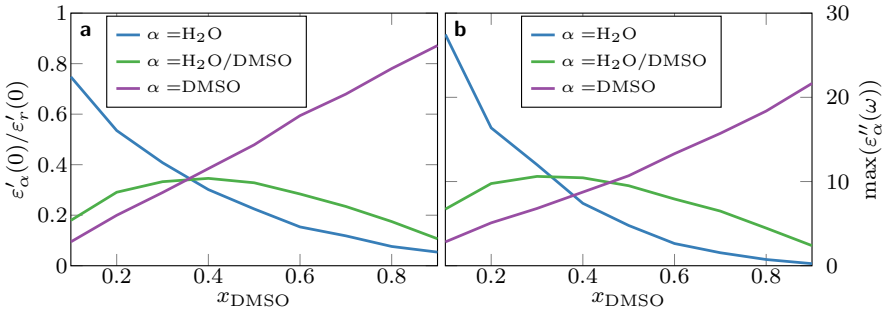

Abbildung 1.2: a: Relative Beiträge $\varepsilon'_\alpha(0)/\varepsilon'_r(0)$ der einzelnen Molekülsorten und Kreuzkorrelationsbeiträge an der gesamten statischen dielektrischen Permittivität $\varepsilon'_r(0)$ als Funktion des Stoffmengenanteils von DMSO (x_{DMSO}). **b**: Maximale Absorptionsamplitude $\max(\varepsilon''_\alpha(\omega))$ der unterschiedlichen Beiträge in Abhängigkeit von x_{DMSO}. Blaue Linien beschreiben die Beiträge des Wasseranteils, während violette den DMSO-Beitrag und grüne den Anteil der gegenseitigen Wasser-DMSO-Beeinflussung darstellen. Aus den Maxima der jeweiligen Interaktionsterme in den beiden Graphen lässt sich folgern, dass der größte Einfluss der Nichtidealität auf die Dynamik des Systems bei DMSO-Stoffmengenanteilen im Bereich von $0.3 < x_{DMSO} < 0.4$ liegt.

Der konzentrationsabhängige Anteil des Interaktionsterms im statischen Limes $\varepsilon'_{H_2O/DMSO}(0)/\varepsilon'_r(0)$ (grüne Linie in Abbildung 1.2a) legt nahe, dass der Einfluss der Nichtidealität im Bereich eines DMSO-Anteils $0.3 < x_{DMSO} < 0.4$ am größten ist. Dieses Verhalten ist auch in den Absorptionsamplituden $\max(\varepsilon''_\alpha(\omega))$ (Abbildung 1.2b) erkennbar. Alle anderen diesbezüglichen Ergebnisse, Berechnungen und deren Interpretation werden in der vorliegenden Arbeit nicht weiter diskutiert, sodass an dieser Stelle auf die entsprechende Referenz 17 verwiesen sei.

1.2 Bewertung von Molekulardynamik-Kraftfeldern

Zumal es eine stetig größerwerdende Anzahl an in der einschlägigen Literatur vorhandenen experimentell gemessenen dielektrischen Spektren unterschiedlichster Substanzen gibt, stellt die Berechnung solcher Spektren aus MD-Simulationen nicht nur eine Möglichkeit zur Erforschung prinzipieller dynamischer Effekte dar, sondern kann umgekehrt auch zur Validierung der Parametersätze molekularer Modelle (sogenannte *Kraftfelder*), welche in MD-Simulationen eingesetzt werden, herangezogen werden. Dementsprechend setzten wir unsere Berechnungsmethoden in Zussamenarbeit mit SimTech-Projekt 2-15 dazu ein, verschiedene Kraftfelder, welche für die Simulation von Trimethylamin N-oxid (TMAO) verwendet werden können, hinsichtlich ihrer Genauigkeit in der Vorhersage dynamischer Messgrößen zu bewerten. Abbildung 1.3 zeigt die Ergebnisse dieser Untersuchung bezüglich dreier Größen, welche die wichtigsten Eigenschaften der entsprechenden dielektrischen Spektren verdeutlichen.

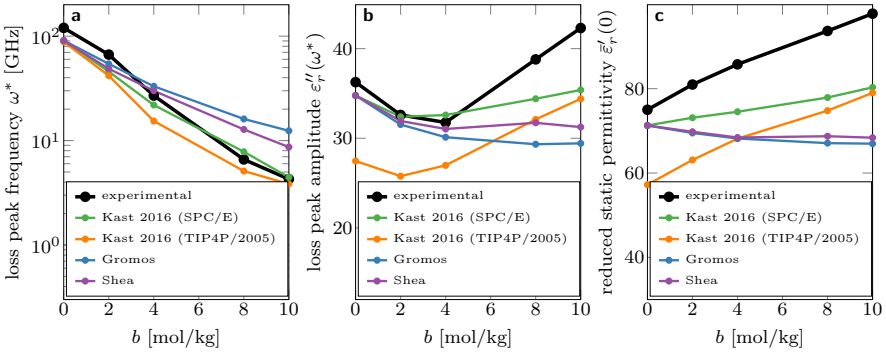

Abbildung 1.3: Vergleich konzentrationsabhängiger dielektrischer Eigenschaften wässriger TMAO-Lösungen, welche durch den Einsatz verschiedener TMAO-Modelle berechnet wurden, mit entsprechenden experimentellen Daten.[18] **a**: Frequenz ω^* entsprechend der Lage der Maximalamplitude in der dielektrischen Absorption $\varepsilon_r''(\omega)$. **b**: Maximalamplitude $\varepsilon_r''(\omega^*)$ der dielektrischen Absorption. **c**: Reduzierte statische Permittivität $\bar{\varepsilon}_r'(0) := \varepsilon_r'(0) - \varepsilon_r^\infty$.

Das Kast-2016-Modell unter gleichzeitiger Verwendung des TIP4P/2005-Wassermodells (orange) reproduziert die experimentllen Daten qualitativ erstaunlich gut, jedoch unterschätzt es alle dielektrischen Eigenschaften quantitativ um einem fast konstanten aber relativ großen Faktor. Die beste quantitative Übereinstimmung ergibt sich für dasselbe Modell, wenn es zusammen mit dem SPC/E-Wassermodell verwendet wird (grün). Leider vergrößert sich hierbei die quantitative Abweichung von $\varepsilon_r''(\omega^*)$ and $\bar{\varepsilon}_r'(0)$ vom Experiment bei hohen TMAO-Konzentrationen signifikant. Sowohl das Gromos- als auch das Shea-Modell versagen weitgehend in der Reproduktion experimenteller Daten bei hohen TMAO-Konzentrationen, und die statische Permittivität wird auch bei niedrigen Konzentrationen qualitativ und quantitativ eher unzureichend abgebildet.

Die anhand des Kast-2016-Modells mit SPC/E-Wasser berechneten dielektrischen Spektren sind über den gesamten erfassten Frequenzbereich in Abbildung 1.4 für TMAO-Molalitäten von 0 bis 10 mol/kg dargestellt und zeigen die relative gute Übereinstimmung dieser Modellkombination mit den aus Referenz 18 entnommenen experimentellen Daten.

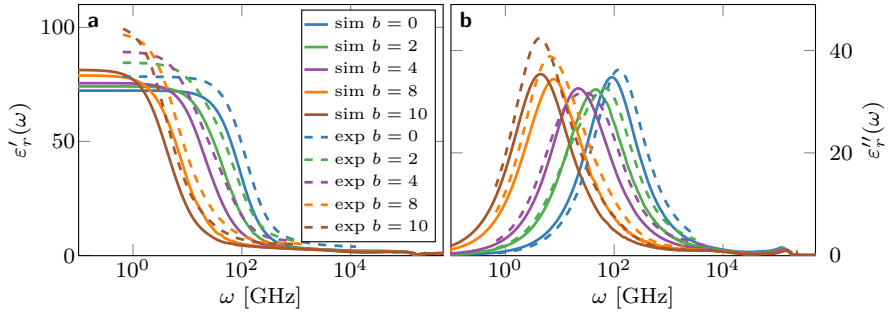

Abbildung 1.4: **a**: Dielektrische Dispersions- ($\varepsilon_r'(\omega)$) und **b**: Absorptionsspektren ($\varepsilon_r''(\omega)$) wässriger TMAO-Lösungen bei unterschiedlichen Molalitäten b. Die experimentellen Daten[18] werden qualitativ recht gut reproduziert, und auch die quantitativen Abweichungen, welche zum Teil auf das verwendete Wassermodell zurückzuführen sind, sind mit der Ausnahme von $\lim_{\omega\to 0}\varepsilon_r'(\omega)$ bei hohen TMAO-Konzentrationen eher klein.

Detailliertere Beschreibungen dieser und weiterer Ergebnisse finden sich in Referenz 19 und werden in dieser Arbeit nicht eingehender diskutiert.

1.3 Einfluss organischer Kosolute auf die lokale Wasserdynamik

Desweiteren nutzten wir die Möglichkeit der Zerlegung dielektrischer Spektren in die spezifischen Anteile unterschiedlicher Molekülarten, um den Einfluss organischer Kosolute auf die Dynamik von Wasser zu untersuchen. Organische Kosolute haben einen starken Einfluss auf die Stabilität, Funktion und Aktivität von Biomolekülen wie Proteine oder Enzyme in wässriger Lösung und sind deshalb von großer biologischer Relevanz.[20] Beispiele für solche Kosolute sind Trimethylamin N-oxid (TMAO) oder (S)-2-Methyl-3,4,5,6-Tetrahydropyrimidin-4-Carbonsäure (Ectoin), welche es Mikroorganismen erlauben unter extremen Umweltbedingungen zu überleben.[21] Die vorteilhafteste Eigenschaft dieser Moleküle ist vornehmlich ihre stabilisierende Wirkung auf die native Struktur von Proteinen[22–24] und den Erhalt der Fluidität von molekularen Doppelschichtstrukturen.[25,26] Aufgrund dieser Eigenschaften werden Moleküle wie TMAO oder Ectoin als Stabilisatoren bezeichnet.

Im Gegensatz dazu führen hohe Konzentrationen von Molekülen wie Guanidiniumchlorid (GdmCl) oder Harnstoff bei hoher Konzentration bereits bei moderaten Umgebungsbedingungen zur Denaturierung von Proteinstrukturen, weshalb diese Moleküle auch Denaturierer genannt werden. Zusammenfassend lässt sich sagen, dass zwei unterschiedliche Mechanismen[27] in Betracht gezogen werden können, welche die Denaturierung erklären: i) direkte Bindung des denaturierenden Stoffs an das Protein und ii) lösungsmittelinduzierte Effekte. Während die Wirkungsweisen von Denaturierern immer noch häufig diskutiert werden,

so ergab sich doch ein wissenschaftlicher Konsens bezüglich der Wirkungsweise von Stabilisatoren. Sowohl experimentelle Untersuchungen als auch Simulationen zeigten, dass Stabilisatoren bevorzugt keine direkte Bindung mit der Proteinoberfläche eingehen.[28–39] Somit besteht zwischen diesen Molekülen keine signifikante direkte Wechselwirkung und man findet sie oftmals in der zweiten oder dritten Hydratationsschale von Proteinen.[40] Es wird angenommen, dass dieser Ausschlusseffekt hauptsächlich durch die stark hygroskopischen Eigenschaften von Stabilisatoren hervorgerufen wird.[36,40] Aufgrund dieser Betrachtungen wird unterdessen angenommen, dass Stabilisatoren ein sogenanntes *kosmotropisches* (Wasserstruktur-bildendes) Verhalten aufweisen, während Denaturierer im Gegensatz dazu *chaotropisch* (strukturbrechend) wirken im Sinne einer angenommenen unvorteilhaften Beeinflussung der Wasserstruktur.[40,41] Genauer gesagt wurde hervorgehoben, dass kosmotrope Substanzen den Zusammenhalt zwischen Wassermolekülen durch Stabilisierung von Wasserstoffbrückenbindungen stärken, während chaotrope Substanzen diese Bindungen schwächen.

Da wir am Einfluss unterschiedlicher Kosolute auf die Wasserdynamik interessiert sind, richten wir unseren Fokus im Folgenden auf den Anteil $\varepsilon_{\mathrm{W}}(\omega)$ von Wasser-Wasser-Interaktionen an dielektrischen Spektren. Wie anhand der anteiligen Spektren in Abbildung 1.5 zu erkennen ist, rufen die verschiedenen von uns untersuchten Kosolute konzentrationsabhängig spezifische Änderungen hervor.

Die Stabilisatoren Ectoin und TMAO führen eindeutig zu Rotverschiebungen im Absorptionsspektrum von Wasser (siehe Abbildung 1.5b und 1.5d), welche eine Frequenzverschiebung um ungefähr einen Faktor 2 zwischen reinem Wasser und zwei-molaren Lösungen beinhalten.

Dies weist auf eine ausgeprägte Stärkung der Wasserstruktur durch die Verlangsamung der Rotationsdynamik hin und unterstützt somit die Vorstellung einer kosmotropischen Wirkung dieser Kosolute. Harnstoff scheint auch eine Rotverschiebung des Absorptionsspektrums auszulösen, wenn auch mit deutlich geringerer Ausprägung. Tatsächlich be-

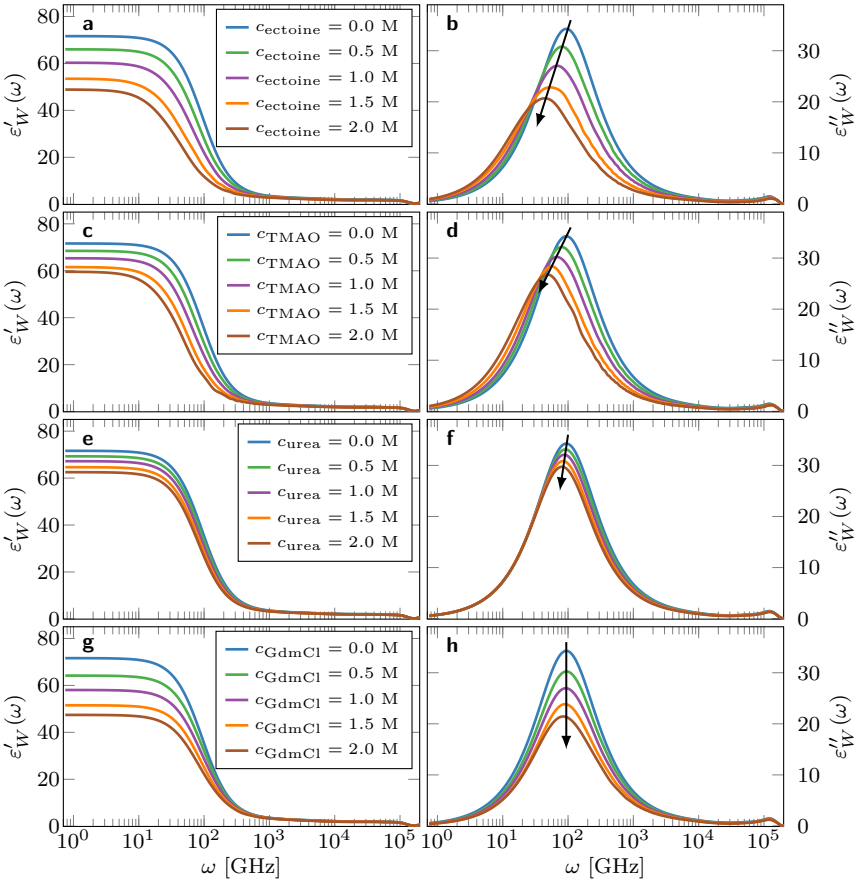

Abbildung 1.5: Wasseranteil $\varepsilon_W(\omega)$ an den dielektrischen Spektren unterschiedlicher wässriger Lösungen. **a**, **b**: Ectoin-Lösung, **b**, **c**: TMAO-Lösung, **d**, **e**: Harnstoff-Lösung, **f**, **g**: GdmCl-Lösung. Man beachte die Rotverschiebung (siehe schwarze Pfeile) des Hauptabsorptionsbereichs von Wasser mit steigender Konzentration der Stabilisatoren Ectoin oder TMAO. Dieser Effekt ist bei Harnstoff bedeutend schwächer, während GdmCl überhaupt keine Frequenzverschiebung im Spektrum zur Folge hat.

läuft sich die beobachtete Verschiebung nicht einmal auf die Hälfte des Effekts von Ectoin oder TMAO. Erstaunlicherweise scheint Guanidiniumchlorid die Reorientierungsdynamik von Wasser in keiner Weise zu beeinflussen, weshalb dieses Kosolut wahrscheinlich eher keinen signifi-

kanten Effekt auf das Wasserstoffbrückennetzwerk des Wassers hat. Die konzentrationsabhängige lineare Abnahme der Absorptionsamplitude ist in allen Spektren gleichermaßen beobachtbar und kann nicht mit einer echten quantitativen Änderung der dielektrischen Permittivität von Wasser einhergehen. Dies ist in der Tat nicht der Fall: Da die Berechnung aller Spektren einen Vorfaktor beinhaltet, der invers proportoinal zum Volumen des *gesamten* Systems ist (siehe Gleichung (1.4)), ist dieses Verhalten aufgrund des abnehmenden Partialvolumens von Wasser zu erwarten. Der Umstand, dass sich die Abnahme der Absorptionsamplitude linear zur Konzentration verhält, spricht desweiteren dafür, dass die Amplitude unverändert bleiben sollte, wenn sie stattdessen mit dem korrekten inversen Partialvolumen von Wasser skaliert wird.

Während die hier gezeigten dielektrischen Spektren bereits Schlüsse auf den Einfluss der unterschiedlichen Kosolute auf die Wasserdynamik zulassen, stellt die Tatsache, dass Wassermoleküle (zumindest in der Simulation) keine Nettoladung besitzen können, ein gewisses Problem dar: Eine rein translatorische Bewegung der neutralen Moleküle kann keine Veränderung in der mittleren Ausrichtung der molekularen Dipolmomente zur Folge haben, was streng genommen bedeutet, dass dielektrische Spektren ausschließlich Schlüsse auf die Reorientierungsdynamik des Wassers zulassen. Obwohl die translatorische Diffusion von Wassermolekülen auf langen Zeitskalen nicht ohne die Reorientierung umgebender Moleküle vonstatten gehen kann, lassen die Frequenzverschiebungen letzendlich keine gute Abschätzung der Stärke dieses Einflusses zu. Um diese Problematik zu umgehen, berechneten wir konzentrationsabhängige translatorische Diffusionskoeffizienten von Wasser, welche in Abbildung 1.6a dargestellt sind.

Während die Stabilisatoren Ectoin und TMAO die translatorische Diffusion von Wasser signifikant verlangsamen, ist der Effekt in Lösungen mit Harnstoff oder GdmCl deutlich weniger ausgeprägt. Dennoch zeigen beide Denaturierer ein schwach kosmotropisches Verhalten bezüglich des Diffusionskoeffizienten.

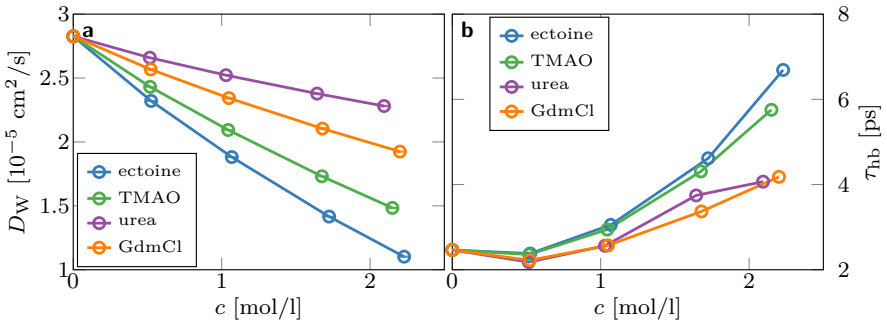

Abbildung 1.6: a: Translatorische Diffusionskoeffizienten D_W von Wasser in unterschiedlichen Lösungen. **b**: Wasser-Wasser Wasserstoffbrückenbindungs-Lebensdauern τ_{hb} in unterschiedlichen Lösungen.

Um den Einfluss der unterschiedlichen Kosolute auf die Stabilität des Wasserstoffbrückenbindungsnetzwerks eingehender zu untersuchen, berechneten wir die Lebensdauer dieser kurzlebigen Bindungen zwischen Wassermolekülen basierend auf der Theorie von Luzard und Chandler.[42,43] Wie aus Abbildung 1.6b hervorgeht, führt die Anwesenheit von Ectoin oder TMAO zu einer deutlich erhöhten Lebensdauer von Wasserstoffbrückenbindungen zwischen Wassermolekülen. Harnstoff zeigt eine ähnliche aber wesentlich schwächere Tendenz, während GdmCl einen vergleichsweise äußerst geringen Einfluss hat. Wenn man zusätzlich berücksichtigt, dass GdmCl die Anzahl der Wasserstoffbrückenbindungen pro Wassermolekül erniedrigt, zeigt GdmCl einen deutlich chaotropischen Einfluss auf die Struktur des Wasserstoffbrückenbindungsnetzwerks zwischen Wassermolekülen.

Desweiteren untersuchten wir die Konzentrationsabhängigkeit weiterer struktureller Eigenschaften von Wasser wie z. B. radiale Paarverteilungsfunktionen oder die Tetrahedralität der Wasserstruktur. Eine umfängliche Analyse und Diskussion all unserer diesbezüglichen Ergebnisse sowie deren Validierung gegenüber experimentellen Daten ist in Kapitel 5 zu finden.

1.4 Polarisierbare Kraftfelder für ionische Flüssigkeiten

In klassischen Molekulardynamiksimulationen werden Atome (der Atomgruppen) üblicherweise als Punktmassen modelliert, welche eine konstante Ladung tragen. Viele Molekularmodelle nehmen zusätzliche Vereinfachungen vor, wie z. B. das Fixieren von Bindungslängen zwischen Atomen eines Moleküls oder deren Bindungswinkel. Ein einfaches Beispiel für ein solches Modell ist SPC/E-Wasser. Somit ist das permanente molekulare Dipolmoment solcher Modelle konstant, und die dipolare Anregung (und somit deren Relaxation) ist ausschließlich über Rotationsbewegungen vollständiger Moleküle möglich. Flexible Molekularmodelle ohne solche Einschränkungen beinhalten weitere innere Freiheitsgrade, was Fluktuationen ihres molekularen Dipolmoments durch Bindungsvibrationen oder dihedrale Schwingungen zulässt. Dennoch tragen die einzelnen Teilchen solcher Modelle konstante Punktladungen.

Echte Atome verhalten sich jedoch so, dass Dipole oder elektrische Momente höherer Ordnung durch ein externes elektrisches Feld und die einhergehende Verschiebung der Elektronen gegenüber den Atomkernen induziert werden können. Obwohl eine rigorose Behandlung solcher Phänomene allgemein quantenmechanische Betrachtungen erfordert, so können sie bei kleinen Feldstärken doch relativ gut durch einfache klassische Modelle approximiert werden. Einer dieser Ansätze ist der klassische *Drude-Oszillator*, wobei die „Elektronenwolke“ eines Atoms durch eine einfache zusätzliche Punktladung modelliert wird, welche sich in einem symmetrischen harmonischen Potential um den Atomkern bewegen kann. Aus Sicht von Computersimulationen hat dieses Modell den großen Vorteil, dass es relativ einfach in bestehende Programme integriert werden kann. Das Prinzip eines Drude-Oszillators ist in Abbildung 1.7 dargestellt. Eine detailliertere Beschreibung kann anderweitig eingesehen werden.[44]

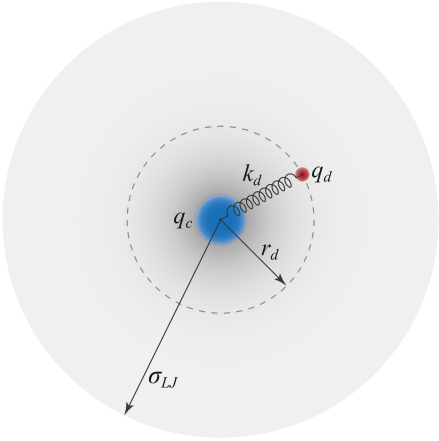

Abbildung 1.7: Skizzierung eines Drude-Oszillators, wie er in MD-Simulationen eingesetzt wird. Ein sogenanntes Drude-Teilchen (rot), welches eine Ladung q_d trägt, wird zu einem Atom mit der Ladung q_c (blau) hinzugefügt, sodass die Summe beider Ladungen die ursprüngliche Gesamtladung $q = q_c + q_d$ ergibt. Die einzige Wechselwirkung dieser beiden Teilchen besteht durch ein abstandsabhängiges harmonisches Potential $V_d(r_d) = \frac{1}{2} k_d r_d^2$, welches sein Minimum bei $r_d = 0$ hat, d.h. es besteht keine Coulomb-Wechselwirkung zwischen q_c und q_d. Die resultierende Polarisierbarkeit dieses Drude-Paars ist gegeben durch $\alpha \propto \frac{q_d^2}{k_d}$, wobei die Proportionalitätskonstante vom gewählten Einheitensystem abhängt. Die Polarisierbarkeit muss dabei bekannt sein, sodass entweder q_d oder k_d so gewählt werden muss, dass $\langle r_d^2 \rangle \ll \sigma_{LJ}$ (σ_{LJ} ist der Lennard-Jones-Durchmesser des Atoms) um dem Fall einer sogenannten „Polarisationskatastrophe“ vorzubeugen.

Ionische Flüssigkeiten (englisch: *ionic liquids* (ILs)) stellen eine relativ neue Materialklasse dar, deren Modellierung von der Berücksichtigung elektronischer Polarisationseffekte profitieren kann. ILs sind Flüssigkeiten, welche ausschließlich aus Ionen bestehen und einen Schmelzpunkt unterhalb von $\approx 400\,\mathrm{K}$ besitzen. Viele dieser Flüssigkeiten haben ihren Schmelzpunkt deutlich unter $300\,\mathrm{K}$ und werden aufgrund ihrer hohen Ladungsträgerdichte und ihres relativ großen elektrochemischen Fensters als Ersatz für konventionelle Dielektrika z. B. in Superkondensatoren eingesetzt. Während viele thermodynamische Größen von ILs auch mit nicht-polarisierbaren Modellen reproduziert werden können, so ist dies für die korrekte Beschreibung ihrer Wechselwirkungen

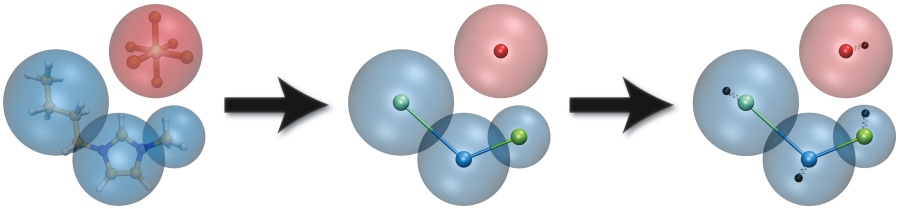

Abbildung 1.8: Schema der Vorgehensweise bei der Modellentwicklung. Auf der linken Seite ist ein atomistisches Modell zu sehen, wobei die entsprechenden Atomgruppen (Butyl, Imidazolium, Methyl und PF_6), welche im vergröberten Modell (ILM1-Modell, Mitte) als jeweils einzelne Punktteilchen zusammengefasst wurden, durch transparente Kugeln markiert sind. Dieser Schritt vom atomistischen hin zum vergröberten, nicht-polarisierbaren Modell war von Roy u. a.[45] bereits durchgeführt. Um den zweiten Schritt vom vergröberten Modell hin zum ebenfalls vergröberten, jedoch explizit polarisierbaren Modell (rechts) zu gehen, verwendeten wir Polarisierbarkeiten, welche durch DFT-basierte ab-initio Rechnungen (durchgeführt von F. Uhlig) ermittelt wurden. Die Größe der transparenten Kugeln entspricht den Lennard-Jones-Radien der jeweiligen Gruppen der vergröberten Modelle. Die Abstände zwischen den Drude-Teichen und den „Kernen" sind deutlich vergrößert dargestellt. Das harmonische Potential zwischen Kernen und Drude-Teilchen ist jeweils durch eine kleine Spiralfeder dargestellt.

mit geladenen Oberflächen weniger leicht möglich. Jedoch ist bisher nicht vollständig bekannt, welche Eigenschaften von ILs durch deren elektronische Polarisierbarkeit besonders beeinflusst werden.

Um zukünftig den Einfluss der expliziten Modellierung elektronischer Polarisierbarkeit auf die Eigenschaften von ILs untersuchen zu können, entwickelten wir ein vergröbertes IL-Kraftfeld in Zusammenarbeit mit SimTech-Projekt 2-3. Beim dafür von uns gewählten IL handelt es sich um 1-Butyl-3-Methylimidazolium Hexafluorophosphat ($[C_4C_1Im]^+[PF_6]^-$), zumal dies eine experimentell relativ gut untersuchte ionische Flüssigkeit ist. Unsere Parametrisierung stützt sich dabei auf das bereits bestehende, nicht-polarisierbare aber bereits vergröberte ILM1-Modell von Roy u. a.,[45] zu welchem wir Drude-Oszillatoren hinzufügten und im Gegenzug die Lennard-Jones-Parameter so anpassten, dass das Modell Massendichte und Diffusionskoeffizienten möglichst gut reproduziert. Abbildung 1.8 zeigt die Geometrie eines atomistischen Modells von $[C_4C_1Im]^+[PF_6]^-$, die des vergröberten ILM1-

Modells, sowie unser polarisierbares Modell. Dadurch, dass wir nun zwei sehr ähnliche Kraftfelder zur Verfügung haben, von denen eines die elektronische Polarisierbarkeit der Ionen explizit modelliert, erhoffen wir uns, direkte Vergleiche im Verhalten dieser Modelle in zukünftigen Arbeiten im Bezug auf den Einfluss der Polarisierbarkeit ziehen zu können. Die gesamte Entwicklung des Kraftfeldes sowie dessen Validierung anhand experimenteller Daten ist in Kapitel 6 beschrieben.

1.5 Ionische Abschirmeffekte im Vollraum und unter räumlichem Einschluss

Innerhalb der letzten Jahre wurde mehrmals experimentell gezeigt, dass der abstandsabhängige Verlauf der abstoßenden Kraft zwischen zwei gleichgeladenen, atomar glatten Oberflächen einem exponentiellen Zerfall mit ungewöhnlich großer Abklinglänge folgt, wenn sich zwischen diesen Oberflächen konzentrierte Elektrolyte oder ionische Flüssigkeiten befinden.[46–51] Dieser Effekt wurde als *Underscreening* bezeichnet und es wurde vermutet, dass er auf ein diesen Substanzen inhärentes, langreichweitiges Verhalten der elektrostatischen Abschirmung innerhalb der Flüssigkeiten zurückzuführen ist.[52] Dennoch konnte der genaue Ursprung dieses Verhaltens bis heute nicht abschließend bestimmt werden, sodass diese Experimente ein wichtiges aber bisher unerklärtes Phänomen begründen.[53] Insbesondere im Hinblick auf die Entwicklung elektronischer Komponenten wie z. B. Superkondensatoren, in denen konzentrierte Elektrolyte und ionische Flüssigkeiten unter starkem räumlichem Einschluss vorliegen, sollte das Verständnis des Underscreening-Phänomens von besonderer Bedeutung sein.

Es ist bekannt, dass das traditionelle Verständnis einer mit zunehmender Elektrolytkonzentration abnehmenden elektrostatischen Abschirmlänge nur für den Bereich geringer Konzentrationen gilt. In diesem Bereich kann das räumliche Verhalten der Abschirmung elektrostatischer

Wechselwirkungen zwischen Ionen in guter Näherung durch die Debye-Hückel-Theorie[54] oder – im Falle der Abschirmung geladener makroskopischer Objekte – durch die Poisson-Boltzmann-Gleichung[55,56] beschrieben werden. In beiden Fällen ergibt sich die Abklingkonstante des asymptotischen Abschirmverhaltens als die sogenannte Debye-Länge λ_D, welche durch

$$\lambda_\mathrm{D}^2 = \frac{\varepsilon_0 \varepsilon_r k_\mathrm{B} T}{\sum_i \rho_i z_i^2 e^2} \tag{1.9}$$

gegeben ist. Dabei bezeichnet ε_0 wiederum die Vakuumpermittivität, ε_r die relative Permittivität eines homogenen Hintergrundmediums, k_B die Boltzmann-Konstante, und T die Temperatur. Im Nenner repräsentieren ρ_i und z_i die Anzahldichte und Valenz der Ionensorte i und e ist die Elementarladung.

Mit steigender Elektrolytkonzentration werden die effektiven Teilchenwechselwirkungen zunehmend durch Dichte- und Ladungskorrelationseffekte beeinflusst, welche durch eine solche Molekularfeldtheorie nicht beschrieben werden können. Dementsprechend gibt es viele Modifizierungen und Erweiterungen der Debye-Hückel- and Poisson-Boltzmann-Theorie sowie andere Ansätze, welche vorhersagen, dass die Korrelationslängen mit steigender Ionenkonzentration ansteigen,[57–69] was somit gleichermaßen einen Anstieg der effektiven elektrostatischen Abschirmlänge zur Folge hat. Diesbezüglich von besonderer Relevanz sind Integralgleichungstheorien[57–59,64,65] basierend auf der Betrachtung radialer Paarverteilungsfunktionen (englisch: *radial pair distribution functions* (RDFs)) $g_{XY}(r)$, welche die Wahrscheinlichkeit beschreiben, ein Teilchen der Sorte Y im Abstand r von einem Teilchen der Sorte X zu finden, und bezüglich der Eintrittswahrscheinlichkeit dieses Falls in einem idealen Gas gleicher Dichte normiert sind. Im Rahmen dieser Theorien zeigen Analysen der Ornstein-Zernike-Gleichung, dass das asymptotische Abklingverhalten von Ionen-Ionen-Wechselwirkungen bei ausreichend hoher Konzentration durch die Funktion

$$\lim_{r\to\infty} w_{XY}(r) \propto \frac{A}{r} \cos\left(k\, r - \phi\right) \exp\left(-\frac{r}{\lambda_\mathrm{S}}\right) \tag{1.10}$$

ausgedrückt werden kann. Dabei bezeichnet w_{XY} das Potential mittlerer Kraft (englisch: *potential of mean force* (PMF)) zwischen den Teilchenspezies X und Y, A und ϕ sind eine von der Teilchensorte abhängige Amplitude and Phasenverschiebung, λ_S ist die asymptotische Abklinglänge des PMFs und die Wellenzahl k bestimmt die Wellenlänge der Oszillation. In einem homogenen Medium kann das PMF zwischen den Teilchensorten X und Y aus der zugehörigen RDF anhand der Beziehung

$$w_{XY}(r) = -k_B T \ln\left(g_{XY}(r)\right) \tag{1.11}$$

berechnet werden. In dieser Arbeit werten wir das Abklingverhalten solcher PMFs aus, welche mit Hilfe von MD-Simulationen extrem großer konzentrierter Elektrolyt- und IL-Systeme berechnet wurden. Dabei weisen unsere Ergebnisse darauf hin, dass es unwahrscheinlich ist, den Underscreening-Effekt durch das den untersuchten Substanzen eigene Abklingverhalten erklären zu können. Als Beispiel dafür ist das PMF zwischen Kationen und Anionen des reinen ILs $[C_4C_1Im]^+[PF_6]^-$in Abbildung 1.9 dargestellt. Die Daten wurden aus Simulationen vollatomistischer Modelle berechnet, welche 108 000 Ionenpaare in einem kubischen Simulationsvolumen mit einer Kantenlänge von $\approx 34\,\mathrm{nm}$ enthalten.

Zusätzlich konnten wir die Ergebnisse solcher großskaliger Vollraum-Simulationen durch weitere Simulationen ionischer Flüssigkeiten im Einschluss zwischen gleichgeladenen Wänden bestätigen. Anders als im Vollraum kann die elektrostatische Abschirmlänge dort durch die Betrachtung der gemittelten Ladungsverteilung in der Flüssigkeit im Bezug auf den Abstand zu den Wänden ermittelt werden.

Im Bereich hoher Konzentrationen zeigen unsere Simulationen, dass die Abschirmlängen tatsächlich mit der Konzentration ansteigen, was im Einklang mit klassischen Flüssigkeitstheorien zu erwarten ist. Unsere Analysen – und das gilt ebenfalls für Systeme, bei denen die ILs räumlich eingeschlossen sind – zeigen jedoch auch, dass in diesen Systemen keine unerwartet hohen Abschirmlängen auftreten. Wie aus Betrachtungen auf Grundlage der statistischen Mechanik zu erwarten ist,[66]

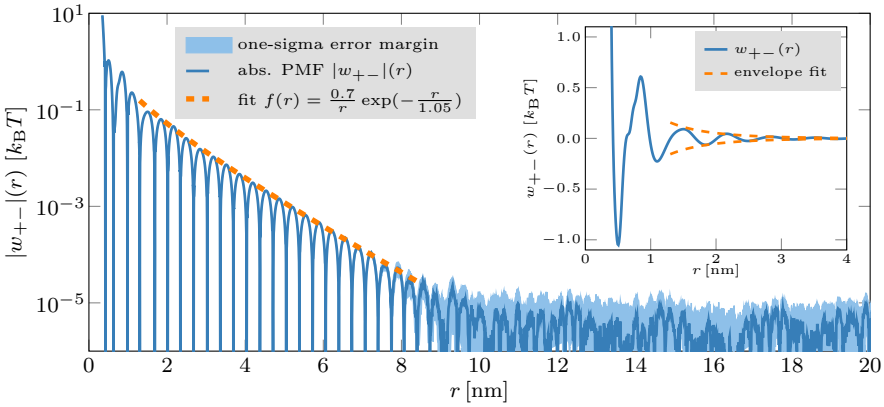

Abbildung 1.9: Absolutbetrag des Potentials mittlerer Kraft (PMF) $|w_{+-}|(r)$ zwischen Kationen und Anionen, welches aus Simulationen von 108 000 Ionenpaaren des reinen ILs $[C_4C_1Im]^+[PF_6]^-$ bei $T = 300\,\mathrm{K}$ und $p = 1\,\mathrm{bar}$ berechnet wurde. Bis zu $r \approx 8.5\,\mathrm{nm}$ folgt $w_{+-}(r)$ dabei einem oszillatorischen Zerfall, dessen Einhüllende (gestrichelte orange Linie) durch die Funktion $f(r) = {}^{a}/_{r} \exp({}^{-r}/_{\lambda_S})$ mit $a = 0.7\,k_B T$ und $\lambda_S = 1.05\,\mathrm{nm}$ beschrieben werden kann. Für $r > 8.5\,\mathrm{nm}$ geht das PMF in einen Bereich mit fast konstanter Amplitude über, wobei der statistische Fehler (hellblauer Bereich) verhältnismäßig hoch ist. Dasselbe PMF $w_{+-}(r)$ ist in der eingefügten Abbildung mit linearer y-Achsenskalierung dargestellt.

stimmen die Abschirmlängen ionischer Flüssigkeiten aus Analysen der Vollraumsysteme sehr gut mit den Ergebnissen unter Einschluss gehaltener Systeme überein. Desweiteren zeigen wir, dass einige theoretische Modelle, die von anderen dazu benutzt wurden, einen Bezug zwischen der gemessenen Abschirmlängen zu anderen physikalischen Messgrößen herzustellen, bei hohen Elektrolytkonzentrationen nicht anwendbar sind.

Unsere Simulationsanalysen bezüglich elektrostatischer Abschirmlängen in konzentrierten Elektrolyten und ionischen Flüssigkeiten werden in Kapitel 7 vollumfänglich dargelegt.

2 Introduction and Overview

The first theoretical concepts of dielectric relaxation processes date back to the early twentieth century and are most prominently known from the works of Peter Debye.[1] Today, the name *dielectric spectroscopy* is actually a collective term for several experimetal techniques that measure the frequency-dependent response coefficient $\varepsilon_r(\omega)$ of a medium to an externally applied electric field $\boldsymbol{E}$ oscillating at an angular frequency ω up to the THz regime.[4] This response coefficient relates the induced polarization $\boldsymbol{P}$ (the response) of the medium to the applied field $\boldsymbol{E}$. For a homogeneous, isotropic dielectric medium and in the limit of low field strengths, the following relation holds:

$$\boldsymbol{P} = \varepsilon_0 \chi_e \boldsymbol{E} = \varepsilon_0(\varepsilon_r - 1)\boldsymbol{E} \tag{2.1}$$

The constant ε_0 denotes the permittivity of free space. The response coefficient $\chi_e = \varepsilon_r - 1$ is called the (dimensionless) *electric susceptibility*, and ε_r the *relative permittivity*, which is in general a complex-valued quantity defined as

$$\varepsilon_r(\omega) = \varepsilon_r'(\omega) - i\varepsilon_r''(\omega)\,, \tag{2.2}$$

where i denotes the imaginary number defined as $i^2 = -1$. Its real part $\varepsilon_r'(\omega)$ is usually referred to as *dielectric dispersion*[a] and is proportional to the energy of the perturbing field $\boldsymbol{E}$ *reversibly* stored in the medium. With increasing frequency, the constituents of the medium

[a] Note that the term 'dispersion' also refers to the general phenomenon that the dielectric permittivity depends nontrivially on the frequency ω, which applies to $\varepsilon_r(\omega)$ as a whole. Here, however, it is used exclusively to denote its real part $\varepsilon_r'(\omega)$.

fail to directly follow the oscillation of the perturbing field due to both inertial and frictional effects, leading to a phase shift between the external field and the response in the medium. This gives rise to a non-zero (negative) imaginary part ε_r'' of the complex permittivity. Since this "lag" is generally related to material-dependent dissipative effects, the amplitude of ε_r'' is a measure for absorption, and therefore called *dielectric loss*. In contrast to dielectric dispersion, the dielectric loss is proportional to the energy *irreversibly* dissipated in the medium. Due to the fact that the frequency-dependent behavior of both the real and imaginary part of $\varepsilon_r(\omega)$ is caused by the same physical processes, there exists a causal (and thus, analytical) relationship between ε_r' and ε_r''.[2] In fact, one can be computed from the other by means of the Kramers-Kronig relations.[3]

In an experiment, the complex permittivity is usually extracted from measurements of the frequency-dependent complex conductivity $\sigma_e(\omega)$ according to[4]

$$\varepsilon_r(\omega) = \varepsilon_r^{\infty} + \frac{i\sigma_e(\omega)}{\varepsilon_0 \omega}\,, \tag{2.3}$$

where the term ε_r^{∞} denotes the so-called "infinite-frequency" or "instantaneous" response. This offset incorporates relaxation processes that are too fast to be captured by a (generally band-limited) measurement, *e.g.*, electronic or nuclear polarization.

During the past century, dielectric spectroscopy has emerged as an important tool in science and technology, helping to gain insights on dynamic processes taking place on different time scales within all kinds of materials. The blue line in fig. 2.1, which represents the number of publications per year involving the terms "dielectric relaxation" or "dielectric spectroscopy" found using Google Scholar,[5] shows that this scientific field is still growing. Dielectric spectroscopy has a broad range of industrially relevant applications ranging from biosensing[6–8] over optimization and quality control in chemical engineering[9–11] and food processing[12–14] to battery engineering.[15]

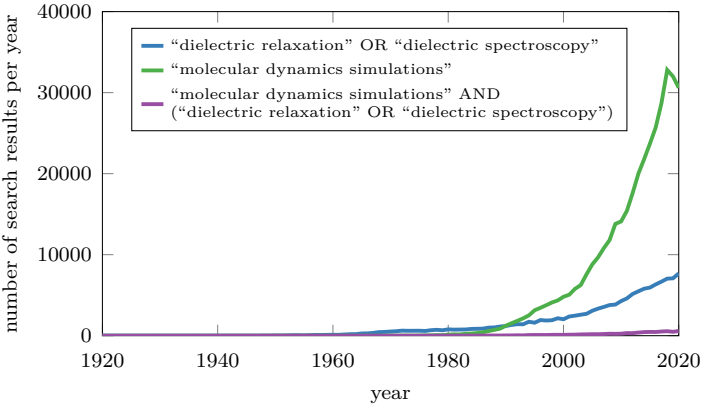

Figure 2.1: Number of Google Scholar[5] search results per year from 1920 to 2020 for the search terms *"dielectric relaxation" OR "dielectric spectroscopy"* (blue line), *"molecular dynamics simulations"* (green line), and *"molecular dynamics simulations" AND ("dielectric relaxation" OR "dielectric spectroscopy")* (purple line). Quite obviously, the number of publications mentioning both dielectric relaxation / spectroscopy and molecular dynamics in conjunction is rather low.

While the different experimental techniques employed to measure dielectric relaxation spectra are well understood, the interpretation of the results in terms of identifying the responsible microscopic mechanisms often proves difficult and is sometimes ambiguous. On the contrary, in molecular dynamics (MD) simulations, a particle-based simulation method allowing to investigate molecular processes with sub-nanometer and femtosecond resolution (see section 3.3 for a detailed description), this is expected to be much more feasible as the microscopic details are directly at hand. While MD simulations have become an extremely popular tool in scientific research (see the green line in fig. 2.1), the prediction of dynamic dielectric material properties from MD simulations has so far received rather little attention as the purple line in fig. 2.1 demonstrates. One of the reasons for this is the high computational cost involved in such calculations, as the extraction of dielectric spectra requires very long total simulation times in the order of microseconds. However, with the advent of powerful hardware

accelerators such as graphics processing units, it is nowadays possible to reach such time scales within reasonable computation time.

In simulations, the calculation of dielectric permittivities could in principle be accomplished in the same way as it is done in experiments, *i.e.*, by applying an oscillating external electric field within the simulations. This, however, would mean that one had to perform separate simulations for each point in the frequency range of interest, and thus, depending on the desired range and resolution, the required computational effort could quickly get out of hand.

In an equilibrium system at finite temperature, particles permanently move in and out of their equilibrium positions even if there is no external field applied. Since the particles in a dielectric medium carry (at least partial) charges, there exist internally created time-dependent electric fields within the medium. The spatial conformation and velocities of all particles in the simulated system are known at every time step of the simulation, so that the system's response to its own fluctuating internal fields can be measured and used to extract the dielectric permittivity spectrum employing a fluctuation-based approach developed by Kubo.[16] This approach will be derived from fundamental statistical-mechanical principles in chapter 3, with the result that the frequency-dependent electric conductivity can be computed from the cumulative current $\boldsymbol{j}(t)$ according to

$$\sigma_e(\omega) = \frac{1}{3Vk_\mathrm{B}T} \int_0^\infty \langle \boldsymbol{j}(0)\, \boldsymbol{j}(\tau) \rangle\, e^{i\omega\tau}\, \mathrm{d}\tau\,, \tag{2.4}$$

where V is the volume of the system, T denotes temperature, k_B is the Boltzmann constant, the operator $\langle\cdot\rangle$ is the canonical average, and the current $\boldsymbol{j}(t)$ is obtained from each particle's charge q and velocity $\boldsymbol{v}(t)$ according to

$$\boldsymbol{j}(t) = \sum_i q_i\, \boldsymbol{v}_i(t)\,. \tag{2.5}$$

The frequency-dependent dielectric permittivity $\varepsilon_r(\omega)$ can then be obtained from eq. (2.3).

Originally, the title of this thesis was intended to simply read "Predicting Dielectric Spectra by Computer Simulations". However, after having successfully developed a computational framework facilitating the extraction of dielectric spectra from MD simulations as described in detail in chapter 4, it turned out that these computational tools can be leveraged and extended to support the work on a broad range of topics requiring the knowledge of dielectric properties of the investigated sytems. In the following, these topics are briefly summarized in the light of our contributions to collaborations with other research projects and our own work.

2.1 Nonideality of Solutions

As mentioned above, MD simulations have the advantage over experiments that the microscopic molecular conformations and dynamics are directly accessible. In particular, for the analysis of dielectric spectra, this means that contributions from different species can be separated, as well as the contributions arising from interactions between the different species. Since the current $\boldsymbol{j}(t)$ is additive and the Fourier-Laplace transform in eq. (2.4) is linear, the contributions of different molecular species A, B in a binary system to the overall spectrum can be calculated by summing over the corresponding molecules $\{n \in A\}$, $\{m \in B\}$ individually:

$$\boldsymbol{j}(t) = \boldsymbol{j}_{\mathrm{A}}(t) + \boldsymbol{j}_{\mathrm{B}}(t) = \sum_{n \in A} q_n \boldsymbol{v}_n(t) + \sum_{m \in B} q_m \boldsymbol{v}_m(t) \tag{2.6}$$

Thus, it follows that equation (2.4) can be written as

$$\begin{aligned} \sigma_e(\omega) &= \frac{1}{3Vk_{\mathrm{B}}T} \left(\langle \boldsymbol{j}_{\mathrm{A}}(0) \boldsymbol{j}_{\mathrm{A}}(t) \rangle_\omega + \langle \boldsymbol{j}_{\mathrm{B}}(0) \boldsymbol{j}_{\mathrm{B}}(t) \rangle_\omega + 2 \langle \boldsymbol{j}_{\mathrm{A}}(0) \boldsymbol{j}_{\mathrm{B}}(t) \rangle_\omega \right) \\ &=: \sigma_{\mathrm{A}}(\omega) + \sigma_{\mathrm{B}}(\omega) + \sigma_{\mathrm{AB}}(\omega) \,, \end{aligned} \tag{2.7}$$

where we have used the subscript ω as a short-hand notation for the Fourier-Laplace transform. The dielectric permittivity spectrum (2.3)

can be decomposed accordingly:

$$\begin{aligned}\varepsilon_r(\omega) &= \varepsilon_r^\infty + \frac{i}{\varepsilon_0 \omega}\left(\sigma_{\mathrm{A}}(\omega) + \sigma_{\mathrm{B}}(\omega) + \sigma_{\mathrm{AB}}(\omega)\right) \\ &=: \varepsilon_r^\infty + \varepsilon_{\mathrm{A}}(\omega) + \varepsilon_{\mathrm{B}}(\omega) + \varepsilon_{\mathrm{AB}}(\omega) \end{aligned} \tag{2.8}$$

The ability to directly extract the interaction part $\varepsilon_{\mathrm{AB}}(\omega)$ of the spectra provides the possibility to investigate correlation effects in the dynamics of binary solutions.[b] Thus, it stands to reason that we use it to examine properties of systems where correlation effects play a major role, as it is the case in nonideal solutions. To this aim, in collaboration with SimTech project 1-2, we investigated the properties of aqueous dimethyl sulfoxide (DMSO) solutions.[17] Our results show that it is indeed the cross-term $\varepsilon_{\mathrm{H_2O/DMSO}}(\omega)$ exhibiting the nonideal behavior of the solution. Figure 2.2 displays the concentration-dependent characteristic features of the different contributions $\varepsilon_{\mathrm{H_2O}}(\omega)$, $\varepsilon_{\mathrm{DMSO}}(\omega)$, and $\varepsilon_{\mathrm{H_2O/DMSO}}(\omega)$.

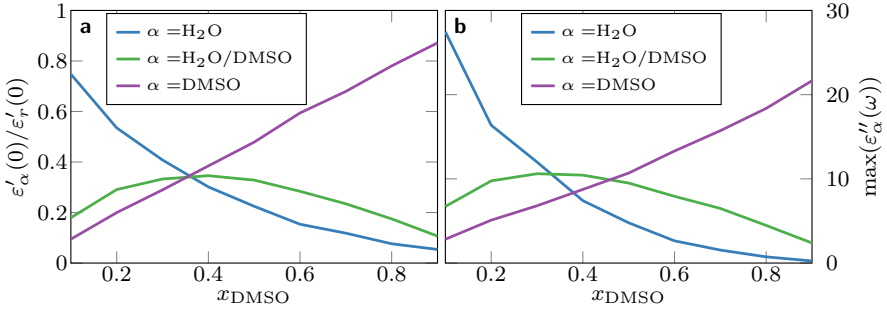

Figure 2.2: **a**: Relative contributions $\varepsilon'_\alpha(0)/\varepsilon'_r(0)$ of the individual species and cross correlation contributions to the resulting total dielectric constant $\varepsilon'_r(0)$ with respect to the molar fraction of DMSO (x_{DMSO}). **b**: Maximum loss peak amplitudes $\max(\varepsilon''_\alpha(\omega))$ of the different contribution as a function of x_{DMSO}. Blue lines denote the results for water contributions whereas purple lines represent the results for DMSO, and correlated water-DMSO contributions are depicted by green lines. The maxima of the interaction terms in both graphs indicate a maximum influence of the nonideality on dynamics at molar fractions of DMSO in the range of $0.3 < x_{\mathrm{DMSO}} < 0.4$.

[b] Equations (2.7) and (2.8) are of course not limited to binary solutions; extending them to multi-component systems is straightforward.

The concentration-dependent relative contribution of the interaction term in the static limit $\varepsilon'_{\mathrm{H_2O/DMSO}}(0)/\varepsilon'_r(0)$ (green line in fig. 2.2a) indicates that the maximum effect of the nonideality on dynamics lies in the range of molar DMSO fractions $0.3 < x_{\mathrm{DMSO}} < 0.4$. This behavior is also reflected in the loss peak amplitudes $\max(\varepsilon''_\alpha(\omega))$ depicted in fig. 2.2b. Further results and an in-depth discussion of the matter can be found in the corresponding publication (reference 17), which will not be further discussed in this thesis.

2.2 Force Field Evaluation

Since an ever-growing number of experimentally measured dielectric relaxation spectra covering a plethora of different chemical substances are available in the literature, dielectric spectra obtained from computer simulations are not only a valuable tool to answer basic scientific questions, they can also be used to validate the molecular models (the so-called *force fields*) employed in the underlying MD simulations. In cooperation with SimTech project 2-15, we used dielectric spectroscopy to assess the performance of different models of trimethylamin N-oxide (TMAO), since the spectra provide a very comprehensive measure for the qualitative and quantitative validity of the models' dynamics. Figure 2.3 provides a comparison of the performance of three of the assessed models with respect to their dielectric properties.

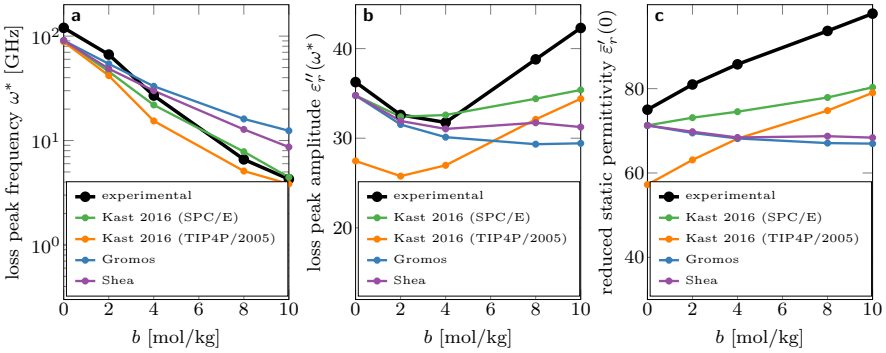

Figure 2.3: Comparison of concentration-dependent dielectric properties of aqueous TMAO solutions obtained with different TMAO models against experimental data.[18] **a**: loss peak frequency ω^*, *i.e.*, the frequency where the maximum of the absorption peak $\varepsilon''_r(\omega)$ is located. **b**: loss peak amplitude $\varepsilon''_r(\omega^*)$, the maximum amplitude of $\varepsilon''_r(\omega)$, located at $\omega = \omega^*$. **c**: reduced static permittivity $\bar{\varepsilon}'_r(0) := \varepsilon'_r(0) - \varepsilon^\infty_r$.

The Kast 2016 model in conjunction with the TIP4P/2005 water model (orange) follows the experimental data qualitatively remarkably well, however, it underestimates all dielectric properties by an almost constant but rather large factor. The best quantitative agreement is found for the same TMAO model but in combination with SPC/E water (green). Unfortunately, the quantitative deviation of $\varepsilon_r''(\omega^*)$ and $\bar{\varepsilon}_r'(0)$ from the experiment becomes large for high TMAO concentrations. The Gromos and Shea models completely fail to reproduce the experiment at high concentrations, and even for low molalities the static permittivity is both quantitatively and qualitatively insufficient.

In fig. 2.4, the dielectric spectra of aqueous TMAO solutions are shown for different concentrations ranging from 0 to 10 mol/kg. These spectra were obtained using the Kast 2016 model (TMAO-V3) in combination with SPC/E water and show the good agreement of this model with experimental data extracted from reference 18.

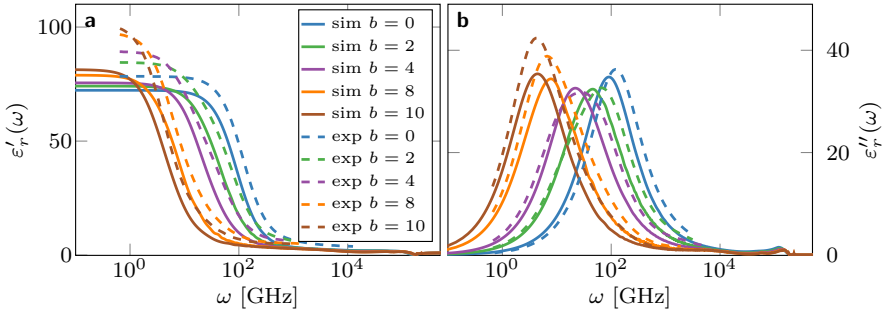

Figure 2.4: **a**: Dielectric dispersion $\varepsilon_r'(\omega)$ and **b**: Loss spectra $\varepsilon_r''(\omega)$ of aqueous TMAO solutions for different TMAO molalities b. The experimental data[18] are qualitatively well reproduced, and also the quantitative deviations, which are partly due to the water model, are rather small except for $\lim_{\omega\to 0} \varepsilon_r'(\omega)$ at high TMAO concentrations.

The full force field comparison was published in ref. 19 and will not be further discussed in this thesis.

2.3 Influence of Organic Cosolutes on Local Water Dynamics

We further exploited the ability to decompose dielectric spectra into individual contributions for the investigation of the effects of organic cosolutes on water dynamics. Organic cosolutes have a strong impact on the stability, function, and activity of biomolecules such as proteins or enzymes in aqueous solution, and are therefore of great biological relevance.[20] Common examples are trimethylamine N-oxide (TMAO) or ectoine, which allow microorganisms to survive under extreme environmental conditions.[21] Beneficial properties of these molecules are the stabilization of native protein structures[22–24] and the maintenance of the fluidity of bilayers.[25,26] Due to these properties, molecules such as TMAO or ectoine are commonly called protectants or stabilizers. In contrast, guanidinium chloride (GdmCl) or urea at high molar concentrations denature protein structures even at moderate environmental conditions and are therefore referred to as denaturants or destabilizers. In summary, two distinct reasons were proposed[27] to explain the denaturation mechanism: i) a direct binding between the denaturant and the protein in contrast to ii) solvent-mediated effects. Whereas the properties of denaturants are even nowadays often discussed, a consensus was found for the behavior of protein protectants. Experimental findings as well as computer simulations revealed that protectants are usually excluded from protein surfaces[28–39] in terms of a preferential exclusion behavior. Thus, they do not directly interact with protein surfaces and are often located in the second or third hydration shell.[40] It was assumed that the exclusion effect is mainly induced by the strong hygroscopic properties of protectants.[36,40] Due to these findings, protectants are assumed to be kosmotropic (water structure making) whereas denaturants are *vice versa* assigned to be chaotropic (water structure breaking) in terms of their unfavorable perturbation of the water structure.[40,41] In more detail, it was pointed out that kosmotropes strengthen the local interaction between water molecules, *i.e.*, the hydrogen bond network, whereas chaotropes weaken these bonds.

Since we are interested in the effect of the different cosolutes on water dynamics, we will focus on the water-water interaction parts $\varepsilon_W(\omega)$ of the spectra in the following. As we can see in the graphs shown in fig. 2.5, these exhibit distinct cosolute-dependent changes of their features at different cosolute concentrations.

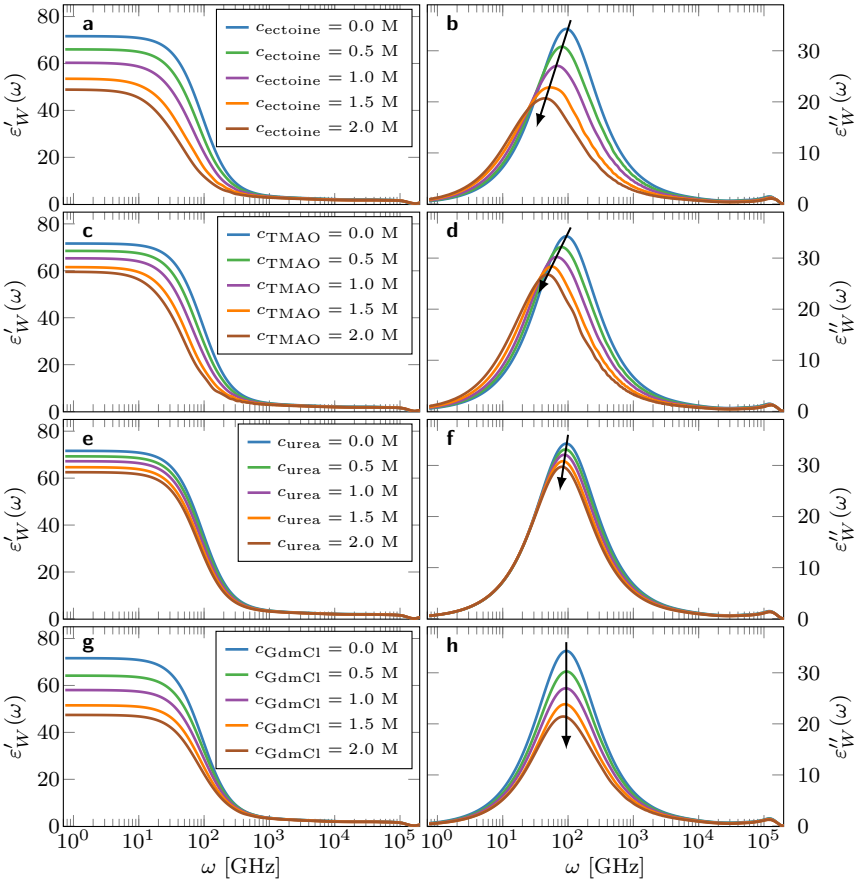

Figure 2.5: Contributions $\varepsilon_W(\omega)$ of water to the spectra of different aqueous solutions. **a**, **b**: ectoine solution, **b**, **c**: TMAO solution, **d**, **e**: urea solution, **f**, **g**: GdmCl solution. Note the red-shift of the main water absorption peaks for increasing concentrations (indicated with black arrows) of the stabilizers ectoine or TMAO. The effect is much weaker or not present at all for the denaturants urea and GdmCl, respectively.

The protectants ectoine and TMAO clearly induce a significant red-shift of the corresponding water absorption peaks (see fig. 2.5b and 2.5d), leading to a decrease of the peak frequency by about a factor of 2 from 0 to 2-molar concentrations. This indicates a pronounced strengthening of the water structure by slowing down reorientational water dynamics, supporting the suggested kosmotropic behavior of those cosolutes. Urea also seems to induce a red shift in the water absorption peak, however to a much lesser extent. In fact, the observed red shift is not even half as strong as for ectoine or TMAO. Surprisingly, guanidinium chloride does not seem to influence water reorientation dynamics at all, and thus is very unlikely to have a strengthening effect on the water hydrogen bond network. The linear decrease in amplitude clearly visible in all spectra cannot be attributed to any real quantitative change in the permittivity of water. In fact, quite the contrary is likely to be true: Since the computation of all spectra involves a prefactor inversely proportional to the volume of the *entire* system (*cf.* equation (2.4)), this behavior is expected due to the decreasing partial volume of water in the system. The circumstance that the decrease is linear with respect to the cosolute concentration is a further hint that the spectra would quantitatively remain unaltered when scaled with the correct inverse *partial* volume of water in the system instead.

While the dielectric spectra shown above already yield valuable insights on the influence of the different cosolutes on water dynamics, the fact that water molecules do not carry a net charge (at least not in the simulations) poses a problem: Purely translational motion of overall electrically neutral molecules does not induce changes in the orientation of their dipole moments, and thus, strictly speaking, dielectric spectra only provide insights into the reorientational dynamics of water. Even though this cannot be entirely true since the translational diffusion of water molecules on long time scales is hardly possible without concurrent rotations, the observed frequency shifts in the dielectric absorption spectra do not provide a good estimate of how strongly translational motion is affected. To resolve this issue, we calculated concentration-

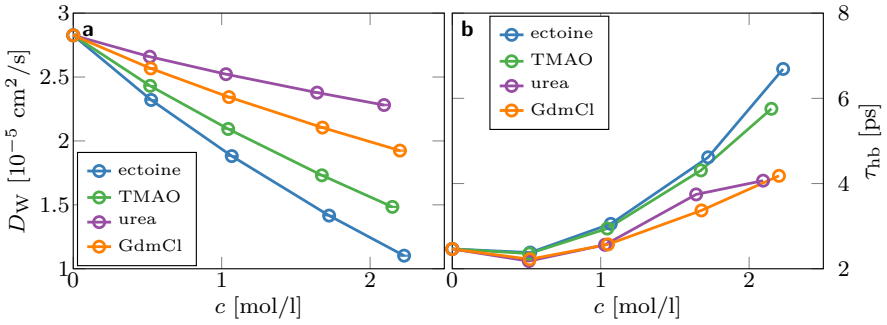

Figure 2.6: **a**: Average translational diffusion coefficients D_W of water in different aqueous solutions. **b**: Water-water hydrogen bond life times τ_{hb} in different aqueous solutions.

dependent average translational diffusion coefficients of water, which are plotted in fig. 2.6a.

While the protectants ectoine and TMAO significantly slow down the translational diffusion of water, the effect is less pronounced in solutions containing the denaturants urea or GdmCl. Nevertheless, in terms of translational diffusion, also the denaturants exhibit a slightly kosmotropic behavior.

Moreover, to better quantify the influence of the different cosolutes on the water hydrogen bond network, we calculated average water-water hydrogen bond life times according to the theory of Luzard and Chandler.[42,43] As it is shown in fig. 2.6b, the presence of ectoine leads to a significant increase of water-water hydrogen bond life times. Urea solutions show a similar but much weaker tendency, while GdmCl even leads to a slight decrease of the life times. Taking into account that GdmCl decreases the average number of hydrogen bonds per water molecule, GdmCl definitely exhibits chaotropic behavior by dynamically weakening the water-water hydrogen bond structure.

We furthermore investigated the dependence on cosolute concentration of many other dynamical as well as structural properties of water, such as rotational diffusion coefficients, radial distribution functions,

and tetrahedrality order parameters. A comprehensive and conclusive analysis of all our findings including their validation against experimental data is presented in chapter 5.

2.4 Polarizable Force Fields for Ionic Liquids

In classical molecular dynamics simulations, atoms (or groups of atoms) are usually modeled as point masses carrying constant charges. Many molecular models make further simplifications by constraining the bond lengths between the atoms of a molecule or even by fixing the angles between bonds to a constant value. A simple example is SPC/E water, a completely rigid three-site model. Thus, its dipole moment is permanent and constant, and the only possible dipolar "excitation" and (thus, relaxation) in this model is by reorientation of the whole molecule. Flexible molecular models where such constraints are not applied have additional internal degrees of freedom, and therefore their permanent dipole moments can fluctuate due to bond vibrations and angular or dihedral oscillations. Nevertheless, the atoms of such models still have constant point charges. In real atoms, however, dipole or higher-order multipole moments can be induced under the influence of an electric field by displacing their electrons with respect to their nuclei. Even though a rigorous treatment of the phenomenon generally involves quantum mechanics, it can be approximated by simple classical models in the limit of low field strengths. One such approach is the *classical Drude oscillator*, where an atom's electron "cloud" is modeled by a point charge residing in a (usually radially symmetric) harmonic potential centered at the nucleus. From a simulational point of view, this model bears the advantage that it can be readily implemented into existing code since it involves only harmonic potentials and pairwise electrostatic point charge interactions. The principle of a Drude oscillator is sketched and briefly explained in figure 2.7, more detailed information on the subject can be found elsewhere.[44]

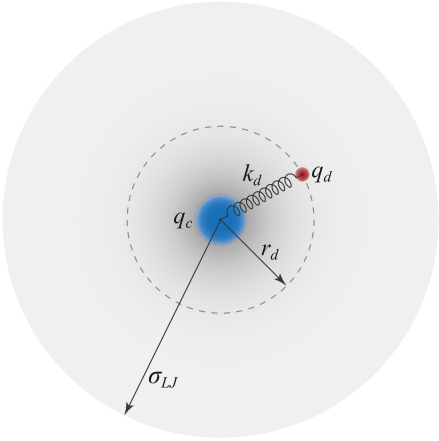

Figure 2.7: Sketch of a drude oscillator. A Drude particle (red) carrying a charge q_d is added to an atom (blue) with charge q_c so that these charges add up to the atom's original charge $q = q_c + q_d$. The only interaction between the two particles is through a distance-dependent harmonic potential $V_d(r_d) = \frac{1}{2}k_d r_d^2$ with its minimum at $r_d = 0$, *i.e.* there is no Coulomb interaction between q_c and q_d. The resulting polarizability of the Drude pair is then given by $\alpha \propto \frac{q_d^2}{k_d}$, where the proportionality constant depends on the chosen unit system. The polarizability must be known *a priori* so that either q_d or k_d has to be chosen in a way that $\langle r_d^2 \rangle \ll \sigma_{LJ}$ (with σ_{LJ} being the atom's Lennard-Jones radius) in order to avoid what is commonly known as a "polarization catastrophe".

A novel class of substances requiring to incorporate explicit electronic polarizability in the respective molecular models are ionic liquids (ILs). In recent years, ILs gained an increasing technological relevance due to their unique properties. ILs are substances with a melting point below $\approx 400\,\mathrm{K}$ and consist entirely of ions. Many of them have their melting point well below $300\,\mathrm{K}$, and due to their high density of charge carriers and large electrochemical window, they are used as dielectrics in nanoporous supercapacitors, replacing conventional electrolytes. While it may be possible to reproduce several thermodynamic observables of ILs in the bulk with non-polarizable models, this is much harder to achieve for the correct description of their interactions with charged surfaces. However, it is not known which properties are particularly influenced by electronic polarization.

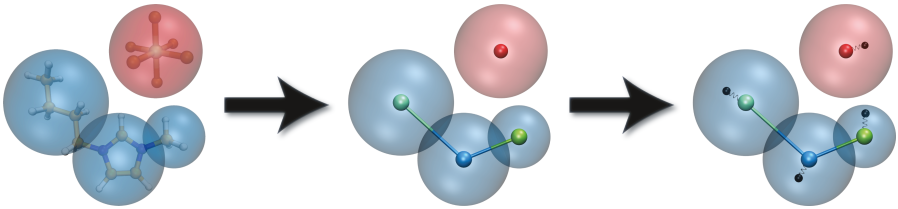

Figure 2.8: Schematic of the model development. On the left, an atomistic ball-and-stick model is shown with the respective coarse-grained groups (butyl, imidazolium, methyl, and PF_6) indicated by transparent overlays. The coarse-graining step from the atomistic model to the coarse-grained non-polarizable model has already been done by Roy *et al.*.[45] We then used polarizabilities from ab-initio and DFT-based calculations performed by Frank Uhlig to proceed with the parametrization of our polarizable coarse-grained model depicted on the right. The size of the transparent spheres correspond to the Lennard-Jones radii of the respective groups used in the coarse-grained models. The distances of the Drude particles from the "cores" are exaggerated for better visibility. The harmonic potential between cores and Drude particles is illustrated by small springs.

To investigate the effect of explicitly modeled electronic polarizability on the properties of ILs, we parametrized a coarse-grained polarizable model ionic liquid force field in cooperation with SimTech project 2-3. The substance we chose to model is 1-butyl-3-methylimidazolium hexafluorophosphate ($[C_4C_1Im]^+[PF_6]^-$), since it is a rather common and experimentally relatively well-studied IL. Our parametrization is based on the pre-existing non-polarizable coarse-grained ILM1 model by Roy *et al.*,[45] to which we added Drude oscillators and reparametrized the Lennard-Jones parameters by fitting them against density and diffusion constants. Figure 2.8 depicts the geometries of an atomistic $[C_4C_1Im]^+[PF_6]^-$model, the coarse-grained ILM1 model, and our re-parametrized polarizable model. Having two very similar coarse-grained models at hand whereof one incorporates explicit electronic polarizability should provide us with the possibility to make direct comparisons between them in order to assess polarizability effects in future work. The procedure of the force field development and its validation against experimental data are described in chapter 6.

2.5 Ionic Screening in Bulk and Under Confinement

Recent experiments have shown that the repulsive force between atomically flat, like-charged surfaces confining room-temperature ionic liquids or concentrated electrolytes exhibits an anomalously large decay length.[46–51] Termed underscreening, this effect was suggested to be a property of bulk electrolytes.[52] However, its exact origin is still under debate so that the experimental measurements constitute an important but not yet understood[53] phenomenon. Understanding the origin of these findings should be especially important for the design of devices where concentrated electrolytes or ILs are strongly confined between highly charged surfaces, as, *e.g.*, in modern supercapacitors.

The traditional view that the electrostatic screening length decreases with increasing electrolyte concentration is well-known to be valid only at low ion concentrations. In the low-concentration regime, the spatial decay of ion-ion interactions is usually well-described by approaches such as the Debye-Hückel theory,[54] or, for the electrostatic screening of immersed charged objects, the Poisson-Boltzmann equation.[55,56] In both cases, the asymptotic decay length of electrostatic interactions equals the Debye length λ_D defined as

$$\lambda_\mathrm{D}^2 = \frac{\varepsilon_0 \varepsilon_r k_\mathrm{B} T}{\sum_i \rho_i z_i^2 e^2} \,. \tag{2.9}$$

Here, ε_0 is the permittivity of free space, ε_r the relative dielectric permittivity of a homogeneous background medium, k_B the Boltzmann constant, and T denotes absolute temperature. In the denominator, ρ_i and z_i represent the number density and valency of ionic species i, and e is the elementary charge.

With rising electrolyte concentration, interactions are increasingly influenced and eventually dominated by excluded-volume and charge correlations, which are difficult to describe by such mean-field approaches. There are many modifications and extensions of

the Debye-Hückel and Poisson-Boltzmann theory and other approaches predicting that correlation lengths increase with concentration,[57–69] therefore resulting in an increasing effective screening length[c]. Especially relevant are integral-equation theories[57–59,64,65] based on descriptions of the radial distribution functions (RDFs) $g_{XY}(r)$, which describe the probability of finding a particle of species Y at a distance r from a particle of species X and is normalized with respect to the corresponding probability in an ideal gas at the same concentration. Within these frameworks, analyses of the Ornstein-Zernike equation show that for sufficiently high concentrations, the asymptotic decay of ion-ion interactions can be expressed as

$$\lim_{r\to\infty} w_{XY}(r) \propto \frac{A}{r}\cos\left(k\,r-\phi\right)\exp\left(-\frac{r}{\lambda_{\mathrm{S}}}\right)\,, \tag{2.10}$$

where w_{XY} denotes the potential of mean force (PMF) between species X and Y, A and ϕ are species-dependent amplitudes and phase shifts, λ_{S} is the PMF's asymptotic decay length, and the wave vector k determines the wavelength of its oscillation. In spatially homogeneous systems, the PMF between species X and Y can be obtained from their RDF according to

$$w_{XY}(r) = -k_{\mathrm{B}}T\ln\left(g_{XY}(r)\right)\,. \tag{2.11}$$

Here, we show by evaluating the decay of PMFs obtained from extremely large-scale molecular dynamics simulations of concentrated electrolytes and ILs that the underscreening effect is unlikely to be a feature of bulk electrolytes. As an example, the PMF between cations and anions obtained from simulations containing 108 000 ion pairs of the pure IL $[\mathrm{C_4C_1Im}]^+[\mathrm{PF_6}]^-$in a cubic simulation box with an edge length of $\approx 34\,\mathrm{nm}$ is displayed in fig. 2.9.

We corroborate these findings by expanding our investigations to ionic liquids under confinement. Unlike in bulk systems, where screening

[c]Note that we use the term 'screening length' also for the decay of oscillatory modes.

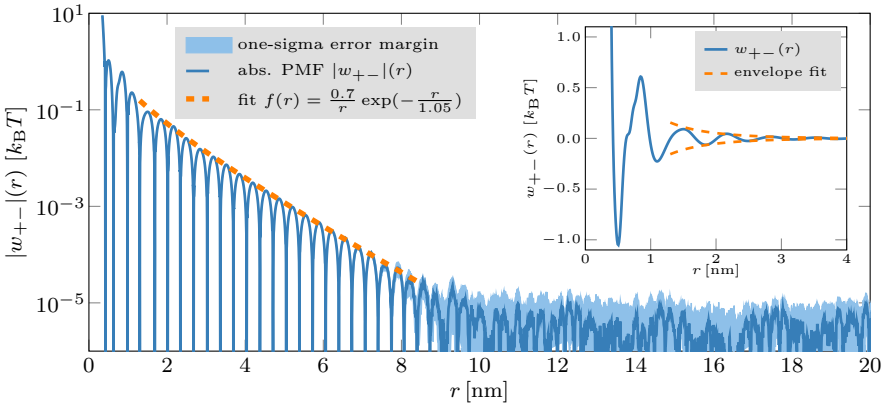

Figure 2.9: Absolute value of the potential of mean force (PMF) $|w_{+-}|(r)$ between cations and anions obtained from a simulation of 108 000 ion pairs of the pure IL $[C_4C_1Im]^+[PF_6]^-$ at $T = 300\,K$ and $p = 1\,bar$. $w_{+-}(r)$ follows an oscillatory decay up to $r \approx 8.5\,nm$, with the decay envelope (dashed, orange line) described by $f(r) = {}^{a}/_{r} \exp(-{}^{r}/_{\lambda_S})$ with $a = 0.7\,k_B T$ and $\lambda_S = 1.05\,nm$. For $r > 8.5\,nm$, the potential enters a region of almost constant noise level with rather high uncertainty (light blue area). Inset: The same anion-cation PMF $w_{+-}(r)$ with linear y-axis scaling.

lengths are computed from the decay of interionic potentials of mean force (PMFs), we extract such data in confined systems from cumulative charge distributions. At high concentrations, our simulations show increasing screening lengths with increasing electrolyte concentration, consistent with classical liquid state theories. However, our analyses demonstrate that—also for confined systems—there is no anomalously large screening length. As expected from statistical-mechanical considerations,[66] the screening lengths determined for ionic liquids under confinement are in good quantitative agreement with the screening lengths of the same ionic systems in bulk. In addition, we show that some theoretical models used in the literature to relate the measured screening lengths to other observables are inapplicable to highly concentrated electrolytes. Our findings regarding ionic screening in concentrated electrolytes and ionic liquids are presented and discussed in a comprehensive manner in chapter 7.

Published Work

The following list contains publications I wrote or contributed to during the course of my work as a doctoral student. Note that only the framed items will be discussed within this thesis.

1. M. B. Hahn, T. Solomun, R. Wellhausen, S. Hermann, H. Seitz, S. Meyer, H.-J. Kunte, J. Zeman, F. Uhlig, J. Smiatek and H. Sturm, Influence of the Compatible Solute Ectoine on the Local Water Structure: Implications for the Binding of the Protein G5P to DNA, *The Journal of Physical Chemistry B* **119**, 15212–15220 (2015)

2. A. N. Krishnamoorthy, J. Zeman, C. Holm and J. Smiatek, Preferential solvation and ion association properties in aqueous dimethyl sulfoxide solutions, *Physical Chemistry Chemical Physics* **18**, 31312–31322 (2016)

3. D. Markthaler, J. Zeman, J. Baz, J. Smiatek and N. Hansen, Validation of Trimethylamine-N-oxide (TMAO) Force Fields Based on Thermophysical Properties of Aqueous TMAO Solutions, *The Journal of Physical Chemistry B* **121**, 10674–10688 (2017)

4. J. Zeman, F. Uhlig, J. Smiatek and C. Holm, A coarse-grained polarizable force field for the ionic liquid 1-butyl-3-methylimidazolium hexafluorophosphate, *Journal of Physics: Condensed Matter* **29**, 504004 (2017)

5. F. Uhlig, J. Zeman, J. Smiatek and C. Holm, First-Principles Parametrization of Polarizable Coarse-Grained Force Fields for Ionic Liquids, *Journal of Chemical Theory and Computation* **14**, 1471–1486 (2018)

6. M. P. Schlaile, J. Zeman and M. Mueller, It's a match! Simulating compatibility-based learning in a network of networks, *Journal of Evolutionary Economics* **28**, 1111–1150 (2018)

7. J. Michalowsky, J. Zeman, C. Holm and J. Smiatek, A polarizable MARTINI model for monovalent ions in aqueous solution, *The Journal of Chemical Physics* **149**, 163319 (2018)

8. M. P. Schlaile, T. Knausberg, M. Mueller and J. Zeman, Viral ice buckets: A memetic perspective on the ALS Ice Bucket Challenge's diffusion, *Cognitive Systems Research* **52**, 947–969 (2018)

9. J. Zeman, C. Holm and J. Smiatek, The Effect of Small Organic Cosolutes on Water Structure and Dynamics, *Journal of Chemical & Engineering Data* **65**, 1197–1210 (2020)

10. J. Zeman, S. Kondrat and C. Holm, Bulk ionic screening lengths from extremely large-scale molecular dynamics simulations, *Chemical Communications* **56**, 15635–15638 (2020)

11. J. Zeman, S. Kondrat and C. Holm, Ionic screening in bulk and under confinement, *The Journal of Chemical Physics* **155**, 204501 (2021)

3 Theoretical Framework

3.1 Linear Response Theory

The basic idea behind the concept of linear response is that the spatiotemporal evolution of a physical system subject to a weak external disturbance can be well approximated by a linear superposition of the system's natural (*i.e.*, unperturbed) evolution with an additional term describing the influence of the disturbance. The fundamental insight of this approach is that the relaxation of the disturbed system back to equilibrium is governed by the same physics as the relaxation of its thermal fluctuations about equilibrium, so that a system's dynamic response to a weak disturbance is entirely determined by its dynamics at thermal equilibrium.

With respect to this thesis, the most relevant results of linear response theory are the form of the response function $\phi_{AB}(\tau)$, and, consequently, that of the generalized susceptibility $\chi_{AB}(\omega)$ for systems maintained at a constant temperature T. The response function $\phi_{AB}(\tau)$ describes a system's response in terms of the expected change $\langle \Delta B(\tau) \rangle$ of an observable B to a unit pulse of an external force $F(t) = \delta(t)$ with conjugate displacement A at the time τ after the pulse. As will be shown below, it is given by

$$\phi_{AB}(\tau) = \frac{1}{k_{\mathrm{B}} T} \langle \dot{A}(0)\, B(\tau) \rangle_{\mathrm{eq}} \,,$$

where k_{B} is the Boltzmann constant and the operator $\langle \cdot \rangle_{\mathrm{eq}}$ denotes the expected value at thermal equilibrium. The generalized susceptibility $\chi_{AB}(\omega)$ describes the frequency-dependent proportionality of

the response $\langle \Delta B(\tau) \rangle$ to the periodic disturbance $F(\omega, t) = F_0\, e^{-i\omega t}$ according to

$$\langle \Delta B(\tau) \rangle = \chi_{AB}(\omega)\, F(\omega, t)$$

and is given by

$$\begin{aligned} \chi_{AB}(\omega) &= \frac{1}{k_\mathrm{B} T} \int_0^\infty \phi_{AB}(\tau)\, e^{i\omega\tau}\, \mathrm{d}\tau \\ &= \frac{1}{k_\mathrm{B} T} \int_0^\infty \langle \dot{A}(0)\, B(\tau) \rangle_\mathrm{eq}\, e^{i\omega\tau}\, \mathrm{d}\tau\,. \end{aligned}$$

In the following section 3.1.1, we will provide a general derivation of these findings along the lines of the most relevant publications of R. Kubo,[16,79] including some ideas of V. Balakrishnan's excellent lecture[80] on the topic. Thereafter, in section 3.1.2, the general results will be applied to constant-temperature statistical ensembles since those are the relevant ones for this thesis.

Note: Any reader who is already familiar with the framework of linear response theory is advised to skip the following sections 3.1.1 and 3.1.2, and continue with section 3.2, where the theory will be applied to the specific case of dielectric response.

3.1.1 General derivation

Let us consider an isolated thermodynamic system at equilibrium, which is fully described by the Hamiltonian $\mathcal{H}(\boldsymbol{p}, \boldsymbol{q})$ with canonical coordinates $\boldsymbol{q} = \{q_i\}$ and conjugate momenta $\boldsymbol{p} = \{p_i\}$ spanning its phase space Ω with infinitesimal volume elements $\mathrm{d}\Omega = \mathrm{d}\boldsymbol{q}\mathrm{d}\boldsymbol{p}$. The system's microscopic time evolution is uniquely defined by Hamilton's equations

$$\dot{\boldsymbol{p}} = -\frac{\partial \mathcal{H}}{\partial \boldsymbol{q}}\,, \qquad \dot{\boldsymbol{q}} = \frac{\partial \mathcal{H}}{\partial \boldsymbol{p}}\,, \tag{3.1}$$

where the dot symbol is a short-hand notation for the derivative with respect to time $\left(\dot{x} := \frac{\mathrm{d}x}{\mathrm{d}t}\right)$.

According to *Liouville's theorem*, the system's probability density function $\rho(\boldsymbol{p}, \boldsymbol{q}, t)$ of microscopic states $(\boldsymbol{q}, \boldsymbol{p})$ in the statistical ensemble is stationary, *i.e.*

$$\dot{\rho} = \frac{\partial \rho}{\partial t} + \sum_i \left(\frac{\partial \rho}{\partial q_i} \dot{q}_i - \frac{\partial \rho}{\partial p_i} \dot{p}_i \right) = 0 \,, \tag{3.2}$$

so that by inserting eq. (3.1), its time evolution is governed by the Liouville equation

$$\frac{\partial \rho}{\partial t} = \{\mathcal{H},\, \rho\} \,, \tag{3.3}$$

where the expression $\{\cdot,\, \cdot\}$ on the right hand side represents the *Poisson bracket*

$$\{f,\, g\} := \sum_i \left(\frac{\partial f}{\partial q_i} \frac{\partial g}{\partial p_i} - \frac{\partial f}{\partial p_i} \frac{\partial g}{\partial q_i} \right) . \tag{3.4}$$

Since the system is at equilibrium, the expected value

$$\langle X \rangle = \int_{\Omega} X(\boldsymbol{q}, \boldsymbol{p})\, \rho(\boldsymbol{q}, \boldsymbol{p}, t)\, \mathrm{d}\boldsymbol{q}\mathrm{d}\boldsymbol{p} \tag{3.5}$$

of any observable $X(\boldsymbol{q}, \boldsymbol{p})$ must be time invariant so that

$$\frac{\mathrm{d}\langle X \rangle}{\mathrm{d}t} = \frac{\partial \langle X \rangle}{\partial t} = \int_{\Omega} X(\boldsymbol{q}, \boldsymbol{p})\, \frac{\partial \rho(\boldsymbol{q}, \boldsymbol{p}, t)}{\partial t}\, \mathrm{d}\boldsymbol{q}\mathrm{d}\boldsymbol{p} = 0 \,. \tag{3.6}$$

According to Liouville's theorem, the phase space volume is conserved, so that for the integral to vanish, it follows that $\frac{\partial \rho}{\partial t} = 0$. Thus, the equilibrium Liouville equation must satisfy

$$\frac{\partial \rho_{\mathrm{eq}}}{\partial t} = \{\mathcal{H}_{\mathrm{eq}},\, \rho_{\mathrm{eq}}\} = 0 \,, \tag{3.7}$$

where the subscripts indicate equilibrium conditions.

Let us now perturb the system by applying a generalized external force $F(t)$ adiabatically turned on in the infinite past such that $F(-\infty) = 0$ and $\dot{F}(-\infty) = 0$, *i.e.*, the system is in equilibrium at $t = -\infty$. The perturbation energy is then given by $\mathcal{H}_{\text{ext}} = -AF(t)$, where $A = A(\boldsymbol{q}, \boldsymbol{p})$ is the conjugate displacement associated with F. Assuming that the force is small, we can express the Hamiltonian $\tilde{\mathcal{H}}$ of the perturbed system in a first-order (*i.e.*, linear) approximation as the superposition of the unperturbed Hamiltonian $\mathcal{H}_{\text{eq}}$ and the perturbation energy $\mathcal{H}_{\text{ext}}$, yielding

$$\tilde{\mathcal{H}}(t) = \mathcal{H}_{\text{eq}} + \mathcal{H}_{\text{ext}}(t) = \mathcal{H}_{\text{eq}} - AF(t)\,. \tag{3.8}$$

Similarly, the assumption of a small perturbation enables us to write the probability density function $\tilde{\rho}(t)$ affected by the perturbation by superimposing the unperturbed function ρ_{eq} with a small time-dependent change $\Delta\rho(t)$ so that

$$\tilde{\rho}(t) = \rho_{\text{eq}} + \Delta\rho(t)\,. \tag{3.9}$$

The corresponding equation of motion for the perturbed system's phase space probability density function $\tilde{\rho}(t)$ then reads

$$\begin{aligned}
\frac{\partial}{\partial t}\tilde{\rho}(t) &= \left\{\tilde{\mathcal{H}}(t),\, \tilde{\rho}(t)\right\} \\
&= \underbrace{\{\mathcal{H}_{\text{eq}},\, \rho_{\text{eq}}\}}_{=0} + \{\mathcal{H}_{\text{eq}},\, \Delta\rho(t)\} \\
&\quad + \{\mathcal{H}_{\text{ext}}(t),\, \rho_{\text{eq}}\} + \underbrace{\{\mathcal{H}_{\text{ext}}(t),\, \Delta\rho(t)\}}_{=0 \text{ (to first order)}} \\
&= \{\mathcal{H}_{\text{eq}},\, \Delta\rho(t)\} + \{\mathcal{H}_{\text{ext}}(t),\, \rho_{\text{eq}}\}\,,
\end{aligned} \tag{3.10}$$

where the last term in the second row has been dropped because both $\mathcal{H}_{\text{ext}}(t)$ and $\Delta\rho(t)$ are small first-order changes so that $\{\mathcal{H}_{\text{ext}}(t),\, \Delta\rho(t)\}$ is of second order and therefore vanishes in a first-order approximation.

Furthermore, due to $\frac{\partial}{\partial t}\rho_{\text{eq}} = 0$, it follows that $\frac{\partial}{\partial t}\Delta\rho(t) = \frac{\partial}{\partial t}\tilde{\rho}(t)$. Inserting this identity together with the definition of $\mathcal{H}_{\text{ext}}$ into eq. (3.10)

yields

$$\frac{\partial}{\partial t}\Delta\rho(t) = \{\mathcal{H}_{\text{eq}},\, \Delta\rho(t)\} - F(t)\,\{A,\, \rho_{\text{eq}}\}\ . \tag{3.11}$$

To find a solution to this equation, we employ the equilibrium *Liouville operator*

$$i\mathcal{L}_{\text{eq}}(\cdot) := \{\cdot,\, \mathcal{H}_{\text{eq}}\}\ , \tag{3.12}$$

where i denotes the imaginary number defined as $i^2 = -1$. Using Hamilton's equations of motion defined in eq. (3.1), we can express $i\mathcal{L}_{\text{eq}}$ as a differential operator

$$i\mathcal{L}_{\text{eq}} = \dot{\boldsymbol{q}}\frac{\partial}{\partial \boldsymbol{q}} + \dot{\boldsymbol{p}}\frac{\partial}{\partial \boldsymbol{p}}\,. \tag{3.13}$$

By applying the operator to an arbitrary state $\boldsymbol{\gamma} = (\boldsymbol{q}, \boldsymbol{p})$, we obtain the equation of motion

$$i\mathcal{L}_{\text{eq}}\,(\boldsymbol{\gamma}) = \dot{\boldsymbol{\gamma}}\,. \tag{3.14}$$

With the initial condition $\boldsymbol{\gamma}(0) = (\boldsymbol{q}(0), \boldsymbol{p}(0))$, the formal solution of eq. (3.14) is

$$\boldsymbol{\gamma}(t) = e^{it\mathcal{L}_{\text{eq}}}\boldsymbol{\gamma}(0) \tag{3.15}$$

so that the operator $e^{it\mathcal{L}_{\text{eq}}}$ acts as an equilibrium time evolution propagator.

Likewise, the solution of the first-order differential equation (3.11) with the initial condition $\Delta\rho(-\infty) = 0$ is

$$\Delta\rho(t) = -\int_{-\infty}^{t} e^{-i(t-t')\mathcal{L}_{\text{eq}}}\,\{A,\, \rho_{\text{eq}}\}\,F(t')\,\mathrm{d}t'\,. \tag{3.16}$$

A proof for this solution can be found in appendix 3.A.

Now that we obtained a description for the evolution of the time-dependent change in the phase space probability density function, we can use it to compute the *response* of the system, *i.e.*, the expected

change $\langle \Delta B(t) \rangle$ of an observable $B = B(\boldsymbol{q}, \boldsymbol{p})$ affected by the external disturbance $F(t)$:

$$\begin{aligned} \langle \Delta B(t) \rangle &= \int_{\Omega} B \, \Delta\rho(t) \, \mathrm{d}\boldsymbol{q}\mathrm{d}\boldsymbol{p} \\ &= -\int_{\Omega} B \int_{-\infty}^{t} e^{-i(t-t')\mathcal{L}_{\mathrm{eq}}} \{A, \, \rho_{\mathrm{eq}}\} \, F(t') \, \mathrm{d}t' \, \mathrm{d}\boldsymbol{q}\mathrm{d}\boldsymbol{p} \end{aligned} \tag{3.17}$$

Since the phase space volume is a conserved quantity, we can change the order of integration, yielding

$$\langle \Delta B(t) \rangle = -\int_{-\infty}^{t} F(t') \int_{\Omega} \left[e^{-i(t-t')\mathcal{L}_{\mathrm{eq}}} \{A, \, \rho_{\mathrm{eq}}\} \right] B \, \mathrm{d}\boldsymbol{q}\mathrm{d}\boldsymbol{p} \, \mathrm{d}t' \, . \tag{3.18}$$

Due to the fact that $\mathcal{L}_{\mathrm{eq}}$ is Hermitian, the propagator $e^{-i(t-t')\mathcal{L}_{\mathrm{eq}}}$ is unitary, so that we can express eq. (3.18) as

$$\begin{aligned} \langle \Delta B(t) \rangle &= -\int_{-\infty}^{t} F(t') \int_{\Omega} \{A, \, \rho_{\mathrm{eq}}\} \, e^{i(t-t')\mathcal{L}_{\mathrm{eq}}} B \, \mathrm{d}\boldsymbol{q}\mathrm{d}\boldsymbol{p} \, \mathrm{d}t' \\ &= \int_{-\infty}^{t} F(t') \int_{\Omega} \{\rho_{\mathrm{eq}}, \, A\} \, B(t-t') \, \mathrm{d}\boldsymbol{q}\mathrm{d}\boldsymbol{p} \, \mathrm{d}t' \, . \end{aligned} \tag{3.19}$$

By expanding the Poisson bracket in the innermost integrand and applying the derivative product rule, we see that

$$\{\rho_{\mathrm{eq}}, \, A\} \, B(t-t') = \rho_{\mathrm{eq}} \left\{A, \, B(t-t')\right\} + \left\{\rho_{\mathrm{eq}} B(t-t'), \, A\right\} \, . \tag{3.20}$$

The phase space integral of the second addend on the right hand side vanishes (as can be shown by partial integration), so that eq. (3.19)

becomes

$$\begin{aligned}\langle \Delta B(t) \rangle &= \int_{-\infty}^{t} F(t') \int_{\Omega} \rho_{\text{eq}} \left\{ A,\, B(t-t') \right\} \mathrm{d}\boldsymbol{q}\mathrm{d}\boldsymbol{p}\, \mathrm{d}t' \\ &= \int_{-\infty}^{t} F(t') \left\langle \left\{ A,\, B(t-t') \right\} \right\rangle_{\text{eq}} \mathrm{d}t' \,, \end{aligned} \tag{3.21}$$

where we identified the phase space integral as the expected value of the Poisson bracket $\{A,\, B(t-t')\}$ at equilibrium. Strikingly, this result implies that in the linear approximation, the change of any observable due to a weak external disturbance is entirely determined by the *equilibrium* dynamics of the system!

Equation (3.21) allows us to define the system's *response function* $\phi_{AB}(\tau)$ as

$$\begin{aligned}\phi_{AB}(\tau) &:= \int_{\Omega} \rho_{\text{eq}} \left\{ A(0),\, B(\tau) \right\} \mathrm{d}\boldsymbol{q}\mathrm{d}\boldsymbol{p} \\ &= \left\langle \left\{ A(0),\, B(\tau) \right\} \right\rangle_{\text{eq}} \,, \end{aligned} \tag{3.22}$$

which corresponds to the change $\langle \Delta B(\tau) \rangle$ of the observable B at time τ after a unit pulse $F(t) = \delta(t)$ of an external force that is conjugate to A, where $\delta(\cdot)$ is the discrete Dirac delta function defined as

$$\delta(x) = \begin{cases} 1 & \text{if } x = 0\,, \\ 0 & \text{otherwise}\,. \end{cases} \tag{3.23}$$

Inserting the response function back into eq. (3.21) yields the well-known *Kubo equation*

$$\langle \Delta B(t) \rangle = \int_{-\infty}^{t} F(t')\, \phi_{AB}(t-t')\, \mathrm{d}t' \,, \tag{3.24}$$

which means that the change in the observable B is given by the superposition of unit delta responses weighted by the external force. We notice that this response is not only *linear*, but due to the fact that the time integral is cut-off at t, it is also *causal*, and furthermore *retarded* because ϕ_{AB} is a function of $\tau = t - t'$. Another noteworthy fact is that $\phi_{AB}(\tau) \in \mathbb{R}$ because it depends only on physical observables.

If the external force is oscillating at a constant frequency ω so that $F(\omega, t) = F_0\, e^{-i\omega t}$, the expected response in B is

$$\langle \Delta B(t) \rangle = F_0 \int_{-\infty}^{t} e^{-i\omega t'}\, \phi_{AB}(t - t')\, \mathrm{d}t' \,, \tag{3.25}$$

and by substituting $t - t' = \tau$, we obtain

$$\begin{aligned} \langle \Delta B(t) \rangle &= F_0 \int_{0}^{\infty} \phi_{AB}(\tau)\, e^{-i\omega(t-\tau)}\, \mathrm{d}\tau \\ &= \int_{0}^{\infty} \phi_{AB}(\tau)\, e^{i\omega\tau}\, \mathrm{d}\tau\, F_0\, e^{-i\omega t} \,. \end{aligned} \tag{3.26}$$

This expression allows us to define the generalized complex *susceptibility* (also called *admittance*)

$$\chi_{AB}(\omega) := \int_{0}^{\infty} \phi_{AB}(\tau)\, e^{i\omega\tau}\, \mathrm{d}\tau \,, \tag{3.27}$$

which is nothing but the *Fourier-Laplace transform* of the response function $\phi_{AB}(\tau)$. With this definition, eq. (3.27) attains the simple form

$$\langle \Delta B(t) \rangle = \chi_{AB}(\omega)\, F(\omega, t) \,. \tag{3.28}$$

We note that due to $\phi_{AB}(\tau) \in \mathbb{R}$, it follows that $\chi_{AB}(\omega) \in \mathbb{C}$, and as a consequence of the factor $e^{i\omega\tau}$ in eq. (3.27), we conjecture that

$$\mathrm{Re}\left[\chi_{AB}(\omega)\right] = \mathrm{Re}\left[\chi_{AB}(-\omega)\right] , \tag{3.29}$$

$$\mathrm{Im}\left[\chi_{AB}(\omega)\right] = -\,\mathrm{Im}\left[\chi_{AB}(-\omega)\right] , \tag{3.30}$$

i.e., that the real part of the susceptibility is an even function and its imaginary part an odd function of ω, provided that $\omega \in \mathbb{R}$.

3.1.2 Linear response in constant-temperature ensembles

Up to this point, we have not made any assumptions about the exact nature of the system's phase space probability density function ρ_{eq}, so that the meaning of the Poisson bracket appearing in the response function $\phi_{AB}(\tau)$ as per eq. (3.22) was not exactly defined either. To add more physical meaning to the theory derived above, we will now proceed by applying it to an equilibrium system represented by a statistical ensemble which is maintained at a constant absolute temperature (see also section 3.3.5 for an overview of relevant ensembles). The most prominent example for such an ensemble is the *canonical* ensemble, where the system's equilibrium Hamiltonian $\mathcal{H}_{\mathrm{eq}}(N, V, T)$ is uniquely defined by the state variables N (number of particles), V (volume), and T (temperature). Note, however, that the following considerations also apply to other constant-temperature ensembles such as the *isothermal-isobaric* or the *grand canonical* ensemble; we only require the temperature T to be one of the state variables.

From statistical mechanics, we know that the phase space distribution function at constant temperature is given by the *Boltzmann distribution*, so that the corresponding probability density function obeys

$$\rho_{\mathrm{eq}} = \frac{1}{\mathcal{Z}}\, e^{-\beta\mathcal{H}_{\mathrm{eq}}} , \tag{3.31}$$

where $\mathcal{Z}$ is the partition function of the respective ensemble and $\beta := (k_{\mathrm{B}}T)^{-1}$ with the Boltzmann constant k_{B}. Recalling that

the response function is defined as

$$\begin{aligned}\phi_{AB}(\tau) &:= \int_{\Omega} \rho_{\mathrm{eq}} \, \{A(0),\, B(\tau)\} \, \mathrm{d}\boldsymbol{q}\mathrm{d}\boldsymbol{p} \\ &= \int_{\Omega} \{\rho_{\mathrm{eq}},\, A(0)\} \, B(\tau) \, \mathrm{d}\boldsymbol{q}\mathrm{d}\boldsymbol{p}\,, \end{aligned} \tag{3.32}$$

we can now evaluate the Poisson bracket $\{\rho_{\mathrm{eq}},\, A(0)\}$ by inserting eq. (3.31):

$$\begin{aligned}\{\rho_{\mathrm{eq}},\, A(0)\} &= \frac{1}{\mathcal{Z}} \sum_i \left(\frac{\partial e^{-\beta \mathcal{H}_{\mathrm{eq}}}}{\partial q_i} \frac{\partial A(0)}{\partial p_i} - \frac{\partial e^{-\beta \mathcal{H}_{\mathrm{eq}}}}{\partial p_i} \frac{\partial A(0)}{\partial q_i} \right) \\ &= -\frac{\beta}{\mathcal{Z}} \, e^{-\beta \mathcal{H}_{\mathrm{eq}}} \sum_i \left(\frac{\partial \mathcal{H}_{\mathrm{eq}}}{\partial q_i} \frac{\partial A(0)}{\partial p_i} - \frac{\partial \mathcal{H}_{\mathrm{eq}}}{\partial p_i} \frac{\partial A(0)}{\partial q_i} \right) \\ &= \beta \rho_{\mathrm{eq}} \, \{A(0),\, \mathcal{H}_{\mathrm{eq}}\} \\ &= \beta \rho_{\mathrm{eq}} \, i\mathcal{L}_{\mathrm{eq}}(A(0)) \\ &= \beta \rho_{\mathrm{eq}} \, \dot{A}(0) \end{aligned} \tag{3.33}$$

Plugging this result back into the response function yields

$$\begin{aligned}\phi_{AB}(\tau) =& \beta \int_{\Omega} \rho_{\mathrm{eq}} \, \dot{A}(0) \, B(\tau) \, \mathrm{d}\boldsymbol{q}\mathrm{d}\boldsymbol{p} \\ =& \beta \, \langle \dot{A}(0) \, B(\tau) \rangle_{\mathrm{eq}} \,, \end{aligned} \tag{3.34}$$

so that the complex susceptibility $\chi_{AB}(\omega)$ in a constant temperature ensemble becomes

$$\chi_{AB}(\omega) = \beta \int_0^{\infty} \langle \dot{A}(0) \, B(\tau) \rangle_{\mathrm{eq}} \, e^{i\omega\tau} \, \mathrm{d}\tau \,. \tag{3.35}$$

If the system is ergodic, the phase space average $\langle \cdot \rangle_{\mathrm{eq}}$ can be replaced by the corresponding time average so that the term $\langle \dot{A}(0) \, B(\tau) \rangle_{\mathrm{eq}}$ is

identified as the temporal (cross-)correlation

$$\langle \dot{A}(0)\, B(\tau)\rangle = (\dot{A} \star B)(\tau) := \int_{-\infty}^{\infty} \dot{A}(t) B(t+\tau)\, \mathrm{d}t\,. \tag{3.36}$$

The most important consequence of ergodicity is therefore that the knowledge of the temporal evolution of both $\dot{A}(t)$ and $B(t)$ in *any particular* representation of the statistical ensemble is sufficient to obtain the susceptibility $\chi_{AB}(\omega)$.

3.2 Linear Dielectric Response

The dielectric response of a statistical ensemble is the expected change $\langle \Delta \boldsymbol{P}(t)\rangle$ of the system's polarization $\boldsymbol{P}$ due to an external electric field $\boldsymbol{E}_{\mathrm{ext}}(t)$. Thus, the generalized perturbing force is the external electric field, and the conjugate displacement is the system's dipole moment $\boldsymbol{M}$, so that the perturbation energy is given as $\mathcal{H}_{\mathrm{ext}}(t) = -\boldsymbol{M}\boldsymbol{E}_{\mathrm{ext}}(t)$. Since the polarization $\boldsymbol{P}$ is nothing but a dipole density, we have $\boldsymbol{M} = V\boldsymbol{P}$, where V is the volume of the system under consideration. The perturbation energy can therefore be expressed as

$$\mathcal{H}_{\mathrm{ext}}(t) = -V\boldsymbol{P}\boldsymbol{E}_{\mathrm{ext}}(t)\,. \tag{3.37}$$

Thus, according to eq. (3.34), the linear dielectric response function is given as

$$\vec{\boldsymbol{\phi}}_{\boldsymbol{PP}}(\tau) = \frac{V}{k_{\mathrm{B}}T} \langle \dot{\boldsymbol{P}}(0) \otimes \boldsymbol{P}(\tau)\rangle\, \mathrm{d}\tau\,, \tag{3.38}$$

where the symbol $\otimes$ denotes the dyadic product. The subscript indicating equilibrium conditions has been dropped for brevity, and we will stick to this notation in the following. Taking the dyadic product is necessary for dielectrically anisotropic systems, where the system's polarization response depends on the direction of the perturbing external electric field. Consequently, the dielectric response

function $\vec{\vec{\phi}}_{\boldsymbol{PP}}$ is generally a second-rank tensor as indicated by the double arrows. Likewise, the complex dielectric susceptibility is also a tensorial quantity, reading

$$\vec{\vec{\chi}}_{\boldsymbol{PP}}(\omega) = \frac{V}{k_\mathrm{B}T} \int_0^\infty \langle \dot{\boldsymbol{P}}(0) \otimes \boldsymbol{P}(\tau) \rangle \, e^{i\omega\tau} \, \mathrm{d}\tau \,, \tag{3.39}$$

or, alternatively,

$$\vec{\vec{\chi}}_{\boldsymbol{PP}}(\omega) = \frac{1}{Vk_\mathrm{B}T} \int_0^\infty \langle \dot{\boldsymbol{M}}(0) \otimes \boldsymbol{M}(\tau) \rangle \, e^{i\omega\tau} \, \mathrm{d}\tau \,. \tag{3.40}$$

In spatially isotropic systems, the polarization response is independent of the direction of the perturbing field so that the dielectric susceptibility tensor reduces to its trace average, yielding

$$\chi_{\boldsymbol{PP}}(\omega) = \frac{1}{3Vk_\mathrm{B}T} \int_0^\infty \langle \dot{\boldsymbol{M}}(0) \, \boldsymbol{M}(\tau) \rangle \, e^{i\omega\tau} \, \mathrm{d}\tau \,. \tag{3.41}$$

Note that for the remainder of this work, it will be generally assumed that systems are spatially isotropic unless otherwise stated.

A closer look at eq. (3.41) reveals that $\chi_{\boldsymbol{PP}}(\omega)$ has the expected dimensions of a dipole moment density (*i.e.*, polarization) divided by an electric field (in SI base units: $\mathrm{A^2 s^4 kg^{-1} m^{-3}}$), showing that the relation

$$\boldsymbol{P} = \chi_{\boldsymbol{PP}} \, \boldsymbol{E} \tag{3.42}$$

is obviously dimensionally correct. However, the dielectric susceptibility is usually given as the *dimensionless* electric susceptibility χ_e fulfilling the relation

$$\boldsymbol{P} = \varepsilon_0 \, \chi_e \, \boldsymbol{E} \,, \tag{3.43}$$

where ε_0 is the permittivity of free space. Thus, it follows immediately that

$$\chi_e(\omega) = \frac{1}{3\varepsilon_0 Vk_\mathrm{B}T} \int_0^\infty \langle \dot{\boldsymbol{M}}(0) \, \boldsymbol{M}(\tau) \rangle \, e^{i\omega\tau} \, \mathrm{d}\tau \,. \tag{3.44}$$

Taking the limit $\omega \to 0$ and using the property of autocorrelations of stationary processes $\langle \dot{A}(0)\, A(\tau)\rangle = -\frac{\mathrm{d}}{\mathrm{d}\tau}\langle A(0)\, A(\tau)\rangle$ (see appendix 3.B), we obtain the static electric susceptibility

$$\chi_e^{\text{static}} := \lim_{\omega\to 0} \chi_e(\omega) = \frac{\langle \boldsymbol{M}^2\rangle}{3\varepsilon_0 V k_\mathrm{B} T}\,. \tag{3.45}$$

Knowing the expected value of the squared total dipole moment of a system at equilibrium is therefore sufficient to deduce its static electric susceptibility.

Even though this equation appears to be rather simple, in the following, however, we will see that applying this equation to molecular simulation data can be a non-trivial task.

3.3 Classical Molecular Dynamics Simulations

Note: This section provides a brief overview of classical force field Molecular Dynamics simulations and is restricted to aspects relevant to this work. It is mostly based on references 81 and 82, which cover the topic comprehensively.

The Molecular Dynamics (MD) method is a computer simulation technique aiming to describe the dynamics of physicochemical many-particle systems at the molecular scale, where each particle is modeled as a point mass which may additionally carry a charge. Typically, in so-called *all-atom* MD simulations, these particles correspond to atoms, so that their true interactions are governed by the laws of quantum mechanics. However, the computational effort required to evaluate many-body interactions within any reasonably-sized molecular system using quantum-mechanical methods would quickly become prohibitively large. Therefore, in *classical* MD simulations, the forces acting between particles are approximated as classical and conservative, so that their interactions can be described by distance-dependent effective potentials. As both the assumption of point masses and charges as well as the classical interaction potentials are an approximation, the parameters entering the potential functions depend sensitively on the employed molecular models. A set of molecular models together with their parametrized interaction potentials is called a *force field*, so that the simulation technique is also referred-to as *force field Molecular Dynamics*.

3.3.1 Interaction potentials

The two major categories of interaction potentials are *bonded* and *nonbonded* potentials. Bonded potentials are used to describe interactions among neighboring atoms within a molecule. These cover potentials for covalent bonds, which are usually described by harmonic potentials between two neighboring particles, as well as angular

and dihedral potentials involving three and four neighboring particles, respectively. The two most prevalent types of nonbonded interactions in molecular systems are van der Waals and Coulomb interactions, where the former are due to induced dipoles and are most often modeled by the empirical Lennard-Jones[82,83] pair potential.

3.3.2 Integrators

Since the particles and their interactions are assumed to be classical, the temporal evolution of the system can be obtained by propagating the particles' positions and momenta by numerically integrating Newton's equations of motion

$$\dot{\boldsymbol{r}}_i = \boldsymbol{v}_i \,, \tag{3.46}$$

$$\dot{\boldsymbol{v}}_i = \frac{\boldsymbol{F}_i(\boldsymbol{r}_i)}{m_i} \,, \tag{3.47}$$

where m_i, $\boldsymbol{r}_i$, and $\boldsymbol{v}_i$ are the mass, position, and velocity of the ith particle, and the dot denotes the derivative with respect to time. The force $\boldsymbol{F}_i(\boldsymbol{r}_i)$ acting on the ith particle is obtained from

$$\boldsymbol{F}_i(\boldsymbol{r_i}) = -\nabla_i U(\boldsymbol{r_i}; \{\boldsymbol{r}_1, \ldots, \boldsymbol{r}_n\}) \,, \tag{3.48}$$

where the operator ∇_i denotes the gradient taken at the position of the ith particle, and $U(\boldsymbol{r_i}; \{\boldsymbol{r}_1, \ldots, \boldsymbol{r}_n\})$ is the superposition of all interaction potentials at position $\boldsymbol{r_i}$, which depends on the set of all particle coordinates $\{\boldsymbol{r}_1, \ldots, \boldsymbol{r}_n\}$ in a system comprising n particles.

In a many-body system with $3\,n$ position and $3\,n$ velocity coordinates, the coupled set of ordinary differential equations (3.46) and (3.47) can only be solved numerically, which entails the discretization of both space and time into finite steps. The relative spatial resolution is usually determined—and, thus, limited—only by the numerical precision offered by the machine executing the simulation code. The temporal resolution, however, is determined by the *time step* Δt, which

is an input parameter of the simulation, and must be chosen small enough to ensure numerical stability of the algorithm used to integrate Newton's equations of motion, the so-called *integrator*.

Important requirements for an integrator are that it should be time-reversible, symplectic, energy-conserving, long-term stable, and—last but not least—easy to implement. Therefore, the most widely-used integrators in MD simulations are the Velocity-Verlet algorithm[84] and a mathematically equivalent variant thereof, the so-called leapfrog integration scheme,[85] which is used in this work. In the leapfrog integration scheme, position and velocity updates are computed in an alternating fashion (hence the term "leapfrog") according to

$$\boldsymbol{v}_i\left(t+\frac{\Delta t}{2}\right) = \boldsymbol{v}_i\left(t-\frac{\Delta t}{2}\right) + \frac{\Delta t}{m}\boldsymbol{F}_i(\boldsymbol{r}_i,t)\,, \tag{3.49}$$

$$\boldsymbol{r}_i(t+\Delta t) = \boldsymbol{r}_i(t) + \Delta t\,\boldsymbol{v}_i\left(t+\frac{\Delta t}{2}\right)\,, \tag{3.50}$$

where t denotes time, and Δt is the time step. Thus, if this integrator is employed, it will be crucial for certain analyses to keep in mind that positions and velocities are never known at the exact same time, but are shifted by $\frac{\Delta t}{2}$.

3.3.3 Spatiotemporal limitations

In all-atom MD simulations, the time step is typically restricted to values as small as $\Delta t \leq 2\,\mathrm{fs}$, which currently limits the total accessible simulation time of any reasonably sized system to a few microseconds.

Apart from temporal restrictions, however, MD simulations are also subject to spatial limitations. While in principle, the simulation volume—and, therefore, the maximum distance in the system—can be arbitrarily large, it is the number of particles required to fill that

volume which sets severe limits to the spatial extent of an MD simulation. The most efficient algorithms used to compute the long-ranged Coulomb forces acting on each particle usually exhibit an asymtotic scaling of $\mathcal{O}(n \log_2(n))$, where n is the number of particles. The most prominent examples of such algorithms are the smooth particle-mesh Ewald (SPME)[86,87] and the particle-particle/particle-mesh (P^3M)[88] methods. Even when parallelized on modern supercomputers, this limits the number of particles a simulation can cover to a few million. A macroscopic system, however, contains a number of particles in the order of 10^{23}, *i.e.*, a number that is about 10^{17} times larger than what could be covered by an MD simulation.

3.3.4 Periodic boundary conditions

Without any further action, the limited number of particles would constrain the applicability of MD simulations to nano-confined systems, whose structural and dynamic properties are strongly influenced by the nature of the confining boundaries. This restriction is overcome by employing *periodic boundary conditions* (PBC), which enable MD simulations to effectively model the behavior of bulk systems. In a simulation with PBC, the simulation volume is represented as a box with toroidal boundaries in all three dimensions, *i.e.*, any particle leaving the box on one side will enter the box from the opposite side. This means that by employing PBC, one effectively simulates an infinitely periodic system consisting of identical boxes (often called *images*) replicated in all three dimensions as illustrated in fig. 3.1.

While applying PBC is necessary to simulate bulk behavior, the resulting toroidal geometry also implies that the definition of the distance between any pair of particles is ambiguous. It is therefore common practice to define distances according to the *minimum image convention*, where the distance r_{ij} between any two points $\boldsymbol{r}_i, \boldsymbol{r}_j$ in space is taken as the smallest distance between any two of their periodic images. For an orthorhombic simulation box with edge lengths L_x, L_y, L_z, the

squared minimum image distance is therefore given as

$$r_{ij}^2 := \sum_{d\in\{x,y,z\}} \Bigg((r_d \bmod L_d) + h\left(-(r_d \bmod L_d) - \frac{L_d}{2}\right) L_d - h\left((r_d \bmod L_d) - \frac{L_d}{2}\right) L_d \Bigg)^2 , \tag{3.51}$$

where r_d denotes the coordinate in direction $d \in \{x, y, z\}$ of the vector $\boldsymbol{r} = \boldsymbol{r}_j - \boldsymbol{r}_i$, mod is the modulo operator, and $h(\cdot)$ denotes the Heaviside step function defined as

$$h(x) = \begin{cases} 1 & \text{if } x > 0 \\ 0 & \text{otherwise}\,. \end{cases} \tag{3.52}$$

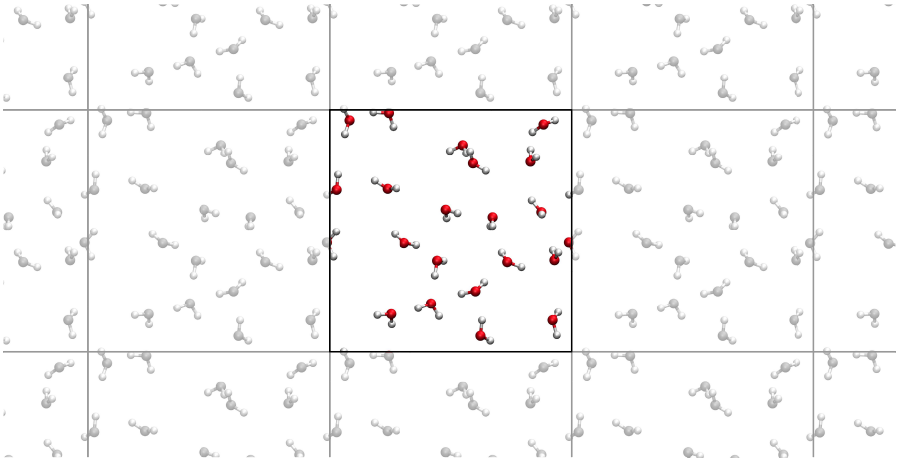

Figure 3.1: Two-dimensional slice of a simulation of water vapor in a cubic simulation box with periodic boundary conditions. Even though the simulation contains only the atoms in the central image (black square with colored molecules), the system is equivalent to an infinite system with periodically replicated images (gray squares with grayed-out molecules) in all directions due to periodic boundary conditions.

As will be shown below, employing PBC entails severe consequences for the computation of distance-dependent observables such as dipole moments. Moreover, as a system with PBC extends infinitely in all periodic dimensions, this poses practical problems for the evaluation of log-ranged interactions. For LJ interactions, where the interaction potential decays asymptotically with r_{ij}^{-6}, it is usually sufficient to stop the summation of pairwise interactions beyond a suitable cutoff distance and apply analytic tail corrections assuming a homogeneous background beyond the cutoff. However, for the much longer-ranged Coulomb interactions, where the potential decays with r_{ij}^{-1}, such an approach is not possible and one would basically have to compute pairwise Coulomb interactions beyond the central image to infinity. To overcome the problem of infinite direct summations, one usually employs algorithms based on Ewald summation[89] such as the *smooth particle mesh Ewald*[87] (SPME) or *particle-particle-particle-mesh Ewald*[90–92] (P^3M) methods, where the summation is split into a short-ranged part using direct summation up to a cutoff distance and a long-range part leveraging the periodicity of the system by computing the summations in reciprocal space using Fourier transforms.

3.3.5 Statistical ensembles

In statistical physics, MD simulations are used as a tool to investigate the temporal evolution of microscopic configurations representing possible microstates of an equivalent thermodynamic system. The entirety of all such states is called a *statistical ensemble*. For the ensemble to represent a macroscopic system at thermodynamic equilibrium, it must be in statistical equilibrium, *i.e.*, the expected value $\langle A \rangle$ (called the *ensemble average*) of any macroscopic observable A (a function of the microstates) must be constant, which entails that the probability distribution of microstates must be stationary.

Depending on the thermodynamic variables defining the system, there exist corresponding statistical ensembles:

Microcanonical ensemble (NVE) Completely isolated system with constant volume, no exchange of energy or particles with its surrounding. The number of particles N, volume V, and total energy E are conserved.

Canonical ensemble (NVT) Closed system with constant volume in contact with a heat bath, no exchange of particles with its surrounding. The number of particles N, volume V, and temperature T are fixed. The Helmholtz free energy F is conserved.

Isothermal-isobaric ensemble (NpT) Closed system in contact with heat bath, no exchange of particles with surrounding. The number of particles N is fixed, and the pressure p and temperature T are constant. The Gibbs free energy G is conserved.

Grand canonical ensemble (μVT) Open system with constant volume and chemical potential in contact with a heat bath, particles are exchanged with surrounding. The chemical potential μ, volume V, and temperature T are fixed. The Landau free energy (often called the *grand potential*) is conserved.

In this work, the majority of MD simulations were performed in the isothermal-isobaric ensemble, however, in some cases, the canonical ensemble was used.

3.3.6 Thermostats and barostats

To ensure that the system is maintained at a constant temperature, a so-called *thermostat* is required, *i.e.*, an algorithm coupling the system to a virtual heat bath. Two of the most widely-used algorithms are the Andersen[93] and the Langevin (also referred-to as stochastic dynamics)[81] thermostat. These thermostats mimick the coupling to

a heat bath in terms of random forces acting on the particles in the system and a dissipative force that is proportional to the particles' velocities. However, while these algorithms reproduce the correct Maxwell-Boltzmann distribution of particle velocities, and the system's static properties are therefore physically correct, the random forces impose a bias on the system's dynamics. Thus, such thermostats are not suitable for simulations which shall correctly reproduce dynamic properties such as dielectric spectra. In that case, a better choice is the *Nosé-Hoover* thermostat,[94,95] which employs an extended-Lagrangian approach with an additional variable used to impose the constraint of a constant temperature.[82] Since the algorithm is deterministic, the correct dynamics of the system are retained.

If the system is simulated in the NpT ensemble, an additional algorithm has to be employed to keep the system at a constant pressure, ensuring that the simulation volume fluctuates according to the system's stress tensor in a physically consistent manner. Such algorithms are called *barostats*. As of today, the most frequently employed barostat algorithm is that of Parrinello and Rahman,[96] which, in contrast to other approaches such as Berendsen's weak-coupling scheme,[97] reproduces the correct physical ensemble. Consequently, all simulations conducted for this work employ the Nosé-Hoover thermostat in conjunction with the Parrinello-Rahman barostat unless otherwise stated.

3.4 Dielectric Response in Molecular Dynamics Simulations

Now that the basic theory of linear dielectric response has been layed out and the basic concepts of MD simulations were introduced, we will combine this information to derive a method for extracting the dielectric response of a simulated system from equilibrium MD simulations.

We recall eq. (3.44), which states how the frequency-dependent linear electric susceptibility $\chi_e(\omega)$ in spatially homogeneous and isotropic systems can be obtained from the equilibrium system's fluctuating total dipole moment $\boldsymbol{M}(t)$ via a Fourier-Laplace transform:

$$\chi_e(\omega) = \frac{1}{3\varepsilon_0 V k_\mathrm{B} T} \int_0^\infty \langle \dot{\boldsymbol{M}}(0)\, \boldsymbol{M}(\tau) \rangle\, e^{i\omega\tau}\, \mathrm{d}\tau$$

The total dipole moment of a system comprising n charges $\{q_i\}$ located at positions $\boldsymbol{r}_i$ with respect to a reference position located at $\boldsymbol{r} = 0$ is given as

$$\boldsymbol{M} = \sum_{i=1}^{n} q_i\, \boldsymbol{r}_i \tag{3.53}$$

so that, in principle, it might appear straightforward to obtain $\boldsymbol{M}(t)$ from an MD simulation by simply evaluating eq. (3.53) in every time step. However, this is not easily possible in simulations employing PBC for two reasons:[98] First, in periodic systems, the choice of origin of the coordinate system defining the particle positions is arbitrary, leaving the value of the system's total dipole moment ill-defined. Second, if particles cross periodic boundaries, the fact that their positions are folded back into the simulation box will cause $\boldsymbol{M}(t)$ to suffer from an artificial jitter whose magnitude depends on the size of the simulation box.

In systems consisting entirely of overall charge-neutral molecules, these problems can be overcome by taking the total dipole moment as the sum of all molecular dipole moments, each computed in the respective molecule's reference frame with PBC undone. This is possible because the total dipole moment of such a system depends only on the rotational orientations of molecular dipole moments and is independent of the molecules' positions. However, in simulations involving free charges or non-neutral molecules, this is no longer possible as in addition to these rotational contributions, the system's total dipole moment will

also have a translational component arising from intermolecular contributions.

To solve this issue, instead of computing $\chi_e(\omega)$ directly from the dipole moment $\boldsymbol{M}(t)$, we will use its temporal derivative $\dot{\boldsymbol{M}}(t)$, which we identify as the system's total current

$$\boldsymbol{j}(t) := \dot{\boldsymbol{M}}(t) = \frac{\mathrm{d}}{\mathrm{d}t} \sum_{i=1}^{n} q_i \, \boldsymbol{r}_i(t) = \sum_{i=1}^{n} q_i \, \boldsymbol{v}_i(t) \,. \tag{3.54}$$

Since the charges q_i are constant, the temporal evolution of $\boldsymbol{j}$ only depends on the particles' velocities $\boldsymbol{v}_i$. This has the advantage that, in contrast to positions, the particles' velocities are independent of the choice of origin of the coordinate system and remain continuous when particles cross periodic boundaries. By inserting $\boldsymbol{j}(t)$ for $\dot{\boldsymbol{M}}(t)$ in eq. (3.44) and integrating by parts, we obtain

$$\begin{aligned}
\chi_e(\omega) =& \frac{1}{3\varepsilon_0 V k_\mathrm{B} T} \int_0^\infty \langle \boldsymbol{j}(0) \, \boldsymbol{M}(\tau) \rangle \, e^{i\omega\tau} \, \mathrm{d}\tau \\
=& \frac{1}{3\varepsilon_0 V k_\mathrm{B} T} \Bigg(\left[\left(\frac{\mathrm{d}}{\mathrm{d}\tau} \langle \boldsymbol{M}(0) \boldsymbol{M}(\tau) \rangle \right) \frac{i}{\omega} e^{i\omega\tau} \right]_0^\infty \\
& + \frac{i}{\omega} \int_0^\infty \langle \boldsymbol{j}(0) \, \boldsymbol{j}(\tau) \rangle \, e^{i\omega\tau} \, \mathrm{d}\tau \Bigg) \,,
\end{aligned} \tag{3.55}$$

where we have used the property of autocorrelations of real-valued stationary ramdom processes (see appendix 3.B for a brief derivation) $\frac{\mathrm{d}}{\mathrm{d}\tau} \langle A(0) A(\tau) \rangle = \langle A(0) \, \dot{A}(\tau) \rangle = -\langle \dot{A}(0) \, A(\tau) \rangle$.

The term in square brackets vanishes for $\tau = 0$ due to the fact that the autocorrelation $\langle \boldsymbol{M}(0) \boldsymbol{M}(\tau) \rangle$ is an even function, implying that its derivative vanishes at $\tau = 0$. As $\boldsymbol{M}(t)$ is subject to random thermal noise, its autocorrelation (and therefore, also the derivative thereof)

must vanish for $\tau \to \infty$ so that eq. (3.55) simplifies to

$$\chi_e(\omega) = \frac{1}{3\varepsilon_0 V k_\mathrm{B} T} \frac{i}{\omega} \int_0^\infty \langle \boldsymbol{j}(0)\, \boldsymbol{j}(\tau) \rangle\, e^{i\omega\tau}\, \mathrm{d}\tau\,. \tag{3.56}$$

We recall that χ_e relates the polarization $\boldsymbol{P}$ to the applied electric field $\boldsymbol{E}$ according to

$$\boldsymbol{P}(\omega) = \varepsilon_0\, \chi_e(\omega)\, \boldsymbol{E}(\omega)\,.$$

By taking the derivative with respect to time and remembering that we previously defined the external field as $\boldsymbol{E}(\omega) = E_0 e^{-i\omega t}$, we obtain the current density $\boldsymbol{J}(\omega) := \dot{\boldsymbol{P}}(\omega)$ as

$$\boldsymbol{J}(\omega) = -i\omega\, \varepsilon_0\, \chi_e(\omega)\, \boldsymbol{E}(\omega)\,. \tag{3.57}$$

Comparing this expression to Ohm's law $\boldsymbol{J} = \sigma_e\, \boldsymbol{E}$, we identify the frequency-dependent complex conductivity $\sigma_e(\omega)$ as

$$\sigma_e(\omega) = -i\omega\, \varepsilon_0\, \chi_e(\omega) = \frac{1}{3V k_\mathrm{B} T} \int_0^\infty \langle \boldsymbol{j}(0)\, \boldsymbol{j}(\tau) \rangle\, e^{i\omega\tau}\, \mathrm{d}\tau\,. \tag{3.58}$$

Solving for $\chi_e(\omega)$ yields the fundamental relation

$$\chi_e(\omega) = \frac{i\sigma_e(\omega)}{\varepsilon_0\, \omega}\,. \tag{3.59}$$

Using the definition of the relative permittivity $\varepsilon_r = (1 + \chi_e)$, we obtain the complex frequency-dependent relative permittivity, also called the *dielectric spectrum* of the system, as

$$\varepsilon_r(\omega) = 1 + \frac{i\sigma_e(\omega)}{\varepsilon_0\, \omega}\,. \tag{3.60}$$

Comparing this result to the previous definition of $\varepsilon_r(\omega)$ from eq. (2.3), we see that in principle, the infinite-frequency response ε_r^∞ is unity.

For dielectric spectra obtained from MD simulations, this equality holds because both the positions and velocities of all particles are known at every time step, implying that there exists no fast relaxation process that cannot be captured. However, note that even in bulk simulations employing PBC, there may be electrostatic boundary conditions influencing the system's dynamics in terms of a so-called reaction field, *i.e.*, a background medium with finite permittivity surrounding the simulation volume at a far distance that causes ε_r^∞ to differ from unity.[99] Nevertheless, in this work, all simulations employ metallic boundary conditions at infinity so that according to the tinfoil theorem,[100] ε_r^∞ indeed reduces to unity.

According to eq. (3.58), the imaginary part of $\sigma_e(\omega)$ vanishes for $\omega \to 0$ so that the *static* conductivity $\sigma_e^{\text{static}} := \sigma_e(\omega = 0)$ is a real-valued quantity. In systems comprising free charges, *i.e.*, ions or charged molecules, the real part of $\sigma_e(\omega)$ does not vanish for $\omega \to 0$ due to the translational flow of charges. In that case, eq. (3.60) implies that the dielectric loss $\varepsilon_r''(\omega)$ diverges for $\omega \to 0$ due to the factor ω^{-1}. We therefore follow the common experimental practice to calculate an *apparent* dielectric permittivity $\tilde{\varepsilon}_r(\omega)$ by substituting $\sigma_e(\omega) \to \tilde{\sigma}_e(\omega) - \sigma_e^{\text{static}}$ in eq. (3.60), yielding

$$\tilde{\varepsilon}_r(\omega) = 1 + \frac{i\left(\sigma_e(\omega) - \sigma_e^{\text{static}}\right)}{\varepsilon_0 \omega}\,. \tag{3.61}$$

This definition will be used throughout the remainder of this work, however, the tilde notation will be dropped for convenience.

Appendix of Chapter 3

3.A Proof of the Solution (3.16) to Eq. (3.11)

According to the *Leibniz integral rule*, the derivative $\frac{df(t)}{dt}$ of a function $f(t)$ of the form

$$f(t) = \int_{a(t)}^{b(t)} g(t, t')\, dt' \tag{3.62}$$

is given as

$$\frac{\partial f(t)}{\partial t} = \frac{\partial b(t)}{\partial t}\, g(t, b(t)) + \frac{\partial a(t)}{\partial t}\, g(t, a(t)) + \int_{a(t)}^{b(t)} \frac{\partial}{\partial t} g(t, t')\, dt' \tag{3.63}$$

under the condition

$$-\infty < a(t),\, b(t) < \infty\,. \tag{3.64}$$

In section 3.1, eq. (3.16), given by

$$\Delta\rho(t) = -\int_{-\infty}^{t} e^{-i(t-t')\mathcal{L}_{\mathrm{eq}}}\, \{\boldsymbol{A},\, \rho_{\mathrm{eq}}\}\, \boldsymbol{F}(t')\, dt' \tag{3.65}$$

was proposed as a solution to the differential equation (3.11), reading

$$\frac{\partial}{\partial t}\Delta\rho(t) = \{\mathcal{H}_{\mathrm{eq}},\, \Delta\rho(t)\} - \boldsymbol{F}(t)\, \{\boldsymbol{A},\, \rho_{\mathrm{eq}}\}\,. \tag{3.66}$$

Clearly, eq. (3.65) is an improper integral violating the condition (3.64) for the lower bound $a(t)$, and it is not obvious whether the integrand of eq. (3.65) generally fulfills the necessary requirements to expand the Leibniz rule to $a(t) = -\infty$. Nevertheless, it is *assumed* that the integrand is sufficiently well-behaved at the boundaries so that the Leibnitz rule remains valid in this case. Applying it to eq. (3.65) yields

$$\frac{d}{dt}\Delta\rho(t) = -\boldsymbol{F}(t)\,\{\boldsymbol{A}, \rho_{\mathrm{eq}}\} + \int_{-\infty}^{t} i\mathcal{L}_{\mathrm{eq}} \left(e^{-i(t-t')\mathcal{L}_{\mathrm{eq}}}\,\{\boldsymbol{A},\, \rho_{\mathrm{eq}}\}\,\boldsymbol{F}(t') \right) dt' \,. \tag{3.67}$$

Since the equilibrium Liouville operator $i\mathcal{L}_{\mathrm{eq}}(\cdot) = \{\mathcal{H}_{\mathrm{eq}}\,, \cdot\,\}$ is independent of time, we can move it in front of the integral, yielding

$$\begin{aligned} \frac{d}{dt}\Delta\rho(t) &= -\boldsymbol{F}(t)\,\{\boldsymbol{A}, \rho_{\mathrm{eq}}\} - i\mathcal{L}_{\mathrm{eq}} \underbrace{\left(-\int_{-\infty}^{t} e^{-i(t-t')\mathcal{L}_{\mathrm{eq}}}\,\{\boldsymbol{A},\, \rho_{\mathrm{eq}}\}\,\boldsymbol{F}(t')\,dt' \right)}_{=\Delta\rho(t)} \\ &= \{\mathcal{H}_{\mathrm{eq}}\,, \Delta\rho(t)\} - \boldsymbol{F}(t)\,\{\boldsymbol{A}, \rho_{\mathrm{eq}}\}\,, \end{aligned} \tag{3.68}$$

which is again eq. (3.66), showing the validity of the solution (3.65).(■)

3.B Derivatives of Autocorrelation Functions of Stationary Random Processes

The autocorrelation function $R_{AA}(\tau)$ of a stationary random process $A(t)$ is defined as

$$R_{AA}(\tau) := \langle A(0)\, A(\tau)\rangle = \int_{-\infty}^{\infty} A(t)\, A(t+\tau)\, \mathrm{d}t = \int_{-\infty}^{\infty} A(t-\tau)\, A(t)\, \mathrm{d}t\,, \tag{3.69}$$

Taking its derivative with respect to τ, it follows immediately that

$$\dot{R}_{AA}(\tau) = R_{A\dot{A}}(\tau) = -R_{\dot{A}A}(\tau)\,, \tag{3.70}$$

or, expressed differently:

$$\frac{\mathrm{d}}{\mathrm{d}\tau}\langle A(0)\, A(\tau)\rangle = \langle A(0)\, \dot{A}(\tau)\rangle = -\langle \dot{A}(0)\, A(\tau)\rangle\,. \tag{3.71}$$

Likewise, it follows for the second derivative that

$$\frac{\mathrm{d}^2}{\mathrm{d}\tau^2}\langle A(0)\, A(\tau)\rangle = -\langle \dot{A}(0)\, \dot{A}(\tau)\rangle\,. \tag{3.72}$$

4 Computational Framework

In the previous chapter, we have derived the theory required to obtain dielectric spectra from bulk equilibrium MD simulations. The central outcomes of this derivation were that the spectrum of the frequency-dependent relative permittivity $\varepsilon_r(\omega)$ is related to that of the complex conductivity $\sigma_e(\omega)$ according to eq. (3.61), and that the latter can be obtained via a Fourier-Laplace transform of the autocorrelation of the total current $\boldsymbol{j}(t)$ according to eq. (3.58). However, what is still missing is a computationally feasible approach to obtain $\boldsymbol{j}(t)$ from simulations, correct numerical estimators to compute autocorrelations, an efficient way to compute Fourier-Laplace transforms, and, last but not least, a robust method to compute the static conductivity σ_e^{static}.

Before we start developing such a computational framework, it is of utmost importance to realize that we are dealing with simulation data, which are—just like data from experimental measurements—subject to various types of errors. Therefore, in the following section, we discuss how statistical errors of observables obtained from MD simulations can be estimated in a rigorous and numerically correct manner.

4.1 Statistical Error Estimation for Molecular Dynamics Simulation Data

Note: The contents of this section have been previously made available online in similar form.[101]

In any simulation capturing real-world phenomena, one has to make assumptions about the nature of the system the simulation shall represent. This is a general fact applying to any kind of simulation, and is therefore neither limited to the employed simulation method nor to the field of research. Consequently, a simulation will never yield a perfect picture of reality, and is therefore subject to errors, which can arise from many different sources, *e.g.*, from model assumptions (choice of parameters, level of detail, governing equations, etc.), bad choices of initial conditions, spatial boundaries, system size, temporal resolution and / or total simulation time, or flaws in the analysis and interpretation of simulation results. These errors can be categorized into two general types, namely *systematic* and *statistical* errors. As the latter type can be dealt with using generally applicable techniques, the analysis of statistical errors will be discussed in the following.

In classical equilibrium statistical physics, the fundamental property of a microscopic system is its partition function $\mathcal{Z}$. Taking the example of the canonical ensemble, it reads

$$\mathcal{Z} = \frac{1}{\hbar^3} \int_{\Omega} e^{-\frac{E(s)}{k_\mathrm{B} T}} \, \mathrm{d}\Omega \,, \tag{4.1}$$

which is an integral of the Boltzmann weights of all microscopic states s with energy $E(s)$ over the phase space $\Omega = \{s\}$ accessible to the system, where k_B is the Boltzmann constant, T denotes absolute temperature, $\mathrm{d}\Omega$ is an infinitesimal phase space volume element, and $\hbar$ is Planck's constant. The probability $P(s)$ of finding the system in any

particular state s is then given by

$$P(s) = \frac{1}{\mathcal{Z}} e^{-\frac{E(s)}{k_B T}} . \tag{4.2}$$

Consequently, the expected value $\langle A \rangle$ of any microscopic observable $A(s)$ can be expressed in terms of the Partition function as

$$\langle A \rangle = \frac{1}{\mathcal{Z}} \int_{\Omega} A(s)\, e^{-\frac{E(s)}{k_B T}}\, \mathrm{d}\Omega . \tag{4.3}$$

From eq. (4.3) it becomes evident that any thermodynamic observable $\langle A \rangle$ is the expected value of a Boltzmann-weighted random variable A from a statistical physics point of view.
Its expected quadratic deviation $\sigma^2(A)$[a], *i.e.*, the *variance* of A, is

$$\begin{aligned} \sigma^2(A) &= \langle (A - \langle A \rangle)^2 \rangle \\ &= \langle A^2 \rangle - 2 \langle \langle A \rangle A \rangle + \langle \langle A \rangle^2 \rangle \\ &= \langle A^2 \rangle - \langle A \rangle^2 . \end{aligned} \tag{4.4}$$

In classical equilibrium MD simulations, one samples the temporal evolution of microscopic states $s(\{\boldsymbol{q}\}, \{\boldsymbol{p}\})$ of n-particle systems with generalized positions $\{\boldsymbol{q}\} = (\boldsymbol{q}_1, \boldsymbol{q}_2, ..., \boldsymbol{q}_n)$ and conjugate momenta $\{\boldsymbol{p}\} = (\boldsymbol{p}_1, \boldsymbol{p}_2, ..., \boldsymbol{p}_n)$ governed by a suitable Hamiltonian $\mathcal{H}(\{\boldsymbol{q}\}, \{\boldsymbol{p}\})$ by integrating Newton's equations of motion. Apart from the fact that the number of particles n in the system must be large enough to faithfully represent the system's behavior in the thermodynamic limit ($n \to \infty$), it is clearly impossible to sample the entire phase space of such a microscopic system within finite simulation time. Thus, the expected value $\langle A \rangle$ of an observable $A(s)$, and, consequently, also its variance $\sigma^2(A)$, are not directly measurable in MD simulations. However, by integrating Newton's equation of motion in a suitable thermodynamic ensemble, the sampled states in a phase space trajectory $s(t) := s(\{\boldsymbol{q}(t)\}, \{\boldsymbol{p}(t)\})$ obtained from an equlibrium MD simulation

[a] Not to be mistaken for the conductivity σ_e in section 3.4!

are inherently Boltzmann-weighted. One can therefore estimate $\langle A \rangle$ from the temporal average of $A(t) := A(s(t))$

$$\langle A \rangle \approx \frac{1}{t_{\text{sim}}} \int_0^{t_{\text{sim}}} A(t)\, \mathrm{d}t\,, \tag{4.5}$$

provided that the system is ergodic. In a computer simulation, the simulation time t_{sim} is discretized into N_t time steps δt, and $A(t)$ is usually sampled at regular intervals of width $\Delta t \geq \delta t$ so that eq. (4.5) becomes

$$\langle A \rangle \approx \bar{A} := \frac{1}{N} \sum_{i=1}^{N} A_i\,, \tag{4.6}$$

where N denotes the total number of samples with measured values $A_i = A(i\,\Delta t)$.

4.1.1 Error estimation of uncorrelated data

Since the estimator $\bar{A}$ only *approximates* $\langle A \rangle$, it is important to know the statistical accuracy of this approximation. The variance of $\bar{A}$ is

$$\begin{aligned}
\sigma^2(\bar{A}) &= \left\langle \left(\bar{A} - \langle A \rangle\right)^2 \right\rangle \\
&= \frac{1}{N^2} \sum_{i=1}^{N} \sum_{j=1}^{N} \langle A_i A_j \rangle - \frac{2}{N} \sum_{i=1}^{N} \langle A_i \rangle \langle A \rangle + \langle A \rangle^2 \\
&= \frac{2}{N^2} \sum_{i=1}^{N} \sum_{j=i+1}^{N} \langle A_i A_j \rangle + \frac{1}{N} \langle A^2 \rangle - \langle A \rangle^2\,.
\end{aligned} \tag{4.7}$$

If we assume uncorrelated (*i.e.*, statistically independent) samples, then $\langle A_i A_j \rangle = \langle A_i \rangle \langle A_j \rangle = \langle A \rangle^2$ for all $i \neq j$, so that

$$\begin{aligned}\sigma^2\big(\bar{A}\big) &= \frac{N\,(N-1)}{N^2}\langle A\rangle^2 + \frac{1}{N}\langle A^2\rangle - \langle A\rangle^2 \\ &= \frac{1}{N}\left(\langle A^2\rangle - \langle A\rangle^2\right) \\ &= \frac{1}{N}\sigma^2(A). \end{aligned} \tag{4.8}$$

The standard error ϵ of the mean $\bar{A}$ is defined as the square root of its variance (also known as its *standard deviation*), and is thus given as

$$\epsilon\left(\bar{A}\right) := \sigma\left(\bar{A}\right) = \frac{\sigma(A)}{\sqrt{N}}\,. \tag{4.9}$$

Due to the fact that we cannot directly measure $\sigma(A)$, we employ the estimator $\bar{A} \approx \langle A \rangle$ to construct an estimator for $\sigma^2(A)$:

$$\begin{aligned}\left\langle \overline{A^2} - \bar{A}^2 \right\rangle &= \left\langle \overline{A^2} \right\rangle - \left\langle \bar{A}^2 \right\rangle \\ &= \langle A^2\rangle - \frac{1}{N^2}\sum_{i=1}^{N}\sum_{j=1}^{N}\langle A_i A_j\rangle \\ &= \langle A^2\rangle - \frac{1}{N}\langle A^2\rangle - \frac{2}{N^2}\sum_{i=1}^{N}\sum_{j=i+1}^{N}\langle A_i A_j\rangle \end{aligned} \tag{4.10}$$

Assuming again that the samples A_i, A_j, $i \neq j$ are statistically independent, we obtain

$$\begin{aligned}\left\langle \overline{A^2} - \bar{A}^2 \right\rangle &= \langle A^2\rangle - \frac{1}{N}\langle A^2\rangle - \frac{2}{N^2}\sum_{i=1}^{N}\sum_{j=i+1}^{N}\langle A\rangle^2 \\ &= \frac{N-1}{N}\left(\langle A^2\rangle - \langle A\rangle^2\right) \\ &= \frac{N-1}{N}\sigma^2(A)\,. \end{aligned} \tag{4.11}$$

Replacing the expected value on the LHS of eq. (4.11) by its estimator and rearranging for $\sigma^2(A)$ yields the estimator for the variance

$$\hat{\sigma}^2(A) = \frac{N}{N-1}\left(\overline{A^2} - \bar{A}^2\right), \tag{4.12}$$

and combining eqs. (4.6), (4.9) and (4.12) yields the estimator for the standard error of the mean

$$\hat{\epsilon}\left(\bar{A}\right) = \sqrt{\frac{\hat{\sigma}^2(A)}{N}} = \sqrt{\frac{1}{N\,(N-1)}\left(\sum_{i=1}^{N} A_i^2 - \frac{1}{N}\left(\sum_{i=1}^{N} A_i\right)^2\right)}. \tag{4.13}$$

4.1.2 Error estimation of correlated data

Due to the fact that the sampled states $s(t_i)$, $s(t_j)$ obtained from an MD simulation are correlated for small $(j-i)$ due to the system's inertia, the above assumption of uncorrelated samples does not hold in general. Moreover, the time interval $(j-i)\Delta t$ required for the sampled states to become uncorrelated is not known *a priori*. Hence, we generally have to assume that $\langle A_i A_j\rangle \neq \langle A\rangle^2$, thereby invalidating the simplification employed to obtain eq. (4.8) from eq. (4.7), and, likewise, eq. (4.11) from eq. (4.10). Nevertheless, we can measure the time scale on which the correlations between successive samples A_i, A_j decay by analyzing the *auto-covariance function* $R^{AA}(\tau)$ of the time-dependent (but stationary!) random variable $A(t) \in \mathbb{R}$, which is defined as

$$\begin{aligned} R^{AA}(\tau) &= \langle (A(t) - \langle A\rangle)\,(A(t+\tau) - \langle A\rangle)\rangle \\ &= \langle A(t)A(t+\tau)\rangle - \langle A\rangle^2 . \end{aligned} \tag{4.14}$$

Since A is real and stationary, we can substitute $t \to t-\tau$ so that the symmetry

$$\begin{aligned} R^{AA}(\tau) &= \langle A(t)A(t+\tau)\rangle - \langle A\rangle^2 \\ &\overset{t\to t-\tau}{=} \langle A(t-\tau)A(t)\rangle - \langle A\rangle^2 \\ &= R^{AA}(-\tau) \end{aligned} \tag{4.15}$$

immediately follows, and consequently, the auto-covariance function of a real variable is an even function.
If A is sampled at regular time intervals Δt, we can discretize eq. (4.14) to obtain

$$R_j^{AA} := R^{AA}(j\,\Delta t) = \langle A_i A_{i+j}\rangle - \langle A\rangle^2\,. \tag{4.16}$$

Note that by definition, the auto-covariance function at $j = 0$ is $R_0^{AA} = \langle A^2\rangle - \langle A\rangle^2 = \sigma^2(A)$.

We now proceed by recalling eq. (4.7), which describes the variance $\sigma^2(\bar{A})$ of the estimator $\bar{A}$:

$$\sigma^2\big(\bar{A}\big) = \frac{2}{N^2}\sum_{i=1}^{N}\sum_{j=i+1}^{N}\langle A_i A_j\rangle + \frac{1}{N}\langle A^2\rangle - \langle A\rangle^2$$

By rewriting the last term as

$$\begin{aligned}\langle A\rangle^2 &= \langle A\rangle^2 - \frac{1}{N}\langle A\rangle^2 + \frac{1}{N}\langle A\rangle^2\\ &= \frac{N-1}{N}\langle A\rangle^2 + \frac{1}{N}\langle A\rangle^2\\ &= \frac{2}{N^2}\sum_{i=1}^{N}\sum_{j=i+1}^{N}\langle A\rangle^2 + \frac{1}{N}\langle A\rangle^2\end{aligned} \tag{4.17}$$

we obtain

$$\sigma^2\big(\bar{A}\big) = \frac{2}{N^2}\sum_{i=1}^{N}\sum_{j=i+1}^{N}\left(\langle A_i A_j\rangle - \langle A\rangle^2\right) + \frac{1}{N}\left(\langle A^2\rangle - \langle A\rangle^2\right)\,. \tag{4.18}$$

Shifting the index of the inner sum $j \to j - i$ yields

$$\begin{aligned}\sigma^2\big(\bar{A}\big) &= \frac{2}{N^2}\sum_{i=1}^{N}\sum_{j=1}^{N-i}\left(\langle A_i A_{i+j}\rangle - \langle A\rangle^2\right) + \frac{1}{N}\sigma^2(A)\\ &= \frac{2}{N^2}\sum_{i=1}^{N}\sum_{j=1}^{N-i}R_j^{AA} + \frac{1}{N}R_0^{AA}\,.\end{aligned} \tag{4.19}$$

A closer look at the double sum reveals that in total, each addend R_j^{AA} occurs exactly $N - j$ times so that we can express eq. (4.19) as

$$\sigma^2(\bar{A}) = \frac{2}{N^2} \sum_{j=1}^{N-1} (N - j)\, R_j^{AA} + \frac{1}{N} R_0^{AA}\,. \tag{4.20}$$

Moreover, we know that $R_j^{AA} = R_{-j}^{AA}$ due to the symmetry of the auto-covariance function. This allows us to further simplify the above expression, which then reads

$$\sigma^2(\bar{A}) = \frac{1}{N} \sum_{j=-N+1}^{N-1} \frac{N - |j|}{N} R_j^{AA}\,. \tag{4.21}$$

Nevertheless, since both the expected value $\langle A \rangle$ as well as the variance $\sigma^2(A)$ are not directly accessible, the same applies to the true auto-covariance function R_j^{AA}. Hence, we are still missing a way to obtain an estimate of R_j^{AA} from the measured data, which will be discussed in the following.

Let us consider a random variable A^0 with an expected value $\langle A^0 \rangle = 0$ so that its auto-covariance function equals its autocorrelation function and is therefore given by

$$R_j^{A^0A^0} = \left\langle \left(A_i^0 - \langle A^0 \rangle\right) \left(A_{i+j}^0 - \langle A^0 \rangle\right) \right\rangle = \langle A_i^0 A_{i+j}^0 \rangle = \langle A_i^0 A_{i+|j|}^0 \rangle\,, \tag{4.22}$$

where the last equality holds due to the symmetry $R_j^{A^0A^0} = R_{-j}^{A^0A^0}$. By applying the estimator for the mean, we obtain the autocorrelation estimator

$${}^b\hat{R}_j^{A^0A^0} = \frac{1}{N} \sum_{i=1}^{N} A_i^0 A_{i+|j|}^0 = \begin{cases} \dfrac{1}{N} \displaystyle\sum_{i=1}^{N-|j|} A_i^0 A_{i+|j|}^0 & \text{for } 0 \leq |j| < N \\ 0 & \text{otherwise}\,, \end{cases} \tag{4.23}$$

where we have implicitly set the values outside the measurement range to $A_i^0 = \langle A^0 \rangle = 0$ for all $i > N$, which is justified if N is sufficiently large so that $R_j^{A^0A^0}$ already vanishes before $j = N$.

The expected value of this estimator is

$$\begin{aligned}\left\langle {}^{b}\hat{R}_j^{A^0A^0} \right\rangle &= \frac{1}{N} \sum_{i=1}^{N-|j|} \langle A_i^0 A_{i+|j|}^0 \rangle \\ &= \frac{1}{N} \sum_{i=1}^{N-|j|} R_j^{A^0A^0} \\ &= \frac{N-|j|}{N} R_j^{A^0A^0} \,. \end{aligned} \tag{4.24}$$

We see that this estimator is *biased* (hence the prescript b) by the factor $\frac{N-|j|}{N}$ and becomes only asymptotically unbiased for $N \gg j$. However, we can solve eq. (4.24) for $R_j^{A^0A^0}$ to obtain the *unbiased* estimator

$${}^{u}\hat{R}_j^{A^0A^0} = \frac{1}{N-|j|} \sum_{i=1}^{N-|j|} A_i^0 A_{i+|j|}^0 \,. \tag{4.25}$$

If we consider the general case of a random variable $A(t)$ with an unknown, *i.e.*, potentially non-zero expected value $\langle A \rangle$, we cannot neglect it in the respective auto-covariance function, which is then again given by eq. (4.14). We can include the expected value in terms of its estimator $\bar{A} \approx \langle A \rangle$ into the estimators ${}^{b}\hat{R}_j^{A^0A^0}$ and ${}^{u}\hat{R}_j^{A^0A^0}$ to obtain the auto-covariance estimators

$${}^{b}\hat{R}_j^{AA} = \frac{1}{N} \sum_{i=1}^{N-|j|} \left(A_i - \bar{A}\right) \left(A_{i+|j|} - \bar{A}\right) \,, \tag{4.26}$$

$${}^{u}\hat{R}_j^{AA} = \frac{1}{N-|j|} \sum_{i=1}^{N-|j|} \left(A_i - \bar{A}\right) \left(A_{i+|j|} - \bar{A}\right) \,. \tag{4.27}$$

By doing so, we add an (additional) small, asymptotically vanishing bias of $\mathcal{O}(1/N)$ to either of the estimators, which can be shown by

calculating their expected values. This means that if an observable is known to possess an expected value of zero, it is actually *wrong* to subtract the mean from a data series of such an observable for the estimation of the corresponding auto-covariance function! Generally speaking, if it is known, it is more accurate to subtract the expected value instead of the average.

Nevertheless, we use the estimator ${}^{u}\hat{R}_j^{AA}$ to approximate the true auto-covariance function R_j^{AA} in eq. (4.21), yielding the estimator for the variance of the mean

$$\begin{aligned} {}^{c}\hat{\sigma}^2(\bar{A}) &= \frac{1}{N}\sum_{j=-N+1}^{N-1}\frac{N-|j|}{N}\,{}^{u}\hat{R}_j^{AA} \\ &= \frac{1}{N}\sum_{j=-N+1}^{N-1}\frac{1}{N}\sum_{i=1}^{N-|j|}\left(A_i-\bar{A}\right)\left(A_{i+|j|}-\bar{A}\right) \\ &= \frac{1}{N}\sum_{j=-N+1}^{N-1}{}^{b}\hat{R}_j^{AA}\,, \end{aligned} \tag{4.28}$$

where the prescript c indicates that the estimator is now also valid for correlated data series. The estimator for the standard error of the mean follows immediately as

$${}^{c}\hat{\epsilon}(\bar{A}) = \sqrt{\frac{1}{N}\sum_{j=-N+1}^{N-1}{}^{b}\hat{R}_j^{AA}}\,. \tag{4.29}$$

We see that to obtain an (almost) unbiased estimate of the standard error of the mean, we have to compute the integral of a *biased* estimate of the auto-covariance function!

However, for reasons we will discuss below, the integrated auto-covariance estimate can only be reliably evaluated up to $|j_{\max}| < \frac{N}{2}$, which is still to be determined. Restricting the summation limits in

eq. (4.29) accordingly yields the correlated error estimate

$$ {}^{c}\hat{\epsilon}(\bar{A}) = \sqrt{\frac{1}{N} \sum_{j=-j_{\max}}^{j_{\max}} {}^{b}\hat{R}_{j}^{AA}} \,. \tag{4.30} $$

Note that eq. (4.30) remains valid for uncorrelated data series because then, the auto-covariance function vanishes except for $j = 0$ so that eq. (4.30) reduces to eq. (4.13).
Also note that because eq. (4.30) employs an *unnormalized* estimate of the auto-covariance function, it remains numerically stable even if $A_i = \bar{A}$ for all i. The method derived here is therefore more robust than other related methods for correlated error analysis[102] from a practical point of view.

4.1.3 Important considerations for the evaluation of integrated auto-covariance estimates

We have seen that the jth value of the auto-covariance estimator ${}^{b}\hat{R}_{j}^{AA}$ is computed from $N - |j|$ sample pairs, so that the tail of the auto-covariance is expected to become increasingly noisy. Likewise, we expect the integrated auto-covariance to suffer from fluctuations, making it hard to precisely estimate its asymptotic value. We define the running integral of the auto-covariance as

$$ {}^{b}\hat{R}_{\mathrm{int},j}^{AA} := \sum_{m=-j}^{j} {}^{b}\hat{R}_{m}^{AA} \,, \quad j = 0, \ldots, N-1 \,. \tag{4.31} $$

We can evaluate the integral ${}^{b}\hat{R}^{AA}_{\mathrm{int},j}$ at $j = N-1$ analytically:

$$
\begin{aligned}
{}^{b}\hat{R}^{AA}_{\mathrm{int},(N-1)} &= \sum_{m=-N+1}^{N-1} {}^{b}\hat{R}^{AA}_{m} \\
&= 2\sum_{m=1}^{N-1} {}^{b}\hat{R}^{AA}_{m} + {}^{b}\hat{R}^{AA}_{0} \qquad (4.32) \\
&= \frac{2}{N}\sum_{m=1}^{N-1}\sum_{i=1}^{N-m}\left(A_i - \langle A\rangle\right)\left(A_{i+m} - \langle A\rangle\right) + \frac{1}{N}\sum_{i=1}^{N}\left(A_i - \langle A\rangle\right)^2, \qquad (4.33)
\end{aligned}
$$

where we used the symmetry of the auto-covariance function ${}^{b}\hat{R}^{AA}_{m} = {}^{b}\hat{R}^{AA}_{-m}$ in the second step, and thereafter inserted eq. (4.26) *without* employing the estimator $\bar{A} \approx \langle A\rangle$.

By explicitly writing out the double sum of the first addend of eq. (4.33), we see that we can change the order of summation, yielding

$$
\begin{aligned}
{}^{b}\hat{R}^{AA}_{\mathrm{int},(N-1)} &= \frac{2}{N}\sum_{i=1}^{N-1}\sum_{m=i+1}^{N}\left(A_i - \langle A\rangle\right)\left(A_m - \langle A\rangle\right) + \frac{1}{N}\sum_{i=1}^{N}\left(A_i - \langle A\rangle\right)^2 \\
&= \frac{1}{N}\sum_{i=1}^{N}\sum_{m=1}^{N}\left(A_i - \langle A\rangle\right)\left(A_m - \langle A\rangle\right) \\
&= \frac{1}{N}\sum_{i=1}^{N}\sum_{m=1}^{N}\left(A_i\,A_m - A_i\langle A\rangle - A_m\langle A\rangle + \langle A\rangle^2\right) \\
&= N\left(\bar{A}^2 - 2\bar{A}\langle A\rangle + \langle A\rangle^2\right) \\
&= N\left(\bar{A} - \langle A\rangle\right)^2 . \qquad (4.34)
\end{aligned}
$$

It is now obvious that by replacing the unknown expected value $\langle A\rangle$ by the mean $\bar{A}$, we introduce a bias to the auto-covariance estimator ${}^{b}\hat{R}^{AA}_{j}$ which forces its integral to zero at $j = N-1$, so that by construction, ${}^{b}\hat{R}^{AA}_{\mathrm{int},(N-1)} = 0$.

Clearly, we need to know the maximum lag $j_{\max}$ where the auto-covariance integral ${}^{b}\hat{R}^{AA}_{\mathrm{int},j}$ is still reliable. Following the previous analytical calculation from eq. (4.32), we can express ${}^{b}\hat{R}^{AA}_{\mathrm{int},j}$ as

$$
\begin{aligned}
{}^{b}\hat{R}^{AA}_{\mathrm{int},j} &= 2\sum_{m=1}^{j} {}^{b}\hat{R}^{AA}_{m} + {}^{b}\hat{R}^{AA}_{0} = \underbrace{2\sum_{m=1}^{N-1} {}^{b}\hat{R}^{AA}_{m} + {}^{b}\hat{R}^{AA}_{0}}_{={}^{b}\hat{R}^{AA}_{\mathrm{int},(N-1)}=0} - 2\sum_{m=j+1}^{N-1} {}^{b}\hat{R}^{AA}_{m} \\
&= -\frac{2}{N}\sum_{m=j+1}^{N-1}\sum_{i=1}^{N-m} \left(A_i - \langle A\rangle\right)\left(A_{i+m} - \langle A\rangle\right) . \qquad (4.35)
\end{aligned}
$$

Again, we can change the order of summation, yielding

$$
{}^{b}\hat{R}^{AA}_{\mathrm{int},j} = -\frac{2}{N}\sum_{i=1}^{N-j-1} \left(A_i - \langle A\rangle\right) \sum_{m=i+j+1}^{N} \left(A_m - \langle A\rangle\right) . \qquad (4.36)
$$

We see that for $j = \frac{N}{2} - 1$, the index of the outer sum covers the range $i \in [1, \frac{N}{2}]$, and the inner sum covers $m \in [\frac{N}{2} + i, N]$, so that for $j < \frac{N}{2}$, all available samples enter the estimate ${}^{b}\hat{R}^{AA}_{\mathrm{int},j}$ at least once. Any further increase of j to $\frac{N}{2}+k$, $k \geq 0$ will result in omitting $2(k+1)$ of the available samples, so that the estimate ${}^{b}\hat{R}^{AA}_{\mathrm{int},j}$ will become less accurate by construction. Thus, even if the expected value is known, there is *no benefit* in evaluating the auto-covariance estimate ${}^{b}\hat{R}^{AA}_{j}$ for lags $j \geq \frac{N}{2}$.

Unfortunately, this only tells us that the maximum suitable lag must be $j_{\max} < \frac{N}{2}$. Nevertheless, in order to obtain information on the lag-dependent statistical accuracy of the auto-covariance integral ${}^{b}\hat{R}^{AA}_{\mathrm{int},j}$, we can estimate its statistical error!

To this aim, we divide the data series into N_B blocks of length k and compute the auto-covariance estimator ${}^{b}\hat{R}^{AA}_{n,j}$ for each of the blocks

according to

$$ {}^{b}\hat{R}^{AA}_{n,j} = \frac{1}{k} \sum_{i=1}^{k-|j|} \left(A_{(n-1)k+i} - \bar{A}_n\right) \left(A_{(n-1)k+i+|j|} - \bar{A}_n\right) , \quad n = 1, \ldots, N_B , \tag{4.37} $$

where $\bar{A}_n$ denotes the average of the nth block. Assuming that the blocks are large enough for the samples to decorrelate within one block, the lag-dependent error of the integral can then be estimated from the uncorrelated error of the set of N_B integrated block-auto-covariances ${}^{b}\hat{R}^{AA}_{\mathrm{int},n,j}$ for each j.

We can then set $j_{\max}$ to a value where the error $\hat{\epsilon}\left({}^{b}\hat{R}^{AA}_{\mathrm{int},j}\right)$ is smaller than a chosen threshold and either simply cut the integral at this point or (better!) determine its asymptotic value by fitting a suitable function (usually, but not always, an exponential approach). Note that for such a fit to be reliable, the error needs to be taken into account in the fitting procedure.

4.1.4 Numerical evaluation of autocorrelation or auto-covariance estimators

According to eqs. (4.26) and (4.27), the estimators of auto-covariance functions reduce to those of autocorrelation functions if the expected value $\langle A \rangle$ (or its estimator $\bar{A}$) is subtracted from all data points A_i prior to evaluation. The notation in the following discussion will therefore not distinguish between the two and assume that the subtraction has already been carried out, or that the expected value is known to be $\langle A \rangle = 0$ so that the auto-covariance function equals the autocorrelation function by construction.

The evaluation of the estimators for all accessible lag times $\tau = j\,\Delta t$ has a computational complexity of $\mathcal{O}\left(N^2\right)$, which quickly becomes infeasible for large values of N. We recall that the autocorrelation function

of a continuous time-dependent variable $A(t) \in \mathbb{R}$ is defined as

$$R^{AA}(\tau) := \langle A(t)A(t+\tau)\rangle = \int_{-\infty}^{\infty} A(t)A(t+\tau)\,\mathrm{d}t\,.$$

According to the convolution theorem, the integral on the RHS can be expressed as

$$\int_{-\infty}^{\infty} A(t)A(t+\tau)\,\mathrm{d}t = \mathcal{F}^{-1}\Big\{\mathcal{F}\left\{A(\tau)\right\}^{*}(\omega)\cdot\mathcal{F}\left\{A(\tau)\right\}(\omega)\Big\}(\tau)\,,$$

where the asterisk * denotes the complex conjugate, $\mathcal{F}\{\cdot\}$ denotes the Fourier transform defined as

$$\mathcal{F}\left\{A(t)\right\}(\omega) = \int_{-\infty}^{\infty} A(t)\exp(-i\omega t)\,\mathrm{d}t =: \tilde{A}(\omega)\,,$$

and $\mathcal{F}^{-1}\{\cdot\}$ its inverse

$$\mathcal{F}^{-1}\Big\{\tilde{A}(\omega)\Big\}(t) = \frac{1}{2\pi}\int_{-\infty}^{\infty}\tilde{A}(\omega)\exp(i\omega t)\,\mathrm{d}\omega\,.$$

Due to the fact that $A(t)$ is measured at discrete time steps Δt during a finite simulation time $t_{\mathrm{sim}} = N\,\Delta t$, $A(t)$ is discretized as $A_j := A(j\,\Delta t)$, $j = 0, 1, ..., N-1$, and the Fourier transform $\mathcal{F}\left\{A(t)\right\}(\omega)$ is replaced by a numerical estimator

$$\hat{\mathcal{F}}_k\left\{A\right\} = \sum_{j=0}^{N-1} A_j \exp\left(-2\pi i\frac{jk}{N}\right) =: \tilde{A}_k$$

with inverse

$$\hat{\mathcal{F}}_j^{-1}\left\{\tilde{A}\right\} = \frac{1}{N}\sum_{k=0}^{N-1}\tilde{A}_k\exp\left(2\pi i\frac{jk}{N}\right)\,.$$

However, since these estimators assume that the time series A_j is periodic in time, we cannot directly employ them to estimate the autocorrelation functions of nonperiodic time series. To prevent the estimators from "round-tripping" the data, we extend the data series (after subtraction of the expected value!) by an equal number of zeros, so that the Fourier transform estimators of the *zero-padded* data (indicated by the prescript z) are given by

$$ {}^{z}\hat{\mathcal{F}}_k\{A\} = \sum_{j=0}^{2N-1} A_j \exp\left(-2\pi i \frac{jk}{2N}\right) =: {}^{z}\tilde{A}_k\,, \quad A_j = 0 \text{ for all } j \geq N \tag{4.38} $$

and

$$ {}^{z}\hat{\mathcal{F}}_j^{-1}\left\{{}^{z}\tilde{A}\right\} = \frac{1}{2N} \sum_{k=0}^{2N-1} {}^{z}\tilde{A}_k \exp\left(2\pi i \frac{jk}{2N}\right)\,. \tag{4.39} $$

The autocorrelation estimators ${}^{b}\hat{R}_j^{AA}$ and ${}^{u}\hat{R}_j^{AA}$ can then be obtained from

$$ {}^{b}\hat{R}_j^{AA} = \frac{1}{N} {}^{z}\hat{\mathcal{F}}_{|j|}^{-1}\left\{{}^{z}\tilde{A}^* \, {}^{z}\tilde{A}\right\}\,, \tag{4.40} $$

$$ {}^{u}\hat{R}_j^{AA} = \frac{1}{N-|j|} {}^{z}\hat{\mathcal{F}}_{|j|}^{-1}\left\{{}^{z}\tilde{A}^* \, {}^{z}\tilde{A}\right\}\,. \tag{4.41} $$

If the Fourier transforms are computed using the fast Fourier transform (FFT) method[103] as provided, *e.g.*, by the FFTW package,[104] the computational complexity of the evaluation of autocorrelation or autocovariance estimators is reduced from $\mathcal{O}(N^2)$ to $\mathcal{O}(N \log_2(N))$, which allows their fast evaluation even if N is in the order of billions.

4.2 Extracting Dielectric Spectra from Molecular Dynamics Simulations

According to the derivation given in chapter 3, dielectric spectra can be obtained from equilibrium MD simulations by computing the cumulative current autocorrelation in the system and taking its Fourier-Laplace transform. In the previous section, we have shown how autocorrelation functions of discrete time series can be estimated numerically in an efficient and accurate manner. Here, we will discuss technical requirements and challenges regarding the simulation itself as well as the further analysis of the recorded data.

4.2.1 Simulation and data acquisition

To sufficiently resolve the low-frequency modes of the permittivity spectrum $\varepsilon_r(\omega)$, the autocorrelation $\langle \boldsymbol{j}(0)\boldsymbol{j}(\tau)\rangle$ has to be evaluated over a large interval. This requires very long simulation runs, typically in the order of microseconds. On the other hand, to ensure stable integration of the equations of motion, the maximum time step in an MD simulation is usually limited to the order of a femtosecond. Furthermore, the obtained correlations are generally noisy, and while their statistical quality strongly depends on the total simulation time, it also depends on the number of particles in the system. Thus, it is evident that extracting dielectric spectra from MD simulations is computationally expensive as it requires simulating sufficiently large systems for about 10^8 to 10^9 time steps. Due to these demands, we used the GROMACS[105–111] software package to perform all MD simulations. This choice was motivated not only by the high performance that GROMACS provides in terms of computational speed but—equally important—by the fact that its source code is publicly available and, therefore, can be modified and extended.

Traditionally, analyses of MD simulations are based on trajectory data that has been written to disk during the simulation. To compute

the cumulative current $\boldsymbol{j}(t)$ from such a trajectory, it must contain the velocities of all particles in the system with sufficiently high temporal resolution. For a simulation with only 5000 particles and the trajectory stored at every time step in single precision during a total simulation time of one microsecond, the trajectory would comsume about 56 TiB of disk space. Considering the fact that one usually aims to compare the results obtained from different simulations, *e.g.*, with varying concentrations of different kinds of molecular species, the storage space requirements of such post-processing analyses quickly become prohibitively high. To reduce the computational cost and keep disk space requirements low, we chose to compute the cumulative currents according to eq. (3.54) already during the run time of the simulation, *i.e.*, while the charges and velocities of all particles are available in main memory anyway. The GROMACS source code was modified accordingly, preserving the full support of hybrid CPU/GPU parallelization as well as checkpointing while providing a convenient user interface. This reduced the storage requirements dramatically by a factor corresponding to the number of particles in the system, while providing the maximum temporal resolution and without imposing any significant computational overhead.

4.2.2 Data analysis

The time series of the cumulative currents $\boldsymbol{j}(t)$ obtained as described above can then be used to compute dielectric relaxation spectra $\varepsilon_r(\omega)$ according to eqs. (3.58) and (3.61) using a separately developed post-processing tool, where the correlations $\langle \boldsymbol{j}(0)\boldsymbol{j}(\tau)\rangle$ are computed rapidly according to eq. (4.41) using FFT algorithms provided by the FFTW library.[104] Nevertheless, the evaluation of eq. (3.58) also involves a Fourier-Laplace transform, and the time required for a direct evaluation of the transform of an N-point time series would scale with $\mathcal{O}(N^2)$. However, if we realize that the Fourier-Laplace transform is identical to an inverse Fourier transform in τ (neglecting any prefactors) involving

only positive lag times τ, we can rewrite eq. (3.58) as

$$\begin{aligned}\sigma_e(\omega) &= \frac{1}{3Vk_\mathrm{B}T}\int_0^\infty \langle \boldsymbol{j}(0)\,\boldsymbol{j}(\tau)\rangle\, e^{i\omega\tau}\,\mathrm{d}\tau \\ &= \frac{1}{3Vk_\mathrm{B}T}\int_{-\infty}^\infty h(\tau)\,\langle \boldsymbol{j}(0)\,\boldsymbol{j}(\tau)\rangle\, e^{i\omega\tau}\,\mathrm{d}\tau\,,\end{aligned} \tag{4.42}$$

where $h(\cdot)$ denotes the Heaviside step function, which, using the half-maximum convention,[b] is defined as

$$h(x) = \begin{cases} 1, & x > 0 \\ \frac{1}{2}, & x = 0 \\ 0, & x < 0\,. \end{cases} \tag{4.43}$$

In practice, this means that appending[c] a signal of equal length containing only zeros to the signal $\boldsymbol{j}(t)$ and computing the discrete fourier transform is sufficient to obtain $\sigma_e(\omega)$. Finally, the complete equation for the dielectric spectrum now reads

$$\varepsilon_r(\omega) = 1 + \frac{1}{3\varepsilon_0 Vk_\mathrm{B}T}\frac{i}{\omega}\left(\int_{-\infty}^\infty h(\tau)\,\langle \boldsymbol{j}(0)\,\boldsymbol{j}(\tau)\rangle\, e^{i\omega\tau}\,\mathrm{d}\tau - \sigma_e^\mathrm{static}\right). \tag{4.44}$$

[b] Using the half-maximum convention is not strictly necessary for the analytic derivation but required for the correct numerical evaluation if $\boldsymbol{j}(t)$ is a discrete-time signal.

[c] The zeros have to be appended (*not* prepended) because in the implementation of FFT algorithms, the data entering the inverse transform must be arranged in memory such that the positive-frequency part going from zero to the Nyquist frequency must appear *in front* of the negative-frequency part going from negative Nyquist frequency to zero.

4.2.3 Proof of principle: The dielectric spectrum of water

Note: Parts of the contents of this and the following section have been previously published in the supporting information of the article

D. Markthaler, J. Zeman, J. Baz, J. Smiatek and N. Hansen, Validation of Trimethylamine-N-oxide (TMAO) Force Fields Based on Thermophysical Properties of Aqueous TMAO Solutions, *The Journal of Physical Chemistry B* **121**, 10674–10688 (2017).

Only my own contributions are reproduced here.

To show that the theoretical and computational framework can be successfully applied to actual MD simulation data, we computed the dielectric spectrum of pure water using the extended simple point charge[112] (SPC/E) water model. The time series of the cumulative current $\boldsymbol{j}(t)$ required to compute $\varepsilon_r(\omega)$ according to eq. (4.44) was obtained from a simulation of 2180 water molecules in the NpT ensemble at $T = 300\,\mathrm{K}$ and $p = 1\,\mathrm{bar}$ with a total simulation time of $\approx 1\,\mu\mathrm{s}$ (2^{30} steps with a time step of 1 fs). The resulting spectrum is shown in fig. 4.1.

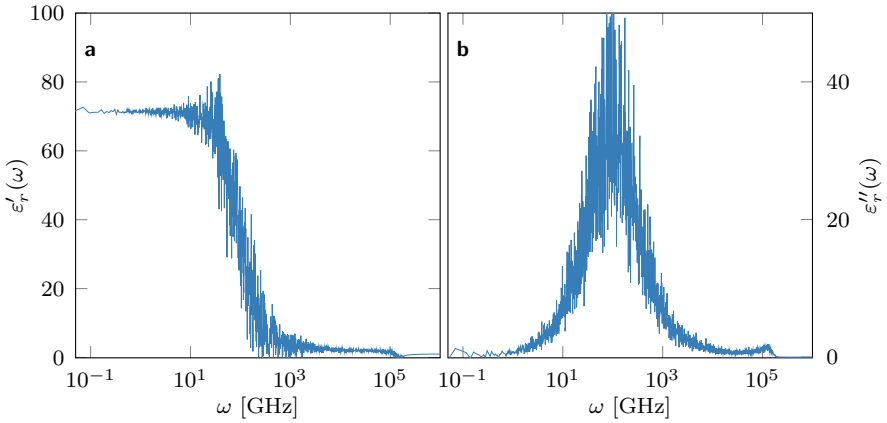

Figure 4.1: Dielectric spectrum of pure SPC/E water at 300 K and 1 bar. **a**: Dielectric dispersion $\varepsilon_r'(\omega)$. The data approaches $\varepsilon_r' \approx 71$ for $\omega \to 0$, which is somewhat lower than the experimental value[18] of 78.4 but corresponds to the value of $\varepsilon_r' = 70.8$ that Reddy and Berkowitz[113] obtained for SPC/E water at 298 K. **b**: Dielectric loss $\varepsilon_r''(\omega)$. The maximum of the dielectric loss peak is centered at $\omega \approx 100\,\mathrm{GHz}$ ($\nu \approx 16\,\mathrm{GHz}$), which is in good correspondence with the experimental value of $\approx 20\,\mathrm{GHz}$ at 298.15 K..[18]

Even though the data was obtained from a rather long simulation run, we see that the spectrum we obtained from the evaluation of the raw data is very noisy. This is a consequence of the general fact that the error of correlation estimates obtained from finite time series of statistical processes will always suffer from statistical noise in their tails, as has been discussed in section 4.1.3. Of course, this is also the case for the autocorrelation $R_{\boldsymbol{jj}}(\tau) := \langle \boldsymbol{j}(0)\boldsymbol{j}(\tau)\rangle$ entering the Fourier transform in eq. (4.44), so that the random noise in the current autocorrelation's tail will yield a noisy spectrum by construction. In fact, even though any further increase in simulation time will increase the statistical accurracy of $R_{\boldsymbol{jj}}(\tau)$ for small τ, its tail will likewise extend to longer lag times and will asymptotically suffer from the same statistical noise. To overcome this problem, in the following section, we will develop a method to reduce the noise in the spectrum in a physically consistent way.

4.2.4 Physically consistent noise reduction

An often-used method for noise reduction is to fit the tail of the autocorrelation with a suitable analytic function $f(\tau)$ starting from an appropriate lag time τ_{tail}. Then, in the analysis, the raw data is used for lag times $\tau < \tau_{\text{tail}}$, and the analytic fit for $\tau \geq \tau_{\text{tail}}$. However, when integral quantities are computed, it is a common misconception to apply a least-squares fit *directly* to the autocorrelation data. When employing the least-squares norm as a convergence criterion for the fit, the problem that arises is that this norm does *not* preserve the integral of the data. An additional problem specific to the calculation of spectra is the abrupt switch at τ_{tail} from the raw data to the fit funtion, which may lead to a small but sudden jump in the data. Such jumps can introduce artifacts in the Fourier transforms known as *spectral leakage*.

We overcome both problems in a mathematically and physically consistent way by determining the fit parameters from the integral of the autocorrelation data and by smoothly tapering the raw data to the fit function. The procedure is as follows:

1. Integrate the raw autocorrelation data $R_{\boldsymbol{jj}}(\tau)$ to obtain $R^{\mathrm{int}}_{\boldsymbol{jj}}(\tau) := \int R_{\boldsymbol{jj}}(\tau)\,\mathrm{d}\tau$.

2. Fit an appropriate integrated analytic function $F(\tau) = \int f(\tau)\,\mathrm{d}\tau + c$ to $R^{\mathrm{int}}_{\boldsymbol{jj}}(\tau)$ starting from τ_{tail}.

3. From the obtained fit parameters of $F(\tau)$, analytically determine the parameters of the fit function $f(\tau)$ that is supposed to fit the original $R_{\boldsymbol{jj}}(\tau)$.

4. On the interval $[\tau_{\mathrm{tail}},\ \tau_{\mathrm{tail}} + \Delta\tau_{\mathrm{taper}}]$, let the autocorrelation data gradually approach the fit function $f(\tau)$ by means of an appropriate taper function $w(\tau)$ to obtain the noise-reduced autocorrelation data $\tilde{R}_{\boldsymbol{jj}}(\tau)$. A linear taper is usually sufficient.

5. Compute the integral $\tilde{R}^{\mathrm{int}}_{\boldsymbol{jj}}(\tau) = \int \tilde{R}_{\boldsymbol{jj}}(\tau)\,\mathrm{d}\tau$ and compare to $R^{\mathrm{int}}_{\boldsymbol{jj}}(\tau)$. If the integral is not preserved, increase τ_{tail} or choose a more appropriate fit function $f(\tau)$ and repeat from step 2.

As an example, we demonstrate the difference between our integral-preserving noise-reduction procedure ("integral-fitted") and the often-used direct approach ("directly fitted") for the same system of pure SPC/E water as used above in section 4.2.3. The raw current autocorrelation data $R_{\boldsymbol{jj}}(\tau)$ of this system is displayed in panel a of fig. 4.2 (blue line). To highlight the importance of this procedure, fig. 4.2 also depicts $\tilde{R}_{\boldsymbol{jj}}(\tau)$ (panel a, dashed black line) and $\tilde{R}^{\mathrm{int}}_{\boldsymbol{jj}}(\tau)$ (panel b, dashed black line), where $\tilde{R}_{\boldsymbol{jj}}(\tau)$ was obtained by fitting $f(\tau)$ directly to $R_{\boldsymbol{jj}}(\tau)$. In panel a, the data obtained by the two different procedures seem to perfectly coincide. However, the dashed black line in the inset of panel b clearly shows that the direct fit procedure fails to reproduce the integral of the original raw data.

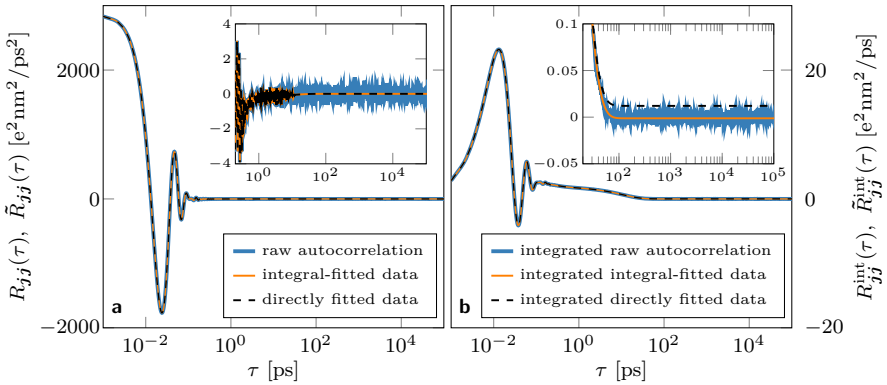

Figure 4.2: Noise reduction example. The data was obtained from an NpT simulation of 2180 SPC/E water molecules at 300 K and 1 bar with a simulation time of $\approx 1\,\mu s$ (2^{30} steps, time step 1 fs). **a**: Current autocorrelation data $R_{\boldsymbol{jj}}(\tau) = \langle \boldsymbol{j}(0)\boldsymbol{j}(\tau)\rangle$ (blue line). The orange line depicts the data obtained from the noise-reduction procedure ("integral-fitted") described above with an exponential fit function and a linear taper. For comparison, a direct fit to the data of the same functional form is shown as a dashed black line ("directly fitted"). Even in the magnified view of the autocorrelation tail provided in the inset, both fits seem to coincide since their difference is much smaller than the line width. **b**: Corresponding integrals of the raw autocorrelation data and fits from panel a (same color code). From the magnified view of the integrals' tails shown in the inset it becomes evident that the direct fit to the autocorrelation data does *not* preserve its integral (dashed black line).

The data displayed in fig. 4.2 were obtained according to the procedure as described above. In detail, the following steps were performed:

1. The integral $R^{\mathrm{int}}_{\boldsymbol{jj}}(\tau)$ shown in panel b (blue line) was evaluated numerically by means of the trapezoidal rule.

2. We then performed a least-squares fit of the function $F(\tau) = a_F \exp(b_F\,\tau) + c_F$ to $R^{\mathrm{int}}_{\boldsymbol{jj}}(\tau)$ for $\tau \geq \tau_{\mathrm{tail}}$ with $\tau_{\mathrm{tail}} = 2\,\mathrm{ps}$.

3. The obtained parameters a_F and b_F were used to determine the parameters of the function $f(\tau) = a_f \exp(b_f\,\tau) \stackrel{!}{=} \frac{\mathrm{d}}{\mathrm{d}\tau}F(\tau)$ as $a_f = a_F\,b_F$, and $b_f = b_F$.

4. On the interval $[\tau_{\mathrm{tail}},\ \tau_{\mathrm{tail}} + \Delta\tau_{\mathrm{taper}}]$ with $\Delta\tau_{\mathrm{taper}} = 10\,\mathrm{ps}$, we let the autocorrelation data approach $f(\tau)$ using a linear taper

$w(\tau) = 1 - (\tau - \tau_{\text{tail}})/\Delta\tau_{\text{taper}}$ so that

$$\tilde{R}_{\boldsymbol{jj}}(\tau) = \begin{cases} R_{\boldsymbol{jj}}(\tau), & \tau < \tau_{\text{tail}} \\ f(\tau) + w(\tau)\left(R_{\boldsymbol{jj}}(\tau) - f(\tau)\right), & \tau_{\text{tail}} \leq \tau \leq \tau_{\text{tail}} + \Delta\tau_{\text{taper}} \\ f(\tau), & \tau > \tau_{\text{tail}} + \Delta\tau_{\text{taper}}\,. \end{cases}$$

The resulting data for $\tilde{R}_{\boldsymbol{jj}}(\tau)$ are depicted in fig. 4.2, panel a (orange line).

5. Once again using the trapezoidal rule, we computed the integral $\tilde{R}^{\text{int}}_{\boldsymbol{jj}}(\tau) = \int \tilde{R}_{\boldsymbol{jj}}(\tau)\,\mathrm{d}\tau$ displayed in fig. 4.2, panel b (orange line). The zoom-in on the tail shown in the inset confirms that $\tilde{R}^{\text{int}}_{\boldsymbol{jj}}(\tau)$ indeed follows $R^{\text{int}}_{\boldsymbol{jj}}(\tau)$.

To show the impact of the noise-reduction technique on dielectric spectra, fig. 4.3 depicts the dielectric spectra obtained from to the data displayed in fig. 4.2 above (same color code).

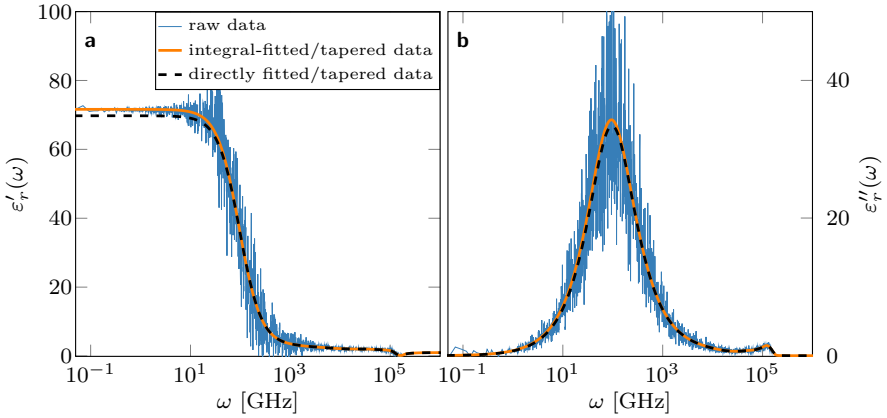

Figure 4.3: Dielectric spectrum of pure SPC/E water at 300 K and 1 bar. **a**: Dielectric dispersion $\varepsilon'_r(\omega)$. **b**: Dielectric loss $\varepsilon''_r(\omega)$. The integral-fitting technique results in a smooth spectrum (orange lines) perfectly following the spectrum computed from raw data (blue lines). The spectrum obtained from the direct fit approach (dashed black lines) clearly underestimates both the low-frequency part of $\varepsilon'_r(\omega)$ and the loss peak amlitude of $\varepsilon''_r(\omega)$.

The spectrum was computed from the current autocorrelation data according to eq. (4.44). Due to the fact that the system contains only net-neutral molecules, the static conductivity σ_e^{static} is zero by construction and therefore must not be considered when evaluating eq. (4.44). While the integral-fitting technique results in a smooth spectrum perfectly following the noisy spectrum obtained from the raw data, the direct fit approach yields a spectrum clearly underestimating the low-frequency part of the dispersion $\varepsilon_r'(\omega)$ and the amplitude of the main loss peak in $\varepsilon_r''(\omega)$.

4.2.5 Validation against experimental data

Now that we are able to obtain high-quality dielectric spectra from MD simulations, we will put the computational framework to a further test and compare the spectra predicted by MD simulations to experimental data. To this aim, we performed simulations of pure water systems using the same parameters as above but employing different atomistic water models, namely the SPC/E,[112] TIP3P,[114] TIP4P/2005,[115] and OPC[116] models. All of these models are completely rigid and non-polarizable[d], implying that they cannot match experimental spectra in the THz regime by construction. We therefore compare to experimental data in the GHz regime which were taken from Hunger *et al.*[117]

The results for the SPC/E and TIP4P/2005 models are in perfect agreement with the spectra computed by Sega and Schröder,[118] confirming that our implementation is correct. From fig. 4.4a it becomes evident that all tested water models reproduce the experimentally measured dielectric dispersion $\varepsilon_r'(\omega)$ (thick black line) qualitatively quite well. The SPC/E model slightly underestimates the static permittivity $\varepsilon_r(\omega \to 0)$, but the qualitative agreement of the curve is excellent. While the TIP3P model strongly overestimates the static permittivity, the TIP4P/2005 model underestimates it by roughly the same amount. The only model reproducing the static permittivity

[d] In MD simulations, a 'polarizable' model refers to one that explicitly models electronic polarizability. While this means that individual atoms cannot be polarized, the entire system still has a polarization response.

correctly is the OPC model. However, the shape of the curve is qualitatively worse than those of the other models. The low-frequency absorption peak of the dielectric loss spectrum $\varepsilon_r''(\omega)$ shown in figure 4.4b is also qualitatively well-reproduced by all models. While the TIP3P model matches the location of the peak on the frequency axis almost perfectly, it strongly overestimates its amplitude. As for the dispersion spectrum, the TIP4P/2005 model strongly underestimates the amplitude of the loss peak, again by roughly the same amount as it is overestimated by the TIP3P model. The OPC model fits the the peak amplitude quite well, but the peak position on the frequency axis is significantly red-shifted. Overall, the best trade-off between qualitative and quantitative agreement can be attributed to the SPC/E model (green line). Because of this and due to the fact that there exists a plethora of compatible models of other molecules, we chose SPC/E as the preferred water model for simulating scenarios requiring an accurate description of dielectric properties.

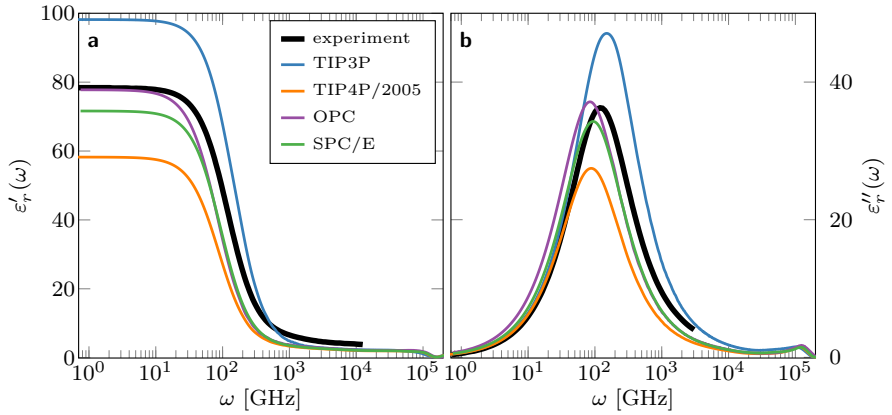

Figure 4.4: Dielectric dispersion (**a**) and loss spectra (**b**) of different atomistic water models (thin colored lines) compared to experimental data[117] (thick black lines). The qualitative shape is reproduced fairly well by all models, while the OPC model shows the best quantitative agreement at low frequency. The best trade-off between qualitative and quantitative agreement can be attributed to the SPC/E model. All spectra were obtained from simulations of 2180 water molecules in the NpT ensemble at $T = 300\,\mathrm{K}$ and $p = 1\,\mathrm{bar}$ with a time step of 1 fs and a simulation time of about 1 µs (2^{30} steps).

4.3 Estimating Static Relative Dielectric Permittivities and Conductivities

Note: The contents of this and the following section have been previously made available online in similar form in the supplementary material of

J. Zeman, S. Kondrat and C. Holm, Ionic Screening in Bulk and under Confinement, *The Journal of Chemical Physics* (accepted)

So far we have seen how we can employ equilibrium MD simulations to predict the frequency-dependent spectrum of the complex relative dielectric permittivity $\varepsilon_r(\omega)$ from that of the complex conductivity $\sigma_e(\omega)$. However, we also saw that according to eq. (4.44), obtaining the apparent relative permittivity requires the knowledge of the static conductivity $\sigma_e^{\text{static}} := \lim_{\omega\to 0} \sigma_e(\omega)$. Taking the limit $\omega \to 0$ of equation eq. (3.58) yields

$$\sigma_e^{\text{static}} = \frac{1}{3Vk_{\text{B}}T} \int_0^\infty \langle \boldsymbol{j}(0)\, \boldsymbol{j}(\tau) \rangle \, \mathrm{d}\tau \,, \tag{4.45}$$

so that the static conductivity can be estimated by evaluating the integral of the current autocorrelation $\langle \boldsymbol{j}(0)\, \boldsymbol{j}(\tau) \rangle$ in the limit of large τ.

As we will see later in chapter 7 in the context of electrostatic screening, another quantity of interest is the static relative permittivity $\varepsilon_r^{\text{static}} := \lim_{\omega\to 0} \varepsilon_r(\omega)$, which is most often simply denoted as ε_r. Inserting eq. (3.45) into the definition $\epsilon_r = 1 + \chi_e$ yields

$$\varepsilon_r = 1 + \frac{\langle \boldsymbol{M}^2 \rangle}{3\varepsilon_0 V k_{\text{B}} T} \,, \tag{4.46}$$

which is the same expression for ε_r as derived by Neumann[120] for MD simulations with electrostatic tin foil boundary conditions at infinity. However, as we have shown in section 3.4, the total dipole moment $\boldsymbol{M}$

is ill-defined in systems with free ionic charges employing PBC and therefore cannot be measured directly. Instead, $\langle \boldsymbol{M}^2 \rangle$ can be obtained from the itinerant total current $\boldsymbol{j}$ according to

$$\langle \boldsymbol{M}^2 \rangle = - \lim_{t \to \infty} \int_0^t \tau \langle \boldsymbol{j}(0) \boldsymbol{j}(\tau) \rangle \, \mathrm{d}\tau \,. \tag{4.47}$$

A proof of this equation is given in appendix 4.A.

In practice, the tail of the current autocorrelation function $\langle \boldsymbol{j}(0) \boldsymbol{j}(\tau) \rangle$ suffers from statistical noise, which is amplified by the factor τ in the integral of eq. (4.47). Thus, determining $\langle \boldsymbol{M}^2 \rangle$ directly from eq. (4.47) is infeasible. This issue is clearly visible in fig. 4.5, which shows the autocorrelation $\langle \boldsymbol{j}(0) \boldsymbol{j}(\tau) \rangle$ (panel a), its running integral $\int_0^\tau \langle \boldsymbol{j}(0) \boldsymbol{j}(\tau') \rangle \, \mathrm{d}\tau'$ (panel b), and the negative integral of the lag time-weighted autocorrelation $- \int_0^\tau \tau' \langle \boldsymbol{j}(0) \boldsymbol{j}(\tau') \rangle \, \mathrm{d}\tau'$ (panel c) of the current $\boldsymbol{j}(t)$ obtained from simulations of a 50 mol% solution of $[\mathrm{C_4C_1Im}]^+ [\mathrm{NTf_2}]^-$ in propylene carbonate.

The system was simulated at a temperature of $T = 300\,\mathrm{K}$ and a pressure of $p = 1\,\mathrm{bar}$ and contained an IL mole fraction of $x_{\mathrm{IL}} = 0.5$ (concentration $c_{\mathrm{IL}} = 2.75\,\mathrm{mol/l}$) comprising 500 ion pairs and 500 solvent molecules. The current $\boldsymbol{j}(t)$ was computed according to eq. (3.54) and recorded at every time step ($\delta t = 2\,\mathrm{fs}$) during the simulation time of $t_{\mathrm{sim}} \approx 1074\,\mathrm{ns}$ (2^{29} time steps) per run from three independent simulation runs. For each run, the autocorrelation functions $\langle j_d(0) j_d(\tau) \rangle$ were computed for each spatial dimension $d \in \{x, y, z\}$ according to eq. (4.41), summed up over d to obtain $\langle \boldsymbol{j}(0) \boldsymbol{j}(\tau) \rangle$, and finally averaged over all runs.

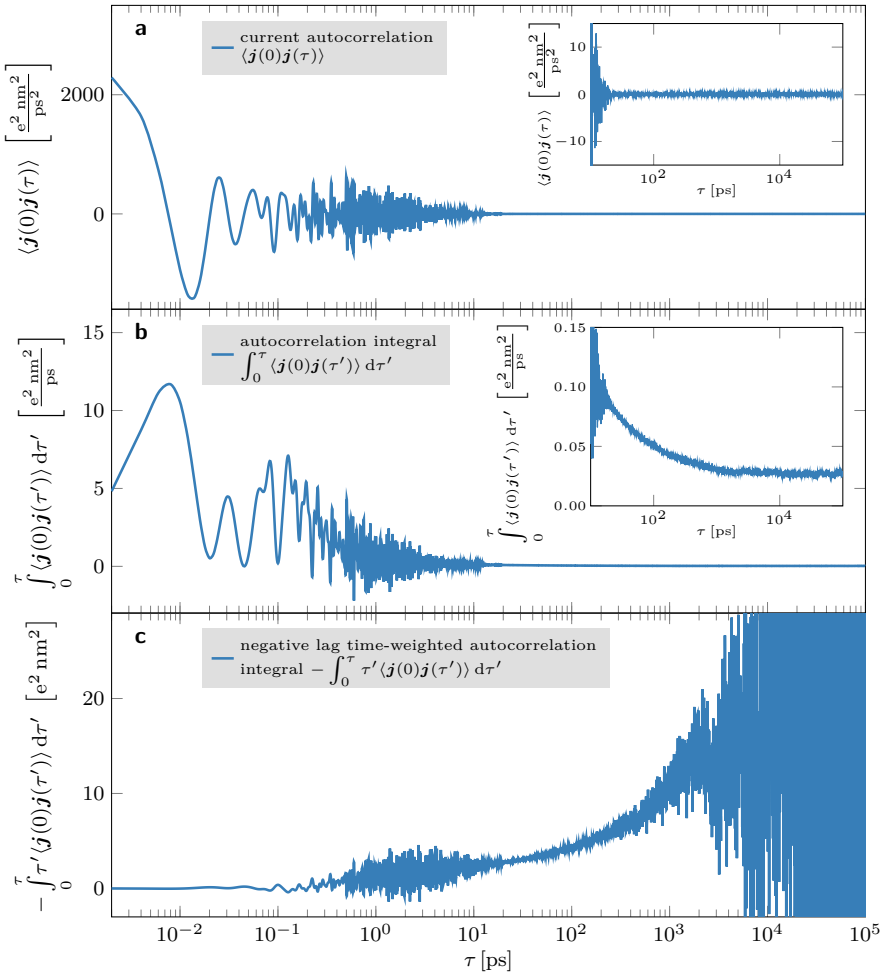

Figure 4.5: Panel a: Current autocorrelation $\langle \boldsymbol{j}(0)\boldsymbol{j}(\tau)\rangle$. Inset: Magnification of the tail region ($10 \leq \tau \leq 10^5$ ps). The autocorrelation seems to have converged to zero at $\tau \approx 30$ ps, and the remaining tail appears to be random noise. Panel b: Running integral $\int_0^\tau \langle \boldsymbol{j}(0)\boldsymbol{j}(\tau')\rangle\,\mathrm{d}\tau'$ of the current autocorrelation. Inset: Magnification of the tail region ($10 \leq \tau \leq 10^5$ ps), from which it becomes evident that the seemingly random noise in the autocorrelation's tail actually still contains information up to $\tau \approx 3 \cdot 10^3$ ps, where the integral has converged to a value of about $0.027\,\mathrm{e}^2\,\mathrm{nm}^2\,\mathrm{ps}^{-1}$. Panel c: Negative running integral $\int_0^\tau \tau'\langle \boldsymbol{j}(0)\boldsymbol{j}(\tau')\rangle\,\mathrm{d}\tau'$ of the lag time-weighted current autocorrelation (RHS of eq. (4.47)). Due to the multiplication with the lag time, the noise in the current autocorrelation's tail is amplified, which makes it practically impossible to obtain a meaningful estimate of the integral's asymptotic value $\langle \boldsymbol{M}^2\rangle$.

4.3.1 The Einstein-Helfand method

An alternative approach is to estimate $\langle \boldsymbol{M}^2 \rangle$ from the itinerant dipole moment's mean square displacement $\langle (\Delta \boldsymbol{M})^2(t) \rangle = \langle [\boldsymbol{M}(t) - \boldsymbol{M}(0)]^2 \rangle$, which will be discussed in the following.

Since $\boldsymbol{M}(t)$ is continuously differentiable, we can express its value at time t as

$$\boldsymbol{M}(t) = \boldsymbol{M}(t_0) + \int_{t_0}^{t} \left(\frac{\mathrm{d}}{\mathrm{d}\tau} \boldsymbol{M}(\tau) \right) \mathrm{d}\tau \,.$$

By inserting the definition of the total current

$$\boldsymbol{j}(t) = \frac{\mathrm{d}}{\mathrm{d}t} \boldsymbol{M}(t) \tag{4.48}$$

and setting $t_0 = 0$, we obtain

$$\int_{0}^{t} \boldsymbol{j}(\tau) \, \mathrm{d}\tau = \boldsymbol{M}(t) - \boldsymbol{M}(0) \,. \tag{4.49}$$

Accordingly, we can express $\langle (\Delta \boldsymbol{M})^2(t) \rangle$ as

$$\begin{aligned} \langle (\Delta \boldsymbol{M})^2(t) \rangle &= \left\langle \left(\int_0^t \boldsymbol{j}(t') \, \mathrm{d}t' \right)^2 \right\rangle \\ &= \int_0^t \left(\int_0^t \langle \boldsymbol{j}(t') \boldsymbol{j}(t'') \rangle \, \mathrm{d}t'' \right) \mathrm{d}t' \,, \end{aligned} \tag{4.50}$$

where we identify $\langle \boldsymbol{j}(t') \boldsymbol{j}(t'') \rangle$ as the autocorrelation function of the itinerant current $\boldsymbol{j}$ centered at t'. Since $\langle \boldsymbol{j}(t') \boldsymbol{j}(t'') \rangle$ is symmetric around t', we can rewrite eq. (4.50) as

$$\langle (\Delta \boldsymbol{M})^2(t) \rangle = 2 \int_0^t \left(\int_0^{t'} \langle \boldsymbol{j}(t') \boldsymbol{j}(t'') \rangle \, \mathrm{d}t'' \right) \mathrm{d}t' \,. \tag{4.51}$$

Furthermore, at equilibrium, the autocorrelation function is invariant under translations in time, so that translating by $-t'$ and substituting $t'' - t' \to \tau$ yields

$$\langle (\Delta \boldsymbol{M})^2(t) \rangle = 2 \int_0^t \left(\int_0^{t'} \langle \boldsymbol{j}(0) \boldsymbol{j}(\tau) \rangle \, \mathrm{d}\tau \right) \mathrm{d}t' \,. \tag{4.52}$$

We can now change the order of integration by expressing the ranges of integration as

$$\underbrace{(0 \leq \tau \leq t')}_{\text{inner}} \wedge \underbrace{(0 \leq t' \leq t)}_{\text{outer}} \Leftrightarrow (0 \leq \tau \leq t' \leq t) \Leftrightarrow \underbrace{(\tau \leq t' \leq t)}_{\text{inner}} \wedge \underbrace{(0 \leq \tau \leq t)}_{\text{outer}} \tag{4.53}$$

to obtain

$$\begin{aligned}
\langle (\Delta \boldsymbol{M})^2(t) \rangle &= 2 \int_0^t \left(\int_\tau^t \langle \boldsymbol{j}(0) \boldsymbol{j}(\tau) \rangle \, \mathrm{d}t' \right) \mathrm{d}\tau \\
&= 2 \int_0^t \langle \boldsymbol{j}(0) \boldsymbol{j}(\tau) \rangle \left(\int_\tau^t \mathrm{d}t' \right) \mathrm{d}\tau \\
&= 2 \int_0^t \langle \boldsymbol{j}(0) \boldsymbol{j}(\tau) \rangle (t - \tau) \, \mathrm{d}\tau \\
&= 2t \int_0^t \langle \boldsymbol{j}(0) \boldsymbol{j}(\tau) \rangle \, \mathrm{d}\tau - 2 \int_0^t \tau \langle \boldsymbol{j}(0) \boldsymbol{j}(\tau) \rangle \, \mathrm{d}\tau \,.
\end{aligned} \tag{4.54}$$

In the limit $t \to \infty$ (or at least for $t \gg \tau_\mathrm{c}$ far beyond the autocorrelation time τ_c), both integrals converge to a constant so that

$$\begin{aligned}
\lim_{t \to \infty} \big(\langle (\Delta \boldsymbol{M})^2(t) \rangle \big) &= 2t \lim_{t \to \infty} \left(\int_0^t \langle \boldsymbol{j}(0) \boldsymbol{j}(\tau) \rangle \, \mathrm{d}\tau \right) - 2 \lim_{t \to \infty} \left(\int_0^t \tau \langle \boldsymbol{j}(0) \boldsymbol{j}(\tau) \rangle \, \mathrm{d}\tau \right) \\
&=: c_1 \, t + c_2
\end{aligned} \tag{4.55}$$

approaches a linear time dependence for large t with slope c_1 and offset c_2. A comparison with eqs. (4.45) and (4.47) immediately shows that $c_2 = 2\langle \boldsymbol{M}^2 \rangle$ and $c_1 = 6Vk_\mathrm{B}T\,\sigma_e^{\mathrm{static}}$. Thus, by fitting a linear function $f(t) = c_1\,t + c_2$ to $\langle (\Delta \boldsymbol{M})^2(t) \rangle$ for large t, we can obtain the static relative permittivity of the system according to

$$\varepsilon_r = 1 + \frac{c_2}{6Vk_\mathrm{B}T\varepsilon_0} \tag{4.56}$$

and the static conductivity as

$$\sigma_e^{\mathrm{static}} = \frac{c_1}{6Vk_\mathrm{B}T}\,. \tag{4.57}$$

This method is also known as the *Einstein-Helfand* method in the literature.[121]

It is important to note that the onset of the linear regime, and, therefore, the start of the fitting range, is generally difficult to determine from $\langle (\Delta \boldsymbol{M})^2(t) \rangle$. Instead, it should be chosen as the time where the integrated current autocorrelation $\int_0^t \langle \boldsymbol{j}(0)\boldsymbol{j}(\tau) \rangle \,\mathrm{d}\tau$ has converged to a constant because this is much easier to identify.

Figure 4.6 shows the itinerant dipole moment's mean square displacement $\langle (\Delta \boldsymbol{M})^2(t) \rangle$ computed according to eq. (4.54) from the autocorrelation data displayed in fig. 4.5a. The curve looks intriguingly linear, so that the least-squares fit (dashed orange line) to the linear function $f(t) = c_1\,t + c_2$ (eq. (4.55)) in the range $3 \cdot 10^3 \leq t \leq 10^5$ matches the data almost perfectly. The fit parameters and corresponding error estimates $c_1 = 0.05378679 \pm 5.9 \cdot 10^{-8}\,\mathrm{e^2nm^2ps^{-1}}$ and $c_2 = 45.4505 \pm 3.4 \cdot 10^{-3}\,\mathrm{e^2nm^2}$ confirm this. If we now compute the system's static relative permittivity according to eq. (4.56), we obtain

$$\varepsilon_r = 1 + \frac{(45.4505 \pm 0.0034)\,\mathrm{e^2nm^2}}{6 \cdot (301.7629 \pm 0.0026)\,\mathrm{nm^3} \cdot \varepsilon_0 \cdot k_\mathrm{B} \cdot 300\,\mathrm{K}} = 18.5707 \pm 0.0013\,. \tag{4.58}$$

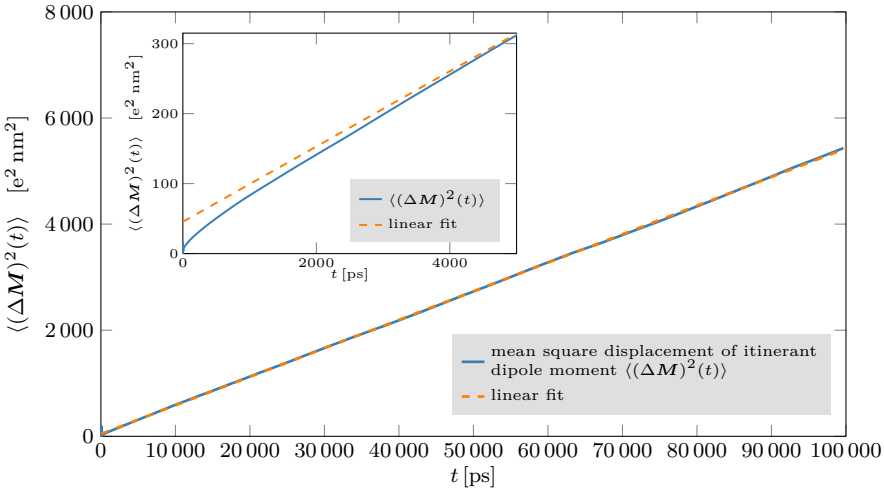

Figure 4.6: Mean square displacement $\langle(\Delta \boldsymbol{M})^2(t)\rangle$ of the system's itinerant dipole moment $\boldsymbol{M}$ (solid blue line) computed according to eq. (4.54) from the autocorrelation data displayed in fig. 4.5a. The dashed orange line represents a least-squares fit of the linear function $f(t) = c_1\, t + c_2$ (eq. (4.55)) in the range $3 \cdot 10^3 \leq t \leq 10^5$, which appears to fit the data extremely well. As discussed in the text, this seemingly perfect fit is misleading, and the actual error is much larger than what one would infer from the covariance matrix of the least squares fit. Inset: Magnification of the mean square displacement's short time behavior (blue line). According to eqs. (4.47) and (4.55), the y-axis offset c_2 can be used to estimate $\langle \boldsymbol{M}^2 \rangle = \frac{1}{2} c_2$.

While the value itself seems reasonable, the error estimate is suspiciously small. In fact, this is for two reasons: (i) the time series used to compute $\langle(\Delta \boldsymbol{M})^2(t)\rangle$ are strongly correlated, which means that the data entering the fit is heavily oversampled, and (ii) the statistical error of $\langle(\Delta \boldsymbol{M})^2(t)\rangle$ is not taken into account. As we will see in the following, even though $\langle(\Delta \boldsymbol{M})^2(t)\rangle$ appears to be perfectly linear in the long time limit, its statistical error is in fact quite substantial.

4.3.2 Error estimation of static permittivities

As mentioned earlier, the analysis of the itinerant dipole moment's mean square displacement $\langle(\Delta \boldsymbol{M})^2(t)\rangle$ in the previous section was based on current autocorrelation data obtained from three independent simulation runs, so that one can perform separate analyses for each system to obtain a better error estimate for the static relative permittivity ε_r. However, this would only yield three independent results, and therefore a rather poor statistical error estimate. In order to improve error estimation, we can make use of the fact that the recorded current $\boldsymbol{j}(t)$ is a vector with three independent components, so that its autocorrelation is the sum of the individual components' autocorrelations

$$\langle \boldsymbol{j}(0)\boldsymbol{j}(\tau)\rangle = \sum_{d\in\{x,y,z\}} \langle j_d(0) j_d(\tau)\rangle \,. \tag{4.59}$$

Since the system under consideration is isotropic, the spatial components $\langle j_d(0) j_d(\tau)\rangle$ must be identical. However, this assumption does not strictly hold for the statistical estimates we are computing from a finite number of samples during a finite simulation time. Thus, together with the fact that j_x, j_y, j_z are statistically independent, we can obtain three independent estimates of $\langle(\Delta \boldsymbol{M})^2(t)\rangle$ from each simulation run according to

$$\begin{aligned}\langle(\Delta \boldsymbol{M})^2(t)\rangle &= 3\,\langle(\Delta M_d)^2(t)\rangle \\ &= 6t \int_0^t \langle j_d(0) j_d(\tau)\rangle \,\mathrm{d}\tau - 6 \int_0^t \tau \langle j_d(0) j_d(\tau)\rangle \,\mathrm{d}\tau \,.\end{aligned} \tag{4.60}$$

Thus, we have nine independent estimates of $\langle(\Delta \boldsymbol{M})^2(t)\rangle$ available for error analysis.

These estimates are displayed in fig. 4.7 and make it quite obvious that the seemingly perfect linear behavior of $\langle(\Delta \boldsymbol{M})^2(t)\rangle$ is the average of many components, which are actually distributed all over the place for

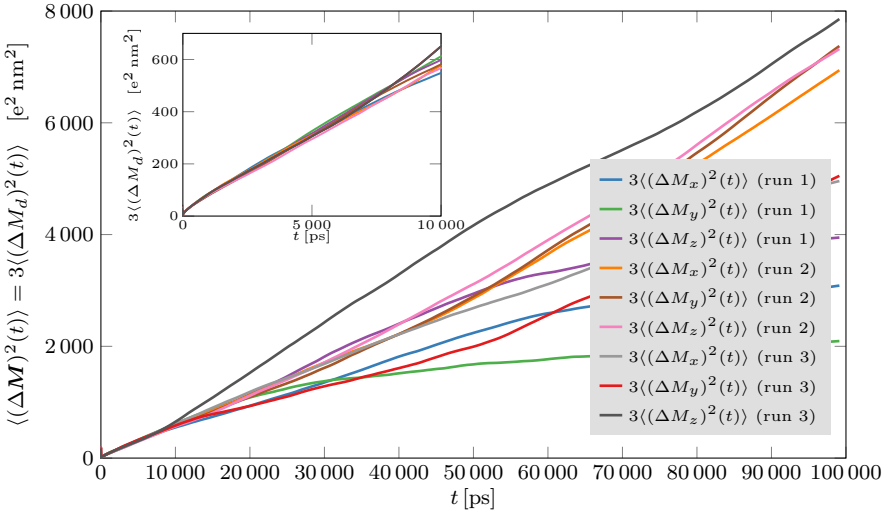

Figure 4.7: Estimates of the mean square displacement $\langle(\Delta \boldsymbol{M})^2(t)\rangle$ of the system's itinerant dipole moment $\boldsymbol{M}$ obtained from separate analyses of the three spatial components of each of three independent simulation runs. Inset: Magnification of the first 10 000 ps.

large t. However, we also see that for $3\,000 \leq t \leq 8\,000$ ps, all traces follow approximately the same linear trend, which can also be seen in the magnification of this region (inset in fig. 4.7). Since the components are statistically independent, we can use them to estimate the standard error $\epsilon\big(\langle(\Delta \boldsymbol{M})^2(t)\rangle\big)$ according to eq. (4.13) for each sampled time t. Figure 4.8 displays $\langle(\Delta \boldsymbol{M})^2(t)\rangle$ (blue line) together with its corresponding statistical one-sigma error margin $\langle(\Delta \boldsymbol{M})^2(t)\rangle \pm \epsilon\big(\langle(\Delta \boldsymbol{M})^2(t)\rangle\big)$ (light blue area). Since for large t, the statistical error is indeed very large and the individual components do not follow a general linear trend anymore, one should refrain from using this data for fitting.

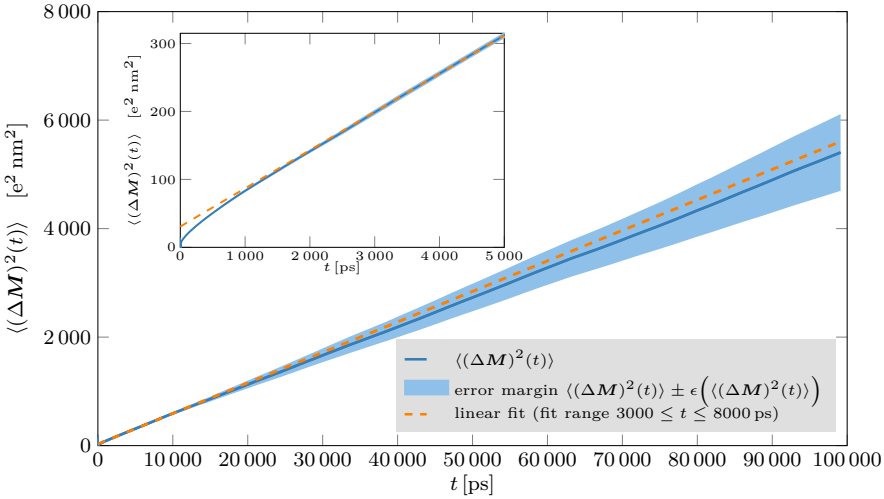

Figure 4.8: Mean square displacement $\langle(\Delta \boldsymbol{M})^2(t)\rangle$ (blue line) of the system's itinerant dipole moment $\boldsymbol{M}$ with corresponding one-sigma error margin (light blue area). Inset: Magnification of the first 5 000 ps.

The start of the fit range must be chosen according to the time where the integrated current autocorrelation converges to a constant (here: $t \approx 3\,000$ ps), and its end according to the time where the individual components $3\langle(\Delta M_d)^2(t)\rangle$ begin to deviate from the general linear trend (here: $t \approx 8\,000$ ps). The resulting fit is shown as a dashed orange line in fig. 4.8.

At this point, it is important to note that we still have the problem of oversampled data. Thus, the statistical error still cannot be inferred from the fit covariance matrix even if $\epsilon\big(\langle(\Delta \boldsymbol{M})^2(t)\rangle\big)$ is taken into account in the fitting procedure. Instead, since all components show the same linear trend in the fit range, the error $\epsilon\big(\langle(\Delta \boldsymbol{M})^2(t)\rangle\big)$ can be entirely attributed to shifts in the amplitude, and thus, the true error of the fit parameter c_2 can be well approximated by the average value of $\epsilon\big(\langle(\Delta \boldsymbol{M})^2(t)\rangle\big)$ in the fit range.

The resulting fit parameter $c_2 = 36.6141 \pm 6.1947\,\mathrm{e}^2\,\mathrm{nm}^2$ now allows us to compute the relative permittivity with a reasonable error estimate, yielding

$$\varepsilon_r = 1 + \frac{(36.6141 \pm 6.1947)\mathrm{e}^2\mathrm{nm}^2}{6 \cdot (301.7629 \pm 0.0026)\,\mathrm{nm}^3 \cdot \varepsilon_0 \cdot k_\mathrm{B} \cdot 300\,\mathrm{K}} = 15.15 \pm 2.39\,. \tag{4.61}$$

Compared to the "naive" result $\varepsilon_r = 18.5707 \pm 0.0013$ we obtained in eq. (4.58), we see that taking the statistical error of $\langle(\Delta \boldsymbol{M})^2(t)\rangle$ into account does not only dramatically increase the statistical error of the permittivity estimate ε_r, it also affects its value quite substantially. Ultimately, we see that the quality of permittivity data obtained via the Einstein-Helfand method is rather questionable if no proper error estimation is performed.

Appendix of Chapter 4

4.A Proof of Equation 4.47

We recall the definition of the autocorrelation function of a stationary process $A(t) \in \mathbb{R}$

$$R_{AA}(\tau) := \langle A(t)A(t+\tau)\rangle\,, \tag{4.62}$$

where the symmetry

$$R_{AA}(\tau) = \langle A(t)A(t+\tau)\rangle \overset{t\to t-\tau}{=} \langle A(t-\tau)A(t)\rangle = R_{AA}(-\tau) \tag{4.63}$$

holds. Provided that $A(t)$ is differentiable in t, by applying the chain rule, we see that its derivative $\dot{R}_{AA}(\tau) := \frac{\mathrm{d}}{\mathrm{d}\tau}R_{AA}(\tau)$ is

$$\dot{R}_{AA}(\tau) = \langle A(t)\dot{A}(t+\tau)\rangle = R_{A\dot{A}}(\tau) \tag{4.64}$$

and

$$\dot{R}_{AA}(\tau) = -\langle \dot{A}(t-\tau)A(t)\rangle \overset{t\to t+\tau}{=} -\langle \dot{A}(t)A(t+\tau)\rangle = -R_{\dot{A}A}(\tau)\,. \tag{4.65}$$

For the second derivative $\ddot{R}_{AA}(\tau) := \frac{\mathrm{d}^2}{\mathrm{d}t^2}R_{AA}(\tau)$, it follows analogously that

$$\ddot{R}_{AA}(\tau) = -R_{\dot{A}\dot{A}}(\tau)\,. \tag{4.66}$$

Likewise, the indefinite integral of $R_{\dot{A}\dot{A}}(\tau)$ is

$$\begin{aligned}\int R_{\dot{A}\dot{A}}(\tau)\,\mathrm{d}\tau &= \langle \dot{A}(t)\int \dot{A}(t+\tau)\,\mathrm{d}\tau\rangle = \langle \dot{A}(t)\,(A(t+\tau)+C)\rangle \\ &= R_{\dot{A}A}(\tau) + C\langle \dot{A}(t)\rangle = -R_{A\dot{A}}(\tau) + C\langle \dot{A}(t)\rangle \end{aligned} \tag{4.67}$$

with the constant of integration C.

Both the total dipole moment $\boldsymbol{M}(t)$ and the total current $\boldsymbol{j}(t)$ in a finite volume of a system in nonsolid state at thermodynamic equilibrium are real-valued, continuously differentiable, and weakly stationary random variables with zero mean. Weak stationarity means that their distributions and, thus, their expected values are time-invariant, so that their autocorrelation functions can be expressed as

$$R_{\boldsymbol{MM}}(\tau) = \langle \boldsymbol{M}(t)\boldsymbol{M}(t+\tau)\rangle = \langle \boldsymbol{M}(0)\boldsymbol{M}(\tau)\rangle\,, \tag{4.68}$$

$$R_{\boldsymbol{jj}}(\tau) = \langle \boldsymbol{j}(t)\boldsymbol{j}(t+\tau)\rangle = \langle \boldsymbol{j}(0)\boldsymbol{j}(\tau)\rangle\,. \tag{4.69}$$

Integrating the RHS of eq. (4.47) by parts yields

$$-\lim_{t\to\infty}\int_0^t \tau\langle \boldsymbol{j}(0)\boldsymbol{j}(\tau)\rangle\,\mathrm{d}\tau = -\lim_{t\to\infty}\left(\left[\tau\int\langle \boldsymbol{j}(0)\boldsymbol{j}(\tau)\rangle\,\mathrm{d}\tau\right]_0^t - \int_0^t\left(\int\langle \boldsymbol{j}(0)\boldsymbol{j}(\tau)\rangle\,\mathrm{d}\tau\right)\mathrm{d}\tau\right)\,.$$

By exploiting the properties of the integrals of autocorrelation functions according to eq. (4.67), we obtain

$$
\begin{aligned}
-\lim_{t\to\infty}\int_0^t \tau\langle \boldsymbol{J}(0)\boldsymbol{J}(\tau)\rangle \,\mathrm{d}\tau &= \lim_{t\to\infty}\left(\left[\tau\langle \boldsymbol{M}(0)\boldsymbol{J}(\tau)\rangle + \tau C\underbrace{\langle \boldsymbol{J}(\tau)\rangle}_{=0}\right]_0^t\right. \\
&\qquad \left. -\int_0^t\left(\langle \boldsymbol{M}(0)\boldsymbol{J}(\tau)\rangle + C\underbrace{\langle \boldsymbol{J}(\tau)\rangle}_{=0}\right)\mathrm{d}\tau\right) \\
&= \lim_{t\to\infty}\left(\underbrace{0\langle \boldsymbol{M}(0)\boldsymbol{J}(0)\rangle}_{=0} + t\langle \boldsymbol{M}(0)\boldsymbol{J}(t)\rangle\right. \\
&\qquad \left. -\int_0^t\langle \boldsymbol{M}(0)\boldsymbol{J}(\tau)\rangle\,\mathrm{d}\tau\right) \\
&= \underbrace{\lim_{t\to\infty}\left(t\langle \boldsymbol{M}(0)\boldsymbol{J}(t)\rangle\right)}_{=0} \\
&\qquad -\lim_{t\to\infty}\left\langle \boldsymbol{M}(0)\int_0^t \boldsymbol{J}(\tau)\,\mathrm{d}\tau\right\rangle . \qquad (4.70)
\end{aligned}
$$

The first term of the RHS of eq. (4.70) vanishes because asymptotically, $\langle \boldsymbol{M}(0)\boldsymbol{j}(t)\rangle$ decays exponentially with t.

Inserting eq. (4.49) into eq. (4.70) yields

$$
\begin{aligned}
-\lim_{t\to\infty}\int_0^t \tau\langle \boldsymbol{j}(0)\boldsymbol{j}(\tau)\rangle\,\mathrm{d}\tau &= -\lim_{t\to\infty}\langle \boldsymbol{M}(0)\left[\boldsymbol{M}(t)-\boldsymbol{M}(0)\right]\rangle . \\
&= -\underbrace{\lim_{t\to\infty}\langle \boldsymbol{M}(0)\boldsymbol{M}(t)\rangle}_{=0} + \lim_{t\to\infty}\langle \boldsymbol{M}(0)\boldsymbol{M}(0)\rangle \\
&= \langle \boldsymbol{M}^2\rangle , \qquad (4.71)
\end{aligned}
$$

proving the validity of eq. (4.47)■

5 The Effect of Small Organic Cosolutes on Water Structure and Dynamics

Note: The contents of this chapter have been previously published in similar form. Reprinted with permission from

J. Zeman, C. Holm and J. Smiatek, The Effect of Small Organic Cosolutes on Water Structure and Dynamics, *Journal of Chemical & Engineering Data* **65**, 1197–1210 (2020).

Leveraging the computational framework developed in chapter 4, we investigate the effect of small organic cosolutes on local water structure and dynamics by means of Molecular Dynamics (MD) simulations. In order to find features distinct to protein stabilizers as compared to denaturants, we investigate aqueous solutions of the osmolytes ectoine and trimethylamine N-oxide (TMAO) as well as of the denaturants urea and guanidinium chloride (GdmCl). For each cosolute, we assess its effects on the surrounding water by analyzing several structural and dynamic properties of the local hydrogen bond network, putting an emphasis on collective changes in the water's dielectric relaxation spectra.

While the concentration-dependent changes in water structure induced by the different cosolutes provide no clear trend, we find that the stabilizing osmolytes severely slow down the collective modes of reorientational water dynamics, whereas the effects on dynamics caused by

denaturants are comparatively small. Our results indicate that the discussion of possible kosmo- or chaotropic cosolute effects only in terms of water structure makers vs. structure breakers provides an ambiguous or incomplete picture if effects on water dynamics are not taken into account.

Organic cosolutes have a strong impact on the stability, function, and activity of biomolecules such as proteins or enzymes in aqueous solution, and are therefore of great biological relevance.[20] Common examples are trimethylamine N-oxide (TMAO) or ectoine, which are low-weight molecules and allow microorganisms to survive under extreme environmental conditions.[21] Beneficial properties of these molecules are the stabilization of native protein structures under high temperatures, high salinity and high pressures[22–24,122] and the maintenance of the fluidity of bilayers,[25,26] which is particularly important for cell signaling processes. Due to these properties, molecules such as TMAO or ectoine are commonly called protectants or stabilizers. In contrast, guanidinium chloride (GdmCl) or urea at high molar concentrations denature protein structures even at moderate environmental conditions and are therefore referred to as denaturants or destabilizers. Interestingly, experimental studies revealed that both denaturants and protectants can be simultaneously found at higher molar concentrations in the microbiological cell interior.[21] Thus, the combined influence of protectants and denaturants balances the individual contributions of each species and verifies a fast reaction to environmental changes.[21,123–129]

Due to the pronounced effects on protein and DNA unfolding, the denaturing properties of urea and GdmCl were discussed in a series of publications.[20,27,130–138] In summary, two distinct reasons were proposed to explain the denaturation mechanism:[27] (i) a direct binding between the denaturant and the protein in contrast to (ii) solvent-mediated effects. Whereas the properties of denaturants remain a much-debated issue, a consensus was reached for the behavior of protein protectants. Experimental findings as well as computer simulations revealed that protectants are usually excluded from protein

surfaces[28–39] in terms of a preferential exclusion behavior. Thus, they do not directly interact with protein surfaces and are often located in the second or third hydration shell.[40] It was assumed that the exclusion effect is mainly induced by the strong hygroscopic properties of protectants.[36,40] Due to these findings, protectants are assumed to be kosmotropic (water structure making) whereas denaturants are *vice versa* assigned to be chaotropic (water structure breaking) in terms of their unfavorable perturbation of the water structure.[40,41,129] More precisely, it was pointed out that kosmotropes strengthen the local interaction between water molecules, *e.g.*, the hydrogen bond network, whereas chaotropes weaken these bonds. Specifically for ions, the Hofmeister series[40,139] ranks the individual species in terms of their kosmotropicity. Due to the good agreement between kosmotropic strength and the protein salting in / salting out tendency of the individual ions, for which the Hofmeister series was originally formulated,[27,139] it was assumed that the distinction between denaturant and protectant behavior is accomplished or even induced by increasing kosmotropicity of the individual species.[40] In contrast to its previous success,[40] recent publications question this simple concept. For instance, recent findings demonstrated that denaturants may reveal slightly kosmotropic properties[134,140,141] and that there are concentration-dependent binding effects for denaturants under certain conditions.[134,142,143] Moreover, it has been found that well-known stabilizers can also induce denaturation.[70,138,144,145] Further theoretical attempts indicated that thermodynamic concepts in terms of cosolute chemical activities are crucial for understanding protein stabilization or destabilization effects.[34,137,146–149] Henceforth, the chemical properties of solutes and osmolytes have to be studied in more detail for a deeper understanding of the resulting accumulation behavior[141,150–154] in order to clearly distinguish between direct cosolute / protein and indirect, water-mediated effects.

Motivated by the discussion of kosmotropicity, the water effects of some cosolutes were experimentally studied in more detail.[18,37,155–157] In fact, it is well known that the properties of the local hydration

shell significantly differ from bulk solution behavior.[158] Specifically for TMAO and ectoine, an increased strength of hydrogen bonds between water molecules was reported.[37,155,157,159,160] However, it was also demonstrated that urea as a typical denaturant reveals non-chaotropic properties.[129] In fact, the hydrogen bond structure and also the local arrangement of water molecules remains almost unchanged in the presence of urea.[155,161] Therefore, it can be concluded that the concept of chaotropicity is questionable for non-ionic cosolutes.

Here, we chose to investigate the effect of urea, ectoine, TMAO and GdmCl since all of them have in common that they are important and well-studied cosolutes in biophysical applications, yet each of them exhibits distinct features. Figure 5.1 shows ball-and-stick models of all investigated cosolutes together with their corresponding Lewis formulae. In order to study how these cosolutes influence the surrounding water, we carried out extensive MD simulations and analyzed various structural and dynamic properties of water at different cosolute concentrations. In our investigations, we deliberately focused on systems with low cosolute concentrations for two reasons: First of all, since one of the employed cosolute models was matched against Kirkwood-Buff integrals at low concentrations, this model is not guaranteed to yield reliable results at high concentrations. Second, but more importantly, cosolute-specific effects on bulk-like water can only be observed at low cosolute concentrations. For example, in a 2 molar aqueous ectoine solution, almost all water molecules reside in the first three hydration layers around ectoine molecules so that there is almost no bulk water left. Both ectoine and TMAO are known to have a stabilizing effect on the native (*i.e.*, folded) state of proteins and are strongly water binding. However, while ectoine is found to appear almost exclusively in its zwitterionic form in aqueous solution,[25,35] there exists no such conformation of TMAO. On the other hand, urea and GdmCl have the tendency to denature proteins at moderate cosolute concentrations. Yet, urea only exists as a neutral species while GdmCl in aqueous solution dissociates completely into guanidinium (Gdm^+) and chloride (Cl^-) ions.

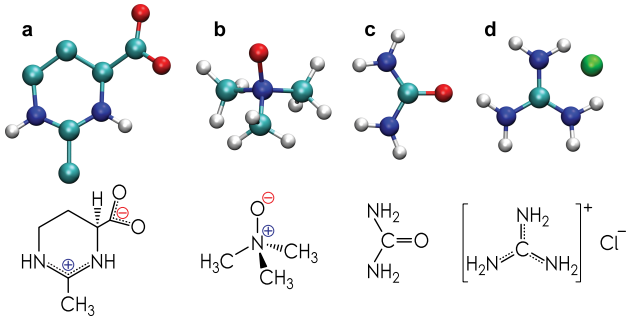

Figure 5.1: Ball-and-stick models and Lewis formulae of the investigated cosolutes. **a:** zwitterionic form of ectoine, **b:** trimethylamine N-oxide (TMAO) **c:** urea, and **d:** guanidinium chloride (GdmCl) ion pair. Carbon atoms are shown in cyan (in the case of ectoine, also the united-atom CH, CH_2, and CH_3 sites), nitrogen atoms in blue, oxygen atoms in red, hydrogen atoms in white, and the chloride ion in green.

While we investigate the influence of these cosolutes on both solvent structure and dynamics, the focus of the latter lies on dielectric relaxation spectroscopy.[4,162] For experimentally measured dielectric spectra, assigning relaxation modes to the underlying molecular mechanisms can be challenging and sometimes ambiguous. In that respect, computer simulations have the advantage that the microscopic molecular conformations and dynamics are directly at hand. In particular, for the analysis of dielectric spectra, this means that solvent and cosolute contributions can be conveniently separated, as well as cosolute-solvent interactions.

5.1 Theoretical Background

According to several experimental and theoretical studies,[163–168] liquid water exhibits a close-to-tetrahedral structural ordering in its hydrogen bond network. In order to assess changes in the structure of water caused by the added cosolutes, we analyzed MD trajectories in terms of the tetrahedral order parameters S_g and S_k originally developed by

Chau and Hardwick[169] and rescaled by Errington and Debenedetti.[170] The order parameter S_g is a measure of orientational tetrahedrality of the spatial arrangement of four neighboring particles around one central reference particle and is defined[170] as

$$S_g = 1 - \frac{3}{8} \sum_{j=1}^{3} \sum_{k=j+1}^{4} \left(\cos\left(\phi_{jk}\right) + \frac{1}{3} \right)^2 . \tag{5.1}$$

Here, ϕ_{jk} is defined as the angle between the vectors pointing from the central particle to its j-th and k-th neighbors. As explained in ref. 170, the order parameter is $S_g = 0$ for a random arrangement corresponding to an ideal gas, and $S_g = 1$ for a perfect tetrahedron formed by the four nearest neighbors with the reference particle at its center of geometry. This order parameter, however, only depends on the orientational arrangement of neighboring particles and is completely insensitive to their distance. Therefore, we also evaluated the sphericity parameter S_k, which measures the normalized variance of the distances between neighboring particles to the central one. It is defined as

$$S_k = 1 - \frac{1}{12\bar{r}^2} \sum_{k=1}^{4} \left(r_k - \bar{r}\right)^2 , \tag{5.2}$$

where r_k is the distance between the central particle and its k-th neighbor, and $\bar{r}$ denotes the arithmetic mean of all r_k. In a perfect tetragonal arrangement, all neighboring particles lie on a sphere with radius $\bar{r} = r_k \, \forall \, k$ so that the second term in eq. (5.2) vanishes and S_k approaches unity. In contrast, S_k approaches zero with decreasing sphericity.

It has been shown previously that for the structural analysis of aqueous solutions, including non-water neighbors is crucial for the correct interpretation of structural parameters.[171] The tetragonal structure of water is governed by its tendency to form hydrogen bonds, and all cosolute species considered in this work comprise N-H groups or oxygen atoms with electron lone pairs being able to act as hydrogen

bond donors or acceptors. Thus, we considered all oxygen and nitrogen atoms present in the system as possible nearest neighbors of water in our analyses of S_g and S_k, while only water oxygen atoms were considered as central particles. For the analyses of GdmCl, we also included the Cl^- anions as nearest neighbor candidates to avoid an artificial distortion of S_g and S_k in the hydration layers of these atoms. This allows us to to include the first hydration shell around cosolute molecules in the analysis, which would be impossible if only water oxygen atoms were considered in the calculations. We also conducted measurements of S_g and S_k with the first two hydration layers around the cosolutes excluded from the set of central particles. The resulting order parameters are then denoted as $S_g^{\setminus 2}$ and $S_k^{\setminus 2}$, respectively.

In order to assess changes in translational solvent dynamics, we calculated water self-diffusion coefficients D from a linear regression of the mean-square displacement $\left\langle \Delta \boldsymbol{r}_{\mathrm{com}}^2(t) \right\rangle$ of molecular centers of mass $\boldsymbol{r}_{\mathrm{com}}$ according the well-known Einstein equation[172]

$$\lim_{t\to\infty} \left\langle \Delta \boldsymbol{r}_{\mathrm{com}}^2(t) \right\rangle = 6Dt + \mathrm{const}\,. \tag{5.3}$$

Moreover, to estimate the cosolutes' influence on the stability of the water hydrogen bond network, hydrogen bond analyses were carried out as described in van der Spoel *et al.*[173] with forward life times calculated according to the approach of Luzar and Chandler.[42,43] As a condition for a hydrogen bond to be present, a maximum separation of interacting donor and acceptor atoms of 0.35 nm coinciding with an interaction angle smaller than 30° was chosen. In all analyses, hydrogen bonds involving the same donor and acceptor atoms but different hydrogen atoms were treated as the same hydrogen bond.

For the investigation of the solvent's rotational dynamics, we computed dielectric relaxation spectra. While dielectric relaxation spectroscopy is a well-known experimental technique,[4] the extraction of dielectric spectra from computer simulations is less established, mostly due to the time scale required to gather sufficient statistics. However, with the advent of powerful hardware accelerators such as graphics processing

units, it is nowadays possible to reach simulation time scales in the order of microseconds within reasonable computation time.

Here, we use the "Green-Kubo" approach based on linear response theory as described in chapters 3 and 4. In an experimental measurement of $\varepsilon_r(\omega)$, the contribution of individual dielectric relaxation modes to the overall spectrum is usually determined by a multi-Debye[117,174,175] or related[176–178] fitting procedure. The attribution of these modes to the different molecular species present in the investigated solution is then accomplished by comparing the spectra from measurements of different cosolute concentrations.[37,117,175,179] In computer simulations, however, all the required information about molecular motion is directly accessible: Since $\boldsymbol{j}(t)$ is additive and the Fourier-Laplace transform is linear, the contributions of different molecular species A, B in a binary system to the overall spectrum can be calculated by summing over the corresponding molecules $\{m \in A\}$, $\{m \in B\}$ individually:[180]

$$\boldsymbol{j}(t) = \boldsymbol{j}_{\mathrm{A}}(t) + \boldsymbol{j}_{\mathrm{B}}(t) = \sum_{m\in A}\sum_{\alpha} q_{m,\alpha}\boldsymbol{v}_{m,\alpha}(t) + \sum_{m\in B}\sum_{\beta} q_{m,\beta}\boldsymbol{v}_{m,\beta}(t) \tag{5.4}$$

Thus, it follows for the complex conductivity $\sigma_e(\omega)$ that

$$\begin{aligned}
\sigma_e(\omega) &= \frac{1}{3Vk_{\mathrm{B}}T}\left[\int_0^\infty \langle \boldsymbol{j}_{\mathrm{A}}(0)\boldsymbol{j}(\tau)\rangle\, e^{i\omega\tau}\,\mathrm{d}\tau + \int_0^\infty \langle \boldsymbol{j}_{\mathrm{B}}(0)\boldsymbol{j}(\tau)\rangle\, e^{i\omega\tau}\,\mathrm{d}\tau\right] \\
&= \frac{1}{3Vk_{\mathrm{B}}T}\left[\int_0^\infty \langle \boldsymbol{j}_{\mathrm{A}}(0)\boldsymbol{j}_{\mathrm{A}}(\tau)\rangle\, e^{i\omega\tau}\,\mathrm{d}\tau + \int_0^\infty \langle \boldsymbol{j}_{\mathrm{B}}(0)\boldsymbol{j}_{\mathrm{B}}(\tau)\rangle\, e^{i\omega\tau}\,\mathrm{d}\tau \right.\right. \\
&\qquad \left.\left. + 2\int_0^\infty \langle \boldsymbol{j}_{\mathrm{A}}(0)\boldsymbol{j}_{\mathrm{B}}(\tau)\rangle\, e^{i\omega\tau}\,\mathrm{d}\tau\right] \right. \\
&=: \sigma_e^{\mathrm{A}}(\omega) + \sigma_e^{\mathrm{B}}(\omega) + \sigma_e^{\mathrm{AB}}(\omega)\,.
\end{aligned} \tag{5.5}$$

The permittivity spectrum $\varepsilon_r(\omega)$ can be decomposed accordingly:

$$\begin{aligned}\varepsilon_r(\omega) = 1 + \frac{i}{\varepsilon_0 \omega}\Big[&\left(\sigma_e^{\mathrm{A}}(\omega) - \sigma_e^{\mathrm{A}}(0)\right) + \left(\sigma_e^{\mathrm{B}}(\omega) - \sigma_e^{\mathrm{B}}(0)\right) \\ &+ \left(\sigma_e^{\mathrm{AB}}(\omega) - \sigma_e^{\mathrm{AB}}(0)\right)\Big] \\ =: 1 + \varepsilon_{\mathrm{A}}(\omega) + \varepsilon_{\mathrm{B}}(\omega) &+ \varepsilon_{\mathrm{AB}}(\omega)\,. \end{aligned} \tag{5.6}$$

Further details on the employed data processing procedures are found in chapter 4. Since we are interested in the influence of the different cosolutes on water dynamics, our analysis will focus on the water self-contribution $\varepsilon_{\mathrm{W}}(\omega)$, and, in particular, on how the water dielectric absorption $\varepsilon''_{\mathrm{W}}(\omega)$ changes with cosolute concentration.

5.2 Simulation Details

MD simulations were performed for all cosolutes with concentrations ranging from 0 to ≈ 2.0 mol/l. For the simulation of ectoine, we employed the united atom model introduced by Smiatek *et al.*,[25] while for TMAO, the TMAO-V3 force field developed by Hölzl *et al.*[181] was used. For urea, we chose the Kirkwood-Buff-derived model by Weerasinghe and Smith,[182] and the force field parameters for GdmCl were taken from Wernersson *et al.*[183] The extended simple point charge[112] (SPC/E) water model was used as the solvent in all simulations. Note that even though the employed TMAO model was originally developed for use with the TIP4P/2005 water model, we have previously shown[19] that it can be used safely with SPC/E water. The fact that all cosolute models are compatible with the same water model is of particular importance since the different cosolutes' effects on water structure and dynamics would otherwise lack a common basis, making concentration-dependent trends much harder to compare. Furthermore, our choice of the employed cosolute models was based on the requirement that these models had either been parametrized and refined for or tested against as many relevant thermophysical properties as possible, since generic

models without further refinement can sometimes yield results which are inconsistent with experimental data or may even fail to faithfully represent concentration-dependent trends.[19]

The simulations were performed with a customized variant of the GROMACS 2016.3 software package[106,108–111] capable of computing the cumulative currents $\boldsymbol{j}_X(t)$ defined in eq. (5.4) during runtime in every time step for individual molecular species. This enabled us to obtain full-resolution time series of these currents without having to store trajectories of the entire systems at every time step. All systems were simulated in the NpT ensemble at $T = 300\,\mathrm{K}$ and $p = 1\,\mathrm{bar}$ using a Nosé-Hoover[82,94,95] thermostat together with a Parrinello-Rahman[96] barostat. Coupling constants were $\tau_T = 1\,\mathrm{ps}$ and $\tau_p = 2\,\mathrm{ps}$, respectively. All systems were equilibrated for at least 10 ns before carrying out any measurements. Van-der-Waals interactions were computed within a cut-off of 9 Å with the potential shifted to zero at the cut-off, and long-range dispersion corrections were applied for both energy and pressure. Electrostatic interactions were calculated by means of the Particle Mesh Ewald method[86] with the same short-range cut-off. Bond lengths of the cosolutes were constrained[a] using the LINCS[184] algorithm, whereas the molecular geometry of water was kept rigid with the SETTLE[185] algorithm. The integration time step was $\delta t = 1\,\mathrm{fs}$ for all simulations, and simulation boxes were cubes with periodic boundary conditions in all three dimensions. All simulated systems contained 50 cosolute molecules and a concentration-dependent number of water molecules ranging from approximately 1000 to more than 5000 with corresponding initial box edge lengths between 3.5 and 5.5 nm. The exact compositions of the different investigated systems are summarized in Table 5.1. The measurement runs were performed using four independently generated replicas per cosolute species and concentration. For the calculation of dielectric spectra, the cumulative currents $\boldsymbol{j}_X(t)$ were recorded for all molecular species X in every time step during simulations with run times of $\approx 268\,\mathrm{ns}$ (2^{28} time steps) per replica and written

[a] For ectoine and urea all bond lengths were constrained, for TMAO and GdmCl only bonds involving hydrogen atoms.

System	c [mol/l]	N_{cs}	N_{water}	L [nm]
pure water	0.00	0	2180	4.03
ectoine	0.53	50	5016	5.41
	1.07	50	2330	4.27
	1.72	50	1343	3.64
	2.23	50	979	3.34
TMAO	0.52	50	5144	5.43
	1.04	50	2454	4.30
	1.68	50	1456	3.67
	2.15	50	1092	3.38
urea	0.52	50	5243	5.44
	1.03	50	2568	4.32
	1.64	50	1562	3.70
	2.09	50	1199	3.41
GdmCl	0.52	50	5130	5.42
	1.05	50	2460	4.29
	1.68	50	1464	3.67
	2.20	50	1071	3.35

Table 5.1: System compositions. The listed values are molar concentration c, number of cosolute molecules N_{cs} (in case of GdmCl: number of ion pairs), number of water molecules N_{water}, and average simulation box edge length L. Values of the average simulation box volumes and mass densities with corresponding error estimates can be found in appendix 5.A.

to disk for *a posteriori* analysis. Simultaneously, particle positions were stored every picosecond for the analysis of translational diffusion coefficients, hydrogen bond life times, as well as sphericity and tetrahedrality order parameters.

The calculation of diffusion coefficients and hydrogen bond life times was performed with standard GROMACS analysis tools, whereas all other analyses were carried out with self-written tools partially based on the MDAnalysis[186,187] framework.

5.3 Structural Analysis

The water hydration layer around proteins is known to have a higher density compared to bulk water.[188,189] The similarity or dissimilarity of the water structure induced by cosolutes with the water structure in the hydration layer of proteins is believed to have a stabilizing or destabilizing effect, respectively.[157] Thus, kosmotropic cosolutes should enhance the density and stabilize the surrounding water structure, while a chaotropic behavior should lead to the opposite. In reference 157, this was investigated mainly with respect to the neighboring water oxygen-oxygen distance. However, since the structure of water cannot be fully determined by this observable, in the following, we assess the influence of cosolutes on several structural properties of water.

5.3.1 Radial distribution functions

The radial distribution functions (RDFs) $g_{XY}(r)$ between species X and Y with respect to their distance r do not only provide information on the relative distribution of atoms in the system, they are also connected to the potential of mean force $U_{XY}^{\mathrm{pmf}}(r) = -k_{\mathrm{B}}T\ln(g_{XY}(r))$, where k_{B} is the Boltzmann constant and T denotes absolute temperature. Thus, higher peaks in the RDF indicate an enhanced interaction between species X and Y. Figure 5.2 displays the oxygen-oxygen RDF $g_{\mathrm{OO}}(r)$ of pure water compared to the same RDFs in the presence of cosolutes at a concentration of $\approx 2\,\mathrm{mol/l}$.[b]

The first RDF peak is clearly enhanced by the presence of any of the cosolutes, indicating a stronger oxygen-oxygen interaction between neighboring water molecules. Furthermore, the magnified view of the first peak in inset a also reveals a very slight shift of the peak positions to smaller distances compared to that of pure water. For ectoine, both effects are most pronounced, followed by TMAO, urea, and finally

[b] The RDFs of all investigated cosolute concentrations are given in appendix 5.B.1.

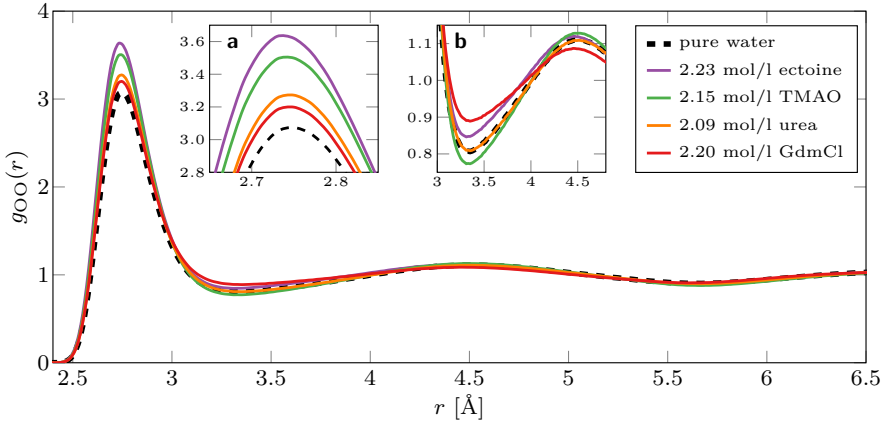

Figure 5.2: Water oxygen-oxygen RDFs of pure water (black, dashed) and aqueous solutions of different cosolutes (ectoine: purple; TMAO: green; urea: orange, GdmCl: red). Inset **a**: Magnification of the first peak. Inset **b**: Magnification of the first minimum and second peak.

GdmCl. Thus, judging from the first RDF peak only, one might conjecture that all cosolutes have a tendency to enhance the water structure and thus act as kosmotropes. On the contrary, when examining the magnification of the first minimum and second peak of $g_{OO}(r)$ displayed in inset b, the situation changes. While urea shows virtually no change compared to pure water, both stabilizers ectoine and TMAO enhance the second peak. However, while TMAO enhances the first minimum, ectoine induces a less pronounced structure here accompanied by a slight shift of the second peak towards smaller distances. The denaturant GdmCl reduces the amplitude of both features, effectively "washing out" the water structure beyond the first peak. From that perspective, TMAO appears to be the strongest "structure maker" followed by ectoine, while urea seems to have no effect on the water structure at all beyond the first peak. GdmCl, however, leads to a less pronounced structure and could therefore be considered a chaotrope.

Since the analysis of the RDFs alone fails to provide an unambiguous picture of the cosolutes' kosmo- or chaotropic influence on the water structure, we proceed by investigating further structural properties of water.

5.3.2 Sphericity

The comparatively narrow first peak of the water oxygen-oxygen RDFs already points to another property of the water structure, which is its sphericity. In bulk water, the neighboring oxygen atoms around a central one lie almost on a spherical shell around the central oxygen atom. If the presence of cosolutes changes this arrangement, this should be reflected in the distribution of the water oxygen sphericity parameters S_k as defined in eq. (5.2). Figure 5.3 depicts the probability densities $p(S_k)$ of sphericity parameters S_k for the different investigated cosolutes at concentrations of $\approx 2\,\mathrm{mol/l}$ in panel a, and the differences $\Delta p(S_k)$ of the distributions with respect to bulk water in panel b.[c]

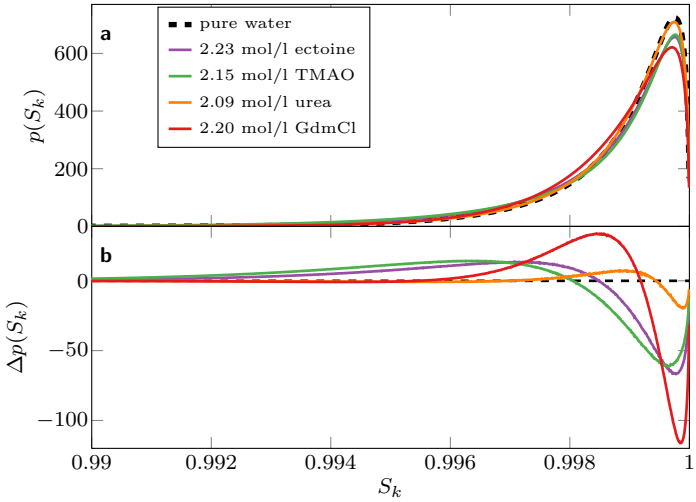

Figure 5.3: **a**: Cosolute-dependent probability densities $p(S_k)$ of sphericity parameters S_k at cosolute concentrations of $\approx 2\,\mathrm{mol/l}$ compared to that of bulk water. **b**: Difference $\Delta p(S_k)$ of the solute-dependent probability densities with respect to that of pure water.

From panel a, it becomes evident that the peak at $S_k = 0.9995$ is lowered by the presence of any cosolute. While urea appears to have very little impact on sphericity, the influence of the osmolytes ectoine and TMAO is stronger, yet not as strong as that of GdmCl. Panel b, however, reveals that the impact is also qualitatively quite different

[c] Distributions for all investigated cosolute concentrations can be found in appendix 5.B.2.

for the different cosolutes. In contrast to GdmCl, which leads to an increase of $p(S_k)$ between $S_k = 0.997$ and $S_k = 0.999$ and a decrease above, both ectoine and TMAO do not lead to such a drastic decrease of the distribution in the upper range but shift the probability density to much lower values. This means that even though the disturbance of sphericity seems to be higher for GdmCl, there exists a larger fraction of water molecules with a more strongly distorted hydration shell in the presence of the stabilizing agents ectoine and TMAO.

Since for the computation of the S_k parameter distributions depicted in fig. 5.3, all water oxygen atoms were taken into account, *i.e.*, also the ones in close vicinity to the cosolutes, we conducted a second measurement where we excluded the first two hydration layers around the cosolutes from the analysis. The resulting probability densities $p(S_k^{\setminus 2})$ are shown in fig. 5.4 along with the differences $\Delta p(S_k^{\setminus 2})$ with respect to the bulk water sphericity distribution.

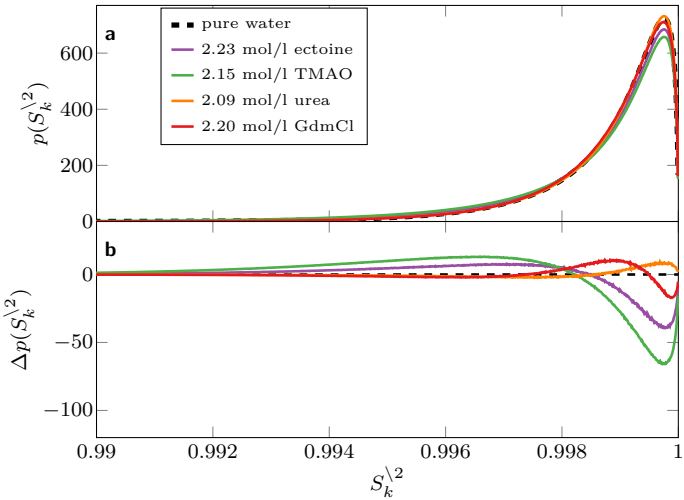

Figure 5.4: **a**: Cosolute-dependent probability densities $p(S_k^{\setminus 2})$ of sphericity parameters $S_k^{\setminus 2}$ at cosolute concentrations of ≈ 2 mol/l compared to that of bulk water with the first and second hydration shells around the cosolutes excluded from the analysis. **b**: Difference $\Delta p(S_k^{\setminus 2})$ of the probability densities with respect to that of pure water.

Panel b in fig. 5.4 clearly reveals a significant change compared to panel b in fig. 5.3: While the influence of the stabilizing osmolytes ectoine and TMAO remained almost as strong as with the first two hydration layers included, the effect of GdmCl is much weaker. In fact, urea even slightly enhances the sphericity of the water structure beyond its second hydration shell. The overall disturbance of the water structure's sphericity is longer-ranged for ectoine and TMAO compared to that caused by GdmCl or urea.

5.3.3 Tetrahedrality

So far we have only considered the water structure in terms of oxygen-oxygen distances. However, RDFs and sphericity parameters provide no information about the water molecules' angular arrangement with respect to each other. As explained in section 5.1, the order parameter S_g provides a measure for the tetrahedrality of the relative angular arrangement of neighboring hydrogen bond donors or acceptors around the water oxygen atoms. Panel a in fig. 5.5 shows the probability densities $p(S_g)$ of tetrahedrality parameters S_g in the presence of cosolutes at concentrations of $\approx 2\,\mathrm{mol/l}$.

The bulk water distribution $p(S_g)$ perfectly reproduces the findings of ref. 170 for SPC/E water at $T = 300\,\mathrm{K}$ with a pre-peak at $S_g \approx 0.5$ and a main peak at $S_g \approx 0.75$. All cosolutes shift the lower edge of the distribution towards smaller values and decrease the amplitude of the main peak, and the pre-peak is enhanced for all cosolutes except for TMAO. As it has been the case in the previous structural analyses, urea again shows the weakest influence, while GdmCl has the strongest impact on tetrahedral order. The differences $\Delta p(S_g)$ of the distributions with respect to that of bulk water as depicted in panel b of fig. 5.5, however, reveal further subtle differences between the effects of different cosolutes. While the effect of ectoine appears qualitatively quite similar to that of GdmCl and the inflection points of $\Delta p(S_g)$ almost coincide for these cosolutes, the inflection points of TMAO and urea

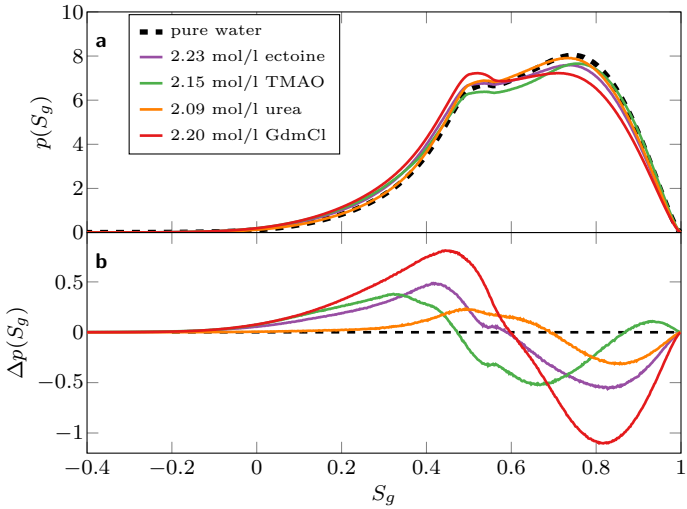

Figure 5.5: **a**: Cosolute-dependent probability densities $p(S_g)$ of tetrahedrality parameters S_g at cosolute concentrations of ≈ 2 mol/l compared to that of bulk water. **b**: Difference $\Delta p(S_g)$ of the probability densities with respect to that of pure water.

are shifted to lower and higher values of S_g, respectively. TMAO even exhibits a second zero-crossing in $\Delta p(S_g)$ and causes a slight increase of $p(S_g)$ for $S_g > 0.85$.

However, if we exclude the first two hydration layers around the cosolutes from the analysis, the impact of the different cosolutes on water tetrahedrality becomes qualitatively more uniform. The corresponding results for $p(S_g^{\setminus 2})$ and $\Delta p(S_g^{\setminus 2})$ are shown in panels a and b of fig. 5.6, respectively. Beyond the first two solute hydration layers, all solutes lead to an increased pre-peak of $p(S_g^{\setminus 2})$ accompanied by a decreasing main peak with the most pronounced reduction at $S_g^{\setminus 2} \approx 0.8$. Likewise, the behavior of $\Delta p(S_g^{\setminus 2})$ is qualitatively similar for all solutes. Also the inflection points of $\Delta p(S_g^{\setminus 2})$ are now closer than before for all solutions, even though that of TMAO solutions is still located at slightly lower values of $S_g^{\setminus 2}$. Nevertheless, the rising pre-peak and falling main peak amplitudes qualitatively correspond to the effect induced by increasing the temperature of bulk water.[170] In fact, the probability density $p(S_g^{\setminus 2})$ of a 2 mol/l urea solution at $T = 300$ K

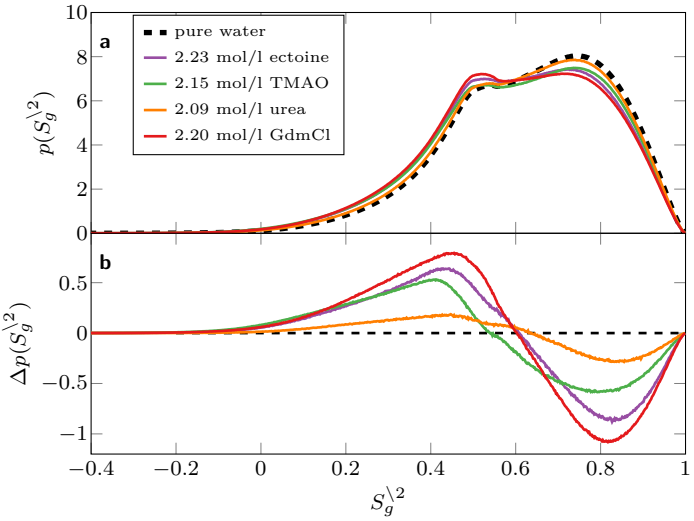

Figure 5.6: a: Cosolute-dependent probability densities $p(S_g^{\backslash 2})$ of tetrahedrality parameters $S_g^{\backslash 2}$ at cosolute concentrations of $\approx 2\,\mathrm{mol/l}$ compared to that of bulk water with the first and second hydration shells around the cosolutes excluded from the analysis. **b**: Difference $\Delta p(S_g^{\backslash 2})$ of the probability densities with respect to that of pure water.

almost perfectly coincides with $p(S_g)$ of pure water at 305 K, and a 2 mol/l GdmCl solution at $T = 300\,\mathrm{K}$ has roughly the same effect on $p(S_g)$ as increasing the bulk water temperature to $T = 325\,\mathrm{K}$.[d] Thus, the induced changes in water tetrahedrality appear to indicate a moderately chaotropic influence of all cosolutes beyond their second hydration shells. However, since it is known that both ectoine and TMAO are able to stabilize the native conformation of proteins without direct interactions, they should have an overall kosmotropic effect.

Clearly, the different and partially contradictory implications drawn from different aspects of our structural analyses yield a highly ambiguous picture of the cosolutes' kosmo- or chaotropic influence on water. Due to the fact that the structural properties of water alone do not even provide satisfactory explanations for the kosmotropic influence of the protecting osmolytes, in the following, we will proceed by examining the influence of the different cosolutes on water dynamics.

[d] A direct comparison of cosolute vs. temperature influence on $p(S_g)$ is given in appendix 5.B.3.

5.4 Analysis of Water Dynamics

In addition to their tendency to exhibit an enhanced water density in their close proximity, proteins also influence the dynamics of their hydration water.[190–193] While the magnitude of the latter effect may depend on the hydrophilic or hydrophobic properties of the corresponding residues in the primary structure,[193] the translational and rotational relaxation of water is generally slowed down in the protein hydration layer.

5.4.1 Translational diffusion

It has been shown previously that for the structural relaxation of proteins in aqueous solution, both rotational as well as translational relaxations of their hydration water are important.[191,192] We therefore start by assessing the concentration-dependent effect of the different cosolutes on translational water dynamics. Figure 5.7 depicts the translational diffusion coefficients D_{W} of water computed according to eq. (5.3) for cosolute concentrations up to about 2 mol/l. All cosolutes exhibit a general trend to slow down translational water diffusion, as D_{W} decreases almost linearly with concentration for all cosolutes. While urea has the smallest influence on the long-term translational dynamics of water and decreases the pure water diffusion coefficient by about 19 % at 2 mol/l, GdmCl has a slightly stronger effect with a reduction by 32 % at roughly the same concentration. Both stabilizers TMAO and ectoine lead to a much stronger attenuation of translational diffusion dynamics, as the water diffusion coefficient is decreased by 47 % in a two-molar TMAO solution, and ectoine even decreases D_{W} by 61 % from $2.83 \cdot 10^{-5}\,\mathrm{cm}^2 s^{-1}$ at 0 mol/l down to $1.10 \cdot 10^{-5}\,\mathrm{cm}^2 s^{-1}$ at $\approx$2 mol/l. Thus, in terms of translational water dynamics, all investigated cosolutes are likely to stabilize the surrounding water structure by reducing diffusive structural reordering. However, the effect due to the protein protectants is much more pronounced compared to that of the

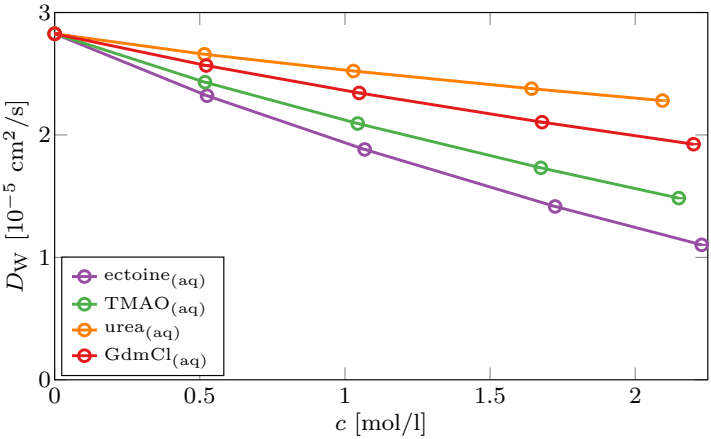

Figure 5.7: Concentration-dependent average translational diffusion coefficients D_W of water molecules in aqueous solutions of ectoine (purple), TMAO (green), urea (orange), and GdmCl (red). Lines serve as guides to the eye. Statistical errors generally do not exceed $\pm 8 \cdot 10^{-8}$ cm^{2}s^{-1} and are therefore not visible in the graph. The presented data are provided in tabular form in appendix 5.C.1.

denaturants. In addition, also concentration-dependent and cosolute-specific viscosity effects cannot be ignored.

5.4.2 Hydrogen bond dynamics

To corroborate the implication of a dynamical structural strengthening drawn from the reduced water diffusivity, we analyzed the life times τ_{hb} of water-water hydrogen bonds. The values of τ_{hb} are shown in fig. 5.8 as a function of cosolute concentration. Indeed, the fact that hydrogen bond life times generally increase with cosolute concentration strongly supports the notion of a structural strengthening in terms of dynamics. Again, the same order of cosolute effects is preserved, with urea showing the least pronounced effect followed by GdmCl, whereas TMAO and ectoine increase the life times of water-water hydrogen bonds to a much greater extent. The only aspect of the qualitative behavior of τ_{hb} that

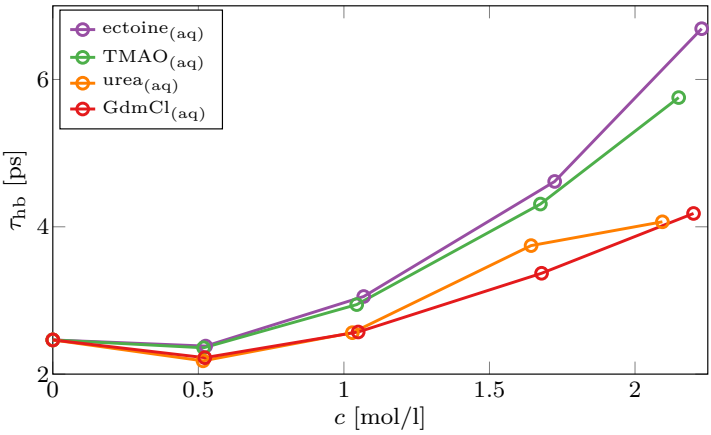

Figure 5.8: Concentration-dependent intermittent water-water hydrogen bond forward life times τ_{hb} in aqueous solutions of ectoine (purple), TMAO (green), urea (orange), and GdmCl (red). Lines serve as guides to the eye. Statistical errors generally do not exceed $\pm 3 \cdot 10^{-3}$ ps and are therefore not visible in the graph. The presented data are provided in tabular form in appendix 5.C.2.

differs from the behavior of diffusion coefficients is the non-linearity at very low cosolute concentrations. Here, we hypothesize that at very low concentrations, the structural disturbance caused by the cosolutes weakens the water hydrogen bond network but cannot be fully compensated by their attenuating effect on solvent dynamics.

5.4.3 Dielectric relaxation spectra

Since the long-term translational motion of water molecules does not provide any conclusive insights on their rotational reorientation dynamics, we computed frequency-dependent dielectric relaxation spectra of all investigated solutions according to eq. (4.44). Dielectric relaxation spectra provide a comprehensive picture of the collective reorientation dynamics in fluids. Furthermore, the aforementioned possibility to dissect the spectra into individual contributions

without having to resort to fitting techniques makes them particularly appealing from the point of MD simulations. Figure 5.9 shows a comparison of the computed concentration-dependent absorption spectra $\varepsilon_r''(\nu) = \varepsilon_r''(\omega/(2\pi))$ with experimental data[18,37,175,179] for aqueous solutions of all investigated cosolutes. Independent of cosolute

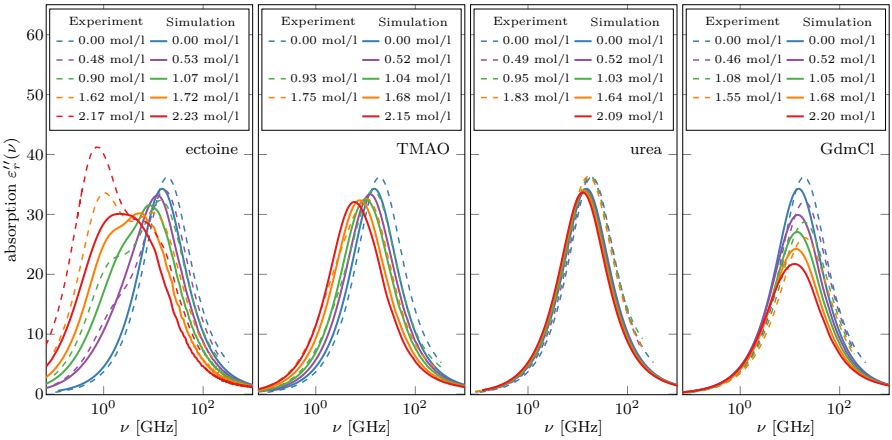

Figure 5.9: Dielectric absorption spectra $\varepsilon_r''(\nu)$ of aqueous ectoine, TMAO, urea, and GdmCl solutions (left to right) for different solute concentrations. Solid lines: Simulation data. Dashed lines: Multi-Debye fits to experimental data. Experimental data are taken from refs. 18, 37, 175, 179.

concentration, all computed spectra have in common that the high-frequency edges of the main absorption peaks are redshifted with respect to experimental data, and the peak amplitudes are slightly lower. For the cosolutes TMAO, urea, and GdmCl, this also applies to the low-frequency edge. Since this is already the case for pure SPC/E water, these systematic deviations can be attributed to the employed water model. In ectoine solutions, the amplitude of the low-frequency peak emerging with increasing cosolute concentration is clearly underestimated by the simulations, and the peak position is blueshifted with respect to experimental data. Nevertheless, the computed absorption spectra of all cosolutes reproduce the qualitative behavior of the experimental data very well, including their

concentration-dependent trends. A comparison of the full spectra including the dispersion $\varepsilon'_r(\nu)$ can be found in appendix 5.C.3.

Now that we have verified the validity of the spectra, we proceed by dissecting them according to eq. (5.6) into contributions due to water $\varepsilon''_{\mathrm{W}}(\nu)$, cosolutes $\varepsilon''_{\mathrm{C}}(\nu)$, and their interaction term $\varepsilon''_{\mathrm{CW}}(\nu)$. Figure 5.10 shows the dissection of the absorption spectra of different aqueous solutions for cosolute concentrations of $\approx 2\,\mathrm{mol/l}$. For

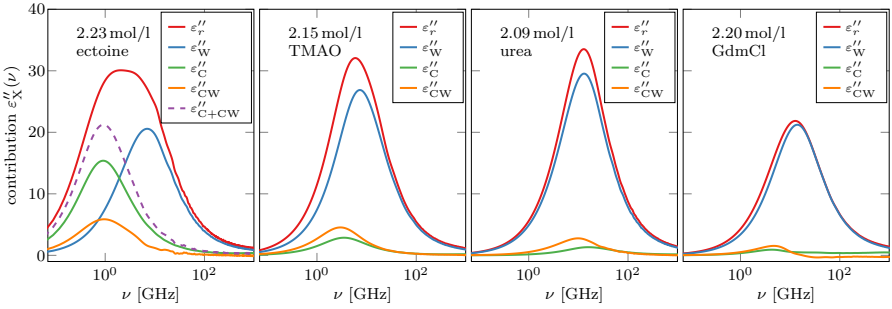

Figure 5.10: Dissection of dielectric absorption spectra $\varepsilon''_r(\nu)$ of aqueous ectoine, TMAO, urea, and GdmCl solutions (left to right) at a concentration of $c \approx 2\,\mathrm{mol/l}$. Entire spectra are marked as red lines, the contributions of water $\varepsilon''_{\mathrm{W}}$ are in blue, cosolute contributions $\varepsilon''_{\mathrm{C}}$ in green, and orange lines represent the cosolute/water interaction terms $\varepsilon''_{\mathrm{CW}}$. Additionally, for the ectoine solution, the sum $\varepsilon''_{\mathrm{C+CW}}(\nu) = \varepsilon''_{\mathrm{C}}(\nu) + \varepsilon''_{\mathrm{CW}}(\nu)$ is shown as a dashed purple line.

the aqueous ectoine solution, the spectrum is composed of distinctively separate absorption peaks with maxima of the cosolute contribution $\varepsilon''_{\mathrm{C}}(\nu)$ and cosolute/water interaction term $\varepsilon''_{\mathrm{CW}}(\nu)$ residing at $\nu \approx 940\,\mathrm{MHz}$ and the water contribution peak $\varepsilon''_{\mathrm{W}}(\nu)$ centered at $\nu \approx 7\,\mathrm{GHz}$, whereas this separation is less pronounced in the deconvolution of the TMAO spectrum, for which the maxima of $\varepsilon''_{\mathrm{C}}(\nu)$ and $\varepsilon''_{\mathrm{CW}}(\nu)$ are located between 3 and 4 GHz and $\varepsilon''_{\mathrm{W}}(\nu)$ at $\nu \approx 7.5\,\mathrm{GHz}$. In the dielectric absorption spectrum of the urea solution, the contributions $\varepsilon''_{\mathrm{C}}(\nu)$ and $\varepsilon''_{\mathrm{CW}}(\nu)$ are located even closer to $\varepsilon''_{\mathrm{W}}(\nu)$. It also becomes evident that the amplitudes of the cosolute and cosolute/water terms decrease from ectoine over TMAO to urea solutions, while the water contribution amplitude increases. However,

this effect can be attributed to the molecular size of the cosolutes, since ectoine occupies a much larger volume fraction compared to TMAO at the same molar concentration, and the partial molar volume occupied by urea molecules is even smaller. In turn, the partial molar volume occupied by water is largest for urea, followed by TMAO and ectoine. This explanation is also supported by the values of N_{water} in table 5.1 for the individual cosolutes as well as by eq. (5.6). The water contribution to the complex dielectric permittivity therefore scales with the volume fraction occupied by water so that a larger water volume fraction corresponds to larger magnitudes (see appendix 5.A.2.1).

The GdmCl solution, however, does not follow the general trends observed for the other solutions. There, the $\varepsilon''_{\mathrm{C}}(\nu)$ and $\varepsilon''_{\mathrm{CW}}(\nu)$ contributions reside at approximately the same peak frequencies as in TMAO solutions, yet with amplitudes even smaller than those of the corresponding contributions in the urea solution. The cosolute/water contribution is even negative for $\nu > 30\,\mathrm{GHz}$ and completely cancels out the cosolute contribution. As for the ectoine solution, the amplitude of the water contribution is also relatively low, which again can be explained by the relatively small partial molar volume occupied by water.

While comparing our computationally obtained spectral decompositions to the deconvolutions performed on experimental dielectric relaxation data of aqueous ectoine solutions,[37] we noticed that the contribution ascribed to the solute very closely coincides with the sum $\varepsilon''_{C+CW}(\nu) := \varepsilon''_{C}(\nu) + \varepsilon''_{CW}(\nu)$ of our data, which is shown in the respective panel of fig. 5.10. In that respect, our data corroborates the mechanistic picture for ectoine brought up by Eiberweiser *et al.*[37] of very tightly bound hydration water undergoing a dielectric relaxation together with the corresponding solute molecules. The qualitative coincidence of the cosolute/water contributions $\varepsilon''_{\mathrm{CW}}(\nu)$ with the relaxation modes ascribed to "slow" water in case of TMAO and urea solutions[18,175] further support this notion, and thus, we can attribute the remaining $\varepsilon''_{\mathrm{W}}(\nu)$ contribution to what is commonly

referred to as bulk or "bulk-like" water. Moreover, our dissection of the aqueous GdmCl solution spectrum explains why there exists no such decomposition of experimental data. Due to the fact that, independent of concentration, all contributions add up to an absorption peak which can be perfectly fitted by a single Debye relaxation, the usually followed experimental approach of fitting spectral data with multiple superimposed relaxations fails here. Thus, to our knowledge, we show here for the first time that the dielectric relaxation of aqueous GdmCl solutions is strongly dominated by bulk-like water contributions, while solute contributions only lead to a small spectral broadening at the low-frequency edge of the main relaxation peak.

The presented spectral decomposition into different molecular contributions finally enables us to explicitly analyze the concentration-dependent effect of cosolutes on the collective dielectric relaxation dynamics of bulk-like water. To this aim, fig. 5.11 depicts the water contributions $\varepsilon''_{\mathrm{W}}(\nu)$ in the presence of cosolutes at concentrations ranging from 0 to approximately 2 mol/l. In aqueous ectoine

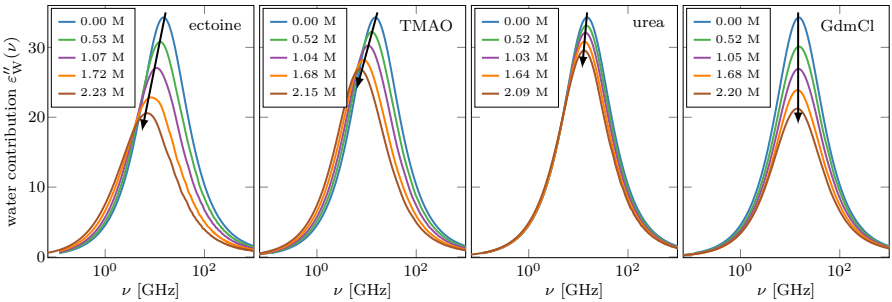

Figure 5.11: Concentration-dependent water contributions $\varepsilon''_{\mathrm{W}}(\nu)$ of the dielectric absorption of aqueous ectoine, TMAO, urea, and GdmCl (left to right) solutions for different cosolute concentrations. Arrows indicate increasing cosolute concentration.

solutions, increasing the cosolute concentration leads to a pronounced redshift of the water contribution with its peak position decreasing from about 15 GHz in pure water by a factor of 2.15 down to approximately 7.0 GHz at 2.23 mol/l. Comparable to the effect of ectoine,

the presence of TMAO induces a retardation of reorientational water dynamics with the peak frequency of $\varepsilon''_{\mathrm{W}}(\nu)$ shifted down to $\approx 7.4\,\mathrm{GHz}$ at 2.15 mol/l TMAO. Relative to the stabilizing osmolytes, the impact of urea on dielectric water relaxation is comparatively small since the addition of 2.09 mol/l urea to water redshifts the water absorption peak by as little as 2 GHz (15 %) to 13 GHz. Remarkably, GdmCl appears to have virtually no effect on the peak frequency position of collective reorientational water dynamics. These results indicate a pronounced dynamical strengthening of the water structure by the stabilizing osmolytes ectoine and TMAO in terms of water reorientation dynamics, while the denaturants urea and GdmCl show only little or no effect. Together with the results obtained from the analysis of translational diffusion coefficients and hydrogen bond life times, these results provide a clearly ordered picture of how the different investigated cosolutes affect water dynamics.

Now that we have observed the attenuating effect on water reorientation dynamics in the GHz regime caused by the presence of the protecting osmolytes, there remains one important question to be answered: Due to the fact that all systems were simulated at the same constant temperature of 300 K, their average kinetic energy per degree of freedom should remain unchanged. Since the collective water reorientation dynamics are slowed down in some of the systems, this energy must have been transferred to other kinetic modes.

Up to this point, we have analyzed the dielectric relaxation spectra in the same frequency range as commonly accessible by experimental dielectric relaxation measurements, which usually does not exceed the upper GHz regime. However, our MD simulations have a temporal resolution of one femtosecond, so that dielectric relaxation data is readily available also in the THz regime. Consequently, fig. 5.12 depicts the water dielectric absorption peaks $\varepsilon''_{\mathrm{W}}(\nu)$ in the high-frequency regime ranging from 0.8 to 30 THz. Opposed to what we observed in the low-frequency regime in fig. 5.11, the different investigated cosolutes now exhibit a blueshift with relative extents corresponding to the order

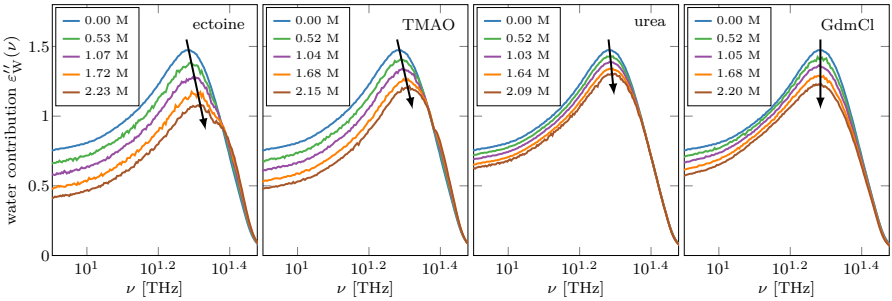

Figure 5.12: Concentration-dependent water contributions $\varepsilon''_W(\nu)$ of the dielectric absorption of aqueous ectoine, TMAO, urea, and GdmCl (left to right) solutions for different cosolute concentrations in the THz regime. Arrows indicate increasing cosolute concentration.

of redshifts in the GHz regime. Again, the effect is very weak for urea, and GdmCl induces no frequency shift at all. Evidently, the protecting osmolytes ectoine and TMAO induce a transfer of kinetic energy from the low- to the high-frequency modes of water reorientation dynamics.

5.5 Summary and Discussion

We have performed extensive MD simulations of aqueous binary solutions comprising different small organic cosolutes at concentrations ranging from 0 to $\approx 2\,\mathrm{mol/l}$ in order to assess their influence on the local water structure and on water dynamics. With ectoine and trimethylamine N-oxide, we chose two important yet intrinsically different protein stabilizers, whereas with urea and guanidinium chloride, we studied two substances commonly known for their denaturing effects on proteins. In order to obtain indicators for the different cosolutes' kosmo- or chaotropic nature, we carried out multiple analyses regarding the concentration-dependent structural arrangement of water, with investigated properties ranging from radial distribution functions to order parameters allowing to quantify the sphericity and tetrahedral

arrangement of neighboring water molecules. Furthermore, we explored how these cosolutes impact the dynamics of water and the stability of its hydrogen bond network. To this aim, we calculated translational water diffusion coefficients and hydrogen bond life times. Furthermore, a modification of the employed simulation software allowed us to conveniently extract dielectric relaxation spectra over a broad frequency range from the upper MHz to the THz regime, which also served to validate the dynamics of the employed force fields via comparison with experimental data. The computational decomposition of the spectra into contributions originating from different molecular species allowed us to analyze the water relaxation kinetics separated from the contributions due to cosolutes and the respective interaction cross-terms.

The main goal of our research was to identify possible ways of how the presence of different cosolutes at low to moderate concentrations could potentially lead to the indirect protection or, likewise, destabilization of native protein conformations by altering the properties of their hydration water. The existence of such indirect, water-mediated effects has been shown experimentally for the protecting osmolyte TMAO,[155,194] and, by means of computer simulations, also for ectoine.[35,195] It has recently been argued that the stabilization or destabilization of proteins by cosolutes depends on the structural compatibility (or incompatibility, respectively) of the cosolutes' hydration shells with that of the protein,[157] with the argument mostly based on neighboring water oxygen-oxygen distances. In that respect, our results based on the analysis of water-water radial distribution functions in the presence of cosolutes indicate a stabilizing tendency for all cosolutes if only the first peak is considered. Since even the denaturants urea and GdmCl can have a stabilizing effect on specific proteins at low to moderate concentrations,[134] our results agree with this picture, provided that the cosolutes are preferentially excluded from the protein surface. The longer-ranged RDF features, however, are less pronounced in the presence of GdmCl, indicating a slightly weakened water structure. If the structural compatibility of hydration shells plays an important role in protein/cosolute

interactions, one might argue that this should not only depend on density but also on other structural parameters such as sphericity or the degree of tetrahedrality. While both sphericity and tetrahedrality are strongly affected in the close vicinity of the investigated cosolutes, the effects differ qualitatively and quantitatively between the cosolutes so that a clear trend distinguishing kosmotropic from chaotropic behavior is difficult to establish. At distances more than two hydration shells away from the cosolutes, the situation changes in a way that all osmolytes induce a pronounced and qualitatively similar disturbance of the water structure. In that sense, urea appears to destabilize the water structure to the least extent, whereas GdmCl causes the strongest disturbance. Nevertheless, this finding does not facilitate distinguishing between water structure-making and -breaking osmolytes, as it stands in contrast to the implications drawn from the RDF analysis. In fact, it has also been argued that a solute's impact on water structure is uncorrelated to its stabilizing or denaturing effect on proteins,[196] contradicting the findings of ref. 157. Yet, this discrepancy can be mitigated if we consider the preferential exclusion of a cosolute from the protein surface as a prerequisite for water-mediated, stabilizing interactions. This proposition is further supported by the fact that direct interaction of common stabilizers such as TMAO or ectoine with proteins or other macromolecules can have a destabilizing effect.[70,145,197] Preferential exclusion, however, rather depends on the cosolute's relative binding affinity, *i.e.*, the relative strength of cosolute/solvent with respect to cosolute/protein interactions. Comparable conclusions were drawn recently also for ions, interfaces, and polyelectrolytes in ternary mixtures.[148,198–202]

Even though a specific cosolute's binding affinity depends on the type of protein it can potentially bind to, compared to weakly water-binding species, molecules which are strongly water binding such as ectoine or TMAO in turn should have a higher probability to be excluded from the protein surface. Despite the fact that both these molecules significantly perturb the water structure, our data regarding water diffusion coefficients and hydrogen bond life times indicate a pronounced stabilization

of the surrounding water structure, especially in terms of translational dynamics. The observed slow-down of water dynamics around proteins in aqueous ectoine solutions was found to have a significant impact on protein stability,[195] which additionally highlights the importance of solvent dynamics.

Since the structural relaxation of proteins requires not only translational diffusion but also rotational reorientation of water molecules, we investigated the effect of different cosolutes on the dielectric relaxation of water. Our computational approach thereby allowed us to isolate the water contributions complementing experimental approaches,[18,37,175,203] as well as in solutions for which the deconvolution of experimentally obtained spectra is not possible. We found that even though the denaturants urea and GdmCl lead to a significant retardation of translational water diffusion, their effect on dielectric water relaxation was negligible compared to the slow-down observed for ectoine and TMAO. Nevertheless, the attenuation of translational water dynamics by the denaturants may very well affect the structural relaxation of proteins and, thus, potentially play a role in the observed stabilizing effect of these cosolutes at low concentrations,[134] where the usually observed tendency towards preferential binding of these cosolutes might be weakened by entropic effects.

Even though our analysis is limited to a small number of cosolutes, our results suggest that the influence of cosolutes on the slow modes of water dynamics are likely to play an important role in indirect protein stabilization mechanisms, provided that cosolutes do not favorably interact with proteins. The fact that other protein stabilizers such as betaine or glycine, which have not been included in this work, show a similar behavior[204,205] provides additional support for this notion. Thus, in future research, the investigation of kosmo- or chaotropic effects should not exclusively focus on structural properties but also on dynamics.

Appendix of Chapter 5

5.A Volumetric System Properties

5.A.1 Mass density

The following table lists the cosolute concentration (c: molarity, m: molality), number of water (N_{W}) and cosolute (N_{CS}) molecules (for GdmCl: the number of ion pairs), the average simulation box volume (V) and mass densities (ρ) of all investigated systems.

Cosolute	c **[mol/l]**	m **[mol/kg]**	N_{W}	N_{CS}	V **[nm^3]**	ρ **[kg/m^3]**
pure water	0.00	0.00	2180	0	65.4042 ±0.0003	997.1437 ±0.0048
ectoine	0.53	0.55	5016	50	158.2655 ±0.0010	1022.7118 ±0.0064
	1.07	1.19	2330	50	77.7394 ±0.0004	1048.4703 ±0.0057
	1.72	2.07	1343	50	48.1538 ±0.0006	1079.4766 ±0.0125
	2.23	2.83	979	50	37.2456 ±0.0004	1103.2618 ±0.0127
TMAO	0.52	0.54	5144	50	160.1640 ±0.0010	999.7406 ±0.0065
	1.04	1.13	2454	50	79.4941 ±0.0003	1001.9648 ±0.0042
	1.68	1.91	1456	50	49.5548 ±0.0003	1004.8417 ±0.0062
	2.15	2.54	1092	50	38.6215 ±0.0004	1007.3547 ±0.0100
urea	0.52	0.53	5243	50	160.9663 ±0.0009	1005.3917 ±0.0055
	1.03	1.08	2568	50	80.7193 ±0.0004	1013.5214 ±0.0046
	1.64	1.78	1562	50	50.5433 ±0.0003	1023.2003 ±0.0055
	2.09	2.31	1199	50	39.6519 ±0.0003	1030.3855 ±0.0087
GdmCl	0.52	0.54	5130	50	159.1113 ±0.0007	1014.3789 ±0.0047
	1.05	1.13	2460	50	79.1790 ±0.0005	1029.6354 ±0.0057
	1.68	1.90	1464	50	49.4354 ±0.0003	1046.4519 ±0.0070
	2.20	2.59	1071	50	37.7274 ±0.0004	1059.5104 ±0.0092

Table 5.A.1: System compositions with parameters N_{W} (number of water molecules), N_{CS} (number of cosolute molecules / ion pairs), and observables c (molarity), m (molality), V (simulation box volume), and ρ (mass density).

5.A.1.1 Comparison with experimental data

Aqueous ectoine solutions

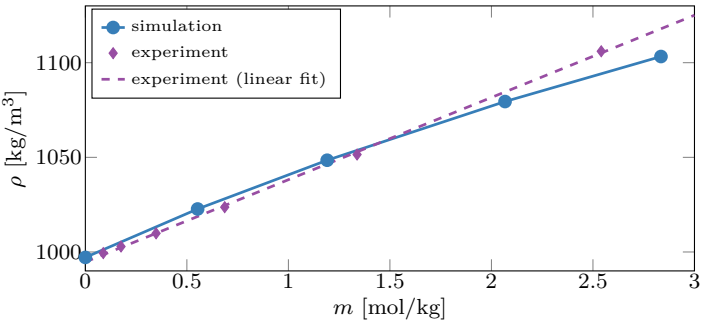

Figure 5.A.1: Comparison of mass density ρ vs. molality m with experimental data for aqueous ectoine solutions. The experimental data points shown for $T = 300\,\mathrm{K}$ are linear interpolations of data for temperatures $T = 298.24\,\mathrm{K}$ and $T = 318.17\,\mathrm{K}$ taken from Held *et al.*.[206] The maximum relative deviation of simulation data from experimental values is $1.2\,\%$ at $m = 2.83\,\mathrm{mol/kg}$.

Aqueous TMAO solutions

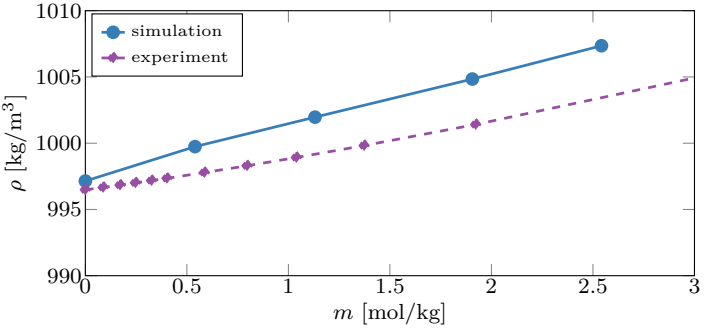

Figure 5.A.2: Comparison of mass density ρ vs. molality m with experimental data for aqueous TMAO solutions. The experimental data points shown for $T = 300\,\mathrm{K}$ are linear interpolations of data for temperatures $T = 298.15\,\mathrm{K}$ and $T = 308.15\,\mathrm{K}$ taken from Makarov *et al.*.[207] The maximum relative deviation of simulation data from experimental values is $0.4\,\%$ at $m = 2.54\,\mathrm{mol/kg}$.

Aqueous urea solutions

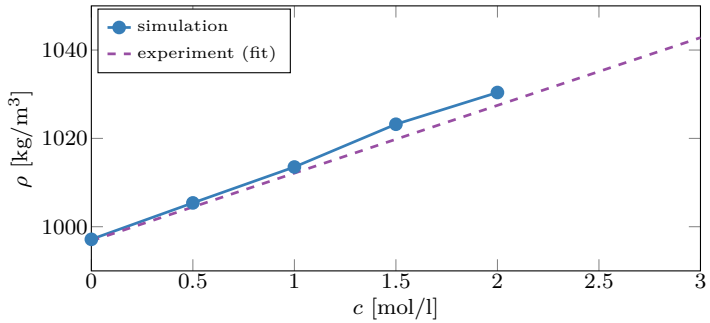

Figure 5.A.3: Comparison of mass density ρ vs. molarity c with experimental data for aqueous urea solutions. The experimental data shown for $T = 300\,\mathrm{K}$ are a linear interpolation of fits to data for temperatures $T = 298.15\,\mathrm{K}$ and $T = 303.15\,\mathrm{K}$ taken from Gucker *et al.*.[208] The maximum relative deviation of simulation data from experimental values is $0.1\,\%$ at $c = 1.64\,\mathrm{mol/l}$.

Aqueous GdmCl solutions

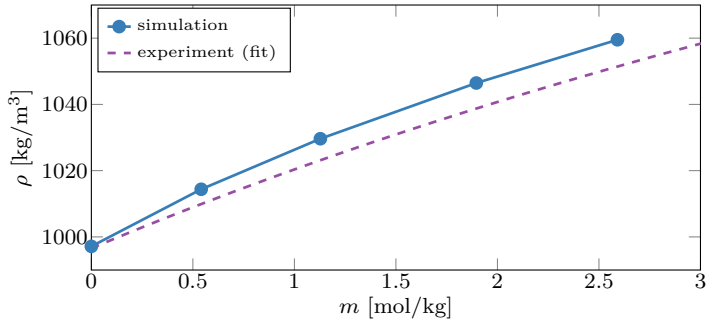

Figure 5.A.4: Comparison of mass density ρ vs. molality m with experimental data for aqueous GdmCl solutions. The experimental data shown for $T = 300\,\mathrm{K}$ correspond to a phenomenological fit function provided by Kawahara and Tanford[209] with the zero-concentration density for $T = 300\,\mathrm{K}$ set to $996.5563\,\mathrm{kg/m^3}$ according to Tanaka *et al.*.[210] The maximum relative deviation of simulation data from experimental values is $0.8\,\%$ at $m = 2.59\,\mathrm{mol/kg}$.

5.A.2 Partial molar volumes

The partial molar volume V_i^{m} of the i-th component in a k-component mixture is defined as the change in the mixture's total volume V caused by adding 1 mol of that component:

$$V_i^{\mathrm{m}} = \left(\frac{\partial V}{\partial n_i}\right)_{p,T,n_{j\neq i}} \tag{5.7}$$

Here, n_i denotes the number of moles of the i-th component in the mixture, and the subscripts $p, T, n_{j\neq i}$ on the right hand side mean that pressure, temperature, and the mole numbers of all other components are kept constant while taking the derivative. Apart from temperature and pressure, its value generally depends on the molecular species and concentration of each component. For any given combination of these variables, the total volume V of the mixture obeys the equation

$$V = \sum_{i=1}^{k} n_i V_i^{\mathrm{m}} \,. \tag{5.8}$$

If we assume that the amount Δn_i added to the mixture is small, we can express eq. (5.7) as a linear approximation

$$V_i^{\mathrm{m}} \approx N_A \left(\frac{\Delta V}{\Delta N_i}\right)_{p,T,N_{j\neq i}} \tag{5.9}$$

where we have changed the notation from mole numbers n_i to the number of molecules N_i by introducing Avogadro's number $N_A = 6.0221409 \cdot 10^{23}\,\mathrm{mol}^{-1}$.

The volume fraction Φ_i occupied by the i-th component in the mixture can then be obtained from eqs. (5.7) to (5.9) as

$$\Phi_i = n_i \frac{V_i^{\mathrm{m}}}{V} \approx \frac{N_i}{V} \left(\frac{\Delta V}{\Delta N_i}\right)_{p,T,N_{j\neq i}} . \tag{5.10}$$

In order to compute the concentration-dependent partial molar volumes $V_{\mathrm{W}}^{\mathrm{m}}$ of water and the volume fraction Φ_{W} it occupies, we performed an additional set of simulation runs following the same protocol as described in section 3 of the main chapter, but this time with a reduced number of water molecules $N'_{\mathrm{W}} \approx 0.98 N_{\mathrm{W}}$. Consequently, the resulting average simulation box volumes V' are slightly smaller than the volumes V of the original simulations. This allows us to estimate the partial molar volumes of water and the volume fraction it occupies by setting $\Delta V = V - V'$ and $\Delta N_{\mathrm{W}} = N_{\mathrm{W}} - N'_{\mathrm{W}}$. Inserting these definitions into eqs. (5.9) and (5.10) finally yields

$$V_{\mathrm{W}}^{\mathrm{m}} \approx N_A \frac{V - V'}{N_{\mathrm{W}} - N'_{\mathrm{W}}} \tag{5.11}$$

and, likewise,

$$\Phi_{\mathrm{W}} \approx \frac{N_{\mathrm{W}}}{N_{\mathrm{W}} - N'_{\mathrm{W}}} \left(1 - \frac{V'}{V}\right) . \tag{5.12}$$

The values of $V_{\mathrm{W}}^{\mathrm{m}}$ and Φ_{W} obtained by this procedure are listed in table 5.A.2.

Cosolute	c' [mol/l]	N'_{W}	V' [nm^3]	$V_{\mathrm{W}}^{\mathrm{m}}$ [cm^3/mol]	Φ_{W} [vol.%]
pure water	0.00	2180	65.4042 ±0.0003	18.0676 ±0.0002	100.00 ±0.00
ectoine	0.53	4916	155.2684 ±0.0007	18.0489 ±0.0208	94.99 ±0.05
	1.09	2283	76.3310 ±0.0006	18.0456 ±0.0257	89.81 ±0.06
	1.75	1316	47.3441 ±0.0003	18.0597 ±0.0394	83.64 ±0.09
	2.27	959	36.6459 ±0.0004	18.0564 ±0.0500	78.81 ±0.11
TMAO	0.53	5041	157.0746 ±0.0005	18.0632 ±0.0185	96.33 ±0.05
	1.06	2405	78.0248 ±0.0004	18.0584 ±0.0182	92.57 ±0.05
	1.71	1427	48.6808 ±0.0004	18.1494 ±0.0278	88.55 ±0.07
	2.19	1070	37.9609 ±0.0004	18.0833 ±0.0408	84.90 ±0.09
urea	0.53	5138	157.8168 ±0.0008	18.0637 ±0.0192	97.70 ±0.05
	1.05	2517	79.1897 ±0.0006	18.0624 ±0.0230	95.42 ±0.06
	1.67	1531	49.6110 ±0.0005	18.1115 ±0.0292	92.94 ±0.07
	2.13	1175	38.9305 ±0.0004	18.1015 ±0.0345	90.89 ±0.09
GdmCl	0.53	5027	156.0258 ±0.0012	18.0406 ±0.0228	96.59 ±0.06
	1.07	2411	77.7139 ±0.0007	18.0071 ±0.0275	92.90 ±0.07
	1.71	1435	48.5719 ±0.0006	17.9300 ±0.0397	88.17 ±0.10
	2.24	1050	37.1038 ±0.0003	17.8848 ±0.0438	84.31 ±0.10

Table 5.A.2: Compositions of systems with a reduced number of water molecules N'_{W}. As in all previous simulations, the number of cosolute molecules (or ion pairs) was kept fixed at $N_{\mathrm{CS}} = 50$. The remaining columns list the observables c' (molarity), V' (simulation box volume), $V_{\mathrm{W}}^{\mathrm{m}}$ (partial molar volume of water), and Φ_{W} (volume fraction occupied by water).

5.A.2.1 Scaling of dielectric absorption peaks with volume fraction

In the discussion of dielectric spectral decompositions into parts originating from the different molecular species (section 4.2.3 of the main chapter), we stated that the absorption peak amplitudes $\max(\varepsilon''_{\mathrm{W}})$ of the water contributions approximately scale with the volume fraction Φ_{W} occupied by water. This behavior is illustrated in fig. 5.A.5 below.

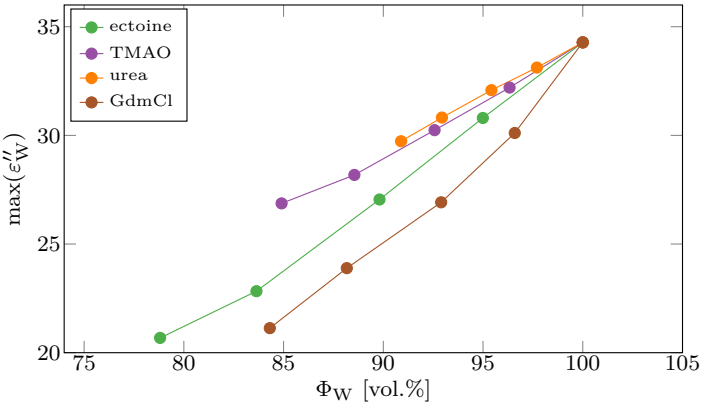

Figure 5.A.5: Scaling of the dielectric water absorption peak $\max(\varepsilon''_{\mathrm{W}})$ with the volume fraction Φ_{W} occupied by water. Clearly, larger values of Φ_{W} correspond to higher peak amplitudes $\max(\varepsilon''_{\mathrm{W}})$.

5.B Structural Properties

So far, we have shown structural properties only for pure water and cosolute concentrations of $c \approx 2$ mol/l. Here, we provide data for all investigated concentrations.

For each cosolute species at each concentration, trajectories were collected from simulations of four independently generated and equilibrated replicas of the respective systems. The trajectories were written to disk every picosecond during runs covering simulation times of $\approx 268\,\mathrm{ns}$, resulting in a total of $\approx 1,072,000$ trajectory frames per cosolute and concentration.

The resolution of the distance histograms used for the computation of water oxygen-oxygen RDFs $g_{\mathrm{OO}}(r)$ was $\delta r = 0.002\,\mathrm{nm}$, whereas the distributions of sphericity (S_k) and tetrahedrality (S_g) parameters were computed with resolutions of $\delta S_k = 10^{-5}$ and $\delta S_g = 5 \cdot 10^{-4}$. All presented curves correspond to the raw histograms *without* any smoothing, which also applies to the corresponding figures in the main chapter.

5.B.1 Radial distribution functions

5.B.1.1 Aqueous ectoine solutions

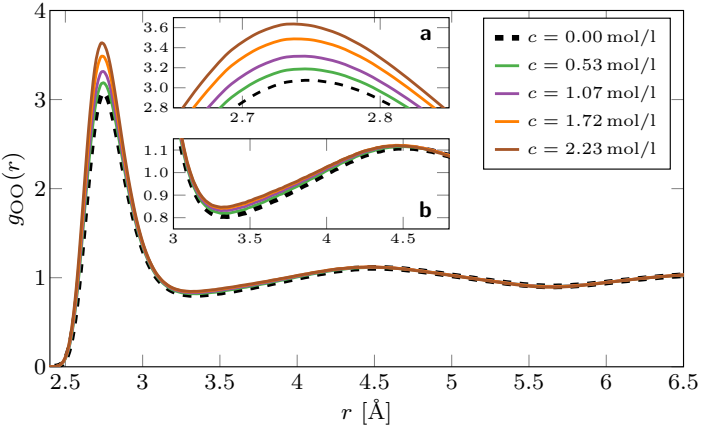

Figure 5.B.1: Concentration-dependent RDFs $g_{OO}(r)$ between water oxygen atoms in aqueous ectoine solutions. Inset **a**: Magnification of the first peak. Inset **b**: Magnification of the first minimum and second peak.

5.B.1.2 Aqueous TMAO solutions

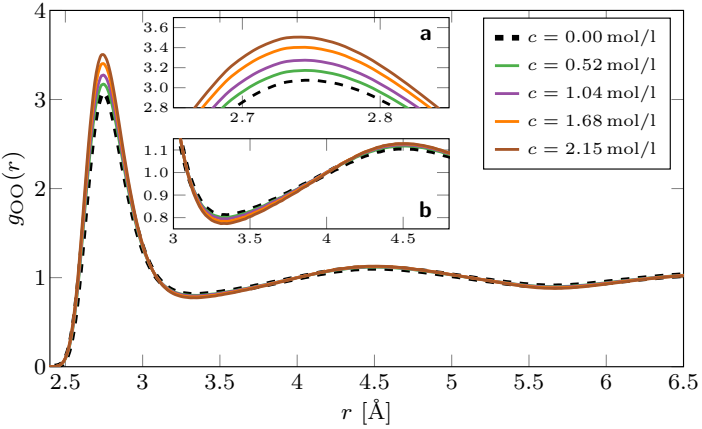

Figure 5.B.2: Concentration-dependent RDFs $g_{OO}(r)$ between water oxygen atoms in aqueous TMAO solutions. Inset **a**: Magnification of the first peak. Inset **b**: Magnification of the first minimum and second peak.

5.B.1.3 Aqueous urea solutions

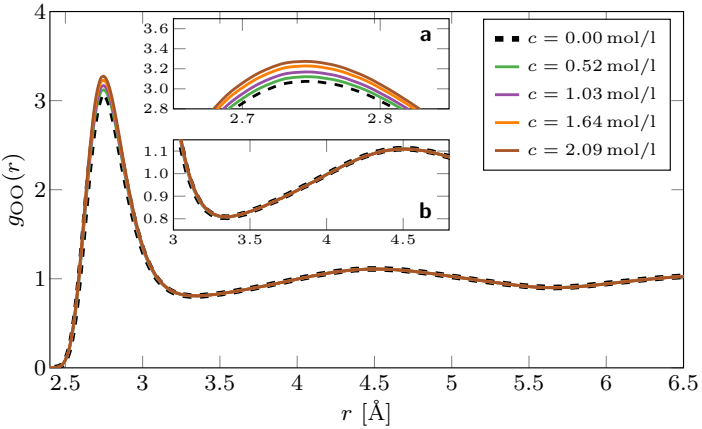

Figure 5.B.3: Concentration-dependent RDFs $g_{OO}(r)$ between water oxygen atoms in aqueous urea solutions. Inset **a**: Magnification of the first peak. Inset **b**: Magnification of the first minimum and second peak.

5.B.1.4 Aqueous GdmCl solutions

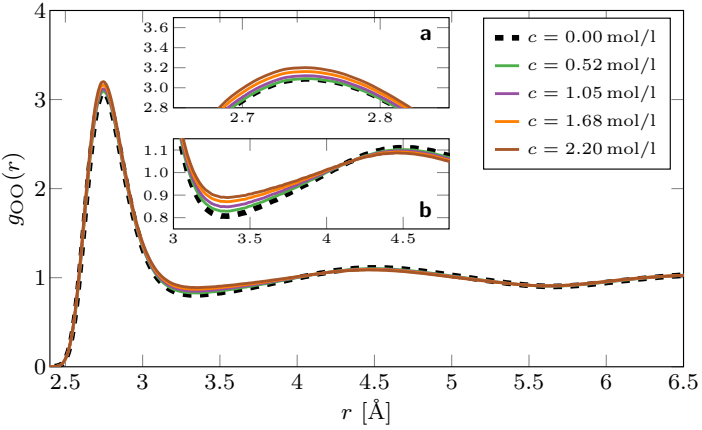

Figure 5.B.4: Concentration-dependent RDFs $g_{OO}(r)$ between water oxygen atoms in aqueous GdmCl solutions. Inset **a**: Magnification of the first peak. Inset **b**: Magnification of the first minimum and second peak.

5.B.2 Sphericity

5.B.2.1 Aqueous ectoine solutions

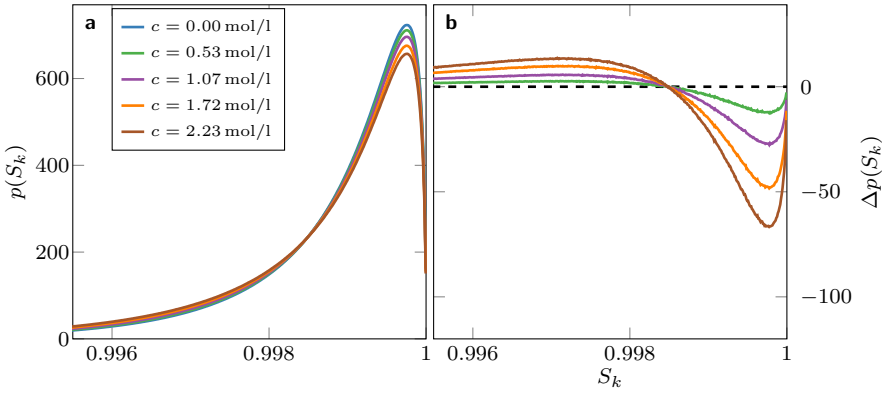

Figure 5.B.5: Concentration-dependent sphericity parameter distributions $p(S_k)$ for water in aqueous ectoine solutions. Panel **a**: Probability density $p(S_k)$ at different cosolute concentrations. Panel **b**: Difference $\Delta p(S_k)$ of the concentration-dependent probability densities with respect to that of pure water.

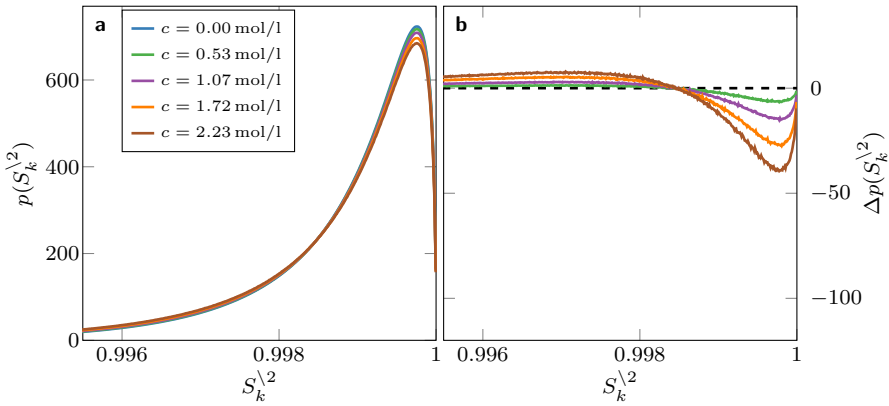

Figure 5.B.6: Concentration-dependent sphericity parameter distributions $p(S_k^{\setminus 2})$ for water in aqueous ectoine solutions with the first and second hydration shells around the solute molecules excluded from the analysis. Panel **a**: Probability density $p(S_k^{\setminus 2})$ at different cosolute concentrations. Panel **b**: Difference $\Delta p(S_k^{\setminus 2})$ of the concentration-dependent probability densities with respect to that of pure water.

5.B.2.2 Aqueous TMAO solutions

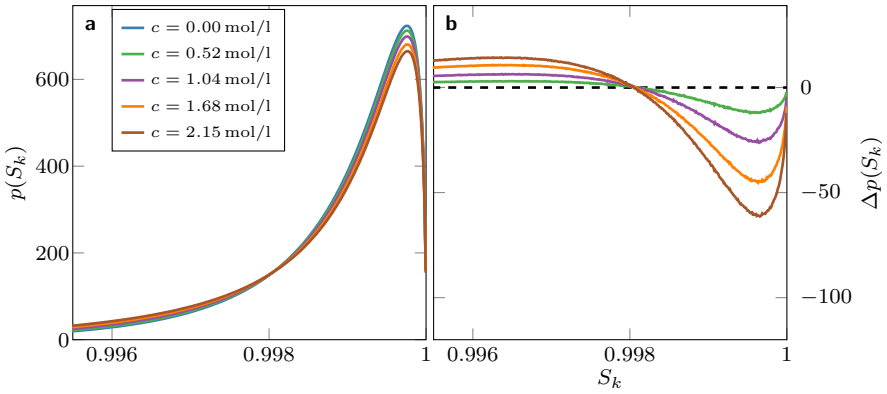

Figure 5.B.7: Concentration-dependent sphericity parameter distributions $p(S_k)$ for water in aqueous TMAO solutions. Panel **a**: Probability density $p(S_k)$ at different cosolute concentrations. Panel **b**: Difference $\Delta p(S_k)$ of the concentration-dependent probability densities with respect to that of pure water.

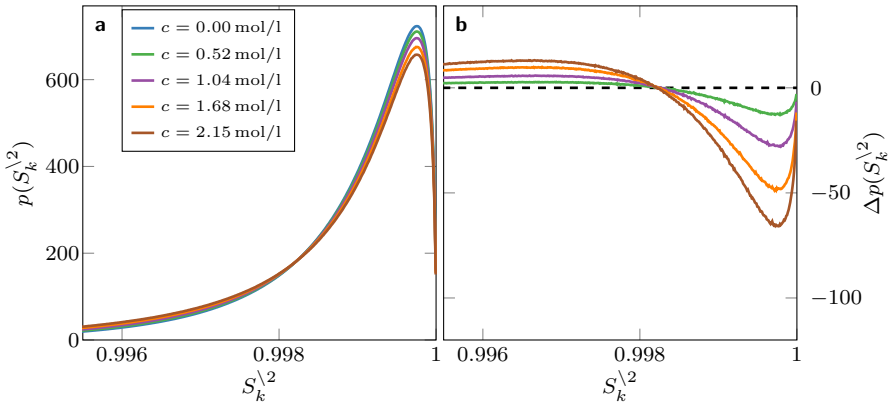

Figure 5.B.8: Concentration-dependent sphericity parameter distributions $p(S_k^{\setminus 2})$ for water in aqueous TMAO solutions with the first and second hydration shells around the solute molecules excluded from the analysis. Panel **a**: Probability density $p(S_k^{\setminus 2})$ at different cosolute concentrations. Panel **b**: Difference $\Delta p(S_k^{\setminus 2})$ of the concentration-dependent probability densities with respect to that of pure water.

5.B.2.3 Aqueous urea solutions

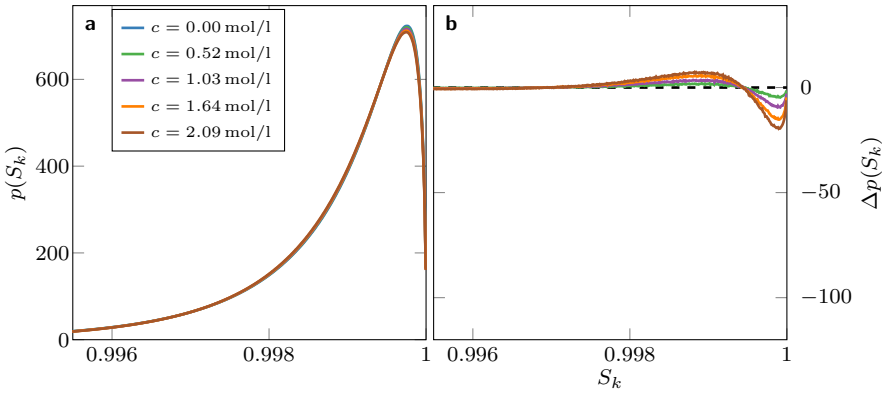

Figure 5.B.9: Concentration-dependent sphericity parameter distributions $p(S_k)$ for water in aqueous urea solutions. Panel **a**: Probability density $p(S_k)$ at different cosolute concentrations. Panel **b**: Difference $\Delta p(S_k)$ of the concentration-dependent probability densities with respect to that of pure water.

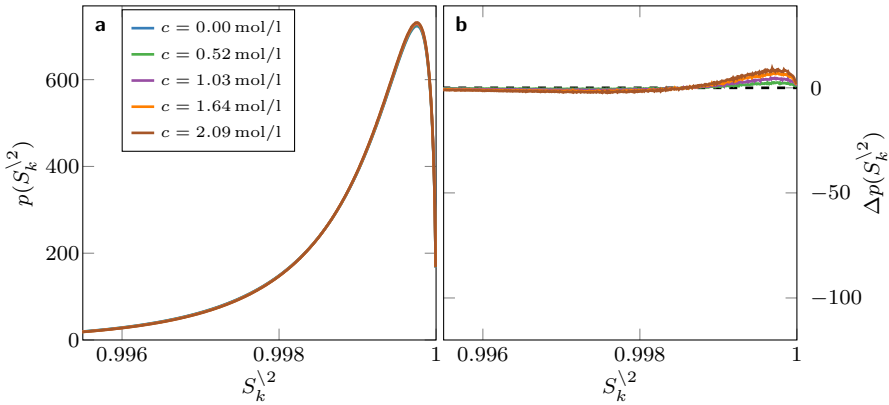

Figure 5.B.10: Concentration-dependent sphericity parameter distributions $p(S_k^{\setminus 2})$ for water in aqueous urea solutions with the first and second hydration shells around the solute molecules excluded from the analysis. Panel **a**: Probability density $p(S_k^{\setminus 2})$ at different cosolute concentrations. Panel **b**: Difference $\Delta p(S_k^{\setminus 2})$ of the concentration-dependent probability densities with respect to that of pure water.

5.B.2.4 Aqueous GdmCl solutions

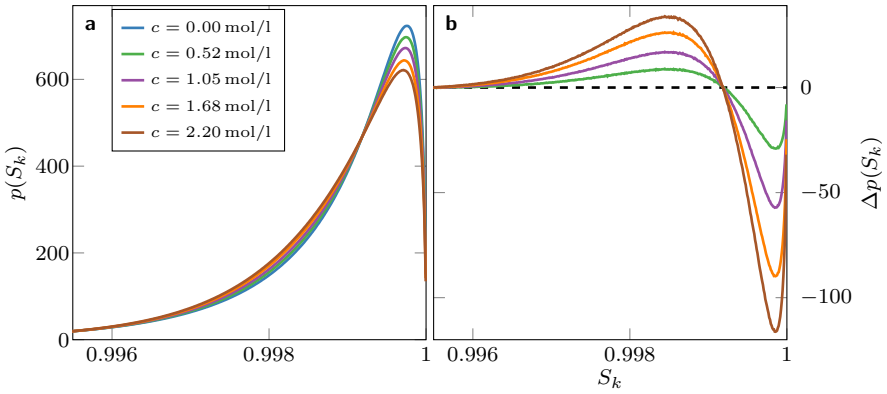

Figure 5.B.11: Concentration-dependent sphericity parameter distributions $p(S_k)$ for water in aqueous GdmCl solutions. Panel **a**: Probability density $p(S_k)$ at different cosolute concentrations. Panel **b**: Difference $\Delta p(S_k)$ of the concentration-dependent probability densities with respect to that of pure water.

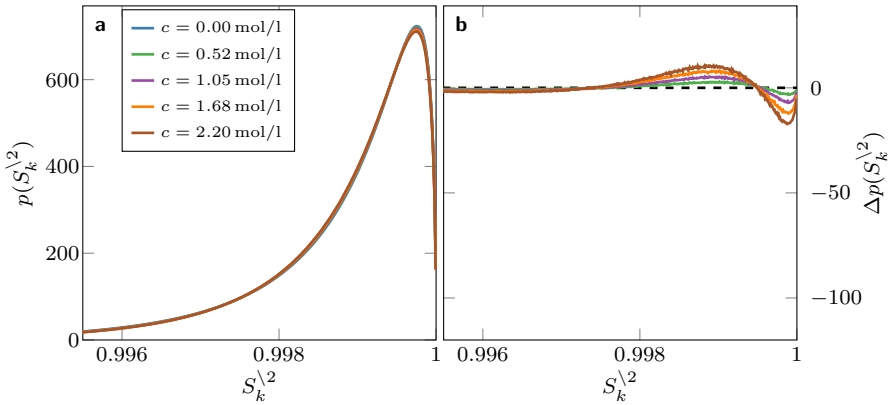

Figure 5.B.12: Concentration-dependent sphericity parameter distributions $p(S_k^{\setminus 2})$ for water in aqueous GdmCl solutions with the first and second hydration shells around the solute molecules excluded from the analysis. Panel **a**: Probability density $p(S_k^{\setminus 2})$ at different cosolute concentrations. Panel **b**: Difference $\Delta p(S_k^{\setminus 2})$ of the concentration-dependent probability densities with respect to that of pure water.

5.B.2.5 Temperature-dependent sphericity of pure SPC/E water

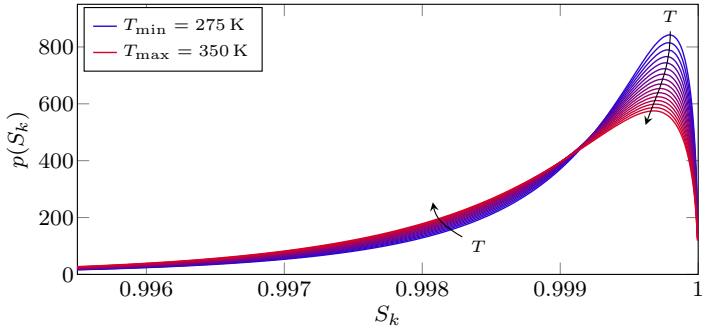

Figure 5.B.13: Temperature-dependent sphericity parameter distributions $p(S_k)$ for pure SPC/E water with temperature ranging from $T = 275\,\mathrm{K}$ to $T = 350\,\mathrm{K}$ in steps of $\Delta T = 5\,\mathrm{K}$. Arrows indicate increasing temperature.

5.B.3 Tetrahedrality

5.B.3.1 Temperature-dependent orientational tetrahedrality of pure SPC/E water

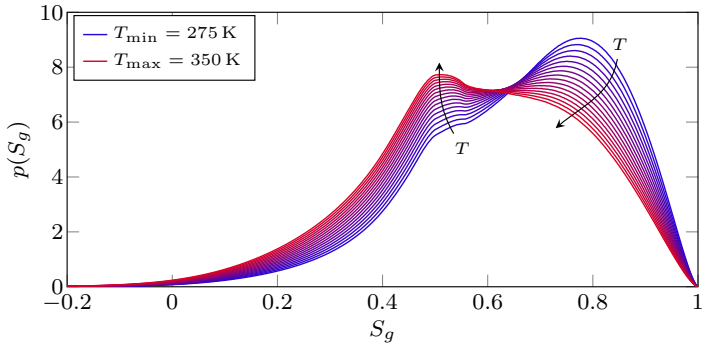

Figure 5.B.14: Temperature-dependent orientational tetrahedrality order parameter distributions $p(S_g)$ for pure SPC/E water with temperature ranging from $T = 275\,\mathrm{K}$ to $T = 350\,\mathrm{K}$ in steps of $\Delta T = 5\,\mathrm{K}$. Arrows indicate increasing temperature.

5.B.3.2 Aqueous ectoine Solutions

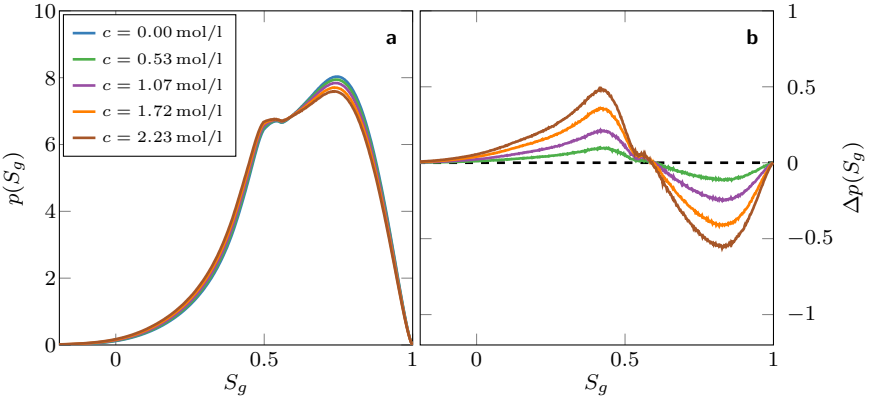

Figure 5.B.15: Concentration-dependent orientational tetrahedrality order parameter distributions $p(S_g)$ for water in aqueous ectoine solutions. Panel **a**: Probability density $p(S_g)$ at different cosolute concentrations. Panel **b**: Difference $\Delta p(S_g)$ of the concentration-dependent probability densities with respect to that of pure water.

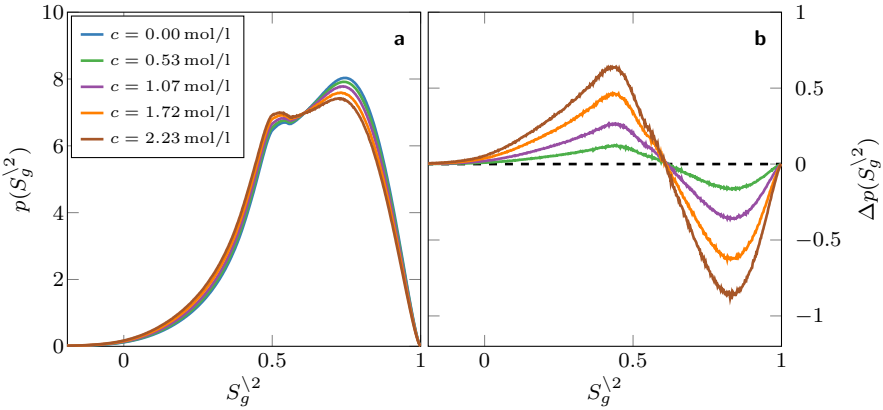

Figure 5.B.16: Concentration-dependent orientational tetrahedrality order parameter distributions $p(S_g^{\backslash 2})$ for water in aqueous ectoine solutions with the first and second hydration shells around the solute molecules excluded from the analysis. Panel **a**: Probability density $p(S_g^{\backslash 2})$ at different cosolute concentrations. Panel **b**: Difference $\Delta p(S_g^{\backslash 2})$ of the concentration-dependent probability densities with respect to that of pure water.

5.B.3.3 Aqueous TMAO solutions

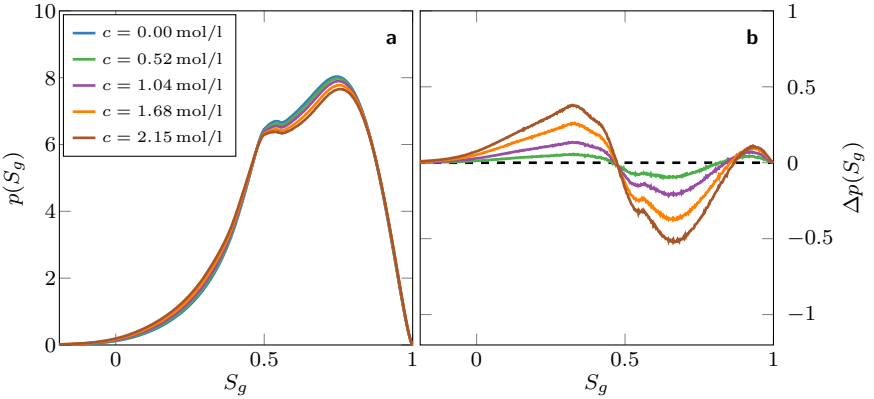

Figure 5.B.17: Concentration-dependent orientational tetrahedrality order parameter distributions $p(S_g)$ for water in aqueous TMAO solutions. Panel **a**: Probability density $p(S_g)$ at different cosolute concentrations. Panel **b**: Difference $\Delta p(S_g)$ of the concentration-dependent probability densities with respect to that of pure water.

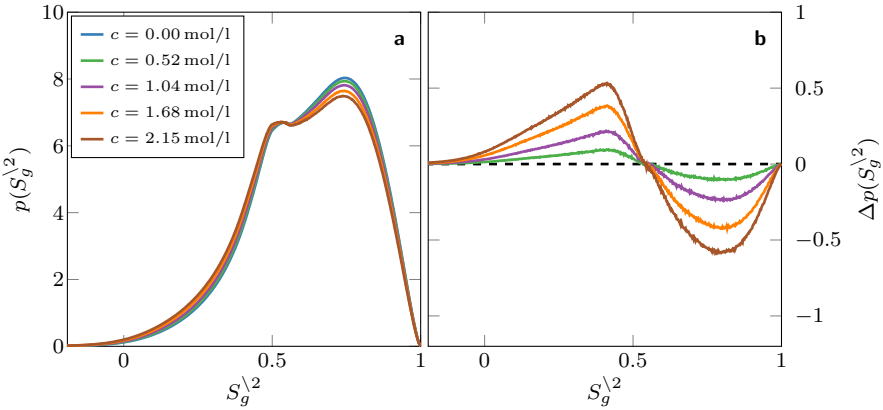

Figure 5.B.18: Concentration-dependent orientational tetrahedrality order parameter distributions $p(S_g^{\backslash 2})$ for water in aqueous TMAO solutions with the first and second hydration shells around the solute molecules excluded from the analysis. Panel **a**: Probability density $p(S_g^{\backslash 2})$ at different cosolute concentrations. Panel **b**: Difference $\Delta p(S_g^{\backslash 2})$ of the concentration-dependent probability densities with respect to that of pure water.

5.B.3.4 Aqueous urea solutions

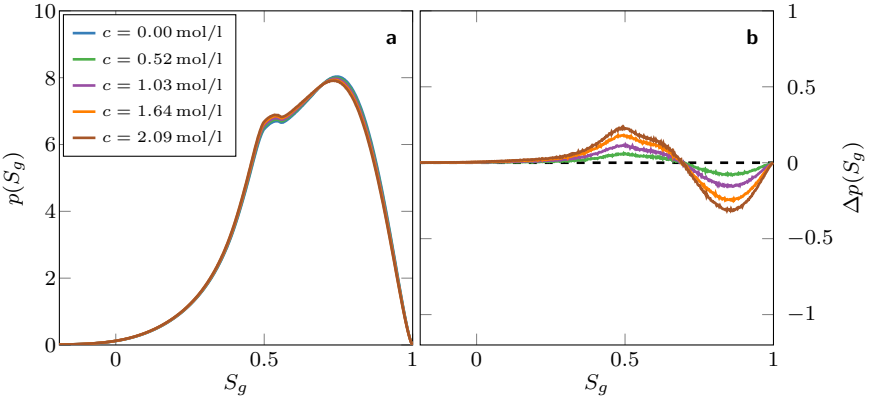

Figure 5.B.19: Concentration-dependent orientational tetrahedrality order parameter distributions $p(S_g)$ for water in aqueous urea solutions. Panel **a**: Probability density $p(S_g)$ at different cosolute concentrations. Panel **b**: Difference $\Delta p(S_g)$ of the concentration-dependent probability densities with respect to that of pure water.

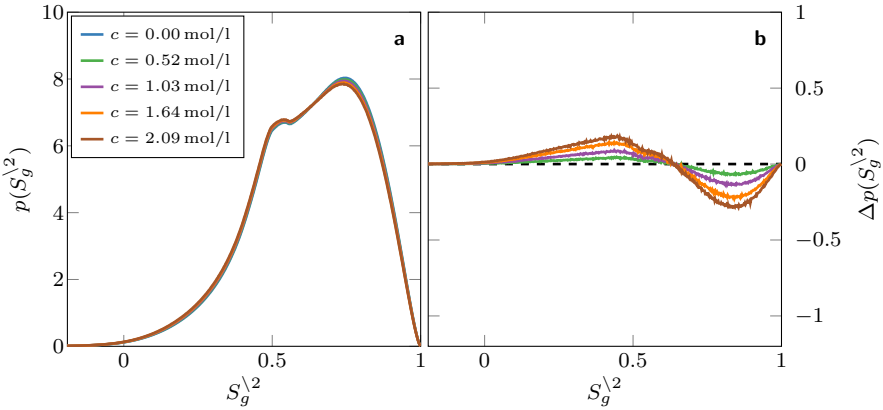

Figure 5.B.20: Concentration-dependent orientational tetrahedrality order parameter distributions $p(S_g^{\backslash 2})$ for water in aqueous urea solutions with the first and second hydration shells around the solute molecules excluded from the analysis. Panel **a**: Probability density $p(S_g^{\backslash 2})$ at different cosolute concentrations. Panel **b**: Difference $\Delta p(S_g^{\backslash 2})$ of the concentration-dependent probability densities with respect to that of pure water.

5.B.3.5 Aqueous GdmCl solutions

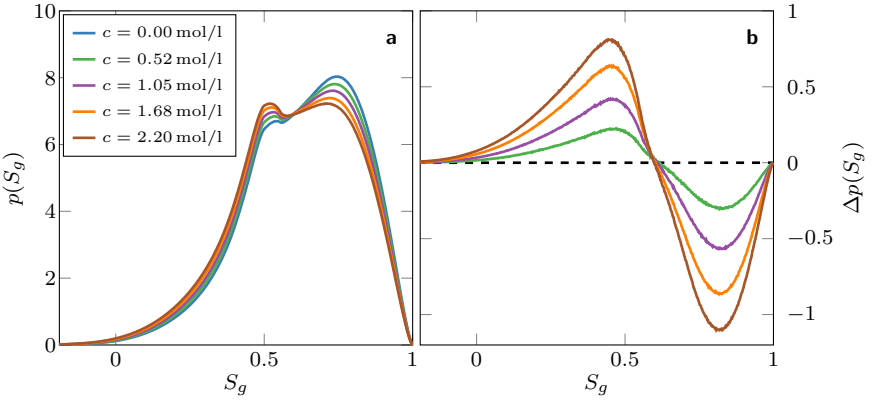

Figure 5.B.21: Concentration-dependent orientational tetrahedrality order parameter distributions $p(S_g)$ for water in aqueous GdmCl solutions. Panel **a**: Probability density $p(S_g)$ at different cosolute concentrations. Panel **b**: Difference $\Delta p(S_g)$ of the concentration-dependent probability densities with respect to that of pure water.

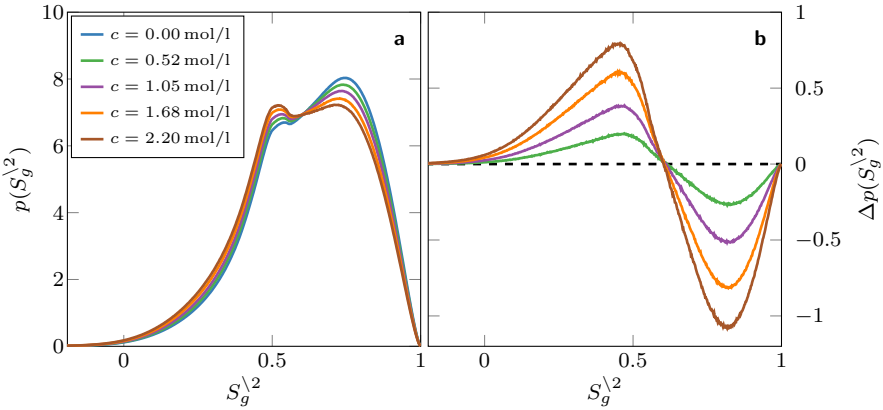

Figure 5.B.22: Concentration-dependent orientational tetrahedrality order parameter distributions $p(S_g^{\backslash 2})$ for water in aqueous GdmCl solutions with the first and second hydration shells around the solute molecules excluded from the analysis. Panel **a**: Probability density $p(S_g^{\backslash 2})$ at different cosolute concentrations. Panel **b**: Difference $\Delta p(S_g^{\backslash 2})$ of the concentration-dependent probability densities with respect to that of pure water.

5.B.3.6 Comparison of water tetrahedrality S_g in a 2 mol/l urea solution at $T = 300\,\mathrm{K}$ with that of pure water at $T = 305\,\mathrm{K}$

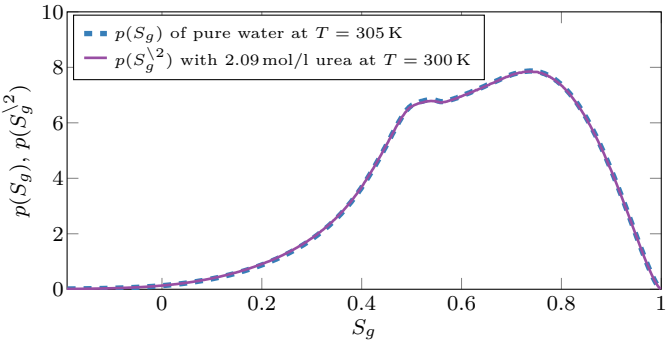

Figure 5.B.23: Comparison of the orientational tetrahedrality order parameter distribution $p(S_g^{\backslash 2})$ for water in a 2-molar aqueous urea solution at $T = 300\,\mathrm{K}$ compared to that of pure water at $T = 305\,\mathrm{K}$.

5.B.3.7 Comparison of water tetrahedrality S_g in a 2 mol/l GdmCl solution at $T = 300\,\mathrm{K}$ with that of pure water at $T = 325\,\mathrm{K}$

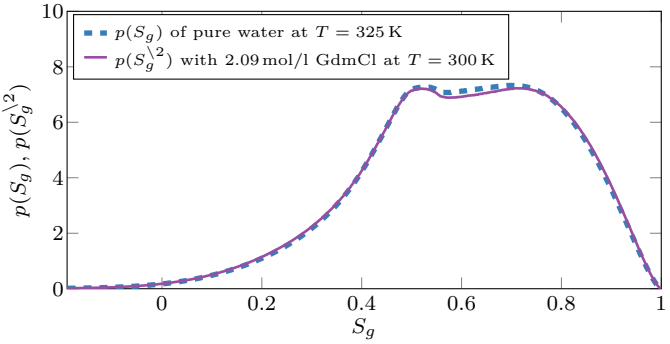

Figure 5.B.24: Comparison of the orientational tetrahedrality order parameter distribution $p(S_g^{\backslash 2})$ for water in a 2-molar aqueous GdmCl solution at $T = 300\,\mathrm{K}$ compared to that of pure water at $T = 325\,\mathrm{K}$.

5.C Dynamic Properties

5.C.1 Translational diffusion coefficients

Here, we provide a table listing the values and error estimates of water self-diffusion coefficients D_{W} in the presence of the investigated cosolutes at different concentrations. The values correspond to the plot presented in fig. 5.7. Additionally, we also list the concentration-dependent self-diffusion coefficients D_{CS} of the different cosolutes.

Cosolute	c **[mol/l]**	D_{W} **[10^{-5} cm^2/s]**	D_{CS} **[10^{-5} cm^2/s]**	
pure water	0.00	2.8264 ±0.0076	–	
ectoine	0.53	2.3206 ±0.0020	0.6456 ±0.0024	
	1.07	1.8815 ±0.0021	0.4716 ±0.0019	
	1.72	1.4160 ±0.0023	0.3127 ±0.0012	
	2.23	1.1024 ±0.0039	0.2213 ±0.0021	
TMAO	0.52	2.4310 ±0.0020	0.9352 ±0.0032	
	1.04	2.0936 ±0.0018	0.7877 ±0.0026	
	1.68	1.7313 ±0.0033	0.6389 ±0.0032	
	2.15	1.4841 ±0.0037	0.5376 ±0.0018	
urea	0.52	2.6590 ±0.0009	1.6341 ±0.0064	
	1.03	2.5223 ±0.0022	1.5237 ±0.0038	
	1.64	2.3781 ±0.0030	1.4284 ±0.0023	
	2.09	2.2810 ±0.0053	1.3571 ±0.0031	
GdmCl			Gdm^+	Cl^-
	0.52	2.5673 ±0.0063	1.2372 ±0.0093	1.4444 ±0.0142
	1.05	2.3431 ±0.0056	1.0716 ±0.0069	1.2888 ±0.0050
	1.68	2.1046 ±0.0060	0.9134 ±0.0064	1.1246 ±0.0079
	2.20	1.9245 ±0.0044	0.8066 ±0.0055	1.0150 ±0.0061

Table 5.C.1: Water (D_{W}) and cosolute (D_{CS}) self-diffusion coefficients at different cosolute concentrations c.

5.C.2 Hydrogen bond life times

The table below lists the values and error estimates of water-water hydrogen bond life times τ_{hb} in the presence of the investigated cosolutes at different concentrations. The values correspond to the plot presented in fig. 5.8.

Cosolute	c **[mol/l]**	τ_{hb} **[ps]**
pure water	0.00	2.4640 ±0.0023
ectoine	0.53	2.3805 ±0.0020
	1.07	3.0538 ±0.0017
	1.72	4.6155 ±0.0018
	2.23	6.6895 ±0.0018
TMAO	0.52	2.3573 ±0.0015
	1.04	2.9438 ±0.0014
	1.68	4.3088 ±0.0009
	2.15	5.7543 ±0.0015
urea	0.52	2.1803 ±0.0006
	1.03	2.5623 ±0.0008
	1.64	3.7448 ±0.0013
	2.09	4.0678 ±0.0006
GdmCl	0.52	2.2233 ±0.0009
	1.05	2.5718 ±0.0005
	1.68	3.3690 ±0.0009
	2.20	4.1809 ±0.0011

Table 5.C.2: Water-water hydrogen bond life times τ_{hb} at different cosolute concentrations c.

5.C.3 Dielectric spectra

The main chapter includes only the absorption part ε_r'' of the computed dielectric spectra, and their spectral decomposition only for cosolute concentrations of $c \approx 2$ mol/l. Here, we provide the full dielectric spectra of all systems for all cosolute concentrations, as well as the corresponding spectral decompositions into the contributions of water (ε_{W}), cosolutes (ε_{C}), and the water/cosolute interaction term ($\varepsilon_{\mathrm{CW}}$).

While in experimentally obtained spectra, the high-frequency limit ε_r^∞ of the permittivity (*cf.* eq. (2.3)) is a concentration-dependent offset, it is always $\varepsilon_r^\infty = 1$ for all computationally obtained dielectric spectra due to electrostatic tinfoil boundary conditions.[120] In order to eliminate this systematic error in the computed spectra and to facilitate the comparison with experimental data, we define the *reduced dielectric permittivity* $\bar{\varepsilon}_r(\omega)$ as

$$\bar{\varepsilon}_r(\omega) := \varepsilon_r(\omega) - \varepsilon_r^\infty \,, \tag{5.13}$$

which equals the electric susceptibility $\chi_e(\omega)$ if (but only if) $\varepsilon_r^\infty = 1$. Since $\varepsilon_r^\infty \in \mathbb{R}$, it contributes to dielectric dispersion $\varepsilon_r'(\omega)$ only. Thus, the dielectric absorption $\varepsilon_r''(\omega) \equiv \bar{\varepsilon}_r''(\omega)$ is not affected by this offset.

Note that the dielectric spectra are plotted with respect to the *linear* frequency $\nu = \omega/(2\pi)$ in the following figures.

5.C.3.1 Aqueous ectoine solutions

Comparison with experimental data

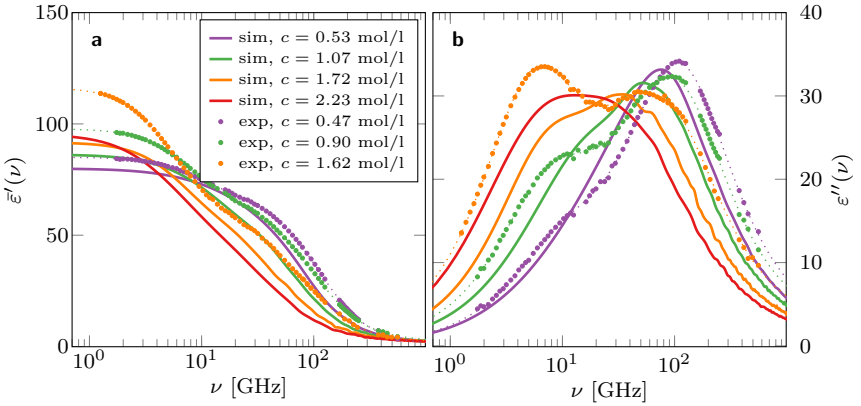

Figure 5.C.1: Dielectric spectra of aqueous ectoine solutions for different solute concentrations. Solid lines: simulation data. Dots: Experimental data. Thin dotted lines: Multi-Debye fits to experimental data. Panel **a**: reduced dielectric dispersion $\bar{\varepsilon}'_r(\nu)$. Panel **b**: dielectric absorption $\varepsilon''_r(\nu)$. Experimental data from reference 37.

Spectral decomposition

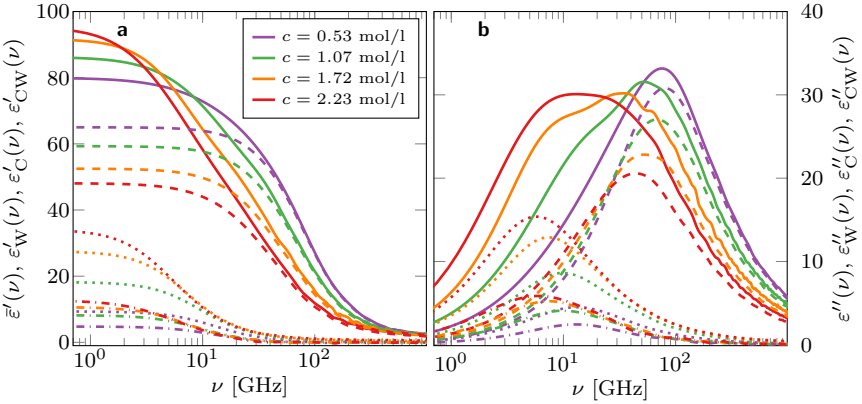

Figure 5.C.2: Spectral decompositions of dielectric spectra (solid lines) of aqueous ectoine solutions into the contributions of water $\varepsilon_{\mathrm{W}}(\nu)$ (dashed lines), cosolutes $\varepsilon_{\mathrm{C}}(\nu)$ (dotted lines), and the cosolute–water interaction terms $\varepsilon_{\mathrm{CW}}(\nu)$ (dash-dotted lines). Panel **a**: Different contributions to dielectric dispersion $\bar{\varepsilon}'_r(\nu)$. Panel **b**: Different contributions to dielectric absorption $\varepsilon''_r(\nu)$.

5.C.3.2 Aqueous TMAO solutions

Comparison with experimental data

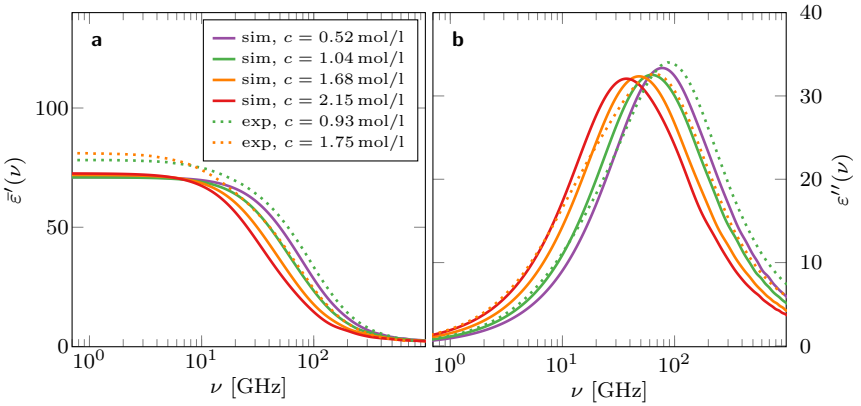

Figure 5.C.3: Dielectric spectra of aqueous TMAO solutions for different solute concentrations. Solid lines: simulation data. Dotted lines: Multi-Debye fits to experimental data. Panel **a**: reduced dielectric dispersion $\bar{\varepsilon}'_r(\nu)$. Panel **b**: dielectric absorption $\varepsilon''_r(\nu)$. Experimental data from reference 18.

Spectral decomposition

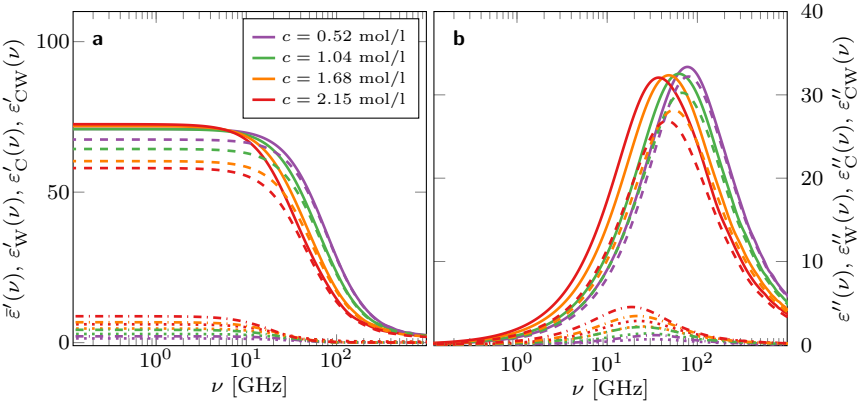

Figure 5.C.4: Spectral decompositions of dielectric spectra (solid lines) of aqueous TMAO solutions into the contributions of water $\varepsilon_{\mathrm{W}}(\nu)$ (dashed lines), cosolutes $\varepsilon_{\mathrm{C}}(\nu)$ (dotted lines), and the cosolute–water interaction terms $\varepsilon_{\mathrm{CW}}(\nu)$ (dash-dotted lines). Panel **a**: Different contributions to dielectric dispersion $\bar{\varepsilon}'_r(\nu)$. Panel **b**: Different contributions to dielectric absorption $\varepsilon''_r(\nu)$.

5.C.3.3 Aqueous urea solutions

Comparison with experimental data

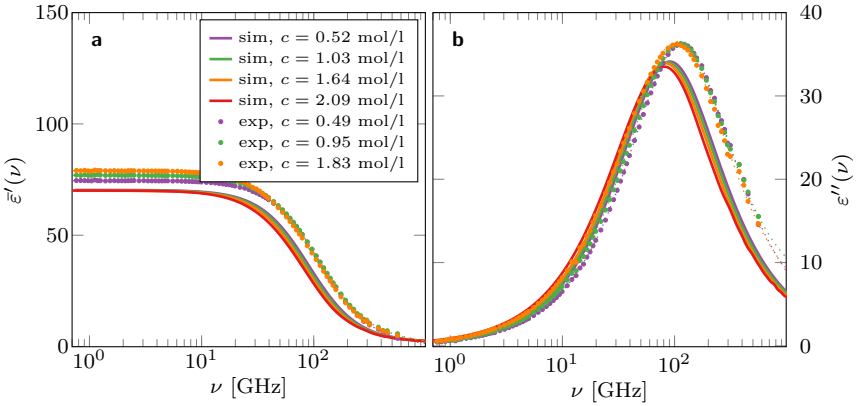

Figure 5.C.5: Dielectric spectra of aqueous urea solutions for different solute concentrations. Solid lines: simulation data. Dotted lines: Multi-Debye fits to experimental data. Panel **a**: reduced dielectric dispersion $\bar{\varepsilon}'_r(\nu)$. Panel **b**: dielectric absorption $\varepsilon''_r(\nu)$. Experimental data from reference 175.

Spectral decomposition

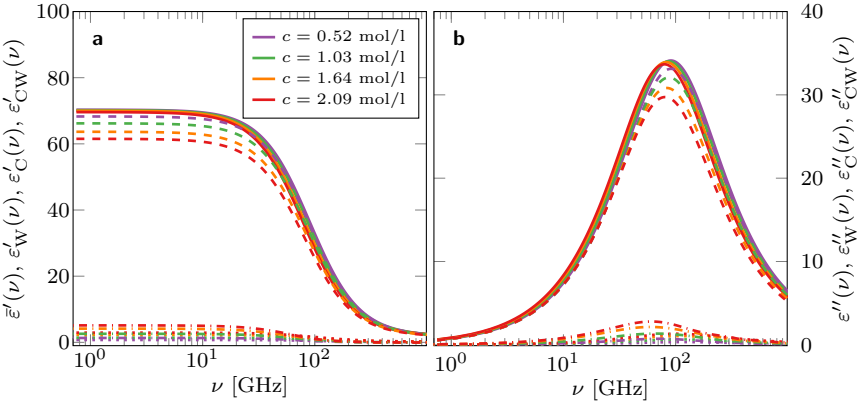

Figure 5.C.6: Spectral decompositions of dielectric spectra (solid lines) of aqueous urea solutions into the contributions of water $\varepsilon_{\mathrm{W}}(\nu)$ (dashed lines), cosolutes $\varepsilon_{\mathrm{C}}(\nu)$ (dotted lines), and the cosolute–water interaction terms $\varepsilon_{\mathrm{CW}}(\nu)$ (dash-dotted lines). Panel **a**: Different contributions to dielectric dispersion $\bar{\varepsilon}'_r(\nu)$. Panel **b**: Different contributions to dielectric absorption $\varepsilon''_r(\nu)$.

5.C.3.4 Aqueous GdmCl solutions

Comparison with experimental data

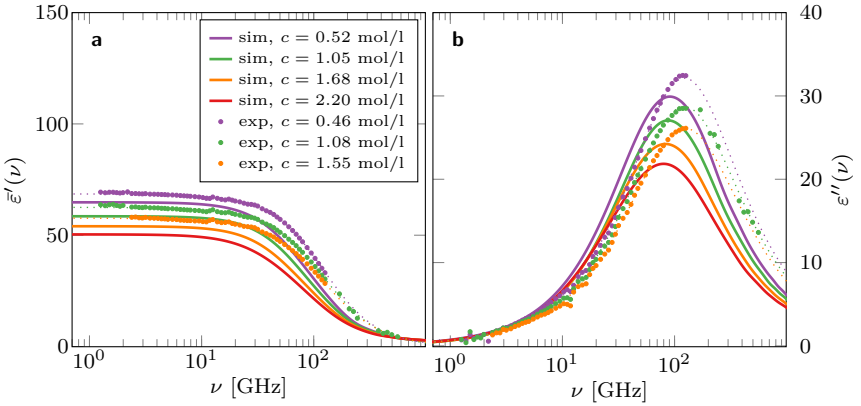

Figure 5.C.7: Dielectric spectra of aqueous GdmCl solutions for different solute concentrations. Solid lines: simulation data. Dotted lines: Multi-Debye fits to experimental data. Panel **a**: reduced dielectric dispersion $\bar{\varepsilon}'_r(\nu)$. Panel **b**: dielectric absorption $\varepsilon''_r(\nu)$. Experimental data from reference 179.

Spectral decomposition

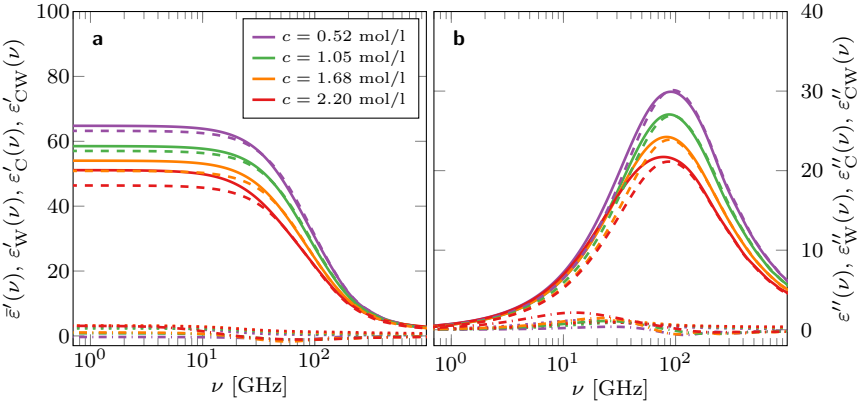

Figure 5.C.8: Spectral decompositions of dielectric spectra (solid lines) of aqueous GdmCl solutions into the contributions of water $\varepsilon_{\mathrm{W}}(\nu)$ (dashed lines), cosolutes $\varepsilon_{\mathrm{C}}(\nu)$ (dotted lines), and the cosolute–water interaction terms $\varepsilon_{\mathrm{CW}}(\nu)$ (dash-dotted lines). Panel **a**: Different contributions to dielectric dispersion $\bar{\varepsilon}'_r(\nu)$. Panel **b**: Different contributions to dielectric absorption $\varepsilon''_r(\nu)$.

6 Coarse-grained Polarizable Force Fields for Ionic Liquids

Note: The contents of this chapter have been previously published in similar form:

J. Zeman, F. Uhlig, J. Smiatek and C. Holm, A coarse-grained polarizable force field for the ionic liquid 1-butyl-3-methylimidazolium hexafluorophosphate, *Journal of Physics: Condensed Matter* **29**, 504004 (2017).

This is the Accepted Manuscript version of an article accepted for publication in *Journal of Physics: Condensed Matter*. IOP Publishing Ltd is not responsible for any errors or omissions in this version of the manuscript or any version derived from it. The Version of Record is available online at doi.org/10.1088/1361-648X/aa99c4.

Note: The determination of electronic polarizabilities including all DFT calculations was performed by F. Uhlig. Using these polarizabilities, the entire force field parametrization and evaluation was performed by J. Zeman.

Even though room temperature ionic liquids (ILs) are known since the early twentieth century,[211] it took almost another century until their technological potential was recognized. During the past two decades, ILs gained a rapidly increasing attention in science and technology. Applications range from lubrication, catalysis, organic synthesis, or nanostructure assembly to energy storage, such as electrochemical devices or supercapacitors.[212–214] Subsequently, in order to investigate ILs in computer simulations, great efforts have been carried

out to develop adequate computational models. For classical molecular dynamics (MD) simulations, there exists a variety of atomically resolved non-polarizable[215–226] as well as polarizable[227–230] force fields (see refs. 231, 232 for a perspective on the topic). It has been shown that in simulations of ILs, accounting for electronic polarizability, *i.e.*, the displacement of electronic charges against the corresponding nuclei, plays a significant role for the correct reproduction of dynamic properties such as translational or rotational diffusion, viscosity, electrical conductivity, or dielectric properties.[227,233,234] However, the simulation of atomically resolved and explicitly polarizable models is computationally very demanding, and thus, accessible length and time scales are limited. A viable method to overcome those limits is to account for electronic polarization by means of charge rescaling. In this approach, the enhanced dielectric screening due to electronic polarization is effectively included into the force field in terms of reduced partial charges.[216,231,235,236] According to ref. 235, the charge rescaling factor for a particular substance is, at least approximately, proportional to the inverse square root of the electronic permittivity $\varepsilon_{\mathrm{el}}$, namely that part of the overall dielectric permittivity which is due to inducible dipoles. Schmidt *et al.*[236] have shown that this charge rescaling comes out naturally from a best fit of partial all-atom charges in order to account for the electronic potential map that has been computed by ab-initio quantum mechanical calculations. In general, this will result in partial charges that are not uniformly scaled down, but according to the polarizability of the local environment, and hence go beyond the mean-field approach. Consequently, attempts have been made for constructing improved force fields exploiting that knowledge.[216,217,237,238] The magnitude of this polarization, however, generally depends on the composition of the investigated substance, which calls the general transferability of charge-reduced models into question. Even though the different scaling factors of pure ILs are often quite close, the polarization of pure ILs is not necessarily comparable to the polarization of ILs in mixtures with other, possibly

neutral components. The explicit treatment of electronic polarizability is therefore likely to be indispensable in transferable force fields.[239]

In 2010, Roy *et al.*[45] showed at the example of 1-butyl-3-methylimidazolium hexafluorophosphate ([BMIm][PF_6]) that many thermodynamic key features of ILs can be reproduced by idealized coarse-grained representations, where groups of atoms or even whole molecules are merged into single interaction sites with effective pair potentials. In order to improve the dynamic properties of their model, Roy and Maroncelli employed reduced charges in the revised version of their force field.[240] Since then, their model became a quite popular alternative to atomistic force field approaches in situations where either the chemical details of specific ILs were of minor importance, the dependence on such details was investigated, or the required system sizes were prohibitively large for the use of atomically resolved models.[233,241–249]

Here, we aim to combine the advantage that comes with a coarse-grained representation in terms of computational feasibility with the explicit treatment of electronic polarizability by means of Drude oscillators. We present a coarse-grained polarizable force field for [BMIm][PF_6] developed on the basis of the model by Roy *et al.* in its first version.[45] When referring to the different models, we will use the notation introduced in ref. 240 and will therefore denote the first[45] and second[240] versions of the model by Roy *et al.* as ILM1 and ILM2 in the following. For our polarizable model, we adopt this notation and will refer to our force field as the ILMpol model. We assess its applicability for bulk IL simulations by examining important thermodynamic properties and compare the results obtained from simulations of both the reduced-charge ILM2 model and our polarizable ILMpol force field to experimental data.

6.1 Methods

6.1.1 Force field parametrization

In general, the parametrization of an MD force field is a very challenging task. One has to find the correct molecular structure and map charge and mass distributions onto suitable interaction sites in a physically meaningful way, and parameters for effective intra- and intermolecular potentials have to be determined. There exists a plethora of different ways to estimate such parameters from ab initio calculations or from empirical fits to experimental data.[231,250,251] Here, we are able to take a much simpler route, since the mapping of the charge and mass distributions onto the coarse-grained interacion sites as well as the parametrization of the intermolecular Lennard-Jones (LJ) interactions is already available from the non-polarizable ILM1 model. Furthermore, since the model is completely rigid, there exist no intramolecular potentials for bond lengths, angles, or dihedrals which would have to be readjusted. The molecular structures of the $BMIm^+$ cation and PF_6^- anion are depicted in fig. 6.1a along with atomistic ball-and-stick models (fig. 6.1b) and the corresponding coarse-grained representation (fig. 6.1c).

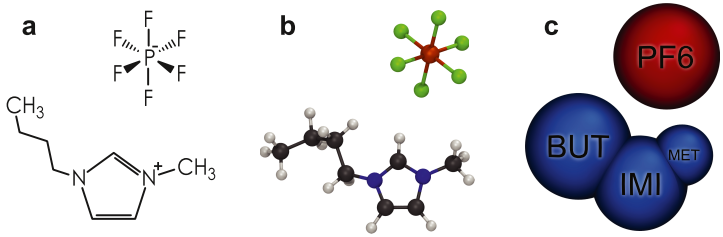

Figure 6.1: **a**: Chemical structure of the PF_6^- anion (top) and $BMIm^+$ cation (bottom). **b**: Corresponding all-atom representations. **c**: Coarse-grained representations. The PF_6^- anion is represented by a single interaction site (PF6), whereas the $BMIm^+$ cation is partitioned into three interaction sites corresponding to the butyl side chain (BUT), the imidazole ring (IMI), and the methyl group (MET).

As a first step, we have to determine the molecular electronic polarizabilities and their distribution onto the individual interaction sites of our model.[a] To this end, we performed quantum-chemical density functional theory (DFT) calculations of single, atomically resolved $BMIm^+$ and PF_6^- ions in vacuum, since liquid phase calculations would already implicitly include many-body effects. For the calculation of polarizabilities, we employed variational density functional perturbation theory.[252,253] The obtained molecular polarizabilities $\tilde{\boldsymbol{\alpha}}_{\mathrm{mol}}$ are tensorial quantities. According to ref. 254, the isotropic molecular polarizability $\alpha_{\mathrm{mol}} = \frac{1}{3}\,\mathrm{Tr}(\tilde{\boldsymbol{\alpha}}_{\mathrm{mol}})$ scales with the molecular volume $V_{\mathrm{mol}}^{\mathrm{el}}$ of the respective electron "cloud". By determining the partial volumes V_i^{el} of the individual interaction sites according to Laidig and Bader's atoms-in-molecules analysis,[255] we exploit this volumetric correlation to determine isotropic per-site polarizabilities α_i as

$$\alpha_i = \alpha_{\mathrm{mol}} \frac{V_i^{\mathrm{el}}}{V_{\mathrm{mol}}^{\mathrm{el}}} \,. \tag{6.1}$$

Since $V_{\mathrm{mol}}^{\mathrm{el}} = \sum_i V_i^{\mathrm{el}}$, the isotropic molecular polarizability is preserved. This method is also described in more detail in the framework of a general coarse-grained model development strategy.[72] The resulting values of partial volumes and isotropic per-site polarizabilities are listed in table 6.1.

Interaction site	**Polarizability α (Å^3)**
BUT	7.3422
IMI	5.8585
MET	2.0439
PF6	5.1825

Table 6.1: Electronic per-site polarizabilities α obtained from gas-phase DFT calculations.

Now that we obtained the required per-site polarizabilities, we have to decide how to incorporate them in our model. Even though electronic

[a] Note that all DFT calculations (and the extraction of polarizabilities thereof) were performed by Frank Uhlig.

polarizability can generally lead to the induction of electric multipoles, its treatment in polarizable MD simulations is usually restricted to inducible dipoles. The most widely used methods to include polarizability in MD simulations are fluctuating charges, inducible point dipoles, or Drude oscillators (see ref. 256 for a detailed review of the topic). The fluctuating charge model, where partial charges are redistributed within molecules in response to the local electric field, is not applicable here. The redistribution of charges in planar molecules only allows for in-plane polarization, which is incorrect for the coarse-grained three-site representation of the $BMIm^+$ cation. Even more importantly, for species represented only by a single point charge such as monoatomic ions or, in this case, the coarse-grained PF_6^- anion, inducing a dipole moment with this approach is simply impossible. In the inducible point dipoles method, interaction sites possess point dipoles in addition to their point charges. During the simulation, the strength and orientation of these dipoles has to be determined self-consistently according to their respective polarizabilities in response to the local electric field. However, this requires an electrostatics solver capable of computing charge-dipole and dipole-dipole interactions. For this work, we therefore opted for the third method. Instead of point dipoles, this method adds Drude oscillators to the interaction sites. A Drude oscillator, also referred to as "charges on a spring", consists of two particles carrying point charges $+q_\mathrm{d}$ and $-q_\mathrm{d}$ and interacting via a harmonic potential

$$V_\mathrm{d}\left(r_\mathrm{d}\right) = \frac{1}{2} k_\mathrm{d} r_\mathrm{d}^2 \,, \tag{6.2}$$

where r_d denotes the relative displacement of the particles. The force constant k_d is related to the respective isotropic per-site polarizability α by

$$k_\mathrm{d} = \frac{q_\mathrm{d}^2}{\alpha} \,. \tag{6.3}$$

In principle, k_d should be chosen as high as numerical limits allow, since this minimizes the average displacement r_d and lets the Drude oscillator approach the limit of a point dipole. However, if the position

of Drude particles is propagated by Newton's equations of motion, this imposes strict limits on the simulation time step, and therefore on the entire time scale accessible to the simulation. This means that for any given polarizability α, one has to choose a suitable value for k_d (or for q_d, depending on the implementation). Here, we choose a value of $k_\mathrm{d} = 4184\,\mathrm{kJ/mol/\AA^2}$ since this value has been proven to yield both accurate results and reliable numerical stability in other polarizable force fields before.[257–259] In an actual implementation, instead of adding two Drude particles to each interaction site, the charge of one of the particles is added to the partial charge of the interaction site, and the remaining Drude particle is attached to the site via the harmonic potential V_d according to eq. (6.2). We assign the negative charge $-q_\mathrm{d}$ to the Drude particle, so that the resulting charge q_c of an interaction site with partial charge q is given as $q_\mathrm{c} = q + q_\mathrm{d}$. The subscript c stands for "core", and we will use this term to distinguish between bare interaction sites (*i.e.*, cores) and their corresponding Drude particles in the remainder of the manuscript.

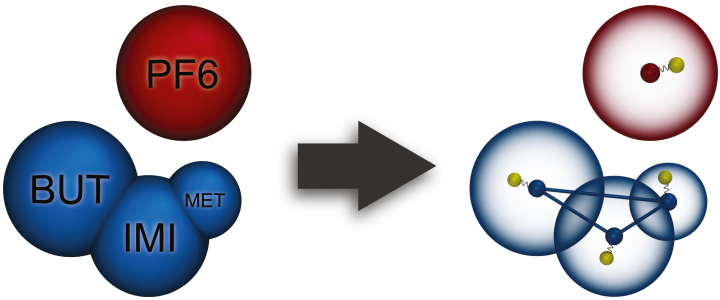

Figure 6.2: Illustration of the ILMpol model development. We use the geometry of the ILM1 model (left) and couple Drude particles to the interaction sites (right). Drude particles are depicted as small yellow beads connected to the bare interaction sites ("cores", small blue and red beads) by springs. The displacement of Drude particles from the corresponding cores is strongly exaggerated for illustration purposes. Intramolecular bonds in the cation are depicted as blue lines between cores. For technical reasons, we added a third bond between the BUT and MET interaction sites (see section 6.1.2 for a detailed explanation).

The general form of the potential energy U_{pot} of the force field is given as

$$U_{\mathrm{pot}} = U_{\mathrm{bond}} + U_{\mathrm{LJ}} + U_{\mathrm{elec}} + U_{\mathrm{self}} \,. \tag{6.4}$$

The first term on the right hand side represents intramolecular contributions from bonds, angles, and dihedrals. Since our model is completely rigid, it effectively does not require any bonded terms, and thus, $U_{\mathrm{bond}} \equiv 0$. The second term describes the contribution of short-range van-der-Waals interactions approximated by the common "12–6" LJ potential of the form

$$U_{\mathrm{LJ}} = \sum_i \sum_{j>i} 4\varepsilon_{ij}^{\mathrm{LJ}} \left[\left(\frac{\sigma_{ij}^{\mathrm{LJ}}}{|\boldsymbol{r}_j - \boldsymbol{r}_i|} \right)^{12} - \left(\frac{\sigma_{ij}^{\mathrm{LJ}}}{|\boldsymbol{r}_j - \boldsymbol{r}_i|} \right)^{6} \right] \tag{6.5}$$

where the double sum runs over all unique pairs of core interaction sites (i, j), $i < j$ in the system with corresponding positions $(\boldsymbol{r}_i, \boldsymbol{r}_j)$. Note, however, that in the ILMpol model intramolecular LJ interactions are excluded from eq. (6.5), and the same applies to the original ILM1 and ILM2 models. The parameters $\varepsilon_{ij}^{\mathrm{LJ}}$ and $\sigma_{ij}^{\mathrm{LJ}}$ correspond to the depth of the potential well and the equilibrium distance, respectively. The third term in eq. (6.4) incorporates all electrostatic interactions between charges of different (!) interaction sites, accounting for core-core, core-Drude, and Drude-Drude interactions. It is given as

$$\begin{aligned} U_{\mathrm{elec}} = & \frac{1}{4\pi\varepsilon_0} \sum_i \sum_{j>i} \left(\frac{q_{\mathrm{c},i} q_{\mathrm{c},j}}{|\boldsymbol{r}_{\mathrm{c},j} - \boldsymbol{r}_{\mathrm{c},i}|} + \frac{q_{\mathrm{c},i} q_{\mathrm{d},j}}{|\boldsymbol{r}_{\mathrm{d},j} - \boldsymbol{r}_{\mathrm{c},i}|} \right. \\ & \left. + \frac{q_{\mathrm{d},i} q_{\mathrm{c},j}}{|\boldsymbol{r}_{\mathrm{c},j} - \boldsymbol{r}_{\mathrm{d},i}|} + \frac{q_{\mathrm{d},i} q_{\mathrm{d},j}}{|\boldsymbol{r}_{\mathrm{d},j} - \boldsymbol{r}_{\mathrm{d},i}|} \right), \end{aligned} \tag{6.6}$$

where ε_0 is the permittivity of free space, and the double sum again runs over all unique pairs (i, j), $i < j$ of interaction sites. Charges and positions are denoted as q and $\boldsymbol{r}$, respectively, and the subscripts c and d are used to discriminate between corresponding core and Drude particles. Unfortunately, incorporating electronic polarizability bears the possibility of a so-called *polarization catastrophe*.[260] This

phenomenon occurs also for Drude oscillators when they are spatially too close, causing their interaction energy to diverge.[261] Polarization catastrophes are therefore most likely to occur between neighboring sites within the same molecule. They can be avoided by introducing an artificial damping term to the electrostatic interactions between Drude oscillators[262] which is usually referred to as Thole screening.[260] The electrostatic interaction energy between the core and Drude particles of two sites i and j with corresponding polarizabilities α_i and α_j then reads

$$U_{\text{Thole}} = \frac{q_{\{\text{c,d}\},i}\, q_{\{\text{c,d}\},j}}{4\pi\varepsilon_0 \left|\boldsymbol{r}_{\{\text{c,d}\},j} - \boldsymbol{r}_{\{\text{c,d}\},i}\right|} \left[1 + \left(\frac{\tilde{r}_{ij}}{2}\right) \exp\left(-\tilde{r}_{ij}\right)\right] \tag{6.7}$$

$$\text{with } \tilde{r}_{ij} = a \frac{\left|\boldsymbol{r}_{\{\text{c,d}\},j} - \boldsymbol{r}_{\{\text{c,d}\},i}\right|}{\left(\alpha_i \alpha_j\right)^{\frac{1}{6}}}, \tag{6.8}$$

where the notation $\{c, d\}$ indicates that all inter-site combinations of core-core, core-Drude, and Drude-Drude interactions are affected. The constant a is an empirical parameter we set to $a = 2.0$, as this value has been used successfully before.[230] Consequently, for intramolecular interactions, the last term of eq. (6.6) is replaced by this damped interaction. Finally, the last addend in eq. (6.4) accounts for the interaction of cores with their corresponding Drude particles within the same interaction site according to eq. (6.2):

$$U_{\text{self}} = \sum_i \frac{1}{2} k_{\text{d}} \left|\boldsymbol{r}_{\text{d},i} - \boldsymbol{r}_{\text{c},i}\right|^2 \tag{6.9}$$

Unfortunately, simply adding Drude particles to a non-polarizable model does not directly yield a correct polarizable force field, so we had to re-parametrize the intermolecular potentials. Using reduced charges in an explicitly polarizable model is hard to justify, since this would mean to account for electronic polarizability twice. Furthermore, due to the issues with charge-reduced models discussed in the introduction, we deliberatly refrain from such practice. Therefore,

as already mentioned above, we develop the ILMpol force field based on the ILM1 model, where no charge reduction had been performed. We successively match our force field to experimental data in terms of density and translational diffusion coefficient by adjusting the LJ interaction parameters. Since the additional dipolar interaction of the Drude oscillators does not fully counteract the strong Coulomb forces excerted by the full partial charges, the depth of the LJ potentials $\varepsilon^{\mathrm{LJ}}$ has to be rescaled accordingly. However, the required scaling factors depend on the particular polarizability α_i of the individual interaction sites. To account for this, we employ the polarizability-dependent scaling method proposed in ref. 263, where the LJ parameter $\varepsilon_i^{\mathrm{LJ}}$ of each interacion site is adjusted according to

$$\varepsilon_{i,\mathrm{scaled}}^{\mathrm{LJ}} = \varepsilon_i^{\mathrm{LJ}} \frac{\lambda\,\alpha_{\max} + \Delta\alpha_i}{\alpha_{\max} + \lambda\,\Delta\alpha_i}\,, \tag{6.10}$$

where $\alpha_{\max}$ is the largest per-site polarizability (here: $\alpha_{\max} = \alpha_{\mathrm{BUT}}$), and $\Delta\alpha_i = \alpha_{\max} - \alpha_i$. The parameter λ can then be used to fit the model against experimental data. For the particle diameters σ_i^{LJ} such a technique is not justified, since they account for the strength and extent of the Pauli repulsion, which has no direct relation to electronic polarizability. Thus, the σ^{LJ} parameters are adjusted by a uniform factor.

6.1.2 Computational details

All gas-phase DFT calculations were performed with the CP2K[264] software, using aug-TZV2P basis sets[265] and an auxiliary plane-wave basis set with a kinetic energy cut-off of 400 Ry together with the revPBE functional.[266] The atomically resolved molecular structures entering the DFT calculations were generated from the widely used CL&P force field,[223] which we validated against ab initio molecular dynamics calculations before, where the decoupling of electrostatic interactions between periodic inmages was performed using density-derived atomic point charges.[267]

For the MD simulations, we used a modified version of the software package GROMACS 2016.3.[105–111] For the simulations reported in,[45,240] Roy *et al.* used the software package DL_POLY_2,[268] and rigid body equations of motion were employed to retain the geometry of the $BMIm^+$ cation. The way constraints on the melocular geometry are handled in GROMACS is somewhat different, though, since it does not provide methods for the integration of rigid body equations of motion. Instead, it employs constraint solvers to account for fixed bond lengths and angles. We employ the LINCS algorithm[184,269] with an additional bond between the BUT and MET interaction sites to constrain the BUT-IMI-MET angle as illustrated in fig. 6.2. In every time step of a simulation, GROMACS first integrates the equations of motion of the *unconstrained* system, and corrects molecular geometries afterwards by applying the constraint solver. For the simulation of a coarse-grained model, where the integration time step can be chosen comparatively large, this has important consequences: Due to the large time step, the relative positions of a molecule's interaction sites may deviate significantly from its true geometry after an unconstrained step, and the corrections performed by the constraint solver are therefore relatively large. The constraint solver, however, only has information concerning the molecular geometry, but not about the actual physics of the system. Thus, the resulting relative arrangement of molecules can slightly deviate from the true configuration one would obtain by integrating rigid body equations of motion. In our simulations, such deviations manifested themselves as a small but noticable jitter in the short-time regime of molecular center of mass mean-square displacements (MSDs). We successfully resolved this issue by adding strong harmonic interactions to all bonds of the $BMIm^+$ cation, having the effect that the molecular geometry is preserved with high accuracy during an unconstrained simulation step and the corrections applied by the linear constraint solver become negligible. Due to the above reasons, the bonded parameters of our polarizable ILMpol force field listed in table 6.3 are also applied to the ILM2 model in our simulations. Note that these bonded interactions do *not* contribute to the

potential energy of the system, so that the term U_{bond} in eq. (6.4) remains zero.

All simulations were conducted in the NpT ensemble (unless otherwise stated) at $p = 1\,\text{bar}$ under 3d-periodic boundary conditions with temperature and pressure controlled by a Nosé-Hoover thermostat[82,94,95] and Parrinello-Rahman barostat[96,270] with relaxation times $\tau_T = 2.0\,\text{ps}$ and $\tau_p = 5.0\,\text{ps}$, respectively. The compressibility parameter of the barostat was left at its default value of $4.5 \cdot 10^{-5}\,\text{bar}^{-1}$. Equations of motion were integrated according to a leapfrog scheme[85] with a time step of $\delta t = 5\,\text{fs}$, with the system's center-of-mass motion subtracted every 40 time steps. Short-range van-der-Waals interactions were computed with a real-space cut-off of $r_{\text{vdW}} = 1.6\,\text{nm}$ and the potential shifted to zero at the cut-off. Effective pairwise LJ parameters were determined according to Lorentz-Berthelot combination rules. Long-range corrections were applied for energy and pressure, and neighbor lists were updated at least every 20 time steps according to a Verlet scheme[271] with a buffer tolerance of $0.005\,\text{kJ/mol/ps}$. Short- and long-range electrostatic interactions were computed using the smooth Particle-Mesh Ewald (PME) method[86] with a short-range cutoff of $r_{\text{Coulomb}} = r_{\text{vdW}} = 1.6\,\text{nm}$, an interpolation order of 4, and a relative convergence tolerance of 10^{-5}. In simulations of the ILMpol model, the position of the (massless) Drude particles were determined self-consistently employing a steepest-descent force minimization procedure with an initial step size of $0.01\,\text{nm}$, a residual force tolerance of $F_{\text{max}} = 0.1\,\text{kJ/mol/nm}$ and a maximum number of 20 iterations. Note that throughout all simulations, the self-consistent minimization always converged after less than 20 iterations. In these simulations, the intramolecular electrostatic interactions between Drude particles are screened according to eq. (6.7) with a Thole parameter $a = 2$. Bond lengths were constrained to their equilibrium lengths by means of a sixth-order linear constraint solver (LINCS)[184,269] with a single iteration per time step. Energies were computed in every time step

Site	m	σ^{LJ}	$\varepsilon^{\mathrm{LJ}}$	q_{c}	q_{d}	α
BUT	57.12	5.17	0.824	4.9369	−4.70	7.3422
IMI	67.07	4.50	1.152	4.7608	−4.20	5.8585
MET	15.04	3.50	0.162	2.6823	−2.48	2.0439
PF6	144.96	5.20	2.120	2.9500	−3.95	5.1825

Table 6.2: Non-bonded force field parameters of the ILMpol model. The values in each row correspond to the respective interaction site in the first column. The listed values (units) are: Mass m (u), LJ parameters σ^{LJ} (Å) and $\varepsilon^{\mathrm{LJ}}$ (kJ/mol), charges q_{c} (e) and q_{d} (e) of core and corresponding Drude interaction sites, respectively, and isotropic polarizability α (Å^3). Effective pairwise LJ parameters are determined according to Lorentz-Berthelot combination rules as $\sigma_{ij}^{\mathrm{LJ}} = \frac{1}{2}\left(\sigma_i^{\mathrm{LJ}} + \sigma_j^{\mathrm{LJ}}\right)$ and $\varepsilon_{ij}^{\mathrm{LJ}} = \sqrt{\varepsilon_i^{\mathrm{LJ}}\varepsilon_j^{\mathrm{LJ}}}$. All values given for q_{d} correspond to a coupling constant in the core-Drude potential (6.2) of $k_{\mathrm{d}} = 4184\,\mathrm{kJ/mol/Å^2}$. Intramolecular Thole screening (6.7) is performed with the screening parameter $a = 2.0$.

and written to disk every picosecond along with trajectories of particle positions unless otherwise stated.

During the parametrization process, systems comprising 343 ion pairs (as used previously[45]) were simulated at a temperature of 350 K for 50 ns following an equilibration run of 10 ns. First, the $\varepsilon^{\mathrm{LJ}}$ parameters were successively adjusted to match the experimental translational diffusion coefficients according to eq. (6.10), for which a scaling parameter of $\lambda = 0.3$ yielded the best results. Thereafter, all σ^{LJ} parameters were uniformly scaled to match the experimental density. Since for the latter, a scaling factor of 0.9963 was sufficient, the impact on diffusion coefficients was negligible and no further adjustment of $\varepsilon^{\mathrm{LJ}}$ parameters was necessary. The final parameters of the ILMpol force field are listed in tables 6.2 and 6.3.

For the assessment of the ILMpol force field and its comparison to the ILM2 model, simulations of systems containing 500 ion pairs were conducted at different temperatures ranging from 300 K to 450 K for both models. Equilibration times range from 50 ns (450 K) to 250 ns (300 K) followed by 500 ns production runs (up to 2 μs for the ILM2 model).

Sites	r_0	k_b
BUT–IMI	3.821 297 16	10 000
MET–IMI	2.707 601 89	10 000
BUT–MET	5.569 155 41	10 000

Table 6.3: Bonded force field parameters of the ILMpol and ILM2 models. The first column lists the interaction sites involved in the respective bond. The listed values (units) are: Equilibrium bond lengths r_0 (Å) and corresponding force constants k_b (kJ/mol/Å^2). Interactions are computed according to a harmonic potential of the form $U_\mathrm{bond}(r) = \frac{1}{2}k_\mathrm{b}(r - r_0)^2$. Note that all bonded interactions exist for technical reasons only and do not contribute to potential energy, since bonds are constrained to their equilibrium positions.

6.2 Results and Discussion

In the following, we assess the performance of our newly developed ILMpol force field with respect to its capability to reproduce several thermodynamic quantities, covering both static and dynamic observables. Since the parametrization of the force field was performed exclusively at a temperature of 350 K, the following analyses are carried out at a broader temperature range in order to assess the general applicability of the model. The observables we analyzed cover mass density, radial distribution functions, translational and rotational diffusion coefficients, enthalpy of vaporization, shear viscosity, and electrical conductivity. We compare our results to the charge-reduced, *i.e.*, implicitly polarized, ILM2 model by Roy and Maroncelli[240] and, whenever available, to experimental data, or alternatively, to results from simulations of the all-atom force field (RTIL-FF) by Sambasivarao and Acevedo.[215]

6.2.1 Mass density

Temperature-dependent mass densities obtained from simulations of the ILMpol (red dots) and ILM2 (blue triangles) models are depicted in fig. 6.3 together with fits to experimental data (dashed and dotted lines).[272,273]

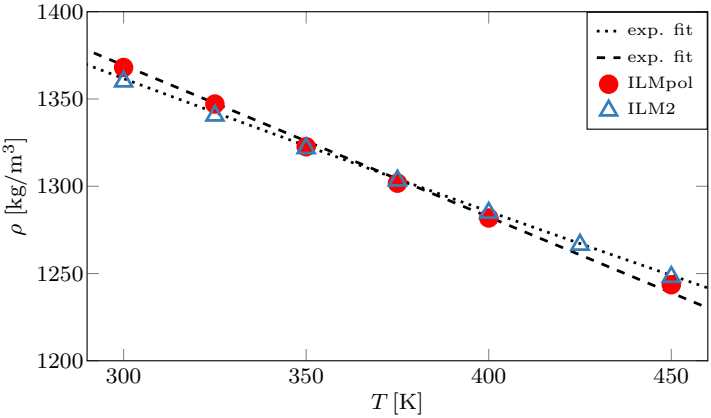

Figure 6.3: Temperature-dependent mass density ρ [kg/m^3] of [BMIm][PF$_6$] for the ILM2 (blue triangles) and ILMpol (red dots) models. Statistical uncertainties are below symbol size. Black dashed and dotted lines are linear fits to experimental data with parameters from Tokuda *et al.*[272] and Machida *et al.*,[273] respectively.

While both models reproduce experimental densities very well, the ILMpol model predicts a slightly stronger temperature dependence than the ILM2 model. Even though for all investigated temperatures the difference is smaller than the discrepancy between experimental measurements, we will see that this small difference bears consequences for the performance of the ILMpol model at low temperatures. Since the mass density provides only very limited insight on the validity of the force field, its correct prediction should rather be considered as a fundamental prerequisite.

6.2.2 Radial distribution functions

In order to investigate the possible impact of explicit polarizability on the internal structure of the IL, we computed center-of-mass radial distribution functions (RDFs) g_{AC}, g_{CC} and g_{AA} between and among anions (A) and cations (C). Figure 6.4 shows RDFs obtained from

simulations of the ILMpol and ILM2 models (blue and red lines, respectively) at $T = 350\,\mathrm{K}$. To get an estimate of how close the internal structures of the coarse-grained models resemble those in an atomistic simulation, we also calculated RDFs from simulations using the full-charge all-atom RTIL-FF (dashed black lines). When comparing the

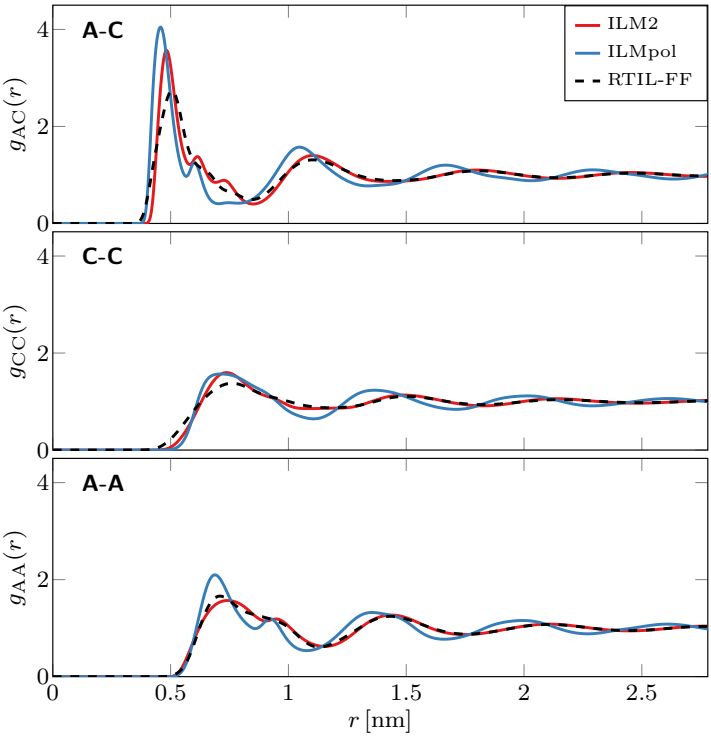

Figure 6.4: Radial center-of-mass distribution functions (RDFs) between anions and cations (A-C, top panel) and among cations (C-C, second panel) as well as among anions (A-A, bottom panel) at $T = 350\,\mathrm{K}$. Blue lines represent RDFs obtained from simulations of the ILMpol model, whereas red lines are results from the ILM2 force field. RDFs obtained from all-atom simulations using the full-charge RTIL-FF[215] are shown for comparison and are indicated by black dashed lines.

different $g_{AC}(r)$ RDFs (top panel), the first and most obvious observation is that compared to the all-atom RDF, the amplitudes of the first

peaks are much higher in case of the coarse-grained models. This is a typical coarse-graining effect originating from the concentration of charges onto fewer interaction sites combined with the rigidity of the models, which is also responsible for the small sidelobes which are smeared-out in the atomistic RDF. The larger amplitude of the ILMpol model's first peak in $g_{\mathrm{AC}}(r)$ compared to the ILM2 model is likely due to its full charges, since the inducible dipole interactions cannot fully screen the electrostatic forces at short distance. Radial distribution functions are related to the distance-dependent potential of mean force $w_{XY}(r)$ between pairs of the considered species (X, Y) according to $g_{XY}(r) = \exp(-w_{XY}/(k_{\mathrm{B}}T))$. The higher first peak in $g_{AC}(r)$ therefore indicates that ion pairs exhibit a stronger direct interaction in the ILMpol force field compared to the ILM2 model. However, the difference in depth of the respective potentials of mean force amounts to as little as $\approx 0.1\, k_{\mathrm{B}}T$, which is rather small. The whole anion-cation RDF of the ILMpol model is slightly shifted to lower distances, but the location of its departure from zero coincides with the the one of the RTIL-FF, and also the relative distances between subsequent peaks seem to be sufficiently well reproduced. The C-C and A-A RDFs show a similar shift as well as a slightly higher first peak in $g_{\mathrm{AA}}(r)$. Overall, since we are dealing with a coarse-grained model, we consider the differences in the RDFs between the models as acceptable.

6.2.3 Enthalpy of vaporization

As discussed in the description of the force field parametrization, the incorporation of explicit electronic polarizability into a pre-existing force field required a quite significant scaling of the interaction parameters. In order to investigate possible differences in energetics in the bulk and the gas phase between the implicitly polarized ILM2 and the explicitly polarizable ILMpol models, we computed temperature-dependent enthalpies of vaporization from corresponding gas- and liquid-phase simulations according to ref. 274. The enthalpy of

vaporization $\Delta H_{\mathrm{vap}}(T)$ at a given temperature T is defined as the difference of the enthalpies $H^{\mathrm{gas}}(T)$ in the gas and $H^{\mathrm{liq}}(T)$ in the the liquid phase. It corresponds to the energy required to transform a certain quantity of a liquid substance into a gas. In the gas phase, aprotic ILs are known to predominantly exist as ion pairs.[275] Here, we therefore compute the enthalpies of vaporization *per ion pair*. The enthalpies in the gas or liquid phase are defined as the sum of the corresponding system's total internal energy $\langle E_{\mathrm{tot}} \rangle$ and the work $p\langle V \rangle$ that has to be done against the ambient pressure p. By virtue of the equipartition theorem, the average kinetic energies $\langle E_{\mathrm{kin}} \rangle$ per ion pair are the same in the liquid and the gas phase at the same temperature T, so that the enthalpy of vaporization per ion pair can be written as

$$\Delta H_{\mathrm{vap}} = \langle E_{\mathrm{pot}}^{\mathrm{gas}} \rangle - \langle E_{\mathrm{pot}}^{\mathrm{liq}} \rangle + p \left(\langle V^{\mathrm{gas}} \rangle - \langle V^{\mathrm{liq}} \rangle \right) \tag{6.11}$$

with the average potential energies per ion pair $\langle E_{\mathrm{pot}}^{\mathrm{gas}} \rangle$ and $\langle E_{\mathrm{pot}}^{\mathrm{liq}} \rangle$ in the gas and liquid phase, respectively. Assuming $\langle V^{\mathrm{gas}} \rangle \gg \langle V^{\mathrm{liq}} \rangle$ and using the ideal gas approximation $pV^{\mathrm{gas}} = k_{\mathrm{B}}T$, one obtains

$$\Delta H_{\mathrm{vap}}\,(T) = k_{\mathrm{B}}T + \langle E_{\mathrm{pot}}^{\mathrm{gas}} \rangle (T) - \langle E_{\mathrm{pot}}^{\mathrm{liq}} \rangle (T)\,, \tag{6.12}$$

where k_{B} is the Boltzmann constant and T the temperature of the simulated system. For the gas phase calculations, a single ion pair was placed in a cubic box with an edge length much larger than the short-range interaction cut-off. Simulations were carried out in the NVT ensemble, where temperature was controlled by a velocity rescaling thermostat including a stochastic term.[276] The change of thermostat is motivated by the fact that the Nosé-Hoover thermostat may fail to reproduce the correct thermodynamic ensemble in systems with few degrees of freedom.[277,278] The system's translational center-of-mass motion was subtracted in every time step to obtain a correct canonical phase space sampling. Long-range dispersion corrections for energy and pressure were switched off and only short-range electrostatic interactions were taken into account. Since we want to compare the models "as is", energy corrections due to different polarization in the gas and liquid phase[112] have not been included for the ILM2 model.

Note that for all investigated temperatures, there exists a discrepancy of approximately $2\,k_\mathrm{B}T$ between our values of ΔH_vap obtained for the ILM2 model and those reported in.[240] The deviations are due to a slightly inaccurate thermalization of the gas-phase ion pair caused by the Nosé-Hoover thermostat without center-of-mass motion removal[b] in the simulations of.[240]

The results obtained from simulations of the ILM2 and ILMpol model at temperatures ranging from 300 K to 450 K are depicted in fig. 6.5 along with experimental data and results from the all-atom RTIL-FF. Apparently, the ILM2 model seems to reproduce experimental data

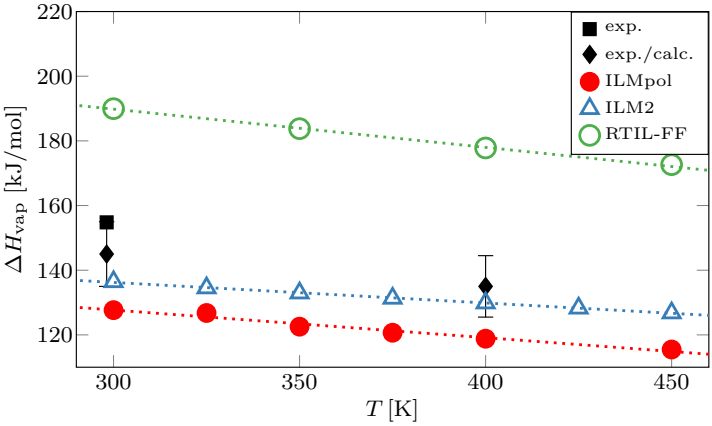

Figure 6.5: Enthalpy of vaporization for the ILMpol model (red dots). Data obtained from simulations of the ILM2 model are shown for comparison (blue triangles). Experimental data from Zaitsau *et al.*[279] and values calculated by Paulechka *et al.*[280] are indicated by a black square and diamond symbols, respectively. Since experimental data are rather sparse, results from all-atom simulations employing the RTIL-FF (green circles) are shown in addition. Uncertainties in the simulation results are in the order of the symbol size and therefore not shown. The dotted lines are linear fits to the corresponding results.

quite well, while the results of the ILMpol model lie about 7 kJ/mol (5%) below. The dependences on temperature of the coarse-grained models

[b] information from private correspondence with Mark Maroncelli and Durba Roy

Model		E_{LJ}	E_C	E_P	E_{pot}
ILM2	E^{gas}	1	−176		−175
	E^{liq}	−55	−250		−305
	ΔE	56	74		130
	$\Delta E/\Delta E_{pot}$	43 %	57 %		100 %
ILMpol	E^{gas}	25	−395	42	−328
	E^{liq}	−11	−453	13	−451
	ΔE	36	58	29	123
	$\Delta E/\Delta E_{pot}$	29 %	48 %	23 %	100 %

Table 6.4: Different contributions to the potential energies per ion pair of the ILM2 and ILMpol models in the liquid (E^{liq}_{pot}) and in the gas phase (E^{gas}_{pot}) at $T = 350\,K$. Listed contributions are Lennard-Jones (E_{LJ}), Coulomb (E_C), and polarization (E_P) energies. Energies are given in kJ/mol and rounded to the nearest integer.

are almost identical, whereas the all-atom RTIL-FF yields much larger values and exhibits a slightly more negative slope. However, the comparison to the experiment has to be taken with a grain of salt since the values indicated by black diamonds were obtained from a combination of experimental data and theoretical estimates (see[280] for details) and error bars are rather large. Nevertheless, we use the opportunity to investigate the origin of the observed differences in ΔH_{vap} between the ILM2 and ILMpol models by examining the contributions of different energy components, which are listed in table 6.4 for $T = 350\,K$. In the case of the ILM2 model, due to its rescaled charges, the contribution of the Coulomb energy ΔE_C to the difference $\Delta E_{pot} = E^{gas}_{pot} - E^{liq}_{pot}$ is comparatively large (57 %), whereas for the ILMpol model, ΔE_C accounts for 48 % only. Also the contribution of the Lennard-Jones interaction energy ΔE_{LJ} to ΔE_{pot} is comparatively small for the ILMpol model (29 % vs 43 %). The large remaining part is therefore due to the high polarization energy in the gas state, which accounts for 23 % of the change in configurational energy. This observation is typical for ILs in general, since their polarization in the gas phase is known to be larger[72] than in the condensed state.[237,238,281] Naturally, the implicitly polarized ILM2 model cannot reproduce this behavior by design.

6.2.4 Translational diffusion coefficients

To study the dynamics of our model, we calculated temperature-dependent translational diffusion coefficients D of the $BMIm^+$ cation and PF_6^- anion according to the Einstein relation

$$\lim_{t\to\infty} \left\langle \Delta \boldsymbol{r}_{\mathrm{com}}^2(t) \right\rangle = 6Dt + \mathrm{const} \tag{6.13}$$

from linear regressions of the molecular center-of-mass mean square displacements

$$\left\langle \Delta \boldsymbol{r}_{\mathrm{com}}^2(t) \right\rangle = \left\langle \left[\boldsymbol{r}_{\mathrm{com}}(t) - \boldsymbol{r}_{\mathrm{com}}(0) \right]^2 \right\rangle \tag{6.14}$$

with time-dependent center-of-mass positions $\boldsymbol{r}_{\mathrm{com}}(t)$ and the average $\langle\cdot\rangle$ taken over all time origins and molecules of the considered species in the system. Figure 6.6 shows a comparison of the results obtained from simulations of the ILMpol and ILM2 models to experimental data.[272] Both models reproduce the experimental trend for temperatures above 350 K very well. The order between cation and anion diffusion coefficients (as measured experimentally) is flipped in the case of the ILMpol model at temperatures $T \geq 400\,\mathrm{K}$. Nevertheless, the values lie within the experimental error estimate. At lower temperatures, the diffusion coefficients obtained from the ILM2 model lie slightly below the experiment, but still within the error. Unfortunately, the ILMpol model exhibited potentially glass-like behavior for temperatures of 325 K and 300 K since they showed a slow but constant negative drift in potential energy. The corresponding data are therefore omitted since the model can be considered as strictly valid only for temperatures $T \geq 350\,\mathrm{K}$. Glassy behavior has also been observed for other IL models at temperatures around 300 K before,[285,286] and coarse-grained models are generally likely to overestimate freezing points due to their reduced degrees of freedom. Coarse-grained simulations of pure ILs are often performed at elevated temperatures of about 400 K,[243,244,247,249,286–288] so that this deficiency of the ILMpol model should not be of practical relevance. Moreover, our intention is

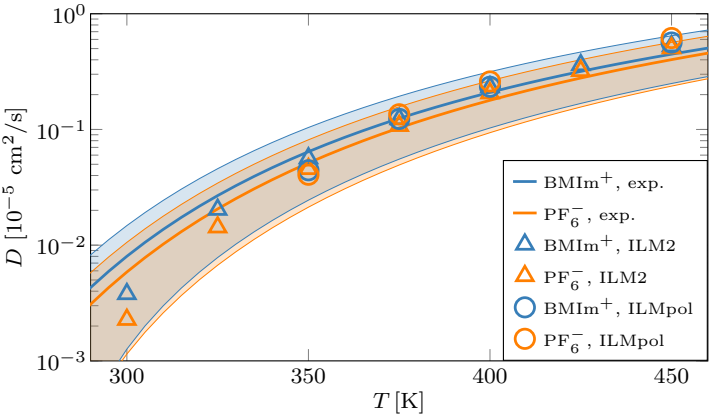

Figure 6.6: Temperature-dependent translational self-diffusion coefficients D [10^{-5} cm^2/s] for BMIm$^+$ (blue symbols) and PF$_6^-$ (orange symbols). Results obtained from simulations of the ILMpol model are depicted as circles, and corresponding results of the ILM2 model are shown as triangles. Statistical errors of the simulation data are within symbol size. Solid lines in corresponding colors are fits of the Vogel-Fulcher-Tamman (VFT) equation[282–284] for diffusion, which is of the form $D = D_0 \exp[-b/(T - T_0)]$, to experimental data. Transparent areas in corresponding colors indicate the uncertainties of the fits. Fit parameters and error estimates are taken from.[272]

to use the model to study polarization effects in solutions in the future, where the low-temperature behavior of the pure IL might be of minor importance.

6.2.5 Rotational diffusion coefficients

We further compare the dynamics of the two models in terms of rotational diffusion coefficients of the BMIm$^+$ cation about its principal axes of inertia. The axes correnspond to the definition in,[45,240] where the index x denotes the out-of-plane axis, z represents the axis with the lowest moment of inertia, and the index y is the remaining axis perpendicular to the others. Rotational diffusion coefficients D_i, $i \in \{x, y, z\}$ were computed from integrals of the corresponding angular velocity

autocorrelation functions according to

$$D_i = \lim_{t\to\infty} \int_0^t \langle \omega_i(0)\, \omega_i(\tau) \rangle \, \mathrm{d}\tau \,, \tag{6.15}$$

where the angular velocities ω_i were determined from projections of the cation's total angular velocity $\boldsymbol{\omega}$ onto the respective axes of inertia. Autocorrelations of the angular velocities about the principal axes of all cations in the system were computed with a temporal resolution of 5 fs (1 simulation time step) over a period of more than 40 ns (2^{23} time steps) and averaged before evaluating the integral according to eq. (6.15). The resulting diffusion coefficients are shown in fig. 6.7. Since the diffusion coeffients D_x and D_y almost conicide regardless of temperature, the latter is ommited for clarity. While the rotation-

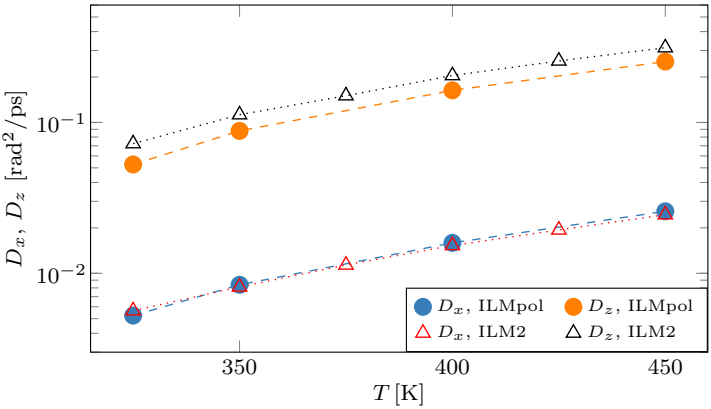

Figure 6.7: Temperature-dependent rotational diffusion coefficients about the principal axes of inertia of the $BMIm^+$ cation obtained from simulations of the ILM2 (red and black triangles) and ILMpol model (blue and orange dots). Diffusion coefficients of rotations about the y-axis coincide with those about the x-axis and are omitted for clarity.

al dynamics of both models about the "slow axes" x and y perfectly coincide for both the ILM2 and ILMpol model, the fast rotation about the z-axis is slightly slowed down in case of the ILMpol model. This

indicates a subtle stabilization of rotational dynamics both due to the stronger Coulomb interactions and the additional dipolar interactions. Surprisingly, the glassy behavior observed at low temperatures had no influence on rotational dynamics.

6.2.6 Shear viscosity

In contrast to all other observables, viscosities were calculated from simulations in the NVT ensemble with box volumes V set to the average volumes of corresponding NpT simulations. The shear viscosity η was then determined from autocorrelations of the fluctating pressure tensor's off-diagonal elements $P_{\alpha\beta}$[81] according to

$$\eta(T) = \frac{V}{k_\mathrm{B}T} \lim_{t\to\infty} \int_0^t \langle P_{\alpha\beta}(0) P_{\alpha\beta}(\tau) \rangle \, \mathrm{d}\tau \tag{6.16}$$

and is depicted in fig. 6.8 for both the ILMpol and ILM2 model. The results from both force fields very much conicide for temperatures down to 350 K and follow the experimental trend quite well. Again, as it was the case for translational diffusion coefficients, data for lower temperatures are not shown.

6.2.7 Electrical conductivity

Bearing in mind the potential use of ILs as a replacement for (or as additives to) conventional electrolytes in energy storage applications, the correct prediction of their electrical conductivity from simulations is important. In dilute electrolyte solutions where ion pairing may be of minor importance, it is often possible to estimate the electrical conductivities from the translational diffusion coefficients of cations and anions. In pure ILs, however, the motions of different ionic species are highly correlated. We therefore calculated electrical conductivities by means of the so-called "Einstein-Helfand" method,[98,289] where such

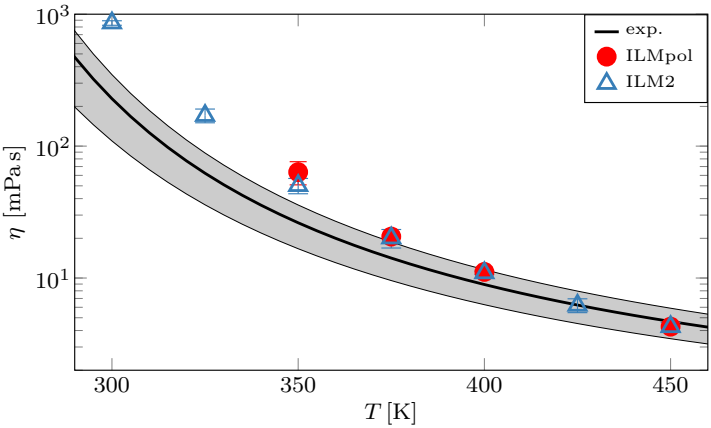

Figure 6.8: Shear viscosity for the ILMpol model (red dots). Data obtained from simulations of the ILM2 model are shown for comparison (blue triangles). The solid black line is a fit of the form $\eta = \eta_0 \exp[-b/(T - T_0)]$ to experimental data. The transparent gray area indicates the uncertainty of the fit. Fit parameters and error estimates are taken from.[272]

correlation effects are taken into account. This method exploits the relation of the electrical conductivity σ to the MSD of the itinerant dipole moment's translational component $\boldsymbol{M}_{\text{trans}}$ in the long-time limit, which is given as

$$\lim_{t\to\infty} \left\langle \Delta \boldsymbol{M}_{\text{trans}}(t)^2 \right\rangle = 2 \left\langle \boldsymbol{M}_{\text{trans}}^2 \right\rangle + 6V k_{\text{B}} T \, \sigma \, t \,. \tag{6.17}$$

The electrical conductivity is then determined from a linear least-squares regression to the long-term linear regime of $\left\langle \Delta \boldsymbol{M}_{\text{trans}}(t)^2 \right\rangle$. In simulations with periodic boundary conditions, however, a direct measurement of $\boldsymbol{M}_{\text{trans}}$ is not possible.[98,180] Instead, we directly compute its MSD from autocorrelations of the fluctuating cumulative

translational current $\boldsymbol{J}_{\text{trans}}$ as

$$\left\langle \Delta \boldsymbol{M}_{\text{tot}}(t)^2 \right\rangle = 2t \int_0^t \langle \boldsymbol{J}_{\text{trans}}(0) \boldsymbol{J}_{\text{trans}}(\tau) \rangle \, d\tau - 2 \int_0^t \tau \, \langle \boldsymbol{J}_{\text{trans}}(0) \boldsymbol{J}_{\text{trans}}(\tau) \rangle \, d\tau \,. \tag{6.18}$$

Cumulative currents were computed during runtime according to $\boldsymbol{J}_{\text{trans}} = \sum_i q_i \boldsymbol{v}_{\text{com},i}$, where the index i runs over all molecules in the system, and q_i and $\boldsymbol{v}_{\text{com},i}$ represent the corresponding molecular net charge and center-of-mass velocity, respectively. For the calculations of the correlation functions, the reduced charges of the ILM2 model were scaled up to unity. In the case of the ILMpol model, conductivities were calculated only for four different temperatures due to the long required simulation times of more than 1 μs. The obtained values are shown in fig. 6.9 together with a fit to experimental data.[272] While both

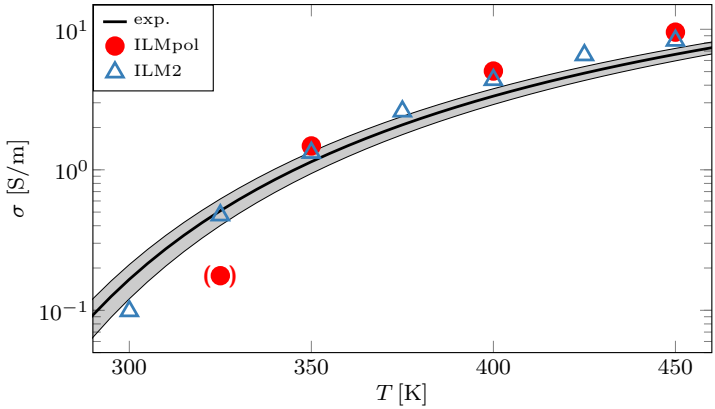

Figure 6.9: Electrical conductivities for the ILMpol (red dots) and ILM2 model (blue triangles). The black line is a fit to experimental data of Tokuda *et al.*.[272] The gray area indicates the uncertainty of the fit.

models reproduce the experimental trend, they slightly overestimate

experimental values. Except for the measurement of the ILMpol model at 325 K, the discrepancy is very small for all investigated temperatures.

6.3 Conclusion and Outlook

Starting from a coarse-grained force field that contained the effects of polarization only implicitly through charge scaling, we developed an explictly dipole-polarizable model for the ionic liquid [BMIm][PF_6] and assessed its capabilities to predict typical static and dynamic quantities investigated in molecular simulations. Our results demonstrate its applicability in simulations of pure ionic liquids in a typically relevant temperature range. With respect to implicitly polarized models, we expect our force field to be an improvement in terms of transferability, and expect a superior performance in situations where the incorporation of explicit electronic polarizability might be crucial. We think here about cases where the ionic liquid experiences interfaces of different dielectric nature, like a metal electrode or a vapor interface. Moreover, ILs in mixtures and with highly charged inclusions might benefit from the explicit treatment of polarization. Furthermore, another benefit of the coarse-grained nature of our model is that we are able to distinguish the effects of polarization from other effects, by being able to turn the explicit dipole-polarization on or off. The low computational complexity of our model will enable us to make larger parameter studies in this respect which will be the topic of future investigations.

7 Ionic Screening in Bulk and under Confinement

Note: Parts of the contents of this chapter have been previously published in similar form as

J. Zeman, S. Kondrat and C. Holm, Bulk ionic screening lengths from extremely large-scale molecular dynamics simulations, *Chemical Communications* **56**, 15635–15638 (2020)

under a Creative Commons CC-BY-NC license, and further parts have been reproduced from

J. Zeman, S. Kondrat and C. Holm, Ionic screening in bulk and under confinement, *The Journal of Chemical Physics* **155**, 204501 (2021).

with the permission of AIP Publishing.

During the past decades, room-temperature ionic liquids (ILs) have gained an increasingly important role in science and technology, with applications ranging from organic synthesis, catalysis, and analytical chemistry to energy storage devices such as electrochemical batteries or supercapacitors.[212–214,290] Due to the vast number of cationic and anionic species, solvents, or additives available for combination, the physicochemical properties of pure ILs and IL-based solutions are highly tunable.[152,214,291–293] The prediction and targeted adjustment of these properties require a fundamental understanding of the intra- and intermolecular mechanisms governing the internal structure and dynamics of the investigated substances.

Recent experiments have shown that the repulsive force between atomically flat, like-charged surfaces confining room-temperature ionic

liquids or concentrated electrolytes exhibits an anomalously large decay length.[46–51] Termed underscreening, this effect was suggested to be a property of bulk electrolytes.[52] However, its exact origin is still under debate so that the experimental measurements constitute an important but not yet understood[53] phenomenon. Understanding the origin of these findings should be especially important for the design of devices where concentrated electrolytes or ILs are strongly confined between highly charged surfaces, as, *e.g.*, in modern supercapacitors.

In the reported surface force balance (SFB) measurements, the electrolyte or IL was confined between two atomically flat, charged surfaces in a cross-cylinder arrangement (see, *e.g.*, ref. 50). The decay length of electrostatic interactions between the surfaces, and thus, across the electrolyte, was obtained from the decay of the distance-dependent force acting between the charged surfaces. Regardless of ionic species and concentrations, the reported force-distance curves exhibited a short-ranged oscillatory decay up to distances of a few nanometers, followed by a long-ranged monotonic exponential decay. In the high-concentration regime, the long-range decay lengths were generally found to increase with electrolyte concentration.[46–51] Since the asymptotic decay of both charge and density correlations around objects immersed in an electrolyte solution is independent of the size of the objects,[59,68] ion-ion interactions within a bulk electrolyte solution should, therefore, exhibit the same asymptotic decay length.

Notwithstanding, in this work, we show by means of large-scale molecular dynamics simulations that the underscreening effect is unlikely to be a feature of bulk electrolytes. Our results yield two screening lengths satisfying distinct scaling relations. However, with an accuracy of $10^{-5}\, k_{\mathrm{B}}T$ in interionic potentials of mean force, we find no signs of underscreening, suggesting that other than bulk effects might be at play in the experiments. Furthermore, we corroborate these findings by expanding our investigations to ionic liquids under confinement. Unlike in bulk systems, where screening lengths are computed from the decay of interionic potentials of mean force (PMFs), we extract

such data in confined systems from cumulative charge distributions. At high concentrations, our simulations show increasing screening lengths with increasing electrolyte concentration, consistent with classical liquid state theories. However, our analyses demonstrate that—also for confined systems—there is no anomalously large screening length. In addition, we show that theoretical models used in the literature to relate the measured screening lengths to other observables are inapplicable to highly concentrated electrolytes.

The traditional view that the electrostatic screening length decreases with increasing electrolyte concentration is well-known to be valid only at low ion concentrations. In the low-concentration regime, the spatial decay of ion-ion interactions is usually well-described by approaches such as the Debye-Hückel theory,[54] or, for the electrostatic screening of immersed charged objects, the Poisson-Boltzmann equation.[55,56] In both cases, the asymptotic decay length of electrostatic interactions equals the Debye length λ_D defined as

$$\lambda_\mathrm{D}^2 = \frac{\varepsilon_0 \varepsilon_r k_\mathrm{B} T}{\sum_i \rho_i z_i^2 e^2} \,. \tag{7.1}$$

Here, ε_0 is the permittivity of free space, ε_r the relative dielectric permittivity of a homogeneous background medium, k_B the Boltzmann constant, and T denotes absolute temperature. In the denominator, ρ_i and z_i represent the number density and valency of ionic species i, and e is the elementary charge. In the limit of infinite dilution, the dielectric permittivity of the background medium equals that of the entire system since it is not altered by the presence of a vanishing amount of free charges.

With rising electrolyte concentration, interactions are increasingly influenced and eventually dominated by excluded-volume and charge correlations, which are difficult to describe by such mean-field approaches. There are many modifications and extensions of the Debye-Hückel and Poisson-Boltzmann theory and other approaches predicting that correlation lengths increase with concentration,[57–69]

therefore resulting in an increasing effective screening length[a]. Especially relevant are integral-equation theories[57–59,64,65] based on descriptions of the radial distribution functions (RDFs) $g_{XY}(r)$, which describe the probability of finding a particle of species Y at a distance r from a particle of species X and is normalized with respect to the corresponding probability in an ideal gas at the same concentration. Within these frameworks, analyses of the Ornstein-Zernike equation show that for sufficiently high concentrations, the asymptotic decay of ion-ion interactions can be expressed as

$$\lim_{r\to\infty} w_{XY}(r) \propto \frac{A}{r}\cos\left(k\,r-\phi\right)\exp\left(-\frac{r}{\lambda_{\mathrm{S}}}\right)\,, \tag{7.2}$$

where w_{XY} denotes the potential of mean force (PMF) between species X and Y, A and ϕ are species-dependent amplitudes and phase shifts, λ_{S} is the PMF's asymptotic decay length, and the wave vector k determines the wavelength of its oscillation. In spatially homogeneous systems, the PMF between species X and Y can be obtained from their RDF according to

$$w_{XY}(r) = -k_{\mathrm{B}}T\ln\left(g_{XY}(r)\right)\,. \tag{7.3}$$

In many theoretical works, eq. (7.2) is applied directly to the correlation functions $h_{XY}(r) := g_{XY}(r) - 1$ under the reasonable assumption that $w_{XY}(r) \ll 1$ for $r \to \infty$, since then, $\ln(g_{XY}(r)) \approx h_{XY}(r)$. However, we will not apply this linearization in our work and, instead, obtain the decay lengths directly from the PMFs. In the limit of high ionic concentrations, λ_{S} increases with concentration and generally exceeds the Debye length λ_{D}.[57] Thus, in principle, the experimentally measured concentration-dependent increase in screening length is expected. However, what is surprising about the experimental observations is that, in contrast to eq. (7.2), the asymptotic decay of surface forces was monotonic and the corresponding decay lengths exceeded theoretical predictions for bulk electrolytes by about an order of

[a] Note that we use the term 'screening length' also for the decay of oscillatory modes.

magnitude. Anomalously large decay lengths have also been indirectly deduced from fluorescence-based concentration measurements in electrolyte solutions confined between silica surfaces[294] and observed in an atomic force microscopy (AFM) experiment[295] (however, there is also an AFM study where large screening lengths were not observed[47]). Regardless of the considered electrolyte, these anomalously large screening lengths (λ_S) followed a cubic scaling with respect to the Debye length λ_D of the form $\lambda_S/\lambda_D \propto (d/\lambda_D)^3$, where d is the effective ion diameter (we note, however, that some SFB experiments[296,297] demonstrated inconsistencies with such a cubic scaling). Lee *et al.*[52,298] interpreted this cubic scaling in terms of charge fluctuations due to defects in a nearly crystalline ionic system, as opposite to dilute electrolytes. However, as noted by Adar *et al.*,[299] this picture is applicable only for electrolyte concentrations above 6 M. In more recent work, Ciach and Patsahan[300] developed a self-consistent field theory and obtained a cubic scaling in the regime of high ion densities. Unlike in the experiments, however, this theoretical cubic scaling appeared in a damped-oscillatory rather than in a monotonic decay of the charge-charge correlation function. Moreover, as estimated by the authors, their calculations are applicable for ion densities $d^3\rho \geq 0.75$, which translates into molar concentrations above 23 mol/l for aqueous sodium chloride (for an average ion diameter $d = 0.3$ nm) and above 5 mol/l for typical ionic liquids (taking $d = 0.5$ nm). However, SFB experiments show that cubic scaling starts even around 1 mol/l, while the solubility limit of NaCl is about 5.3 mol/l and pure room-temperature ionic liquids typically have similar concentrations.[301] The possible existence of ionic interactions exhibiting long-ranged monotonic decays has been shown by Kjellander[66,68] based on dressed ion theory.[302,303] However, we are not aware of applications of this approach to experimental or simulation data of real ionic systems showing cubic scaling or anomalously large screening lengths.

In the following, we aim to gain new physical insights into the long-range behavior of ion interactions in bulk and under confinement using large-scale MD simulations. We consider various systems,

including neat ILs, mixtures of ILs and polar solvents, and concentrated aqueous electrolyte solutions in a broad concentration range and analyze ionic screening lengths and their scaling behavior in details. In addition, we critically review attempts that have been made to connect the measured screening lengths with other experimental observables, seemingly suggesting that underscreening is a bulk property of electrolytes.[52,298]

7.1 Molecular Dynamics Simulations

According to both experimental measurements[51] and theoretical predictions,[57] the enhancement of the asymptotic electrostatic screening length is expected to be most pronounced in pure ILs. Therefore, as a first step, we performed MD Simulations of pure 1-butyl-3-methylimidazolium hexafluorophosphate ($[C_4C_1Im]^+[PF_6]^-$). Our choice was motivated by the fact that there exist well-tested MD force fields for both all-atom and coarse-grained models of this IL. Comparing computational models with different levels of detail will allow us to assess the influence of such molecular details on the resulting asymptotic electrostatic screening length. As a second step, in order to investigate the long-range screening behavior of conventional electrolyte solutions, we performed simulations of aqueous sodium chloride (NaCl) solutions at different concentrations ranging from 1.16 to 5.19 mol/l.

In ref. 51, Smith *et al.* also reported SFB measurements of the IL 1-butyl-1-methylpyrrolidinium bis(trifluoromethylsulfonyl)imide ($[C_4C_1Pyrr]^+[NTf_2]^-$) in propylene carbonate (PC) solutions at different concentrations. To obtain simulation results which are comparable to the experiment, we conducted simulations of systems comprising solutions of 1-butyl-3-methylimidazolium bis(trifluoromethane)-sulfonimide ($[C_4C_1Im]^+[NTf_2]^-$) in a racemic PC mixture (equal amounts of (R)- and (S)-propylene carbonate) with IL mole fractions x covering the range from $x = 0.05$ to $x = 1$ (pure $[C_4C_1Im]^+[NTf_2]^-$). Due to the fact that the chemical structures and, therefore, the sizes of

$[C_4C_1Im]^+$ and $[C_4C_1Pyrr]^+$ are very similar, we likewise expect a very similar behavior of these species in terms of electrostatic screening.

The compositions of all investigated systems are summarized in tables 7.1 and 7.2, and ball-and-stick models together with the corresponding Lewis formulas of all involved molecular species (except for NaCl and water) are depicted in fig. 7.1.

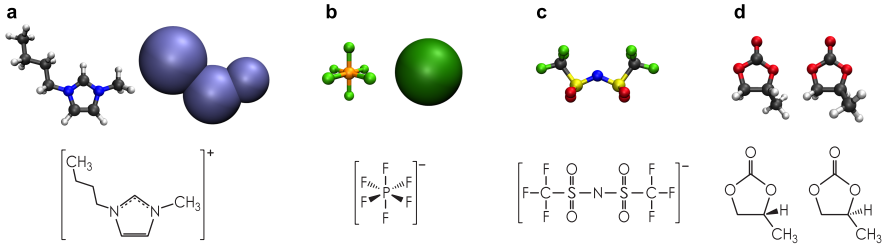

Figure 7.1: Ball-and-stick models (top row, visualized with VMD[304]) and corresponding Lewis formulas (bottom row) of the investigated substances. **a**: 1-butyl-3-methylimidazolium ($[C_4C_1Im]^+$) cation (all-atom (left) and coarse-grained (right)). **b**: Hexafluorophosphate ($[PF_6]^-$) anion (all-atom (left) coarse-grained (right)). **c**: Bis(trifluoromethylsulfonyl)imide ($[NTf_2]^-$) anion. **d**: (R)-propylene carbonate (left) and (S)-propylene carbonate (right).

c (mol/l)	N_{IP}	N_{S}	$\bar{L}$ (nm)	t_{sim} (ns)	t_{eq} (ns)
pure $[C_4C_1Im]^+[PF_6]^-$ (all-atom)					
4.63	108 000	0	33.84	600	300
pure $[C_4C_1Im]^+[PF_6]^-$ (coarse-grained)					
4.78	358 296	0	49.92	700	300
NaCl in water (all-atom)					
4.43	216 000	2 458 296	43.25	200	50
1.16	3750	176 577	17.53	537	50
2.43	3750	81 814	13.68	5369	50
4.86	3750	38 411	10.86	5369	50
5.19	3750	35 625	10.63	5369	50
$[C_4C_1Im]^+[NTf_2]^-$ in PC (all-atom)					
0.00	0	1000	5.19	1074	100
0.53	200	3800	8.54	2147	200
0.97	500	4500	9.51	2147	200
1.63	500	2000	7.99	3221	200
2.10	500	1167	7.34	4295	200
2.47	500	750	6.96	4295	200
2.75	500	500	6.71	4295	200
2.98	500	333	6.53	4295	200
3.17	500	214	6.40	4295	200
3.33	500	125	6.30	4295	200
3.46	500	56	6.21	4295	200
3.58	500	0	6.15	4295	200

Table 7.1: Bulk systems. Listed values: molar ion pair concentration c (mol/l), number of ion pairs N_{IP}, number of solvent molecules N_{S}, average simulation box edge length $\bar{L}$ (nm), total simulation time t_{sim} (ns) after equilibration, and equilibration time t_{eq} (ns). Further details and error estimates can be found in appendix 7.B.1.1.

N_+	N_-	L_z (nm)	t_{sim} (ns)	t_{eq} (ns)
2352	2000	8.246	1000	300
2852	2500	9.902	1000	300
3852	3500	13.200	1000	300
4352	4000	14.837	4×1000	300

Table 7.2: Confined systems. Listed values: number of $[C_4C_1Im]^+$ cations N_+, number of $[NTf_2]^-$ anions N_-, simulation box edge length in the z-direction L_z (nm), total simulation time t_{sim} (ns) after equilibration, and equilibration time t_{eq} (ns). For all systems, the simulation box edge lengths in the x- and y-direction are $L_x = 11.806$ nm and $L_y = 11.928$ nm.

7.1.1 Simulation details

Simulations were performed with a customized version of the GROMACS[105–111] 2016.3 simulation package (2019.4 for the confined system) capable of computing and storing cumulative currents (*cf.* eq. (7.6)) at every integration step. All bulk systems were simulated in the NpT ensemble in cubic boxes with periodic boundary conditions (PBC) in all three dimensions, where temperature and pressure were maintained at $T = 300\,\mathrm{K}$ and $p = 1\,\mathrm{bar}$, respectively. Electrostatic interactions were computed using the smooth particle mesh Ewald method[87] (SPME) with a system-dependent short-range cutoff and a relative accuracy of 10^{-5}. The confined systems were simulated in orthorhombic boxes with PBC in the x- and y-directions only, and the ensemble was changed to NVT after equilibration. Due to the 2d-periodicity of these systems, the SPME method was also used for Lennard-Jones (LJ) interactions,[305] and Ewald summation corrections were applied according to Yeh and Berkowitz.[306]

For simulations of ILs, we employed the 0.8*OPLS-2009IL all-atom force field of Doherty *et al.*,[307] and the ILM2 force field of Roy and Maroncelli[240] for the coarse-grained description of $[C_4C_1Im]^+[PF_6]^-$. These models use ionic charges that are uniformly scaled by a factor of 0.8 and 0.78, respectively, to implicitly account for electronic polarization effects and partial charge transfer that lead to effectively reduced Coulomb interactions in IL systems.[231,235,308] The simplest theoretical explanation for charge scaling can be found in the non-polarizable MDEC (Molecular Dynamics in Electronic Continuum) model of Leontyev and Stuchebrukhov.[309] They use a uniform electronic screening of partial atomic charges to account for the effects of electronic polarization within a mean-field approach. Approaches beyond mean-field theory that derive partial charges from *ab initio* data arrive at very similar rescaled overall ionic charges, albeit with a different distribution of partial charges.[71,72,236–238,310]

For the description of aqueous NaCl, we used the KBFF ion parameters of Weerasinghe and Smith[311] in conjunction with the SPC/E water model.[112] Since in aqueous NaCl systems, the ion polarizabilities and their concentrations are much smaller than for molecular ILs, the respective ion models use full charges of $\pm 1\,e$. In simulations of $[C_4C_1Im]^+\,[NTf_2]^-$ in PC solution, the solvent was described according to parameters provided by Takeuchi *et al.*.[312] For the carbon atoms forming the graphene walls of the confined systems, we employed the same LJ parameters as for those in the imidazolium ring of $[C_4C_1Im]^+$. The parameter sets of all simulations are listed in appendix 7.D.

7.1.2 Analysis methods

7.1.2.1 Potential of mean force

The evaluation of the PMF $w_{XY}(r)$ between ionic species X and Y using eq. (7.3) requires the knowledge of the corresponding RDF $g_{XY}(r)$. In homogeneous systems, the latter is formally defined as

$$g_{XY}(r) = \frac{\langle \rho_{XY}(r) \rangle}{\langle \rho_Y \rangle}\,, \tag{7.4}$$

where $\langle \rho_{XY}(r) \rangle$ denotes the expected density of particles of species Y residing on shells of radius r centered at any particle of species X, and $\langle \rho_Y \rangle$ is the expected density of particles of species Y averaged over the entire system, *i.e.*, their bulk density. Since the computation of RDFs with analysis tools included in the GROMACS package would have taken several years for the large-scale IL systems considered, we developed an optimized analysis tool based on the MDAnalysis[186,187] and MPI for Python[313–315] packages allowing the evaluation of RDFs on hundreds of CPU cores in parallel. Further details regarding the numerical evaluation of eq. (7.4) and error estimation are given in appendix 7.A.1.

7.1.2.2 Dielectric permittivity

According to eq. (7.1), the calculation of the Debye screening length λ_D requires the knowledge of the static relative dielectric permittivity ε_r of the background medium. Since in MD simulations with both ions and solvent modeled explicitly, there is no effective dielectric background medium, we used the static relative dielectric permittivity of the simulated substances. Note that this is questionable within the Debye-Hückel picture, where in the extreme case of a pure IL, one could argue that the background medium should actually be vacuum. However, to make our calculations comparable to the analyses of experimental data, we use the relative permittivity of the entire system as in ref. 298. In equilibrium MD simulations, ε_r can be obtained from the expected value of the square of the system's itinerant dipole moment $\boldsymbol{M}$ according to[99]

$$\varepsilon_r = 1 + \frac{\langle \boldsymbol{M}^2 \rangle}{3Vk_\mathrm{B}T\varepsilon_0} \tag{7.5}$$

under the conditions that the system has PBC in all three dimensions and electrostatic interactions are computed with tinfoil boundary conditions at infinity. If a system consists entirely of charge-neutral molecules, its itinerant dipole moment $\boldsymbol{M}$ at any given time t equals the sum of the molecular dipole moments $\boldsymbol{\mu}$ so that $\boldsymbol{M}(t) = \sum_m \boldsymbol{\mu}_m(t)$, and the time average of $\boldsymbol{M}^2(t)$ serves as an estimator for $\langle \boldsymbol{M}^2 \rangle$. However, in systems with PBC comprising free ionic charges, $\boldsymbol{M}(t)$ has additional intermolecular contributions. The problem which arises is not only that these contributions are discontinuous in time when ions move across periodic boundaries; in fact, $\boldsymbol{M}(t)$ is ill-defined in such systems because its value depends on the choice of the origin of the spatial coordinate system.[98] Nevertheless, its temporal derivative, the itinerant current $\boldsymbol{j}(t) = \frac{d}{dt}\boldsymbol{M}(t)$, does not suffer from any of these problems.[98] It can be computed according to

$$\boldsymbol{j}(t) = \sum_i q_i \boldsymbol{v}_i(t)\,, \tag{7.6}$$

where the index i runs over all atoms with (partial) charges q_i and velocities $\boldsymbol{v}_i(t)$. Provided that the system is at thermal equilibrium at all times t, the time-dependent current $\boldsymbol{j}(t)$ can then be used to obtain the expected squared itinerant dipole moment from eq. (4.47) (see appendix 4.A for a proof)

$$\langle \boldsymbol{M}^2 \rangle = - \lim_{t\to\infty} \int_0^t \tau \langle \boldsymbol{j}(0)\boldsymbol{j}(\tau) \rangle \, \mathrm{d}\tau \,,$$

where $\langle \boldsymbol{j}(0)\boldsymbol{j}(t) \rangle$ is the unnormalized autocorrelation function of $\boldsymbol{j}(t)$. In practice, the direct numerical evaluation of eq. (4.47) is problematic due to the fact that the statistical noise in the tail of the current autocorrelation function is amplified by the factor τ in the integral. A more feasible approach is the so-called Einstein-Helfand method,[121] where one performs a linear regression of the itinerant dipole moment's mean square displacement $\langle (\Delta \boldsymbol{M})^2(t) \rangle$ in the limit of large t, and the right hand side of eq. (4.47) is obtained from the fit value at $t = 0$. The static relative permittivity is then obtained according to eq. (7.5), and, subsequently, the Debye length can be calculated from eq. (7.1). A detailed description of this approach is given in section 4.3.1.

At this point, it is important to mention again that the IL models used in this work employ rescaled charges to implicitly account for the effects of electronic polarizability and partial charge transfer.[71,72,231,235–238,308,310] However, this leads to an underestimation of the current $\boldsymbol{j}(t)$, and, likewise, the dielectric permittivity. Thus, to obtain correct estimates of the permittivity, the ionic charge scaling has to be undone when evaluating eq. (7.6).

7.1.2.3 Analysis of confined systems

In systems where the investigated substance is confined between charged surfaces, the electrostatic screening of the wall charges cannot

be inferred from interionic PMFs as such systems are neither homogeneous nor isotropic. Instead, the electrostatic screening of the surface charge can be extracted from the decay of the electric field $E^{\perp}(z)$ in the z-direction, *i.e.*, normal to the confining surfaces. To this aim, we analyzed the system's volume charge density profile $\rho_q^{\perp}(z)$, which is given by

$$\rho_q^{\perp}(z) = \left\langle \sum_i q_i \delta\left(z - z_i\right) \right\rangle , \tag{7.7}$$

where $\delta\left(\cdot\right)$ is the Dirac delta function, the operator $\langle\cdot\rangle$ denotes the canonical average, and the index i runs over all atoms in the system with charge q_i and position z_i, respectively. For the numerical evaluation of eq. (7.7), the system is discretized in the z-direction into n slabs of width $l_z = {}^{L_z}/_{n}$, where L_z is the length of the simulation box in the z-direction. The volume charge density profile is then calculated according to

$$\rho_q^{\perp}(z) = \left\langle \frac{1}{L_x\, L_y\, l_z} \sum_{\substack{i \\ 2|z-z_i|<l_z}} q_i \right\rangle , \tag{7.8}$$

and the perpendicular component $E^{\perp}(z)$ of the microscopic electric field is obtained from

$$E^{\perp}(z) = \frac{1}{\varepsilon_0} \int_0^z \rho_q^{\perp}(z')\ \mathrm{d}z' \,. \tag{7.9}$$

To assess the influence of confinement on the molecules' dipolar orientation, we computed the normal component $\mu_{\mathrm{rot},j}^{\perp}$ of the rotational dipole moment of molecule j according to

$$\mu_{\mathrm{rot},j}^{\perp} = \sum_{\alpha} q_{\alpha,j} \left(z_{\alpha,j} - z_{\mathrm{com},j}\right) , \tag{7.10}$$

where $z_{\mathrm{com},j}$ represents the z-position of the molecular center of mass and the index α runs over all atoms of molecule j. This allowed us to

compute the system's rotational dipole moment density $m_{\mathrm{rot}}^{\perp}(z)$ according to

$$m_{\mathrm{rot}}^{\perp}(z) = \left\langle \frac{1}{L_x\, L_y\, l_z} \sum_{\substack{j \\ 2|z-z_{\mathrm{com},j}|<l_z}} \mu_{\mathrm{rot},j}^{\perp} \right\rangle, \tag{7.11}$$

where the index j runs over all molecules in the system.

7.2 Results and Discussion

7.2.1 Bulk long-range interionic potentials of mean force

In SFB measurements, the distance-dependent force mediated by electrolytes confined between two mica-coated, like-charged surfaces has been found to follow a relatively fast oscillatory decay for surface separations up to a few nanometers before entering a long-ranged monotonic decay. It has been argued that the observed long-range decay must be a feature of bulk ionic fluids, therefore describing the general asymptotic decay of electrostatic interactions within concentrated electrolytes and ILs. Within these substances, one would therefore expect to observe the same asymptotic decay in effective ion-ion interactions, and, consequently, in the corresponding interionic PMFs. The latter argument has already been brought forward by Kjellander[66] in a well-founded manner.

For pure ILs, the experimentally observed transition from oscillatory to monotonic decay typically occurs at surface separations between 4 and 7 nm.[49,51,53] Thus, in order to see such an effect in bulk MD simulations, the systems under consideration must be large enough to allow the evaluation of interionic PMFs going well beyond that range. In other words, analyzing only the short-range parts of ionic interactions before the crossover region is clearly insufficient, and simulation boxes with edge lengths of at least 20 nm are required to properly

resolve the range of interest. Moreover, due to their high viscosity, ILs exhibit long structural relaxation times, necessitating simulation times of several hundred nanoseconds.[316] Nevertheless, even if these spatiotemporal requirements are fulfilled, the obtained PMFs are rather meaningless without proper estimates of their statistical accuracy. Therefore, for every data point in the computed PMFs, we performed statistical error analyses taking temporal correlations into account (see appendix 7.A.1.3 for details).

7.2.1.1 Neat ionic liquids

The first system we discuss comprises 108 000 ion pairs of pure $[C_4C_1Im]^+[PF_6]^-$(all-atom model with 3 456 000 atoms in total), with the positions of all atoms recorded for *a posteriori* analysis every 2 ps during a total simulation time of 700 ns. Figure 7.2a displays the absolute values of the PMFs $|w_{--}|(r)$ (anion-anion), $|w_{+-}|(r)$ (cation-anion), and $|w_{++}|(r)$ (cation-cation) between the respective molecular centers of mass in units of k_BT together with their one-sigma statistical error margins (light-colored areas) for interionic distances up to 16.5 nm. The ordinate of the main graph is logarithmically scaled to facilitate the detection of any long-ranged but possibly low-amplitude monotonic decay, whereas the inset shows the PMF's short-range part in linear scale.

For the investigation of electrostatic effects, distances below the van der Waals cut-off of 1.3 nm should be excluded from the analysis due to the relatively strong influence of the LJ potential in this region. At larger distances up to $r \approx 8.5\,\text{nm}$, all PMFs are well-described by an exponentially damped, oscillatory decay (7.2). The envelope of this decay is indicated by a dashed black line, which has a decay length of $\lambda_S = 1.05\,\text{nm}$. For distances greater than 8.5 nm, the PMFs become very noisy with an amplitude of about $3{\cdot}10^{-5}\,k_BT$, which is in the order of the statistical uncertainty. One could argue that due to the comparatively high statistical uncertainty in the tails, monotonic decays in

this region might be hidden in the noise. However, experiments with similar ILs[51] suggest an onset of the monotonic decay already before that region, and such an onset is clearly not present in our data.

The long-ranged monotonic decay of electrostatic interactions observed in SFB measurements was found to be a universal feature of concentrated electrolytes and ILs and therefore ought to be independent of the chemical details of the involved ionic species. Thus, we extended our analysis to an even larger system with a box edge length of almost 50 nm comprising 358 296 ion pairs of the same IL, but this time modeled by a coarse-grained representation involving only four interaction sites per ion pair (cf. fig. 7.1a,b). The corresponding cation-anion PMFs are displayed in fig. 7.2b for interionic distances up to 24.5 nm. All PMFs of the coarse-grained representation show the same qualitative behavior as the all atom model. As expected for coarse-grained models, the corresponding decay length of $\lambda_S = 1.43\,\text{nm}$ is comparable to but slightly larger than that of the all-atom model. Due to the larger number of ions in the system, the resulting increased statistical accuracy allows to resolve the oscillatory decay at interionic distances up to 13 nm. For larger distances, the PMFs again enter a region of almost constant amplitude (as low as $5 \cdot 10^{-6}\, k_B T$), which is about the same magnitude as the corresponding statistical one-sigma uncertainties.

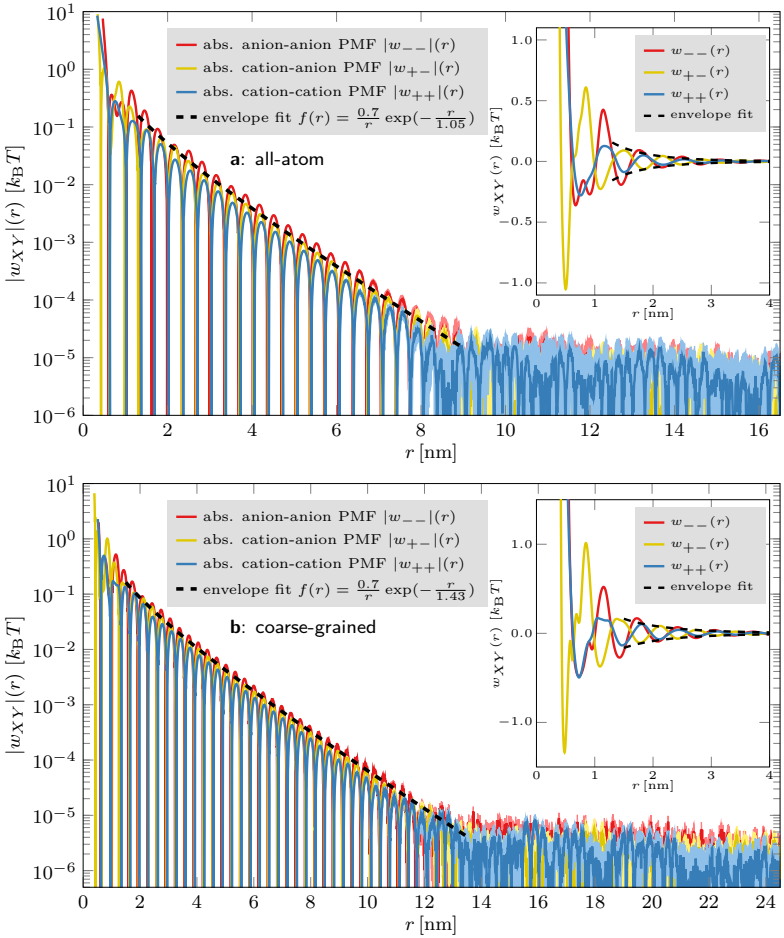

Figure 7.2: Absolute value of the anion-anion ($|w_{--}|(r)$, red), cation-anion ($|w_{+-}|(r)$, yellow), and cation-cation ($|w_{++}|(r)$, blue) potentials of mean force in neat $[C_4C_1Im]^+[PF_6]^-$. a: All-atom model. All PMFs follow an oscillatory decay up to a distance of about 8.5 nm. In this region, the envelope of the decay (dashed, black line) is very well described by a function of the form $f(r) = \frac{a}{r} \exp\left(-\frac{r}{\lambda_S}\right)$ with an amplitude of $a \approx 0.7\, k_B T$ and a decay length of $\lambda_S = 1.05$ nm. For distances larger than 8.5 nm, the potentials enter a region of almost constant amplitude, which is of the same order as the corresponding uncertainties (light-colored areas). b: Coarse-grained model. All PMFs show a qualitatively very similar behavior as for the all-atom model. The envelope of the decay exhibits a longer decay length of $\lambda_S = 1.43$ nm, which can be attributed to the coarse-grained nature of the molecular model. As for the all-atom model, all PMFs eventually enter a region ($r > 13$ nm) of almost constant amplitude with rather high uncertainty. Insets: The same PMFs as in the main graphs with linear y-axis scaling.

7.2.1.2 Concentrated electrolyte solutions

The system that we have investigated is a 4.43 molar aqueous NaCl solution comprising 216 000 ion pairs and 2 458 296 water molecules (7 806 888 atoms in total) in a cubic simulation box with an edge length of 43.25 nm. The corresponding anion-anion, cation-anion, and cation-cation PMFs obtained from a 200 ns simulation run are displayed in fig. 7.3.

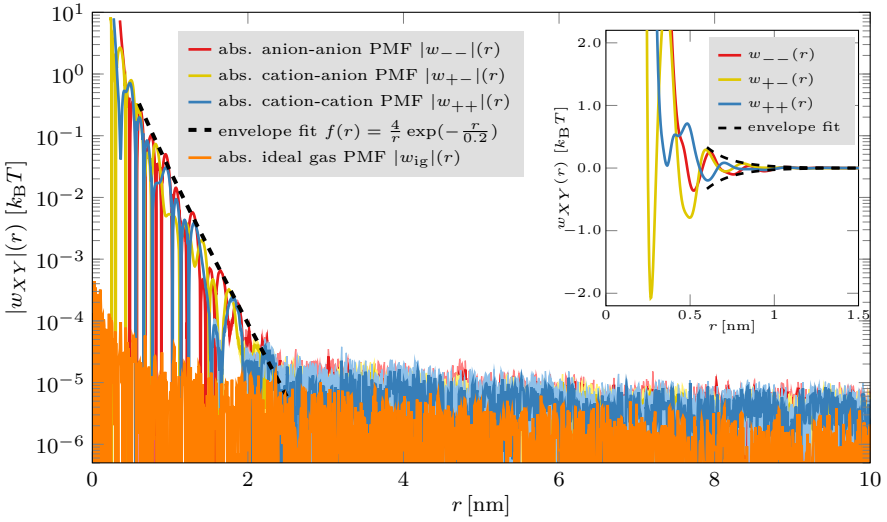

Figure 7.3: Absolute value of the anion-anion ($|w_{--}|(r)$, red), cation-anion ($|w_{+-}|(r)$, yellow), and cation-cation ($|w_{++}|(r)$, blue) potentials of mean force in a 4.43 mol/l aqueous NaCl solution. Up to a distance of about 2.2 nm, all PMFs exhibit an oscillatory decay which, in contrast to the case of neat $[C_4C_1Im]^+[PF_6]^-$, appears to be a superposition of several oscillations with different parameters. Nevertheless, the envelope of the decays (dashed, black line) can be approximated by a function of the form $f(r) = \frac{a}{r}\exp\left(-\frac{r}{\lambda_S}\right)$ with an amplitude of $a = 4.0\,k_{\mathrm{B}}T$ and a decay length of $\lambda_S = 0.2$ nm. For distances larger than 2.2 nm, the potentials lie in the order of the uncertainty levels of about $10^{-5}\,k_{\mathrm{B}}T$. Their further decay is not a feature of the system but simply due to the statistical error, which decreases with increasing distance. This is evident from the noisy orange line, which depicts the PMF $|w_ig|(r)$ of an ideal gas comprising an identical number of particles in the same volume, and exhibits the very same decay. Inset: The same PMFs with linear y-axis scaling. The envelope fit is again depicted by dashed black lines.

In contrast to the pure IL, a single oscillatory decay is not a satisfactory description of the short-range part of any of the interionic PMFs in aqueous NaCl but rather a superposition of several such decays with different amplitudes, wavelengths, phase shifts, and decay lengths. Nevertheless, up to a distance of about 2.2 nm, their envelope can be approximated by that of a single oscillatory decay as has been done before for the pure IL. The corresponding fit (dashed black line in fig. 7.3) has an amplitude of $4\,k_\mathrm{B}T$ and a decay length of $\lambda_\mathrm{S} = 0.2\,\mathrm{nm}$. For distances exceeding 2.2 nm, the PMFs become very noisy, and no distinct oscillations are discernible. In this region, the PMFs' envelopes appears to follow a very long-ranged decay. However, this decay is entirely due to statistical noise, which decreases with distance. In fact, the noise in the PMF of an ideal gas comprising an identical number of particles in the same volume (shown in orange in fig. 7.3) exhibits the very same decay. Thus, the observed long-range decay of the noise amplitude is merely a statistical artifact and must not be interpreted as a feature of the system. Instead, we have to conclude that also in MD simulations of concentrated aqueous NaCl solutions, there is no long-ranged monotonic decay of interionic interactions detectable within an accuracy of $\approx 10^{-5}\,k_\mathrm{B}T$.

7.2.2 Scaling analysis of asymptotic screening lengths in concentrated electrolyte solutions

In order to investigate how the asymptotic decay length λ_S scales with ion concentration, we analyzed the PMFs $w_{+-}(r)$, $w_{++}(r)$, and $w_{--}(r)$ obtained from all-atom MD simulations of $[\mathrm{C_4C_1Im}]^+\,[\mathrm{NTf_2}]^-$ in propylene carbonate (PC) over the entire concentration range covering IL mole fractions x from $x = 0$ to $x = 1$. Since the previously analyzed interionic PMFs of large-scale simulations did not show any additional long-range effects different from those at intermediate ion separations, we chose to simulate smaller systems in favor of covering a larger number of different ion concentrations. Except for the two lowest concentrations, all systems comprised 500 ion pairs and a

suitably adjusted number of PC molecules. For each system composition, up to four independent simulation runs were performed with runtimes covering more than 1 μs per run. As before, interionic PMFs were computed according to eqs. (7.3) and (7.4). To estimate the concentration-dependent effective screening length λ_S in these systems, we fitted the PMFs with a superposition of n oscillatory, exponentially damped functions

$$f(r) = \sum_{i=1}^{n} \frac{A_i}{r} \cos(\omega_i r - \phi_i) \exp\left(-\frac{r}{\lambda_i}\right) . \tag{7.12}$$

We found that setting $n = 2$ was sufficient to obtain an excellent match with the interionic PMFs in the fit range $1.2 \leq r \leq 3.0$ nm. Fitting the data to eq. (7.12) with $n = 3$ terms resulted in extremely unstable results under slight variation of initial fit parameters, while setting $n = 1$ lead to unsatisfactory fits with comparatively large residuals.

For each system, we determined the static dielectric permittivities ε_r and the corresponding Debye screening lengths λ_D. The permittivities of the IL mixtures compare well with experimental measurements for pure PC ($\varepsilon_r = 59.3$ (simulation) vs. $\varepsilon_r = 64.97$ (experiment, see ref. 317)) and pure $[C_4C_1Im]^+ [NTf_2]^-$ ($\varepsilon_r = 9.1$ (simulation) vs. $\varepsilon_r = 11.52$ (experiment, see ref. 318)). The complete sets of permittivities are given in appendix 7.B.1.2.

The knowledge of both the concentration-dependent asymptotic screening lengths λ_S and the corresponding Debye lengths λ_D allowed us to conduct a scaling analysis similar to that by Lee *et al.*.[298] Accordingly, fig. 7.4 shows the ratio of the screening length vs. the Debye length λ_S/λ_D as a function of the inverse Debye length scaled with the average ion diameter d/λ_D. Following ref. 298, the average ion diameter d of the IL was determined from the number concentration of ion pairs in the pure IL as $d = \frac{1}{2} (V/N_{IP})^{\frac{1}{3}} \approx 0.39$ nm. The resulting asymptotic linear and quadratic scaling at high concentrations

$$\frac{\lambda_n}{\lambda_D} \propto \left(\frac{d}{\lambda_D}\right)^n \tag{7.13}$$

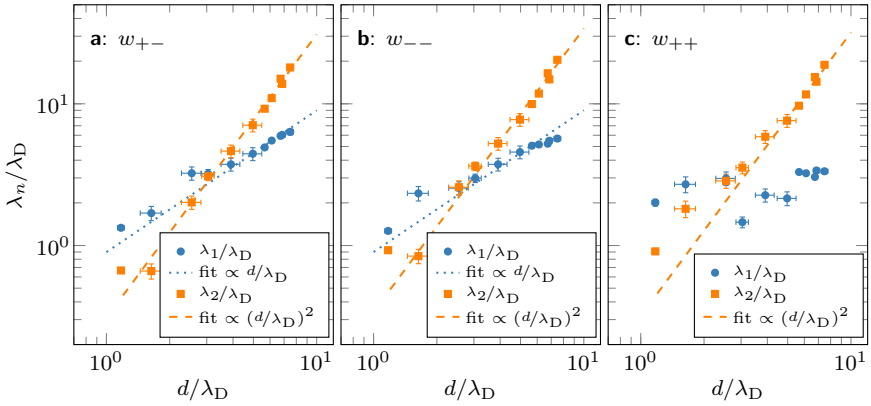

Figure 7.4: Scaling of the concentration-dependent screening lengths of $[C_4C_1Im]^+[NTf_2]^-$ in propylene carbonate as determined by fits of eq. (7.12) to the concentration-dependent cation-anion ($w_{+-}(r)$), anion-anion ($w_{--}(r)$), and cation-cation ($w_{++}(r)$) PMFs. The abscissa displays the average ion diameter d divided by the concentration-dependent Debye length λ_D, whereas the determined screening lengths λ_i divided by λ_D are plotted along the ordinate. For the cation-anion (panel a) and anion-anion (panel b) PMFs, we see two decay lengths (each corresponding to a distinct wavelength $2\pi/\omega_i$) which both exhibit a power law dependence in the plot. For the cation-cation data (panel c), such a dependence can only be established for one of the decay length ratios. In all cases, the asymptotic decay length ratio for high concentrations λ_2/λ_D is clearly proportional to $(d/\lambda_D)^2$.

is clearly visible from the blue and orange dashed lines in fig. 7.4. While the linear scaling of λ_1/λ_D is only present for the cation-anion and anion-anion PMFs, the quadratic scaling at high IL concentrations is retained also in the cation-cation PMFs, as we reported earlier.[77] Such a quadratic scaling has also been obtained by Adar *et al.*,[299] who used an elegant theory based on the modification of the electrostatic kernel accounting for ion size effects, and more recently by Krucker-Velasquez and Swan[319] in simulations of primitive model electrolytes. However, this quadratic scaling stands in contrast to the cubic scaling $\lambda_S/\lambda_D \propto (d/\lambda_D)^3$ obtained from experimental SFB measurements.[298] Moreover, the magnitudes of the effective screening lengths according to SFB measurements exceed our values by up to a factor of ten. A comparison

of the asymptotic screening lengths we obtained from bulk simulations with experimental data is shown in table 7.3.

System	c (mol/l)	λ_S^{sim} (nm)	λ_S^{SFB} (nm)
$[C_4C_1Im]^+[PF_6]^-$	4.63*	1.05	—
$[C_4C_1Im]^+[PF_6]^-$ (coarse-grained)	4.78*	1.43	—
NaCl in water	1.16	0.25	0.52[a]
	2.43	0.20	1.37[a]
	4.86	0.32	2.99[a]
	5.19	0.33	3.21[a]
$[C_4C_1Im]^+[NTf_2]^-$ in PC	0.53	0.67	—
	0.97	0.65	1.33[b]
	1.63	0.50	4.12[b]
	2.10	0.47	6.12[b]
	2.47	0.58	7.68[b]
	2.75	0.61	
	2.98	0.69	
	3.17	0.75	8.83[c]
	3.33	0.85	
	3.46	0.95	
	3.58*	1.07	

* Pure ionic liquid (without solvent).
[a] Data for NaCl in aqueous solution from ref. 51, linearly interpolated in the range $c \in [1.0, 5.0]$ mol/l.
[b] Data for $[C_4C_1Pyrr]^+[NTf_2]^-$ in PC solution from ref. 51, linearly interpolated in the range $c \in [0.9, 2.5]$ mol/l.
[c] Data for $[C_4C_1Pyrr]^+[NTf_2]^-$ in PC solution from ref. 51, average of data in the range $c \in [2.6, 3.4]$ mol/l.

Table 7.3: Comparison of screening lengths in the investigated bulk systems with corresponding values from SFB experiments involving the same or comparable substances. For each concentration, λ_S^{sim} represents the maximum of the three screening lengths obtained from the decays of the PMFs w_{+-}, w_{--}, and w_{++}. Listed values: molar ion pair concentration c (mol/l), screening length from simulations λ_S^{sim} (nm), and screening length from SFB measurements λ_S^{SFB} (nm).

7.2.3 Ionic liquids confined between like-charged surfaces

To investigate the influence of confinement on the screening behavior, we conducted additional simulations with PBC in the x- and y-directions only, where the IL is confined between planar, like-charged walls in the z-direction as illustrated in fig. 7.5.

Depending on the distance between the surfaces, the systems contained between 2000 and 4000 $[C_4C_1Im]^+ [NTf_2]^-$ ion pairs (cf. table 7.2) and an additional number of 352 $[C_4C_1Im]^+$ counterions compensating the negative wall charge. Note that if we used a force field with full charges, the required number of counterions would be smaller (about 282). Since counterions predominantly accumulate close to the surfaces, in both cases, the solid-liquid interaction should not influence the decay lengths and wavelengths of asymptotic decay modes at large distances[66] (see

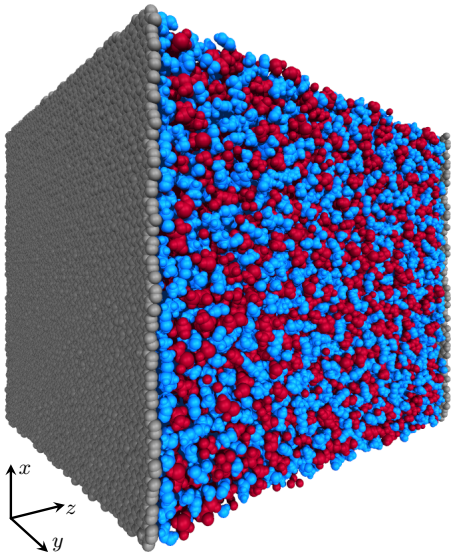

Figure 7.5: Example visualization of a confined IL system. The ionic liquid $[C_4C_1Im]^+ [NTf_2]^-$ (cations: blue; anions: red) is confined in the z-direction between planar, negatively charged graphene walls (gray).

appendix 7.B.3 for a more detailed discussion). In every system, each wall consists of 5376 carbon atoms forming a hexagonal graphene layer with lattice constant $a = 0.246\,\mathrm{nm}$. Each carbon atom carried a charge of $-0.02619\,e$, resulting in a surface charge density of $\sigma_q = -1\,e\,\mathrm{nm}^{-2}$. For the largest system, we generated four independent replicas. All systems were equilibrated for 300 ns. Each system was simulated for 1 µs in production runs, with atom positions stored every 2 ps for *a posteriori* analysis.

To investigate the electrostatic screening in these systems, we computed the perpendicular component $E^{\perp}(z)$ of the microscopic electric field in the z-direction according to eq. (7.9). Since all systems were symmetric in the z-direction with respect to their center at $z = {}^{L_z}/_2$, the charge density profiles $\rho_q^{\perp}(z)$ were taken as the average of $\rho_q^{\perp}(z)$ and $\rho_q^{\perp}(L_z - z)$ prior to evaluating eq. (7.9) to maximize the statistical quality of the data. The absolute values of the resulting electric fields $|E^{\perp}|(z)$ are shown in fig. 7.6.

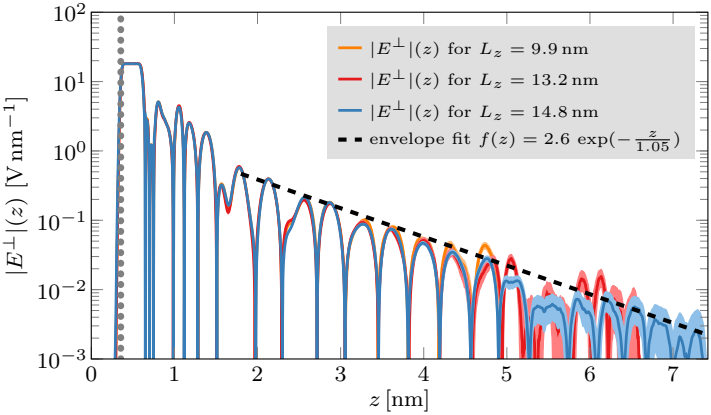

Figure 7.6: Absolute value of the electric field's perpendicular component $|E^{\perp}|(z)$ (log-scale) in $[C_4C_1Im]^+[NTf_2]^-$ confined between like-charged graphene walls. For $z \geq 2\,\mathrm{nm}$, the envelope of $|E^{\perp}|(z)$ can be described by a function of the form $f(z) = a\,\exp(-{}^{z}/_{\lambda_S})$ with an amplitude of $a \approx 2.6\,\mathrm{V}$ and a decay length of $\lambda_S = 1.05\,\mathrm{nm}$ as indicated by the dashed black line. The dotted gray vertical line marks the average wall position.

After a sharp increase due to the wall charge located at $z \approx 0.355\,\mathrm{nm}$, the electric field remains constant in a thin "empty" slab up to $z \approx 0.6\,\mathrm{nm}$ which exists due to LJ repulsion. Thereafter, because of the high surface charge density of the walls, the IL forms alternating cation-anion layers, resulting in an oscillatory behavior of $|E^{\perp}|(z)$. Up to $z \approx 1.5\,\mathrm{nm}$, $|E^{\perp}|(z)$ oscillates with a wavelength that is smaller than the size of the ions. This behavior results from the highly ordered structure of the IL in the vicinity of the walls, where both the rotational and translational motion of the ions is strongly restricted so that their molecular arrangement is almost static. In this arrangement, there exist preferred orientations of the ions with respect to the wall such that certain groups of atoms are predominantly found at specific distances from the wall. Thus, the short oscillation period of the electric field close to the walls is due to intramolecular contributions. A detailed analysis of the contributions of different atom types to the oscillations of the electric field is given in appendix 7.B.2.2. With increasing distance from the walls, ionic motion becomes less restricted, so that at distances larger than $z \approx 2\,\mathrm{nm}$, the electric field's oscillations smooth out with an almost uniform period of 0.76 nm, which corresponds to approximately two ion diameters and is in good agreement with the thickness $\Delta = 0.79\,\mathrm{nm}$ of squeezed-out cation-anion layers measured in SFB experiments using the same IL.[296] The envelope of the electric field then decreases exponentially with a decay constant of $\lambda = 1.05\,\mathrm{nm}$ (dashed black line in fig. 7.6), which is in good agreement with the decay length of interionic forces $\lambda_S = 1.07\,\mathrm{nm}$ obtained from bulk simulations. The fact that the different lines displayed in fig. 7.6 representing $|E^{\perp}|(z)$ in systems with different inter-wall distances all decay in the same manner suggests that the electrostatic screening behavior is independent of system size.

The electric field, however, reflects only the cumulative average distribution of charges in the system, which might mask other important details. To obtain information about the orientation of ions as a function of their distance from the walls, we computed the average value of the molecular rotational dipole moment's perpendicular

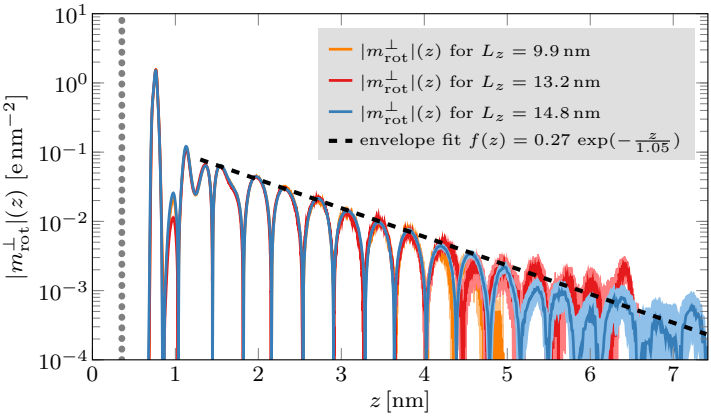

Figure 7.7: Absolute value of the perpendicular component $|m^{\perp}_{\mathrm{rot}}|(z)$ of the rotational dipole moment density (log-scale) in $[C_4C_1Im]^+[NTf_2]^-$ confined between like-charged graphene walls. The envelope of $|m^{\perp}_{\mathrm{rot}}|(z)$ is depicted by the dashed black line, which again has a decay length of $\lambda_S = 1.05\,\mathrm{nm}$ (same as for $|E^{\perp}|(z)$). The average wall position is indicated by the dotted gray vertical line.

component $|m^{\perp}_{\mathrm{rot}}|(z)$ according to eq. (7.11), which is depicted in fig. 7.7 for different system sizes. As the molecular dipole moment is a cumulative quantity per molecule, its average cannot contain intramolecular features by construction. In that respect, it is interesting to see that even though up to $z \approx 1\,\mathrm{nm}$, the system consists almost entirely of cations (see appendix 7.B.2.1), the first cation layer actually consists of two cation layers with opposite dipolar orientation. At distances exceeding $z = 1\,\mathrm{nm}$, the amplitude of the rotational dipole moment's perpendicular component decays in the very same manner as the electric field with a decay constant of $\lambda = 1.05\,\mathrm{nm}$. Again, as it was the case for the electric field, the decay of $|m^{\perp}_{\mathrm{rot}}|(z)$ is the same for all studied system sizes.

7.2.4 Structural decay in confined ionic liquids

Now that we have analyzed the decay of electrostatic observables in the system, we will have a closer look on the relaxation of the local ionic structure. To this aim, for the largest confined system, we divided the system into n slabs of width l_z, each centered at a position $z_i = z_0 + i \cdot l_z$, where z_0 is the minimal reference position. We then computed local, short-ranged RDFs $g_{+-}^{(i)}(r;\, z_i)$ between cations from slab i and all anions. Even though the system is anisotropic and its extent is bounded in the z-direction, these RDFs are spherical to facilitate their comparison with the cation-anion RDF in the bulk. Of course, this requires the reference positions z_i to be located further away from any of the walls than the maximum distance r_{cut} considered in the RDF computation. We took $n = 98$ slabs of width $l_z = \frac{L_z - 2\,z_0}{n} \approx 0.1\,\text{nm}$, chose the minimum reference position $z_0 = 2.5\,\text{nm}$ (maximum $z_n = L_z - z_0$), and evaluated each RDF up to a distance of $r_{\text{cut}} = 2\,\text{nm}$. Furthermore, when computing such RDFs, it is important to account for the fluctuating number of cations within each reference slab. Likewise, to obtain comparable results despite the fluctuating number of anions found within a distance $r < r_{\text{cut}}$, all RDFs have been normalized with respect to the bulk anion density of $\approx 2.154\,\text{nm}^{-3}$. Due to the symmetry of the system, we averaged the results of each pair (z_i, z_{n-i}), yielding a total of $\frac{n}{2} = 49$ independent RDFs, which are displayed in the top panel of fig. 7.8, where the color of the lines change smoothly from the smallest $z_i = z_0$ (red) to the largest $z_i = z_{48}$ (blue). Due to the layered structure of the IL close to the walls, one might expect the shape of those RDFs $g_{+-}^{(i)}(r;\, z_i)$ with small z_i to be significantly different from those with the reference position close to the center of the system, and that the RDF's inherent spherical averaging may lead to a broadening of the peaks of the ones close to the walls. However, it turns out that the shapes and locations of especially the first maxima and minima of the RDFs are all very similar, and their shapes only differ slightly in the region beyond the second maximum. The RDF with the reference group located in the center of the system (the "bluest" line) matches

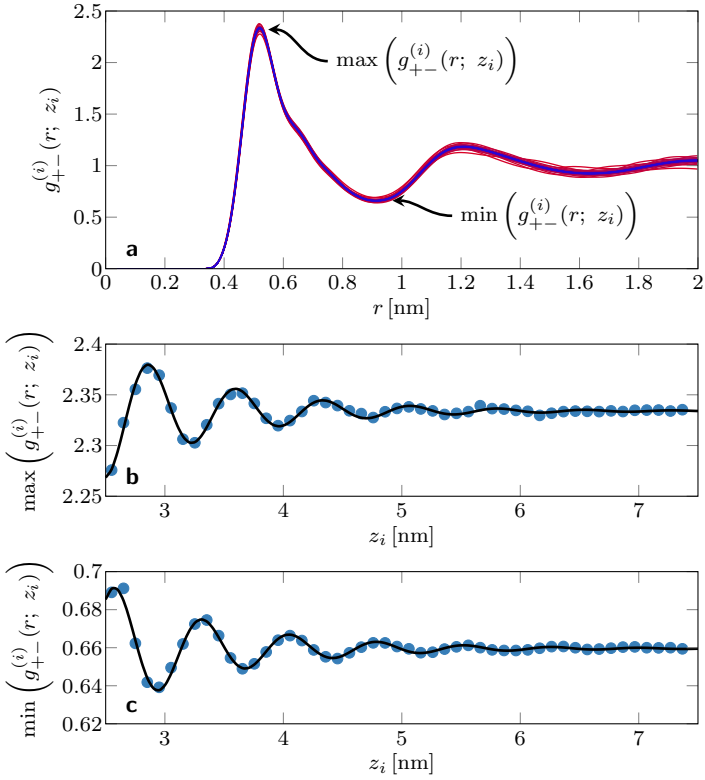

Figure 7.8: **a**: z-position-dependent cation-anion RDFs $g^{(i)}_{+-}(r;\, z_i)$ of $[C_4C_1Im]^+\,[NTf_2]^-$ confined between like-charged graphene walls. The lines are RDFs between those cations that have their centers of mass z_{com} within $2\,|z_i - z_{\mathrm{com}}| \leq l_z$ ($z_i = z_0 + i \cdot \Delta z$ with $z_0 = 2.5\,\mathrm{nm}$, $l_z \approx 0.1\,\mathrm{nm}$) and all anions in the system. The color of the lines changes smoothly with the reference position ranging from $z_i = z_0$ (close to the walls, red) to $z_i = z_{48} = \frac{L_z}{2}$ (center of the system, blue). **b**: Amplitude of the first maximum $\max\left(g^{(i)}_{+-}(r;\, z_i)\right)$ of each of the the RDFs depicted in panel a as a function of the reference distance z_i (blue dots). **c**: Amplitude of the first minimum $\min\left(g^{(i)}_{+-}(r;\, z_i)\right)$ of the same RDFs as a function of the reference distance z_i. The black lines in panels b and c are fits of a oscillatory exponential decays with decay length 1 nm. This shows that the local structure around cations relaxes with increasing distance from the walls towards the bulk structure in a manner that is very similar to the oscillatory decay of the electrostatic screening.

exactly with the cation-anion RDF computed in the bulk system. In the short-range part up to $r \approx 1.2\,\mathrm{nm}$, the only significant deviation can be observed in the amplitudes $\max(g_{+-}^{(i)}(r;\, z_i))$ and $\min(g_{+-}^{(i)}(r;\, z_i))$ of the first local minima and maxima at $r_{\max} \approx 0.52\,\mathrm{nm}$ and $r_{\min} \approx 0.91\,\mathrm{nm}$, respectively. Because the dependence of these amplitudes on the reference positions is not easily visible in fig. 7.8a, we plot $\max(g_{+-}^{(i)}(r;\, z_i))$ and $\min(g_{+-}^{(i)}(r;\, z_i))$ versus z_i separately in fig. 7.8b,c (blue dots). The black lines in these plots are fits of oscillatory exponential decays $f(z) = A\cos(\omega z_i - \varphi)\exp\left(-\frac{z_i}{\lambda}\right) + c$ to the data, which yield a decay length $\lambda = 1\,\mathrm{nm}$ in both cases. We carried out similar analyses for anion-cation, anion-anion, and cation-cation RDFs, which give a very similar picture with decay lengths between 0.9 and 1.1 nm (see appendix 7.B.2.3). This indicates that with increasing distance from the walls, the (spherically averaged) local arrangement of ions decays to the bulk structure in a very similar manner as the previously analyzed electrostatic properties.

7.3 On the Relation of Underscreening to Other Measurements

As the long-range monotonic decay of surface interaction forces mediated by concentrated electrolytes and ILs observed in SFB experiments was suggested to reflect the electrostatic screening behavior of these substances, several attempts have been made to relate the measured screening lengths to other observables.[52,298] Here, we discuss the applicability of some of the theoretical models employed to establish such connections.

7.3.1 Differential capacitance

In ref. 52, Lee *et al.* suggested that the long-range decay of electrostatic interactions is consistent with concentration-dependent measure-

ments of differential double-layer capacitance. The authors of ref. 52 used an approach similar to the Gouy-Chapman-Stern (GCS) model and divided the electrical double-layer into a Stern and a diffuse layer, so that the total differential capacitance C_d could be modeled as two capacitors in series with capacitance C_Stern and C_diffuse, respectively. Unlike C_Stern, however, C_diffuse is not constant and depends on the electrostatic potential at the Helmholtz plane separating the diffuse and Stern layers. Assuming low applied potential differences and constant C_diffuse, approximated by the capacitance at the potential of zero charge, Lee *et al.* estimated $C_\mathrm{diffuse} = \varepsilon_0\varepsilon_r/\lambda_\mathrm{S}$. Note that this expression is the same as the zero-voltage Gouy-Chapman capacitance with λ_D replaced by λ_S. Within these assumptions, Lee *et al.* obtained for the total capacitance

$$C_\mathrm{d} = \left(C_\mathrm{Stern}^{-1} + C_\mathrm{diffuse}^{-1}\right)^{-1} = \frac{\varepsilon_0\varepsilon_r}{a + \lambda_\mathrm{S}}\,. \tag{7.14}$$

The concentration dependence of capacitance to compare with experiments comes from that of λ_S and ε_r.

To compute C_d in our work, we followed the usual practice (see, *e.g.*, ref. 320) and took the width of the Stern layer $a = d/2$, where d ($\approx 0.4\,\mathrm{nm}$ for $[\mathrm{C_2C_1Im}]^+\,[\mathrm{NTf_2}]^-$) is the bare ion diameter. Note that in ref. 52 a different value for a was used, which shifts the curves analyzed in the following but does not change the conclusions of this analysis (see appendix 7.C for details). Figure 7.9a compares direct measurements of C_d for $[\mathrm{C_2C_1Im}]^+\,[\mathrm{NTf_2}]^-$ solutions in PC[321] (black squares) with values obtained according to eq. (7.14) for similar ILs. For the screening lengths λ_S and the relative permittivities ε_r required to evaluate eq. (7.14), we used the data either from SFB experiments with $[\mathrm{C_4C_1Pyrr}]^+\,[\mathrm{NTf_2}]^-$ in PC[51] (orange dots, same as in ref. 52) or from our simulations of $[\mathrm{C_4C_1Im}]^+\,[\mathrm{NTf_2}]^-$ in PC (blue dots). Additionally, the green line in fig. 7.9a depicts the concentration-dependent behavior of C_d according to the GCS model, *i.e.*, with the screening length λ_S in eq. (7.14) replaced by the Debye length λ_D.

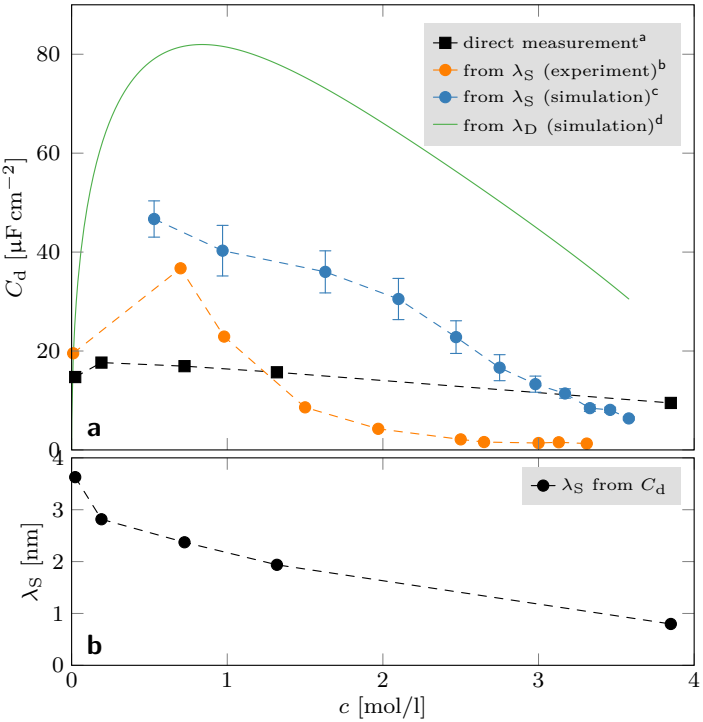

Figure 7.9: Panel a: Comparison of the concentration-dependent differential capacitance C_d at the point of zero charge obtained from direct measurements[321] (black squares) and according to the GCS model as defined by eq. (7.14) (orange dots: SFB measurements,[51] blue circles: simulation). The solid green line shows C_d when λ_S is replaced by λ_D in eq. (7.14).
[a]Differential capacitance for $[C_2C_1Im]^+[NTf_2]^-$ from Bozym *et al.*.[321]
[b]λ_S and ε_r data for $[C_4C_1Pyrr]^+[NTf_2]^-$ from Smith *et al.*.[51]
[c]λ_S and ε_r data from simulations of $[C_4C_1Im]^+[NTf_2]^-$ (this work).
[d]λ_D computed according to eq. (7.1) using interpolated ε_r data from simulations of $[C_4C_1Im]^+[NTf_2]^-$ (this work).
Panel b: Screening length λ_S computed according to the inverted GCS model (eq. (7.15)) with C_d from direct measurements[321] and ε_r interpolated from simulations. In both panels, dashed lines serve as a guide to the eye.

Using eq. (7.14) with data obtained from simulations appears to yield the best agreement with direct measurements at high concentrations,

whereas the SFB-based data fails to reproduce the direct measurements for high concentrations both qualitatively and quantitatively. Interestingly, if λ_S is replaced by the Debye length λ_D in eq. (7.14) (*i.e.*, the GCS model), both the nonmonotonic behavior of C_d and its linear tail are still reproduced quite well (green line). Even in this case, despite the quantitative deviation, the qualitative agreement between the GCS model and direct measurements is better than that of eq. (7.14) with λ_S obtained from SFB experiments. This raises the question whether this approach is capable of establishing any meaningful relation between the screening length and the differential capacitance at high ion concentrations. Furthermore, by solving eq. (7.14) for λ_S, one gets

$$\lambda_S = \frac{\varepsilon_0 \varepsilon_r}{C_d} - a\,. \tag{7.15}$$

By evaluating eq. (7.15) for the directly measured values of C_d, we obtained the corresponding 'prediction' for λ_S, which is depicted in fig. 7.9b. The observed monotonic decrease of λ_S with increasing concentration demonstrates that eq. (7.14) is unable to reproduce the expected nonmononic behavior of λ_S, which, in turn, leads to the conclusion that this model cannot be used to connect the measured C_d values with λ_S at high concentrations.

7.3.2 Excess chemical potential

Another interesting approach to relating bulk electrolyte properties to λ_S was presented in ref. 298, where the screening length of aqueous NaCl solutions obtained from SFB measurements was used to predict the excess chemical potential μ_{ex} of the solution according to

$$\mu_{ex} = -\frac{1}{2}\frac{l_B\, k_B T}{\lambda_S + d} = -\frac{z^2 e^2}{8\pi\varepsilon_0\varepsilon_r\,(\lambda_S + d)}\,, \tag{7.16}$$

where l_B denotes the Bjerrum length (see ref. 52 for a derivation). Note that this expression is identical to what one would obtain from Debye-Hückel theory but with the effective screening length λ_S replacing the Debye length λ_D.[52] In fig. 7.10a, the resulting prediction of μ_{ex} for λ_S obtained from SFB experiments[51] is compared with μ_{ex} obtained from chemical activity coefficients[322] γ according to $\mu_{ex} = k_B T \ln(\gamma)$.

While the quantitative agreement of both data series in fig. 7.10a is indeed remarkable, the qualitative behavior at intermediate to high concentrations appears to be different. To investigate this discrepancy, we invert the model to calculate λ_S from μ_{ex} as

$$\lambda_S = -\frac{z^2 e^2}{8\pi\varepsilon_0\varepsilon_r\mu_{ex}} - d\,, \tag{7.17}$$

which allows us to conduct a scaling analysis in terms of the behavior of λ_S/λ_D with respect to d/λ_D (similar to that in section 7.2.2) for both data series. The resulting scalings are shown in fig. 7.10b. As expected, the screening length λ_S from SFB measurements exhibits the cubic scaling $\lambda_S/\lambda_D \propto (d/\lambda_D)^3$ (orange line) found for the decay of surface forces in many SFB measurements of concentrated electrolytes.[51–53,298] In contrast, the scaling of the screening length computed according to eq. (7.17) (black dots) can be well described by a phenomenological function of the form $f(d/\lambda_D) = a_0 + a_1(a_2 - d/\lambda_D)^\alpha$ (solid black line), which shows a qualitatively entirely different behavior. Since $\alpha < 0$, it diverges for $d/\lambda_D \to a_2$, which corresponds to a diverging screening length λ_S for $\mu_{ex} \to 0$ in eq. (7.17) as the concentration approaches the solubility threshold. However, such a behavior seems unphysical, as it would imply that free ions in a saturated solution were unable to respond to an external electric field.

Thus, as the model fails at high concentrations, it is questionable whether the mere quantitative agreement of the data in fig. 7.10a in this regime allows drawing any meaningful conclusions.

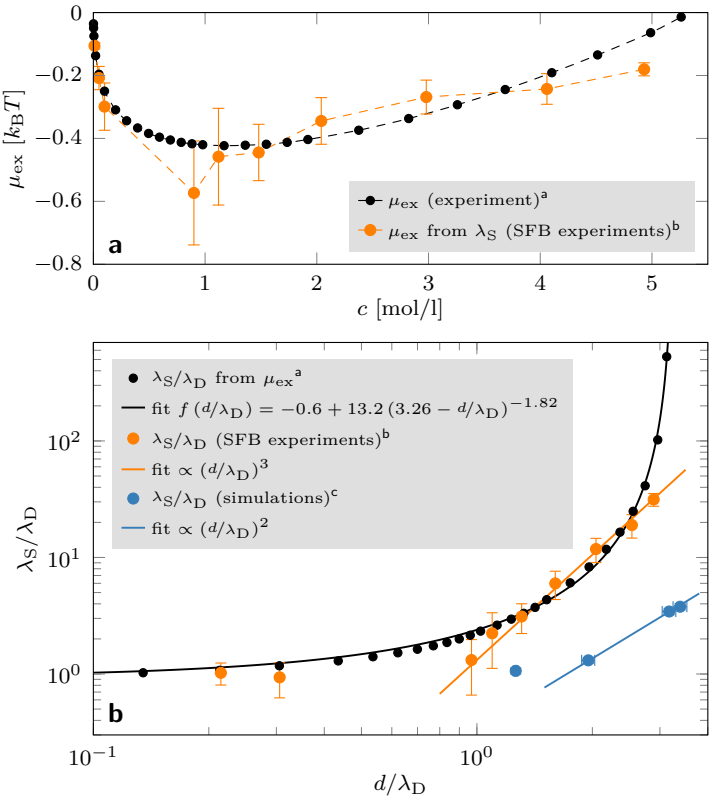

Figure 7.10: Panel a: Excess chemical potential μ_{ex} of aqueous NaCl solutions computed from activity coefficients[322] γ according to $\mu_{ex} = k_BT\ln(\gamma)$ (black dots) and computed via eq. (7.17) with λ_S taken from SFB measurements[51] (orange dots). Dashed lines serve as guides to the eye.
Panel b: Comparison of the scaling λ_S/λ_D versus d/λ_D for λ_S obtained from μ_{ex} of aqueous NaCl solutions according to eq. (7.17) (black dots), for λ_S obtained from corresponding SFB experiments (orange dots), and for λ_S from bulk simulations (blue dots). The solid black line represents a phenomenological fit of the form $f(x) = a_0 + a_1(a_2 - x)^\alpha$ with $x := d/\lambda_D$.
[a]Activity coefficients γ from ref. 322 to obtain $\mu_{ex} = k_BT\ln(\gamma)$.
[b]Screening lengths λ_S and permittivities ε_r (to compute λ_D) from ref. 51.

7.4 Conclusion

We have conducted large-scale MD simulations of concentrated electrolytes and pure ionic liquids in bulk and under confinement and calculated the PMFs between different ionic species with unprecedented precision. The large system sizes and long simulation times allowed us to analyze the PMFs in a range of interionic distances corresponding to the range of surface separations in SFB experiments. In contrast to experimental measurements, we found no evidence for the existence of a long-ranged, monotonic decay of effective interionic interactions. We obtained the characteristic decay lengths λ_S of all analyzed PMFs about an order of magnitude smaller than those inferred from the experiments.

We investigated the concentration-dependent scaling of the effective screening lengths λ_S with respect to the Debye length λ_D by analyzing interionic PMFs in electrolyte solutions for different ion concentrations. We found that there are at least two different decay lengths in the PMFs, with the asymptotic scaling $\lambda_S/\lambda_D \propto (d/\lambda_D)^2$ prevailing at high ion concentrations. We recall that this scaling has also been found theoretically by Adar *et al.*[299] and similar to our earlier results[77] in simulations by Krucker-Velasquez and Swan.[319] However, it contrasts with the experimentally observed scaling $\lambda_S/\lambda_D \propto (d/\lambda_D)^3$ of the decay of forces between charged surfaces across concentrated electrolytes.

Our results for IL systems confined between like-charged surfaces did not show any anomalously long electrostatic decay lengths either, confirming our findings from bulk simulations. The determined values of the screening lengths are in close agreement with the values obtained for the same systems in bulk, confirming the statistical-mechanical finding that solid-liquid interactions do not affect asymptotic decay lengths.[66] Our values compare well with the results of other studies based on smaller all-atom MD simulations[323] as well as with theoretical approaches and simulations of primitive model electrolytes.[299,324,325]

We showed that relating screening lengths in highly concentrated electrolytes to other observables may be of limited value if the employed models fail at high ion concentrations and may therefore yield unphysical predictions in this regime. This highlights the importance of the ongoing efforts in the research on highly concentrated electrolytes and ILs. The physics of such systems remain an intricate subject, and there exist many possible approaches aiming to capture the existence of long-ranged monotonic decays (see, e.g., ref. 53 for an overview). Nevertheless, our simulation results indicate that the experimentally observed long-ranged monotonic decay of surface forces might not be a property of bulk electrolytes or ILs.

As of now, the origin of these forces is not understood. However, from a computational perspective, we see several possible directions for future research. To strengthen the link between simulation studies and analytical descriptions of concentrated electrolytes, the work of Kjellander on dressed ion theory[66,68,69,302,303,326] appears as a prime candidate not only because of its comprehensiveness, but also due to its direct applicability to MD simulation data. As it directly relates an electrolyte's short-range screening behavior to its corresponding asymptotic decay modes, it would be particularly interesting to follow the route Kjellander outlined in ref. 68 (demonstrated for spherical ions in ref. 327) to extract such modes from our high-precision data. Furthermore, with respect to SFB experiments, simulations with static system sizes might be unable to capture dynamic processes that could be important to reproduce and explain the experimental observations. Lhermerout and Perkin[328] and also Han and Espinosa-Marzal[296] have used classical hydrodynamic models to disentangle electrostatic and viscous forces acting during the squeeze-out of ion layers of ILs confined between the mica-coated surfaces of a surface force apparatus. However, the electrostatic screening lengths required to fit the models to the experimental data were still in the same range that had been previously reported without taking fluid viscosity into account. Providing a simulational backing for these approaches in terms of a dynamic microscopic picture will be challenging, as both the spatial and temporal scales

of the experimental procedure are not easily accessible by simulations with molecular resolution. Concerning MD simulations, possible steps towards a more realistic picture with a closer correspondence to the experimental setup might include simulations of confined systems where the lateral pressure component in the center of the system is held constant, simulations at constant chemical potential, or even combinations thereof with dynamically changing confinement.

Appendix of Chapter 7

7.A Numerical Methods

7.A.1 Computation of radial pair distribution functions

In homogeneous systems with a fixed number of particles, the radial pair distribution function (RDF) between two molecular species X and Y is formally defined as

$$g_{XY}(r) = \frac{\langle \rho_{XY}(r) \rangle}{\langle \rho_Y \rangle} \,, \tag{7.18}$$

where $\langle \rho_{XY}(r) \rangle$ denotes the expected number density of particles of species Y residing on shells of radius r centered at any particle of species X, and $\langle \rho_Y \rangle$ is the expected number density of particles of species Y in the entire system, *i.e.*, their bulk number density.

The numerical evaluation of $g_{XY}(r)$ requires the discretization of space into intervals of width Δr, so that we define the discretized distance

$$r_n = \left(n + \frac{1}{2} \right) \Delta r \,, \quad n \in \mathbb{N}_0 \,. \tag{7.19}$$

In a system with orthorhombic volume $V = L_x \, L_y \, L_z$ and periodic boundary conditions in all three dimensions which comprises N_X particles of species X and N_Y particles of species $Y \neq X$, the RDF is then estimated according to

$$g_{XY}(r_n) \approx \hat{g}_{XY}(r_n) := \frac{\hat{\rho}_{XY}(r_n)}{\hat{\rho}_Y} \tag{7.20}$$

with the estimator $\hat{\rho}_Y$ for the expected bulk number density of particles of species Y

$$\hat{\rho}_Y = \frac{N_Y}{\bar{V}}\,, \tag{7.21}$$

where we defined the average system volume

$$\bar{V} := \frac{1}{N}\sum_{i=1}^{N} V_i\,. \tag{7.22}$$

Here, we have averaged over N time steps so that V_i denotes the volume of the system at time step i, allowing for systems with fluctuating simulation box volumes.

The estimator for the expected number density of particles of species Y residing on shells of radius r centered at any particle of species X is defined as

$$\hat{\rho}_{XY}(r_n) = \frac{1}{N\,N_X}\sum_{i=1}^{N}\frac{H_{n,i}^{XY}}{V_{n,i}^{\text{shell}}}\,, \tag{7.23}$$

where $V_{n,i}^{\text{shell}}$ is the shell volume (see below) and the distance histogram $H_{n,i}^{XY}$ is given as

$$H_{n,i}^{XY} := H_i^{XY}(r_n) = \sum_{j=1}^{N_X}\sum_{k=1}^{N_Y}\delta\left(\left\lfloor\frac{\|\boldsymbol{r}_{k,i}-\boldsymbol{r}_{j,i}\|_{\text{pbc}}}{\Delta r}\right\rfloor - n\right)\,. \tag{7.24}$$

Again, we averaged over configurations of N time steps so that $\boldsymbol{r}_{j,i}$ and $\boldsymbol{r}_{k,i}$ are the positions of the particles j and k at time step i. The function $\delta(\cdot)$ is the discrete Dirac delta function, which is defined as

$$\delta(x) = \begin{cases} 1 & \text{if } x = 0 \\ 0 & \text{otherwise}\,, \end{cases} \tag{7.25}$$

and the floor operator $\lfloor\cdot\rfloor$ yields the closest integer smaller than or equal to its argument. The operator $\|\cdot\|_{\text{pbc}}$ is the Euclidean L_2-norm

(*i.e.*, distance) with periodic boundary conditions applied according to the minimum image convention

$$\|\boldsymbol{r}\|_{\text{pbc}}^2 = \sum_{d\in\{x,y,z\}} \Bigg((r_d \bmod L_d) + h\left(-(r_d \bmod L_d) - \frac{L_d}{2}\right) L_d - h\left((r_d \bmod L_d) - \frac{L_d}{2}\right) L_d \Bigg)^2 , \tag{7.26}$$

where $h(\cdot)$ denotes the Heaviside step function defined as

$$h(x) = \begin{cases} 1 & \text{if } x > 0 \\ 0 & \text{otherwise} . \end{cases} \tag{7.27}$$

The shell volumes $V_{n,i}^{\text{shell}} := V_i^{\text{shell}}(r_n)$ could in principle be calculated from the volume difference of two spheres with radii

$$R_n^{\text{outer}} = r_n + \frac{\Delta r}{2} = (n+1)\Delta r ,$$
$$R_n^{\text{inner}} = r_n - \frac{\Delta r}{2} = n\Delta r .$$

Although seemingly trivial, this requires particular attention. According to the minimum image convention defined in eq. (7.26), the maximum possible distance in a 3d-periodic orthorhombic box with edge lengths $L_{x,i}, L_{y,i}, L_{z,i}$ at time step i is

$$r_i^{\max} := \|\boldsymbol{r}_i^{\max}\|_{\text{pbc}} = \frac{1}{2}\sqrt{L_{x,i}^2 + L_{y,i}^2 + L_{z,i}^2} . \tag{7.28}$$

However, the radius of the largest sphere that is completely enclosed by the box at all time steps i is

$$R_{\text{enc}}^{\max} = \frac{1}{2} \min_i \left(L_{x,i}, L_{y,i}, L_{z,i}\right) . \tag{7.29}$$

Thus, if and only if we limit the evaluation of $\hat{g}_{XY}(r_n)$ to distances $r_n \leq R_{\text{enc}}^{\max} - \frac{\Delta r}{2}$, the shell volumes are time-invariant and can be obtained from

$$V_{n,i}^{\text{shell}} \equiv V_n^{\text{shell}} = \frac{4\pi}{3}\left(((n+1)\,\Delta r)^3 - (n\,\Delta r)^3\right), \quad n \leq \frac{R_{\text{enc}}^{\max}}{\Delta r} + 1\,. \tag{7.30}$$

Finally, the complete equation for the numerical RDF estimator reads

$$\hat{g}_{XY}(r_n) = \left(\frac{1}{N\,N_Y}\sum_{i=1}^{N} V_i\right)\frac{1}{N\,N_X\,V_n^{\text{shell}}} \times \sum_{i=1}^{N}\sum_{j=1}^{N_X}\sum_{k=1}^{N_Y}\delta\left(\left\lfloor\frac{\|\boldsymbol{r}_{k,i}-\boldsymbol{r}_{j,i}\|_{\text{pbc}}}{\Delta r}\right\rfloor - n\right). \tag{7.31}$$

If the RDF is to be evaluated among particles of the same species X, we want to exclude pair distances of particles paired with themselves, which is achieved by removing the pairs (j, k) with $j=k$ from the histogram summation. The corresponding RDF estimator then becomes

$$\hat{g}_{XX}(r_n) = \left(\frac{1}{N\,N_X}\sum_{i=1}^{N} V_i\right)\frac{2}{N\,N_X\,V_n^{\text{shell}}} \sum_{i=1}^{N}\sum_{j=1}^{N_X}\sum_{k=j+1}^{N_X}\delta\left(\left\lfloor\frac{\|\boldsymbol{r}_{k,i}-\boldsymbol{r}_{j,i}\|_{\text{pbc}}}{\Delta r}\right\rfloor - n\right), \tag{7.32}$$

where we additionally exploited the symmetry of the Euclidean distance by shifting the initial index of the innermost sum and multiplying by 2.

7.A.1.1 Distance-dependent statistical accuracy of radial pair distribution functions

Let us consider an ideal gas in a 3d-periodic orthorhombic volume with constant edge lengths L_x, L_y, L_z comprising a fixed number of particles N_X at thermal equilibrium. Then, by definition of an ideal gas, the expected number density in any part of the system equals the bulk density so that the expected value of $g_{XX}(r)$ is $\langle g_{XX}(r)\rangle = 1$ for all possible distances r. However, if we measure the estimator $\hat{g}_{XX}(r_n)$ of this system for a given number of time steps N, this measurement will be subject to a statistical error $\epsilon(\hat{g}_{XX}(r_n))$. Because of the constant volume and fixed number of particles, the measured bulk number density $\hat{\rho}_X$ will be time-invariant and equal to its expected value $\langle \rho_X \rangle = \frac{N_X}{V}$. Thus, the statistical error can only be due to the estimator $\hat{\rho}_{XX}(r_n)$. If we assume that the time Δt between measurements is large enough for the system to decorrelate, the different measurements of $\hat{\rho}_{XX}(r_n)$ at subsequent time steps will be uncorrelated. Thus, according to eq. (4.13), the statistical error $\epsilon(\hat{\rho}_{XX}(r_n))$ will be proportional to $\frac{1}{\sqrt{N}}$ for all r_n. Nevertheless, the expected value of this error will also depend on the square root of the expected number of particle distances $\langle N^{\mathrm{dist}}(r_n)\rangle$ contributing to the histogram H_n^{XX}. According to eq. (7.32),

$$\langle N^{\mathrm{dist}}(r_n)\rangle = \frac{1}{2} N_X (N_X - 1) \frac{V_n^{\mathrm{shell}}}{V} \,. \tag{7.33}$$

Since both N_X and V are constant, we conjecture that

$$\langle \epsilon(\hat{g}_{XX}(r_n))\rangle \;\propto\; \frac{1}{\sqrt{V_n^{\mathrm{shell}}}} \,. \tag{7.34}$$

7.A.1.2 Error estimation of radial pair distribution functions

Whenever $g_{XY}(r)$ is estimated in systems with constant simulation box volumes $V_i = \bar{V} = V$, then $\langle \rho_Y \rangle = \rho_Y = \frac{N_Y}{V}$ at all time steps. It follows

that

$$\langle g_{XY}(r)\rangle = \frac{\langle \rho_{XY}(r)\rangle}{\langle \rho_Y\rangle} = \frac{V}{N_Y}\langle g_{XY}(r)\rangle = \left\langle \frac{\rho_{XY}(r)}{\rho_Y}\right\rangle \quad \text{if } V = \text{const.} \tag{7.35}$$

For the estimator $\hat{g}_{XY}(r_n)$, it follows analogously that it can be expressed as the time average

$$\hat{g}_{XY}(r_n) = \frac{1}{N}\sum_{i=1}^{N} \hat{g}_{XY,i}(r_n) \quad \text{if } V = \text{const}\,, \tag{7.36}$$

where $\hat{g}_{XY,i}(r_n)$ denotes $\hat{g}_{XY}(r_n)$ evaluated at a single time step i. In other words, $\hat{g}_{XY}(r_n)$ is the mean of the time series $\hat{g}_{XY}(r_n)(t)$. Thus, we can apply the formulas for the standard error of the mean derived in section 4.1 to estimate the error $\epsilon\left(\hat{g}_{XY}(r_n)\right)$ separately for each distance r_n. Since we cannot safely assume that subsequently measured values $\hat{g}_{XY,i}(r_n)$, $\hat{g}_{XY,i+j}(r_n)$ are uncorrelated, we have to compute the error estimate according to eq. (4.30) so that

$$\hat{\epsilon}\left(\hat{g}_{XY}(r_n)\right) = \sqrt{\frac{1}{N}\sum_{j=-j_{\max}}^{j_{\max}} {}^{b}\hat{R}_j^{\hat{g}\hat{g}}(r_n)} \tag{7.37}$$

with the biased auto-covariance estimator ${}^{b}\hat{R}_j^{\hat{g}\hat{g}}(r_n)$ constructed according to eq. (4.26), which then reads

$${}^{b}\hat{R}_j^{\hat{g}\hat{g}}(r_n) = \frac{1}{N}\sum_{i=1}^{N-|j|}\left(\hat{g}_{XY,i}(r_n) - \frac{1}{N}\sum_{k=1}^{N}\hat{g}_{XY,k}(r_n)\right) \times \left(\hat{g}_{XY,i+j}(r_n) - \frac{1}{N}\sum_{k=1}^{N}\hat{g}_{XY,k}(r_n)\right). \tag{7.38}$$

Of course, ${}^{b}\hat{R}_j^{\hat{g}\hat{g}}(r_n)$ can be equivalently evaluated according to eq. (4.40) for reasons of computational efficiency.

For systems with fluctuating box volumes, eq. (7.35) does not strictly hold because generally, $V_i \neq \bar{V}$. Nevertheless, we can follow the

same procedure as described above because $\langle g_{XY}(r)\rangle \approx \left\langle \frac{\rho_{XY}(r)}{\rho_Y} \right\rangle$ is a sufficiently good approximation for large N_X, N_Y, and N by virtue of the law of large numbers.

It is important to note, however, that there is absolutely no justification for using this approximation for any other purpose except for estimating $\hat{\epsilon}\,(\hat{g}_{XY}(r_n))$. In particular, under no circumstances should it be used for evaluating $\hat{g}_{XY}(r_n)$ because neither could this improve computational efficiency nor numerical accuracy. After all, if anything, it would yield biased results!

7.A.1.3 Error estimation of potentials of mean force

The PMF $w_{XY}(r)$ between species X and Y is computed from the natural logarithm of the corresponding RDF $g_{XY}(r)$ according to

$$w_{XY}(r) = -k_{\mathrm{B}}T\,\ln(g_{XY}(r))\;. \tag{7.39}$$

For large r, $g_{XY}(r) \approx 1$, so that we can approximate the logarithm by its first-order Taylor expansion around 1, which is $\ln(x)|_1 = x - 1 + \mathcal{O}((x-1)^2)$. This linearization allows us to approximate $w_{XY}(r)$ as

$$w_{XY}(r) \approx k_{\mathrm{B}}T\,\left(\frac{\langle\rho_{XY}(r)\rangle}{\langle\rho_Y\rangle} - 1\right) \quad \text{for large } r\,, \tag{7.40}$$

so that by using again the approximation $\langle g_{XY}(r)\rangle \approx \left\langle \frac{\rho_{XY}(r)}{\rho_Y} \right\rangle$, we can obtain the statistical error of the estimator $\hat{w}_{XY}(r)$ in the same manner as we have done for $\hat{g}_{XY}(r)$, reading

$$\hat{\epsilon}\,(\hat{w}_{XY}(r_n)) = \sqrt{\frac{1}{N}\sum_{j=-N}^{N} {}^{b}\hat{R}_j^{\hat{w}\hat{w}}(r_n)} \tag{7.41}$$

with

$$ {}^{b}\hat{R}_j^{\hat{w}\hat{w}}(r_n) = \frac{1}{N}\sum_{i=1}^{N-|j|}\left(\hat{w}_{XY,i}(r_n) - \frac{1}{N}\sum_{k=1}^{N}\hat{w}_{XY,k}(r_n)\right) \times \left(\hat{w}_{XY,i+j}(r_n) - \frac{1}{N}\sum_{k=1}^{N}\hat{w}_{XY,k}(r_n)\right) . \quad (7.42) $$

Since the linearization is only valid for large r where $g_{XY}(r) \approx 1$, this error estimate is not exact for $r \to 0$. Nevertheless, since the statistical error analysis is only relevant for the PMF's asymptotic behavior at large separations, this approach is sufficient for our purposes.

7.B Additional Results

7.B.1 Bulk systems

7.B.1.1 Volumetric system properties

pure $[C_4C_1Im]^+[PF_6]^-$ (all-atom)

c (mol/l)	$\bar{V}$ (nm^3)	$\bar{\varrho}$ (kg/m^3)	ϱ_{exp} (kg/m^3)	$\Delta\varrho$ (%)
4.62987(4)	38,735.0(3)	1,315.735(10)	1,360.47	-3.29

pure $[C_4C_1Im]^+[PF_6]^-$ (coarse-grained)

c (mol/l)	$\bar{V}$ (nm^3)	$\bar{\varrho}$ (kg/m^3)	ϱ_{exp} (kg/m^3)	$\Delta\varrho$ (%)
4.78280(2)	124,396.7(5)	1,359.223(6)	1,360.47	-0.09

$[C_4C_1Im]^+$ $[NTf_2]^-$ in PC (all-atom)

c (mol/l)	$\bar{V}$ (nm^3)	$\bar{\varrho}$ (kg/m^3)	ϱ_{exp} (kg/m^3)	$\Delta\varrho$ (%)
0.00000(0)	139.46(5)	1,215.5(4)	1,197.30	1.52
0.53340(1)	622.628(5)	1,258.31(1)	1,229.92	2.31
0.96600(1)	859.490(1)	1,292.67(1)	1,262.49	2.39
1.62504(1)	510.922(1)	1,345.08(1)	1,307.08	2.91
2.10316(1)	394.772(3)	1,383.12(1)	1,339.01	3.29
2.46649(2)	336.619(3)	1,412.06(1)	1,363.58	3.56
2.75140(2)	301.763(3)	1,434.72(1)	1,382.19	3.80
2.98136(3)	278.487(3)	1,452.98(2)	1,396.75	4.03
3.17022(4)	261.896(3)	1,467.99(2)	1,408.63	4.21
3.32780(4)	249.495(3)	1,480.49(2)	1,418.32	4.38
3.46103(7)	239.891(5)	1,491.00(3)	1,426.15	4.55
3.57732(5)	232.092(3)	1,500.20(2)	1,432.52	4.72

NaCl in SPC/E water (all-atom)

c (mol/l)	$\bar{V}$ (nm^3)	$\bar{\varrho}$ (kg/m^3)	ϱ_{exp} (kg/m^3)	$\Delta\varrho$ (%)
1.155534(2)	5,388.87(1)	1,047.766(2)	1,042.34	0.52
2.432431(8)	2,559.999(8)	1,098.209(4)	1,090.56	0.70
4.433304(9)	80,905.0(2)	1,168.069(2)	1,162.79	0.45
4.86353(2)	1,280.349(5)	1,181.711(5)	1,178.07	0.31
5.19117(3)	1,199.541(7)	1,191.838(7)	1,189.70	0.18

Table 7.B.1: Volumetric system properties. The listed values are molar ion pair concentration c (mol/l), average simulation box volume $\bar{V}$ (nm^3), average mass density $\bar{\varrho}$ (kg/m^3), experimental mass density ϱ_{exp} (kg/m^3), and relative deviation $\Delta\varrho = \frac{\bar{\varrho}-\varrho_{exp}}{\varrho_{exp}}$ (%). The experimental value of ϱ_{exp} for $[C_4C_1Im]^+[PF_6]^-$ at 300 K is a linear extrapolation of temperature-dependent mass density measurements taken from Machida *et al.*,[273] whereas the values of ϱ_{exp} for $[C_4C_1Im]^+$ $[NTf_2]^-$ in PC are linear interpolations of temperature- and concentration-dependent measurements obtained from Vraneš *et al.*[329] For aqueous NaCl, the values of ϱ_{exp} are linear inter- and extrapolations of temperature- and concentration-dependent data from ref. 301.

7.B.1.2 Static relative dielectric permittivities

$[C_4C_1Im]^+[NTf_2]^-$ in PC

x	c (mol/l)	ε_r	λ_D (nm)	λ_S (nm)
0.00	0.00	59.3(6)	—	—
0.05	0.53	46(3)	0.32(1)	0.67(3)
0.10	0.97	39(5)	0.22(1)	0.65(4)
0.20	1.63	28(3)	0.144(8)	0.496(8)
0.30	2.10	23(3)	0.114(8)	0.465(6)
0.40	2.47	20(3)	0.099(7)	0.584(9)
0.50	2.75	15(2)	0.081(6)	0.607(4)
0.60	2.98	13(2)	0.073(4)	0.686(4)
0.70	3.17	12(1)	0.068(3)	0.753(6)
0.80	3.33	10.0(8)	0.060(2)	0.846(8)
0.90	3.46	10.5(7)	0.060(2)	0.95(1)
1.00	3.58	9.1(5)	0.055(1)	1.07(1)

aqueous NaCl

x	c (mol/l)	ε_r	λ_D (nm)	λ_S (nm)
0.02	1.16	53(2)	0.233(3)	0.25(1)
0.04	2.43	47(4)	0.151(6)	0.197(8)
0.09	4.86	35(3)	0.093(4)	0.32(2)
0.10	5.19	33(3)	0.087(4)	0.33(1)

Table 7.B.2: Static relative permittivities ε_r, Debye lengths λ_D, and effective screening lengths λ_S for solutions of $[C_4C_1Im]^+[NTf_2]^-$ in PC (top) and NaCl in water (bottom) at different concentrations. The numbers in parentheses represent the uncertainty of the last digit.

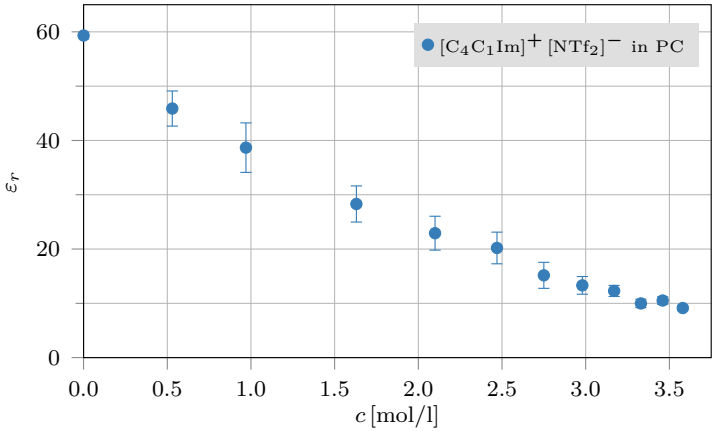

Figure 7.B.1: Static relative dielectric permittivities ε_r of $[C_4C_1Im]^+[NTf_2]^-$ in PC as a function of molar concentration c according to table 7.B.2.

7.B.1.3 PMF behavior over time

As stated in the main chapter, when analyzing simulations of concentrated ionic liquid systems, it is crucial that enough simulation time has been allowed for such systems to reach thermal equilibrium. The following plots show how the PMFs of the largest investigated systems (pure $[C_4C_1Im]^+[PF_6]^-$, AA and CG models) change over time.

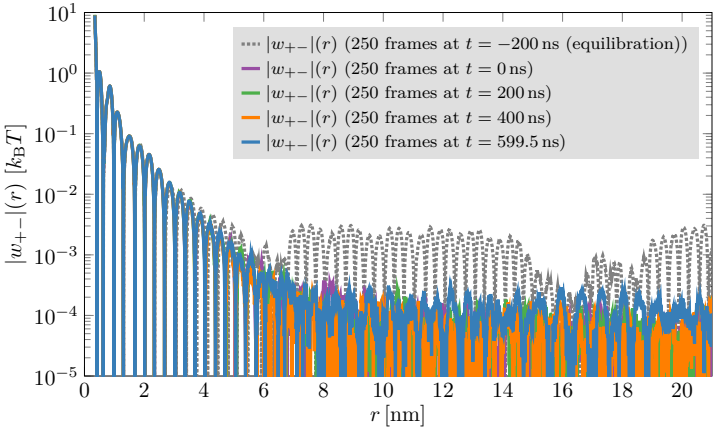

Figure 7.B.2: Absolute value of the potential of mean force $|w_{+-}|(r)$ between anions and cations in neat $[C_4C_1Im]^+[PF_6]^-$ (AA model) for 250 analyzed frames (corresponding to a time span $\Delta t = 0.5$ ns) taken at different time steps t during the simulation. The first PMF at $t = -200$ ns (dashed gray line) was computed from trajectory data during system equilibration. Even though its short-range behavior is similar to the remaining PMF curves, this PMF exhibits comparatively large-amplitude, regular oscillations in its tail, showing that the system is not properly equilibrated at this point in time. The remaining PMFs were computed for the same number of frames but at times $t \in \{0, 200, 400, 599.5\}$ ns after equilibration. After equilibration, all PMFs show the same qualitative behavior with rather noisy tails of similar amplitude, demonstrating that the system has reached an equilibrium state.

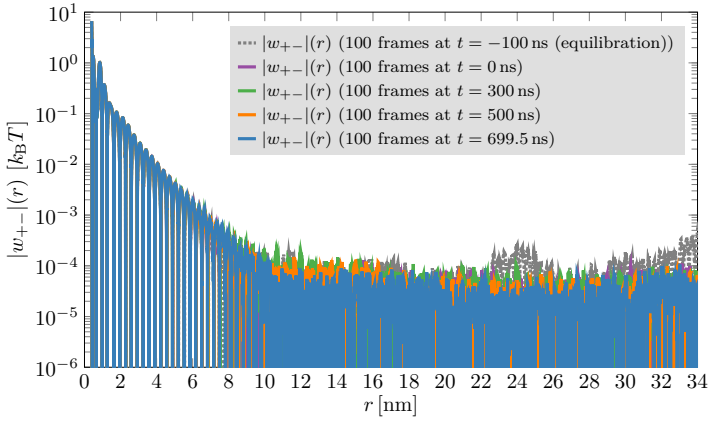

Figure 7.B.3: Absolute value of the potential of mean force $|w_{+-}|(r)$ between anions and cations in neat $[C_4C_1Im]^+[PF_6]^-$ (CG model) for 100 analyzed frames (corresponding to a time span $\Delta t = 0.5$ ns) taken at different time steps t during the simulation. The first PMF at $t = -100$ ns (dashed gray line) was computed from trajectory data during system equilibration. It is clearly visible that there are small structural artifacts in the PMF tail at $r \approx 24$ nm and for $r > 29$ nm, showing that the system is not yet equilibrated at this point in time. The remaining PMFs were computed for the same number of frames but at times $t \in \{0, 300, 500, 699.5\}$ ns after equilibration. Obviously, the structural artifacts have vanished after equilibration, and all PMFs show the same qualitative behavior, demonstrating that the system is indeed equilibrated.

The PMFs shown in figs. 7.B.2 and 7.B.3 demonstrate that the systems are properly equilibrated, however, they do not yield implications about the relaxation of the *cumulative* PMF behavior over time. Therefore, figs. 7.B.4 and 7.B.5 show the PMFs' relaxation behavior depending on the number of analyzed frames after equilibration.

For both molecular models, the extent of the damped oscillatory region increases with simulation time but the qualitative PMF behavior remains unchanged and without any indication for a long-ranged, monotonic decay.

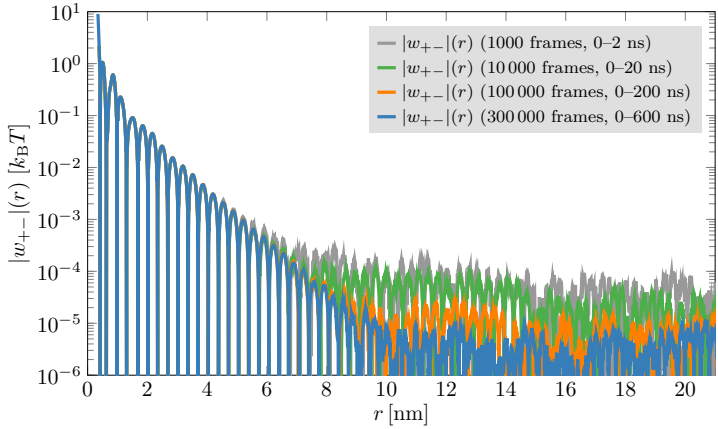

Figure 7.B.4: Absolute value of the potential of mean force $|w_{+-}|(r)$ between anions and cations in neat $[C_4C_1Im]^+[PF_6]^-$(AA model) for different numbers of analyzed frames (i.e., time spans). Regardless of the number of analyzed frames, the PMFs exhibit an exponentially damped oscillatory behavior, followed by rather noisy oscillations of almost constant amplitude. As the number of analyzed frames increases, the extent of the exponentially damped region increases to larger distances and the amplitude of the oscillatory tail decreases. However, there is no sign of any long-range monotonic decay.

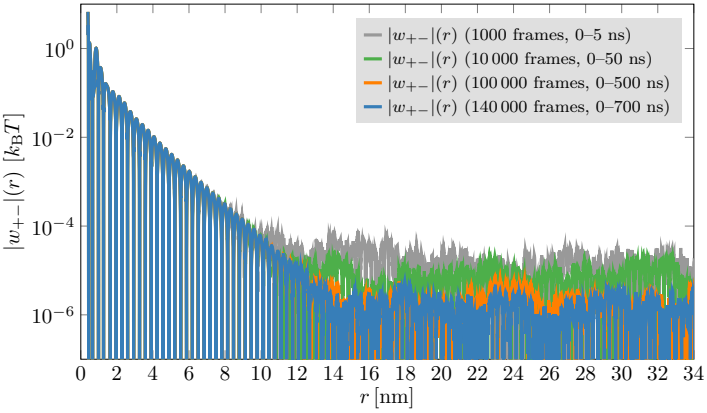

Figure 7.B.5: Absolute value of the potential of mean force $|w_{+-}|(r)$ between anions and cations in neat $[C_4C_1Im]^+[PF_6]^-$(CG model) for different numbers of analyzed frames (i.e., time spans). As for the all-atom model, the PMFs exhibit an exponentially damped oscillatory behavior, followed by rather noisy oscillations of almost constant amplitude. Likewise, as the number of analyzed frames increases, the extent of the exponentially damped region increases to larger distances and the amplitude of the oscillatory tail decreases. Again, there is no sign of any long-range monotonic decay.

7.B.1.4 Screening length scaling analysis of $[C_4C_1Im]^+[NTf_2]^-$ in propylene carbonate

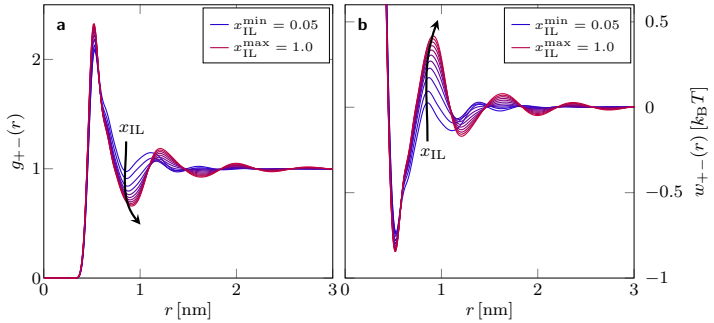

Figure 7.B.6: Panel a: Cation-anion radial distribution functions $g_{+-}(r)$ of $[C_4C_1Im]^+[NTf_2]^-$ in propylene carbonate for different IL mole fractions x ranging from $x = 0.05$ (blue) to $x = 1.0$ (red). Panel b: Corresponding cation-anion potentials of mean force $w_{+-}(r)$ of the same systems (same color code). Arrows indicate increasing IL mole fraction.

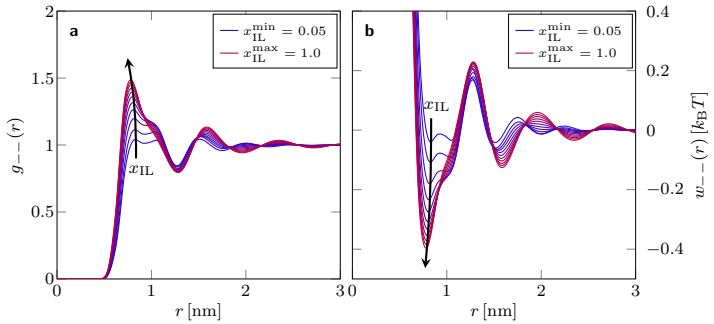

Figure 7.B.7: Panel a: Anion-anion radial distribution functions $g_{--}(r)$ of $[C_4C_1Im]^+[NTf_2]^-$ in propylene carbonate for different IL mole fractions x ranging from $x = 0.05$ (blue) to $x = 1.0$ (red). Panel b: Corresponding anion-anion potentials of mean force $w_{--}(r)$ of the same systems (same color code). Arrows indicate increasing IL mole fraction.

Listed below in tables 7.B.3 to 7.B.5 are the parameters resulting from fits of a superposition of $k = 2$ oscillatory, exponentially damped

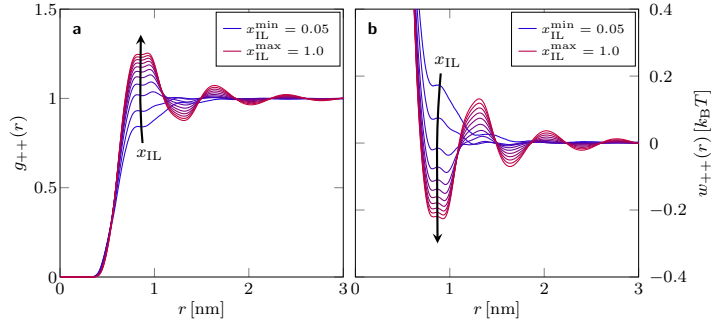

Figure 7.B.8: Panel a: Cation-cation radial distribution functions $g_{++}(r)$ of $[C_4C_1Im]^+\,[NTf_2]^-$ in propylene carbonate for different IL mole fractions x ranging from $x = 0.05$ (blue) to $x = 1.0$ (red). Panel b: Corresponding cation-cation potentials of mean force $w_{++}(r)$ of the same systems (same color code). Arrows indicate increasing IL mole fraction.

functions of the form

$$f(r) = \sum_{n=1}^{k} \frac{A_n}{r} \cos\left(\omega_n\, r - \phi_n\right) \exp\left(-\frac{r}{\lambda_n}\right) \tag{7.43}$$

to the PMFs in solutions of $[C_4C_1Im]^+\,[NTf_2]^-$ in propylene carbonate at different IL mole fractions x.

x	c_{IL} (mol/l)	A_1 ($k_{\mathrm{B}}T$)	λ_1 (nm)	$2\pi/\omega_1$ (nm)	ϕ_1	A_2 ($k_{\mathrm{B}}T$)	λ_2 (nm)	$2\pi/\omega_2$ (nm)	ϕ_2	R^2
0.05	0.53	1.11(4)	0.444(5)	0.477(1)	5.83(5)	-15(2)	0.222(3)	∞	—	0.9955
0.10	0.97	1.13(7)	0.404(6)	0.458(1)	0.38(7)	9534(5496)	0.158(7)	116(1)	2(44)	0.9948
0.20	1.63	0.39(2)	0.496(8)	0.465(3)	5.87(5)	2.8(2)	0.309(5)	0.799(3)	6.04(6)	0.9980
0.30	2.10	0.79(8)	0.41(1)	0.468(6)	5.6(1)	1.6(1)	0.395(7)	0.729(3)	1.37(7)	0.9966
0.40	2.47	1.16(9)	0.373(7)	0.465(5)	5.6(1)	1.42(5)	0.462(4)	0.731(1)	1.56(3)	0.9990
0.50	2.75	1.5(1)	0.348(6)	0.461(5)	5.84(9)	1.14(2)	0.555(3)	0.7383(8)	1.50(2)	0.9996
0.60	2.98	1.7(1)	0.339(6)	0.464(5)	5.73(9)	1.02(1)	0.636(3)	0.7409(6)	1.45(1)	0.9997
0.70	3.17	1.5(1)	0.351(6)	0.467(5)	5.55(9)	0.99(1)	0.700(3)	0.7446(5)	1.35(1)	0.9998
0.80	3.33	1.6(2)	0.343(8)	0.468(7)	5.5(1)	0.90(1)	0.786(4)	0.7457(5)	1.32(1)	0.9998
0.90	3.46	1.6(2)	0.34(1)	0.468(8)	5.53(1)	0.83(1)	0.871(5)	0.7471(5)	1.28(1)	0.9997
1.00	3.58	2.0(3)	0.33(1)	0.48(1)	5.1(2)	0.81(1)	0.941(7)	0.7457(5)	1.28(1)	0.9997

Table 7.B.3: Fit parameters of eq. (7.43) to cation-anion PMFs $w_{+-}(r)$ in solutions of $[C_4C_1Im]^+\,[NTf_2]^-$ in propylene carbonate for different mole fractions x in the fit range $1.2 \leq r \leq 3.0$ nm. The values (units) are IL mole fraction x, concentration c (mol/l), amplitudes A_n ($k_{\mathrm{B}}T$), wavelengths $2\pi/\omega_n$ (nm), phase shifts ϕ_n, and the coefficient of determination R^2. The numbers in parentheses represent the uncertainty of the last digit.

x	c_{IL} (mol/l)	A_1 ($k_{\mathrm{B}}T$)	λ_1 (nm)	$2\pi/\omega_1$ (nm)	ϕ_1	A_2 ($k_{\mathrm{B}}T$)	λ_2 (nm)	$2\pi/\omega_2$ (nm)	ϕ_2	R^2
0.05	0.53	3.8(1)	0.421(4)	0.4843(7)	4.09(3)	4.3(4)	0.308(7)	∞	—	0.9976
0.10	0.97	0.9(1)	0.56(1)	0.463(2)	5.4(1)	88(10)	0.201(4)	0.489(4)	3.7(1)	0.9995
0.20	1.63	3.8(2)	0.389(5)	0.475(3)	4.61(7)	1.9(2)	0.36(1)	0.714(5)	4.8(1)	0.9991
0.30	2.10	3.5(2)	0.382(4)	0.469(3)	4.94(5)	1.75(5)	0.465(6)	0.720(2)	4.82(4)	0.9996
0.40	2.47	3.5(1)	0.373(4)	0.466(2)	5.16(5)	1.69(5)	0.522(4)	0.723(1)	4.79(2)	0.9998
0.50	2.75	3.8(2)	0.358(4)	0.466(3)	5.24(5)	1.40(3)	0.607(4)	0.7282(7)	4.70(2)	0.9998
0.60	2.98	4.0(2)	0.349(4)	0.464(3)	5.37(5)	1.23(2)	0.686(4)	0.7310(7)	4.63(1)	0.9998
0.70	3.17	5.0(4)	0.329(5)	0.464(4)	5.46(8)	1.13(2)	0.753(6)	0.7342(7)	4.54(2)	0.9997
0.80	3.33	6.3(6)	0.312(6)	0.468(6)	5.4(1)	0.98(2)	0.846(8)	0.7371(8)	4.46(1)	0.9996
0.90	3.46	7.5(9)	0.303(7)	0.476(7)	5.1(1)	0.85(2)	0.95(1)	0.7394(8)	4.40(2)	0.9995
1.00	3.58	8(1)	0.296(8)	0.479(8)	5.0(1)	0.76(2)	1.07(1)	0.7388(9)	4.38(2)	0.9994

Table 7.B.4: Fit parameters of eq. (7.43) to anion-anion PMFs $w_{--}(r)$ in solutions of $[\mathrm{C_4C_1Im}]^+\,[\mathrm{NTf_2}]^-$ in propylene carbonate for different mole fractions x in the fit range $1.2 \leq r \leq 3.0\,\mathrm{nm}$. The values (units) are IL mole fraction x, concentration c (mol/l), amplitudes A_n ($k_{\mathrm{B}}T$), wavelengths $2\pi/\omega_n$ (nm), phase shifts ϕ_n, and the coefficient of determination R^2. The numbers in parentheses represent the uncertainty of the last digit.

x	c_{IL} (mol/l)	A_1 ($k_{\mathrm{B}}T$)	λ_1 (nm)	$2\pi/\omega_1$ (nm)	ϕ_1	A_2 ($k_{\mathrm{B}}T$)	λ_2 (nm)	$2\pi/\omega_2$ (nm)	ϕ_2	R^2
0.05	0.53	0.09(1)	0.67(3)	0.47(1)	0.7(1)	2.8(2)	0.302(4)	∞	—	0.9853
0.10	0.97	0.07(1)	0.65(4)	0.46(2)	1.0(1)	0.21(6)	0.43(3)	1.11(2)	6.0(2)	0.8456
0.20	1.63	0.24(3)	0.46(1)	0.48(1)	5.5(1)	0.18(3)	0.44(2)	0.96(2)	0.3(2)	0.9868
0.30	2.10	56(25)	0.19(1)	0.53(2)	4.3(3)	0.3(1)	0.45(3)	0.86(1)	1.6(2)	0.9905
0.40	2.47	12(2)	0.226(6)	0.50(1)	5.0(2)	0.26(2)	0.58(1)	0.740(3)	4.77(7)	0.9990
0.50	2.75	92(34)	0.169(7)	0.45(2)	0.9(4)	0.50(2)	0.597(6)	0.734(2)	4.95(4)	0.9991
0.60	2.98	12(2)	0.227(6)	0.48(1)	5.3(3)	0.56(1)	0.668(3)	0.730(1)	5.12(3)	0.9997
0.70	3.17	24(4)	0.206(4)	0.47(1)	5.8(2)	0.584(7)	0.744(3)	0.7394(5)	4.89(1)	0.9999
0.80	3.33	40(7)	0.193(4)	0.46(1)	0.1(3)	0.606(6)	0.815(3)	0.7411(4)	4.82(1)	0.9999
0.90	3.46	84(16)	0.176(4)	0.43(2)	1.3(3)	0.604(5)	0.895(3)	0.7444(4)	4.72(1)	0.9999
1.00	3.58	104(22)	0.174(4)	0.43(2)	1.6(3)	0.594(4)	0.983(3)	0.7432(4)	4.71(1)	0.9999

Table 7.B.5: Fit parameters of eq. (7.43) to cation-cation PMFs $w_{++}(r)$ in solutions of $[\mathrm{C_4C_1Im}]^+\,[\mathrm{NTf_2}]^-$ in propylene carbonate for different mole fractions x in the fit range $1.2 \leq r \leq 3.0\,\mathrm{nm}$. The values (units) are IL mole fraction x, concentration c (mol/l), amplitudes A_n ($k_{\mathrm{B}}T$), wavelengths $2\pi/\omega_n$ (nm), phase shifts ϕ_n, and the coefficient of determination R^2. The numbers in parentheses represent the uncertainty of the last digit.

Fitting the data to eq. (7.43) with $k = 3$ terms resulted in extremely unstable results under slight variation of initial fit parameters, while setting $k = 1$ lead to large fitting errors.

7.B.2 Confined ionic liquid systems

7.B.2.1 Number density profiles

To investigate the layered structure of the IL in the z-direction of the different confined systems, we computed the center-of-mass-based number densities of ions according to

$$\rho_n^{\pm}(z) = \left\langle \sum_i \delta\left(z - z_i^{\mathrm{com}}\right) \right\rangle, \tag{7.44}$$

where $\delta(\cdot)$ is the Dirac delta function, the operator $\langle\cdot\rangle$ denotes the canonical average, and the index i runs over all molecules in the system with center-of-mass position z_i^{com}, respectively. For the numerical evaluation of eq. (7.44), the system is discretized in the z-direction into n slabs of width $l_z = {}^{L_z}\!/_{n}$, where L_z is the length of the simulation box in the z-direction. The number density profile is then calculated according to

$$\rho_n^{\pm}(z) = \left\langle \frac{1}{L_x\, L_y\, l_z} \sum_{\substack{i \\ 2|z - z_i^{\mathrm{com}}| < l_z}} 1 \right\rangle, \tag{7.45}$$

The top row of fig. 7.B.9 shows snapshots of the x-z-plane of all confined systems (from left to right: $L_z = 8.2\,\mathrm{nm}$, $L_z = 9.9\,\mathrm{nm}$, $L_z = 13.2\,\mathrm{nm}$, $L_z = 14.8\,\mathrm{nm}$). The corresponding center-of-mass-based number densities of $[\mathrm{C_4C_1Im}]^+$ cations ($\rho_n^+(z)$, blue) and $[\mathrm{NTf_2}]^-$ anions ($\rho_n^-(z)$, red) are displayed in the bottom row.

The ion number densities shown in fig. 7.B.9 make it clear that on either side of the systems, the first layer close to each of the negatively charged walls consists entirely of cations, all systems exhibit a very similar structure with alternating cation and anion layers, and this structural feature decays exponentially towards the center of the systems. A closer look at the number density profiles of the first three systems reveals that while all profiles decay in the same manner, the first cation layers close to the walls do not always have the exact same amplitude. This

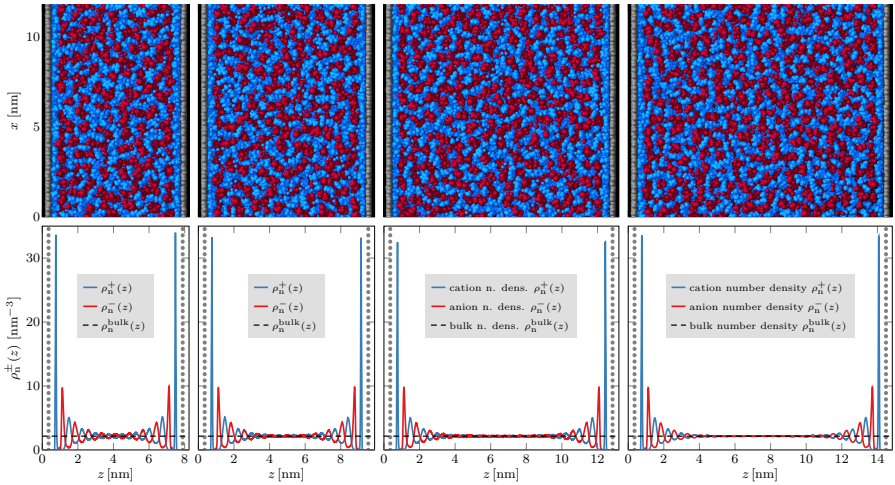

Figure 7.B.9: Top row: Snapshots of the x-z-plane of all confined systems with different simulation box sizes (from left to right: $L_z = 8.2\,\text{nm}$, $L_z = 9.9\,\text{nm}$, $L_z = 13.2\,\text{nm}$, $L_z = 14.8\,\text{nm}$). **Bottom row**: Cation ($\rho_n^+(z)$, blue), anion ($\rho_n^-(z)$, red), and bulk (black, dashed) number density $\rho_n(z)$ of $[C_4C_1Im]^+[NTf_2]^-$ confined between like-charged graphene walls. In the vicinity of the walls (up to $z \approx 1\,\text{nm}$, and likewise, down to $z \approx L_z - 1\,\text{nm}$), the total number density is almost entirely due to cations.

is a consequence of the fact that the total dipole moment of such slab systems fluctuates slowly around zero, and the average ion distributions have not fully converged to perfect symmetry within the simulation times of these systems ($t_{\text{sim}} = 1\,\mu\text{s}$). The largest system (rightmost column in fig. 7.B.9), which is used for our analyses in the main chapter, does not suffer from this inaccuracy due to its much longer simulation time of $t_{\text{sim}} = 4\,\mu\text{s}$. This highlights the very slow dynamics in confined IL systems.

7.B.2.2 Charge density profiles

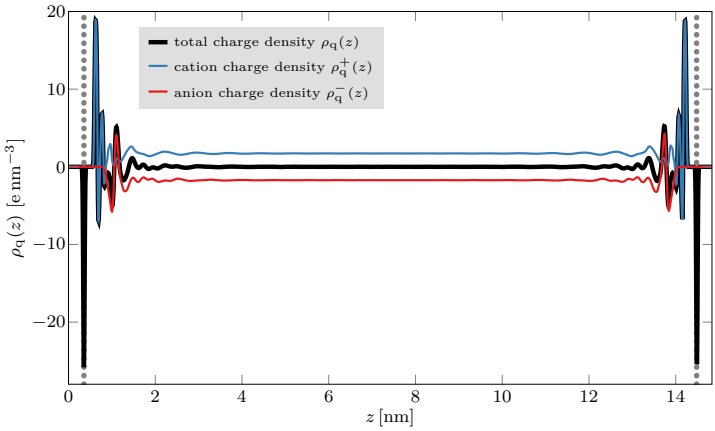

Figure 7.B.10: Cation ($\rho_q^+(z)$, blue), anion ($\rho_q^-(z)$, red), and total (black) charge density $\rho_q(z)$ of $[C_4C_1Im]^+[NTf_2]^-$ confined between like-charged graphene walls. In the vicinity of the walls (up to $z = 0.81$ nm, and likewise, down to $z = L_z - 0.81$ nm), the total charge density is entirely due to cations. Nevertheless, the charge density oscillates around zero in this region, which is due to the negative partial charges of carbon atoms in the cations' butyl and methyl side chains. Due to the typically preferred orientations of cations close the surface, these atoms have a high probability to be located at a specific distance from the surface, yielding a net-negative charge density in this region. Thereafter, between $z = 0.81$ nm and $z = 1.2$ nm, the anion contribution dominates. For larger distances, both cations and anions have relatively similar contributions (in magnitude) to the total charge density. Towards the center of the system, all charge densities converge to their corresponding bulk values.

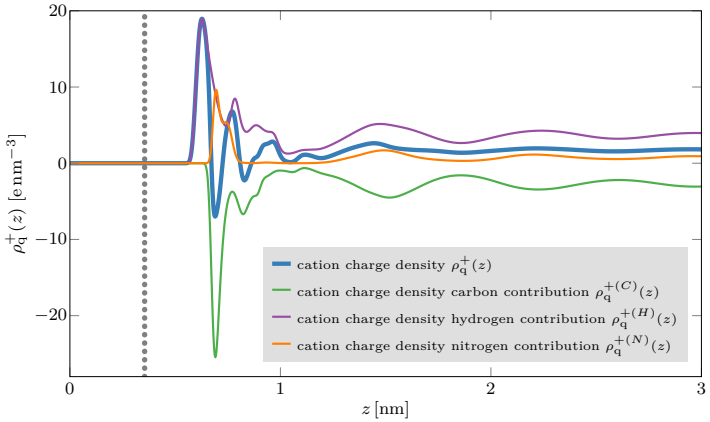

Figure 7.B.11: Different contributions to the cation charge density ($\rho_q^+(z)$ (thick blue line) of $[C_4C_1Im]^+[NTf_2]^-$ confined between like-charged graphene walls. Close to the surface, the $[C_4C_1Im]^+$ ions are highly ordered so that their molecular structure affects the cumulative cation charge density. As a consequence, the first positive peak in $\rho_q^+(z)$ at $z \approx 0.63\,\text{nm}$ is entirely due to the contribution of hydrogen atoms $\rho_q^{+(H)}(z)$ (purple line), and the negative peaks at $z \approx 0.69\,\text{nm}$ and $z \approx 0.83\,\text{nm}$ is caused by the contribution of carbon atoms $\rho_q^{+(C)}(z)$ (green line).

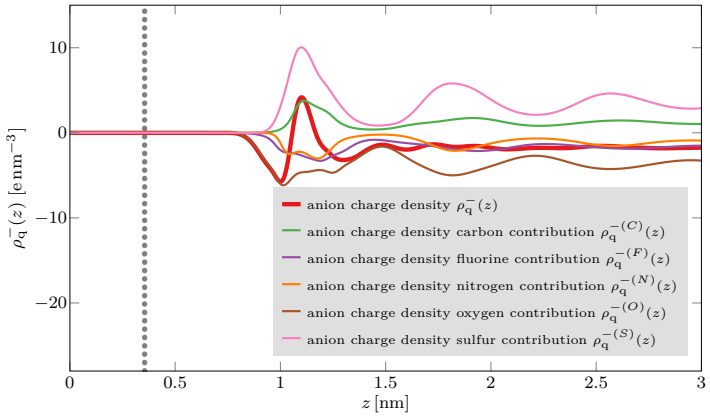

Figure 7.B.12: Different contributions to the anion charge density ($\rho_q^-(z)$ (red) of $[C_4C_1Im]^+[NTf_2]^-$ confined between like-charged graphene walls. The first negative peak in $\rho_q^-(z)$ at $z \approx 1.0\,\text{nm}$ is mostly due to the contribution of oxygen atoms $\rho_q^{-(O)}(z)$ (brown line), and the positive peak at $z \approx 1.1\,\text{nm}$ is caused by the contributions of carbon ($\rho_q^{-(C)}(z)$, green line) and of sulfur atoms ($\rho_q^{-(S)}(z)$, pink line). Thereafter, even though especially the oxygen and sulfur contributions still oscillate, the different contributions mostly cancel out so that the total anion charge density converges rather quickly to its bulk value.

7.B.2.3 Position-dependent RDFs

Computing RDFs $g_{XY}^{(i)}(r;\, z_i)$ between a spatially selective group of species X consisting only of molecules whose center of mass lies within a slab extending in the xy-plane and centered at $z = z_i$ with width l_z, and a second group of molecular species Y without such constraints, requires slight modifications of eqs. (7.31) and (7.32). If the molecular species in X are different from those in Y, i.e., the groups are disjoint, eq. (7.31) has to read

$$\hat{g}_{XY}^{(i)}(r_n, z_i) = \frac{1}{N\, \bar{\rho}_Y^{\text{bulk}}\, V_n^{\text{shell}}} \sum_{m=1}^{N} \frac{1}{N_{X,i,m}} \times \sum_{j=1}^{N_{X,i,m}} \sum_{k=1}^{N_Y} \delta\left(\left\lfloor \frac{\|\boldsymbol{r}_{k,m} - \boldsymbol{r}_{j,m}\|_{\text{pbc}}}{\Delta r} \right\rfloor - n \right), \tag{7.46}$$

where $\bar{\rho}_Y^{\text{bulk}}$ is the average bulk number density of molecules of species Y, and the second sum runs over all $N_{X,i,m}$ molecules of species X whose center of mass positions' z-coordinates z_m^{com} fulfill the condition $2|z_i - z_m^{\text{com}}| \leq l_z$ at time step m.

If $X = Y$, the groups overlap (the first group is a subset of the second) so that one has to exclude distances of molecules with themselves. Since the RDF bin width Δr is usually chosen much smaller than the smallest intermolecular distance, this can be accomplished by simply setting $\hat{g}_{XY}^{(i)}(r_n, z_i) = 0$ if $n = 0$.

Shown below in fig. 7.B.13 are the results of z-position-dependent RDFs $g_{-+}^{(i)}(r;\, z_i)$ (anion-cation), $g_{++}^{(i)}(r;\, z_i)$ (cation-cation), and $g_{--}^{(i)}(r;\, z_i)$ (anion-anion) computed in this manner, as were the cation-anion RDFs displayed in section 7.2.4. The amplitudes of the first maxima and minima (middles and bottom row in fig. 7.B.13) decay with z_i in a similar manner as the ones shown in the main chapter.

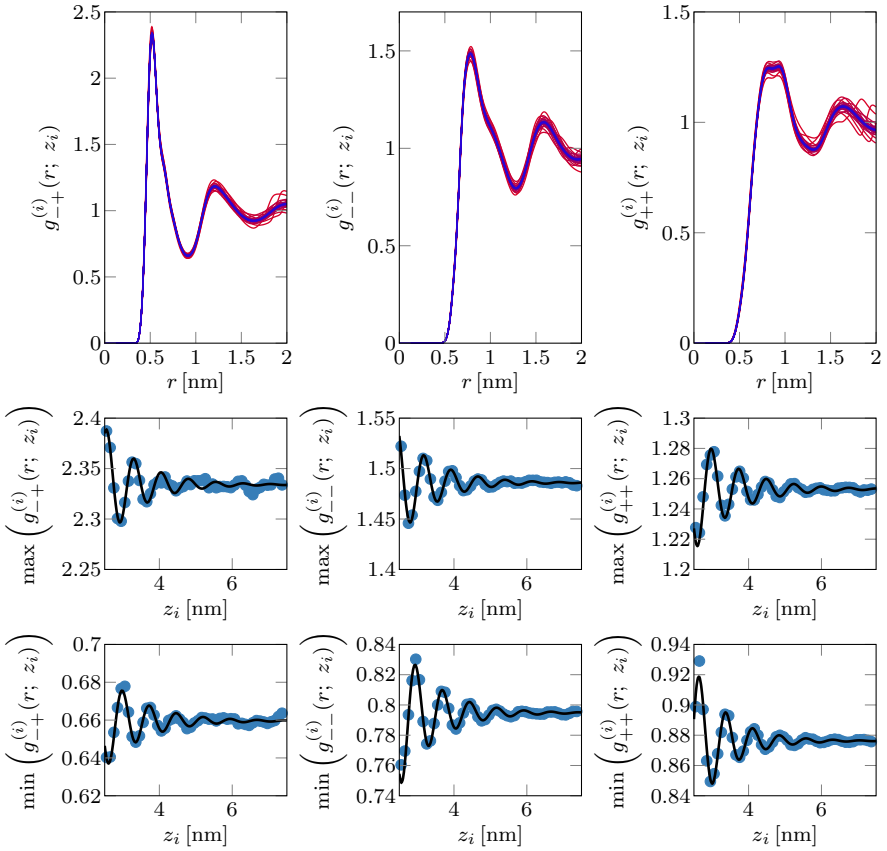

Figure 7.B.13: Top row: z-distance-dependent RDFs $g_{-+}^{(i)}(r;\, z_i)$ (anion-cation, left column), $g_{--}^{(i)}(r;\, z_i)$ (anion-anion, middle column), and $g_{++}^{(i)}(r;\, z_i)$ (cation-cation, right column) of $[C_4C_1Im]^+\,[NTf_2]^-$ confined between like-charged graphene walls. The corresponding amplitudes of the first maxima and minima are plotted against the reference distance z_i in the middle and bottom row, respectively. The black lines are fits to an oscillatory exponential decay with a decay length varying between 0.9 and 1.1 nm, consistent with the behavior shown for cation-anion RDFs in the main chapter.

7.B.3 Using reduced-charge ion models in confined systems

In our simulations of confined ILs, we employed the same reduced-charge model as in our bulk simulations. While reduced charges are used to account for electronic polarization effects in ion-ion interactions (see simulation details in the main article), the same reduced charges do not yield a precise description of solid-liquid interactions. This becomes apparent from the fact that 352 counterions with reduced charge are required to compensate the charge of both walls, whereas a model with full charges would only require about 282 counterions. While the overall charge balance remains correct in our simulations, the volume the additionally required 70 counterions consume would not appear in simulations employing models with full charges. The corresponding change in the total IL volume of about 0.8 % (estimated from 8352 vs. 8282 ions of equal molecular volume) is rather negligible. Nevertheless, as counterions accumulate in higher amounts close to the surfaces, this will likely entail changes in the charge distribution close to the surfaces. While this influence may be non-negligible, according to Kjellander,[66] the specific interactions of ions with the surface only influence the phase and amplitude of the electric field's long-range decay modes towards the bulk but not their characteristic decay- and wavelengths. We therefore argue that if such decay modes existed in our systems, it should still be possible to observe them at large distances.

We want to stress here that using IL models with full charges will *not* improve the situation unless electronic polarizability is explicitly taken into account. In fact, non-polarizable models with full charges are known to overestimate interionic Coulomb interactions in ILs and therefore cannot faithfully reproduce interactions with charged surfaces either. Furthermore, as IL models with full charges severely underestimate the mobility of ions, we would expect the confined systems to be practically frozen on time scales accessible to MD simulations if such models were employed.

The formally best approach to describe both ion-surface and bulk ion-ion interactions of ILs more accurately in MD simulations would be to use polarizable force fields, *i.e.*, molecular models with full ionic charges that take electronic polarizability explicitly into account (*e.g.*, by means of inducible point dipoles or Drude oscillators). However, the additional complexity introduced by such models increases the computational cost for simulations of the required length and time scales prohibitively and would have increased the cumulative runtimes of our simulations from months to years. To date, to the best of our knowledge, the approach we chose here yields the most accurate microscopic description of sufficiently large confined IL systems that is at the same time computationally feasible.

7.C Relating Underscreening to Other Measurements

7.C.1 Differential capacitance estimates for different widths of the Stern layer

In the main chapter, we showed the differential capacitance C_d estimated from from the screening length λ_S according to the GCS model

$$C_\mathrm{d} = \left(C_\mathrm{Stern}^{-1} + C_\mathrm{diffuse}^{-1}\right)^{-1} = \frac{\varepsilon_0 \varepsilon_r}{a + \lambda_\mathrm{S}}\,, \tag{7.47}$$

where we set $a = {}^{d}/_{2} \approx 0.2\,\mathrm{nm}$. The resulting plot showed a behavior of C_d estimated for screening lengths from SFB measurements (orange dots with dashed line in fig. 7.9 of the main chapter) that is qualitatively similar to the original plot by Lee *et al.* shown in figure 8 of reference 52 but differs in amplitude. In fig. 7.C.1 below, we show plots of the very same calculations but with the width of the Stern layer set to $a = 2\,d \approx 0.8\,\mathrm{nm}$. The results are all qualitatievly similar to those presented in the main chapter, but the orange line in panel a representing C_d obtained from SFB measurements now reproduces figure 8 of reference 52 exactly. Thus, we conjecture that Lee *et al.* used $a = 2\,d$ in their calculations. Note that for this value of a, the differential capacity estimate obtained from simulation data (blue line) has a better quantitative and qualitative overall agreement with the direct measurements than all other estimates, and the monotonic behavior of λ_S obtained from direct differential capacitance measurements using the inverted GCS model is retained (panel b of fig. 7.C.1).

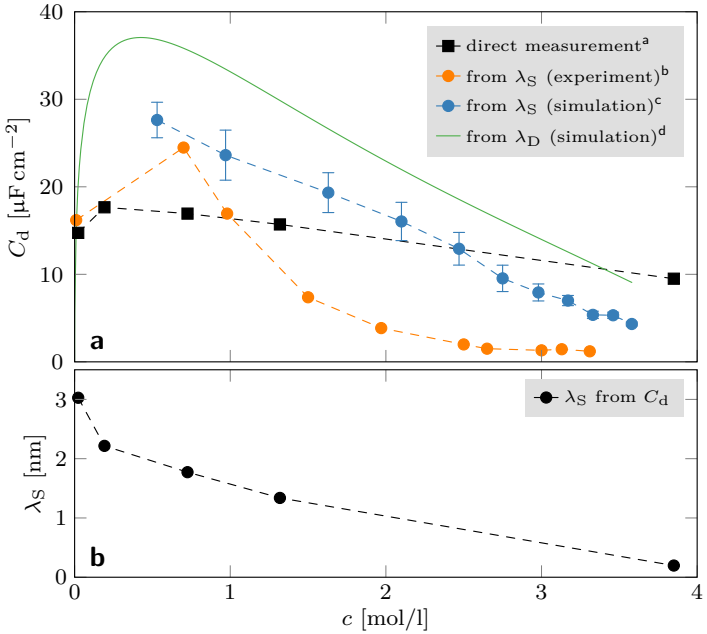

Figure 7.C.1: Panel a: Comparison of the concentration-dependent differential capacitance C_d at the point of zero charge obtained from direct measurements[321] (black squares) and according to the GCS model as defined by eq. (7.47) (orange dots: SFB measurements,[51] blue circles: simulation). The solid green line shows C_d when λ_S is replaced by λ_D in eq. (7.47). Here, we used $a = 2\,d \approx 0.8\,\text{nm}$ for the evaluation of eq. (7.47) instead of $a = d/2$ in the main chapter.
[a]Differential capacitance for $[C_2C_1Im]^+\,[NTf_2]^-$ from Bozym *et al.*.[321]
[b]λ_S and ε_r data for $[C_4C_1Pyrr]^+\,[NTf_2]^-$ from Smith *et al.*.[51]
[c]λ_S and ε_r data from simulations of $[C_4C_1Im]^+\,[NTf_2]^-$ (this work).
[d]λ_D was computed using interpolated ε_r data from simulations of $[C_4C_1Im]^+\,[NTf_2]^-$ (this work).
Panel b: Screening length λ_S computed according to the inverted GCS model (eq. (7.47) solved for λ_S) with C_d from direct measurements,[321] ε_r interpolated from simulations, and $a = 2\,d \approx 0.8\,\text{nm}$.
In both panels, dashed lines serve as a guide to the eye.

7.D GROMACS Simulation Parameters

All bulk systems were simulated in the NpT ensemble in cubic boxes with periodic boundary conditions in all three dimensions, where temperature and pressure were maintained at $T = 300\,\mathrm{K}$ and $p = 1\,\mathrm{bar}$ using a Nosé-Hoover thermostat and Parrinello-Rahman barostat. Short-range van der Waals interactions were computed up to a system-dependent cut-off, and their long-range part was either computed using the smooth particle mesh Ewald (SPME) method with a relative accuracy of 10^{-3}, or taken into account via analytic dispersion corrections for energy and pressure. Long-range Coulomb interactions were computed using the SPME method with a short-range cut-off of at least 1.3 nm, a relative accuracy of 10^{-5} (unless otherwise stated), and tin foil boundary conditions at infinity. The time step of the employed leapfrog integrator was 2 fs for the all-atom models and 5 fs for the coarse-grained IL model.

In the following, we list the GROMACS molecular dynamics parameters used in production runs for all investigated systems.

7.D.1 $[C_4C_1Im]^+[PF_6]^-$(all-atom model)

parameter	value	unit (note)
integrator	md	(leapfrog integrator)
dt	0.002	ps
nsteps	300000000	steps
comm-mode	linear	
nstcomm	50	steps
nstcalcenergy	50	steps
nstxout-compressed	1000	steps
compressed-x-precision	10000	(means 10^{-4} nm)
cutoff-scheme	verlet	
nstlist	40	steps
ns-type	grid	
pbc	xyz	
coulombtype	pme	
coulomb-modifier	potential-shift-verlet	
rcoulomb	1.3	nm
vdwtype	pme	
vdw-modifier	potential-shift-verlet	
rvdw	1.3	nm
tcoupl	nose-hoover	
nsttcouple	5	steps
nh-chain-length	1	
tau-t	2.0	ps
ref-t	300.0	K
pcoupl	parrinello-rahman	
pcoupltype	isotropic	
nstpcouple	5	steps
tau-p	3.0	ps
compressibility	4.5e-5	bar^{-1}
ref-p	1.0	bar
constraints	h-bonds	(fixed length of bonds involving H atoms)
constraint-algorithm	lincs	

Table 7.D.1: GROMACS molecular dynamics simulation parameters used for the simulation of $[C_4C_1Im]^+[PF_6]^-$(all-atom model). Only parameters which differ from the default (or have no default) are listed.

7.D.2 $[C_4C_1Im]^+[PF_6]^-$(coarse-grained model)

parameter	value	unit (note)
integrator	md	(leapfrog integrator)
dt	0.005	ps
nsteps	140000000	steps
comm-mode	linear	
nstcomm	200	steps
nstcalcenergy	200	steps
nstxout-compressed	1000	steps
compressed-x-precision	1000	(means 10^{-3} nm)
cutoff-scheme	verlet	
nstlist	40	steps
ns-type	grid	
pbc	xyz	
coulombtype	pme	
coulomb-modifier	potential-shift-verlet	
rcoulomb	1.6	nm
vdwtype	cut-off	
vdw-modifier	potential-shift-verlet	
dispcorr	enerpres	
rvdw	1.6	nm
tcoupl	nose-hoover	
nh-chain-length	1	
tau-t	5.0	ps
ref-t	300.0	K
pcoupl	parrinello-rahman	
pcoupltype	isotropic	
tau-p	10.0	ps
compressibility	4.5e-5	bar^{-1}
ref-p	1.0	bar
constraints	all-bonds	(rigid molecular geometry)
constraint-algorithm	lincs	

Table 7.D.2: GROMACS molecular dynamics simulation parameters used for the simulation of $[C_4C_1Im]^+[PF_6]^-$(coarse-grained model). Only parameters which differ from the default (or have no default) are listed.

7.D.3 Aqueous NaCl solutions

parameter	value	unit (note)
integrator	md	(leapfrog integrator)
dt	0.002	ps
nsteps	100000000	steps
comm-mode	linear	
nstcomm	50	steps
nstcalcenergy	50	steps
nstxout-compressed	1000	steps
compressed-x-precision	10000	(means 10^{-4} nm)
cutoff-scheme	verlet	
nstlist	40	steps
ns-type	grid	
pbc	xyz	
coulombtype	p3m-ad	
coulomb-modifier	potential-shift-verlet	
rcoulomb	1.2	nm
vdwtype	cut-off	
vdw-modifier	potential-shift-verlet	
dispcorr	enerpres	
rvdw	1.2	nm
ewald-rtol	1.0e-6	
tcoupl	nose-hoover	
nsttcouple	5	steps
nh-chain-length	1	
tau-t	2.0	ps
ref-t	300.0	K
pcoupl	parrinello-rahman	
pcoupltype	isotropic	
nstpcouple	5	steps
tau-p	3.0	ps
compressibility	4.5e-5	bar^{-1}
ref-p	1.0	bar
constraints	all-bonds	(rigid water geometry)
constraint-algorithm	lincs	

Table 7.D.3: GROMACS molecular dynamics simulation parameters used for the simulation of aqueous NaCl solutions. Only parameters which differ from the default (or have no default) are listed.

7.D.4 $[C_4C_1Im]^+[NTf_2]^-$ in PC

parameter	value	unit (note)
integrator	md	(leapfrog integrator)
dt	0.002	ps
nsteps	1073741824	steps ($= 2^{30}$)
comm-mode	linear	
nstcomm	1	steps
nstcalcenergy	50	steps
nstxout-compressed	1000	steps
compressed-x-precision	10000	(means 10^{-4} nm)
cutoff-scheme	verlet	
nstlist	40	steps
ns-type	grid	
pbc	xyz	
coulombtype	pme	
coulomb-modifier	potential-shift-verlet	
rcoulomb	1.3	nm
vdwtype	cut-off	
vdw-modifier	potential-shift-verlet	
dispcorr	enerpres	
rvdw	1.3	nm
tcoupl	nose-hoover	
nsttcouple	5	steps
nh-chain-length	1	
tau-t	2.0	ps
ref-t	300.0	K
pcoupl	parrinello-rahman	
pcoupltype	isotropic	
nstpcouple	5	steps
tau-p	3.0	ps
compressibility	4.5e-5	bar^{-1}
ref-p	1.0	bar
constraints	h-bonds	(fixed length of bonds involving H atoms)
constraint-algorithm	lincs	

Table 7.D.4: GROMACS molecular dynamics simulation parameters used for the simulation of $[C_4C_1Im]^+[NTf_2]^-$ in propylene carbonate. Only parameters which differ from the default (or have no default) are listed.

7.D.5 $[C_4C_1Im]^+[NTf_2]^-$ confined between like-charged graphene walls

parameter	value	unit (note)
integrator	md	(leapfrog integrator)
dt	0.002	ps
nsteps	500000000	steps
comm-mode	linear	
nstcomm	50	steps
nstcalcenergy	50	steps
nstxout-compressed	1000	steps
compressed-x-precision	10000	(means 10^{-4} nm)
cutoff-scheme	verlet	
nstlist	40	steps
ns-type	grid	
pbc	xy	
coulombtype	pme	
coulomb-modifier	potential-shift-verlet	
rcoulomb	1.3	nm
vdwtype	pme	
vdw-modifier	potential-shift-verlet	
dispcorr	no	
rvdw	1.3	nm
ewald-geometry	3dc	
tcoupl	v-rescale	
nsttcouple	-1	steps
tau-t	2.0	ps
ref-t	300.0	K
pcoupl	no	(for equilibration: parrinello-rahman)
pcoupltype	semiisotropic	
nstpcouple	-1	steps
tau-p	3.0	ps
compressibility	0.0 4.5e-5	bar^{-1}
ref-p	1.0 1.0	bar
constraints	h-bonds	(fix length of bonds involving H atoms)
constraint-algorithm	lincs	
nwall	2	
wall-type	harmonic	(not available in a standard GROMACS installation)
wall-r-linpot	-1	
wall-atomtype	WALL WALL	(non-interacting dummy wall atom type)
wall-density	1.0 1.0	(arbitrary, has no effect on harmonic wall coupling)
wall-ewald-zfac	3	

Table 7.D.5: GROMACS molecular dynamics simulation parameters used for the simulation of $[C_4C_1Im]^+[NTf_2]^-$ confined between like-charged graphene walls. Only parameters which differ from the default (or have no default) are listed. The wall type "harmonic" is a custom extension to GROMACS, which is used to couple each graphene wall to its corresponding simulation box face with a harmonic potential. This was necessary during NpT equilibration because the current implementation of reference coordinate scaling does not work in conjunction with semiisotropic pressure coupling. During production runs (NVT ensemble, no pressure coupling), using this wall type has exactly the same effect as applying harmonic position restraints (force constant 10 000 kJ mol^{-1}) to the wall carbon atoms in the z-direction. To constrain the atomic positions in the x- and y-directions, normal position restraints with the same force constant are used. Note that for correct pressure estimates, the forces due to position restraints of the wall atoms and also the forces between atoms *within* each wall have to be excluded from the virial computation. Otherwise, intra-wall forces would invalidate the pressure computation.

References

[1] P. Debye, Polare Molekeln (S. Hirzel, Leipzig, 1929)

[2] J. S. Toll, Causality and the Dispersion Relation: Logical Foundations, *Physical Review* **104**, 1760–1770 (1956)

[3] C. J. Gorter and R. Kronig, On the theory of absorption and dispersion in paramagnetic and dielectric media, *Physica* **3**, 1009–1020 (1936)

[4] F. Kremer and A. Schönhals, eds., Broadband Dielectric Spectroscopy (Springer, Berlin, 2003)

[5] Google Scholar Search Engine, `https://scholar.google.com`, [online; accessed 2021-10-06]

[6] C. Ruan, L. Yang and Y. Li, Immunobiosensor Chips for Detection of Escherichia coli O157:H7 Using Electrochemical Impedance Spectroscopy, *Analytical Chemistry* **74**, 4814–4820 (2002)

[7] A. Soley, M. Lecina, X. Gámez, J. J. Cairó, P. Riu, X. Rosell, R. Bragós and F. Gòdia, On-line monitoring of yeast cell growth by impedance spectroscopy, *Journal of Biotechnology* **118**, 398–405 (2005)

[8] R. Maalouf, C. Fournier-Wirth, J. Coste, H. Chebib, Y. Saïkali, O. Vittori, A. Errachid, J.-P. Cloarec, C. Martelet and N. Jaffrezic-Renault, Label-Free Detection of Bacteria by Electrochemical Impedance Spectroscopy: Comparison to Surface Plasmon Resonance, *Analytical Chemistry* **79**, 4879–4886 (2007)

[9] A. Amirudin and D. Thieny, Application of electrochemical impedance spectroscopy to study the degradation of polymer-coated metals, *Progress in Organic Coatings* **26**, 1–28 (1995)

[10] J. M. McIntyre and H. Q. Pham, Electrochemical impedance spectroscopy; a tool for organic coatings optimizations, *Progress in Organic Coatings* **27**, 201–207 (1996)

[11] P. L. Bonora, F. Deflorian and L. Fedrizzi, Electrochemical impedance spectroscopy as a tool for investigating underpaint corrosion, *Electrochimica Acta* **41**, 1073–1082 (1996)

[12] J. Hollaender, Rapid assessment of food/package interactions by electrochemical impedance spectroscopy (EIS), *Food Additives & Contaminants* **14**, 617–626 (1997)

[13] J.-L. Damez, S. Clerjon, S. Abouelkaram and J. Lepetit, Beef meat electrical impedance spectroscopy and anisotropy sensing for non-invasive early assessment of meat ageing, *Journal of Food Engineering* **85**, 116–122 (2008)

[14] M. Grossi and B. Riccò, Electrical impedance spectroscopy (EIS) for biological analysis and food characterization: a review, *Journal of Sensors and Sensor Systems* **6**, 303–325 (2017)

[15] K. Dokko, M. Mohamedi, Y. Fujita, T. Itoh, M. Nishizawa, M. Umeda and I. Uchida, Kinetic Characterization of Single Particles of $LiCoO_2$ by AC Impedance and Potential Step Methods, *Journal of The Electrochemical Society* **148**, A422 (2001)

[16] R. Kubo, Statistical-Mechanical Theory of Irreversible Processes. I. General Theory and Simple Applications to Magnetic and Conduction Problems, *Journal of the Physical Society of Japan* **12**, 570–586 (1957)

[17] A. N. Krishnamoorthy, J. Zeman, C. Holm and J. Smiatek, Preferential solvation and ion association properties in aqueous dimethyl sulfoxide solutions, *Physical Chemistry Chemical Physics* **18**, 31312–31322 (2016)

[18] J. Hunger, K.-J. Tielrooij, R. Buchner, M. Bonn and H. J. Bakker, Complex Formation in Aqueous Trimethylamine-N-oxide (TMAO) Solutions, *The Journal of Physical Chemistry B* **116**, 4783–4795 (2012)

[19] D. Markthaler, J. Zeman, J. Baz, J. Smiatek and N. Hansen, Validation of Trimethylamine-N-oxide (TMAO) Force Fields Based on Thermophysical Properties of Aqueous TMAO Solutions, *The Journal of Physical Chemistry B* **121**, 10674–10688 (2017)

[20] D. R. Canchi and A. E. García, Cosolvent Effects on Protein Stability, *Annual Review of Physical Chemistry* **64**, 273–293 (2013)

[21] P. H. Yancey, M. E. Clark, S. C. Hand, R. D. Bowlus and G. N. Somero, Living with water stress: evolution of osmolyte systems, *Science* **217**, 1214–1222 (1982)

[22] P. H. Yancey, Organic osmolytes as compatible, metabolic and counteracting cytoprotectants in high osmolarity and other stresses, *Journal of Experimental Biology* **208**, 2819–2830 (2005)

[23] M. A. Schroer, M. Paulus, C. Jeworrek, C. Krywka, S. Schmacke, Y. Zhai, D. C. F. Wieland, C. J. Sahle, M. Chimenti, C. A. Royer, B. Garcia-Moreno, M. Tolan and R. Winter, High-pressure SAXS study of folded and unfolded ensembles of proteins, *Biophysical Journal* **99**, 3430–3437 (2010)

[24] M. A. Schroer, Y. Zhai, D. C. F. Wieland, C. J. Sahle, J. Nase, M. Paulus, M. Tolan and R. Winter, Exploring the Piezophilic Behavior of Natural Cosolvent Mixtures, *Angewandte Chemie, International Edition* **50**, 11413–11416 (2011)

[25] J. Smiatek, R. K. Harishchandra, O. Rubner, H.-J. Galla and A. Heuer, Properties of compatible solutes in aqueous solution, *Biophysical Chemistry* **160**, 62–68 (2012)

[26] J. Smiatek, R. K. Harishchandra, H.-J. Galla and A. Heuer, Low Concentrated Hydroxiectoine Solutions in Presence of DPPC Lipid Bilayers: A Computer Simulation Study, *Biophysical Chemistry* **180**, 102–109 (2013)

[27] Y. Zhang and P. S. Cremer, Chemistry of Hofmeister Anions and Osmolytes, *Annual Review of Physical Chemistry* **61**, 63–83 (2010)

[28] T. Arakawa and S. N. Timasheff, The stabilization of proteins by osmolytes, *Biophysical Journal* **47**, 411–414 (1985)

[29] S. N. Timasheff, The Control of Protein Stability and Association by Weak Interactions with Water: How Do Solvents Affect These Processes?, *Annual Review of Biophysics and Biomolecular Structure* **22**, 67–97 (1993)

[30] S. N. Timasheff, Protein-solvent preferential interactions, protein hydration, and the modulation of biochemical reactions by solvent components, *Proceedings of the National Academy of Sciences of the United States of America* **99**, 9721–9726 (2002)

[31] D. R. Canchi, P. Jayasimha, D. C. Rau, G. I. Makhatadze and A. E. Garcia, Molecular Mechanism for the Preferential Exclusion of TMAO from Protein Surfaces, *The Journal of Physical Chemistry B* **116**, 12095–12104 (2012)

[32] E. S. Courtenay, M. W. Capp, C. F. Anderson and M. T. Record, Vapor Pressure Osmometry Studies of Osmolyte-Protein Interactions: Implications for the Action of Osmoprotectants in Vivo and for the Interpretation of "Osmotic Stress" Experiments in Vitro, *Biochemistry* **39**, 4455–4471 (2000)

[33] S. Shimizu and D. J. Smith, Preferential hydration and the exclusion of cosolvents from protein surfaces, *The Journal of Chemical Physics* **121**, 1148–1154 (2004)

[34] J. Rösgen, B. M. Pettitt and D. W. Bolen, Protein Folding, Stability, and Solvation Structure in Osmolyte Solutions, *Biophysical Journal* **89**, 2988–2997 (2005)

[35] I. Yu, Y. Jindo and M. Nagaoka, Microscopic Understanding of Preferential Exclusion of Compatible Solute Ectoine: Direct Interaction and Hydration Alteration, *The Journal of Physical Chemistry B* **111**, 10231–10238 (2007)

[36] E. Schneck, D. Horinek and R. R. Netz, Insight into the Molecular Mechanisms of Protein Stabilizing Osmolytes from Global Force-Field Variations, *The Journal of Physical Chemistry B* **117**, 8310–8321 (2013)

[37] A. Eiberweiser, A. Nazet, S. E. Kruchinin, M. V. Fedotova and R. Buchner, Hydration and Ion Binding of the Osmolyte Ectoine, *The Journal of Physical Chemistry B* **119**, 15203–15211 (2015)

[38] J. A. Schellman, Protein Stability in Mixed Solvents: A Balance of Contact Interaction and Excluded Volume, *Biophysical Journal* **85**, 108–125 (2003)

[39] J. A. Schellman, Destabilization and stabilization of proteins, *Quarterly Review of Biophysics* **38**, 351–361 (2005)

[40] K. D. Collins, Ions from the Hofmeister Series and Osmolytes: Effects on Proteins in Solution and in the Crystallization Process, *Methods* **34**, 300–311 (2004)

[41] Y. Marcus, Effect of Ions on the Structure of Water: Structure Making and Breaking, *Chemical Reviews* **109**, 1346–1370 (2009)

[42] A. Luzar and D. Chandler, Hydrogen-bond kinetics in liquid water, *Nature* **379**, 55–57 (1996)

[43] A. Luzar, Resolving the hydrogen bond dynamics conundrum, *The Journal of Chemical Physics* **113**, 10663–10675 (2000)

[44] V. M. Anisimov, G. Lamoureux, I. V. Vorobyov, N. Huang, B. Roux and J. Alexander D. MacKerell, Determination of Electrostatic Parameters for a Polarizable Force Field Based on the Classical Drude Oscillator, *Journal of Chemical Theory and Computation* **1**, 153–168 (2005)

[45] D. Roy, N. Patel, S. Conte and M. Maroncelli, Dynamics in an Idealized Ionic Liquid Model, *The Journal of Physical Chemistry B* **114**, 8410–8424 (2010)

[46] M. A. Gebbie, M. Valtiner, X. Banquy, E. T. Fox, W. A. Henderson and J. N. Israelachvili, Ionic liquids behave as dilute electrolyte solutions, *Proceedings of the National Academy of Sciences of the United States of America* **110**, 9674–9679 (2013)

[47] T. Baimpos, B. R. Shrestha, S. Raman and M. Valtiner, Effect of Interfacial Ion Structuring on Range and Magnitude of Electric Double Layer, Hydration, and Adhesive Interactions between Mica Surfaces in 0.05–3 M Li^+ and Cs^+ Electrolyte Solutions, *Langmuir* **30**, 4322–4332 (2014)

[48] R. M. Espinosa-Marzal, A. Arcifa, A. Rossi and N. D. Spencer, Microslips to "Avalanches" in Confined, Molecular Layers of Ionic Liquids, *The Journal of Physical Chemistry Letters* **5**, 179–184 (2014)

[49] H.-W. Cheng, P. Stock, B. Moeremans, T. Baimpos, X. Banquy, F. U. Renner and M. Valtiner, Characterizing the Influence of Water on Charging and Layering at Electrified Ionic-Liquid/Solid Interfaces, *Advanced Materials Interfaces* **2**, 1500159 (2015)

[50] M. A. Gebbie, H. A. Dobbs, M. Valtiner and J. N. Israelachvili, Long-range electrostatic screening in ionic liquids, *Proceedings of the National Academy of Sciences of the United States of America* **112**, 7432–7437 (2015)

[51] A. M. Smith, A. A. Lee and S. Perkin, The Electrostatic Screening Length in Concentrated Electrolytes Increases with Concentration, *The Journal of Physical Chemistry Letters* **7**, 2157–2163 (2016)

[52] A. A. Lee, C. S. Perez-Martinez, A. M. Smith and S. Perkin, Underscreening in concentrated electrolytes, *Faraday Discussions* **199**, 239–259 (2017)

[53] M. A. Gebbie, A. M. Smith, H. A. Dobbs, A. A. Lee, G. G. Warr, X. Banquy, M. Valtiner, M. W. Rutland, J. N. Israelachvili, S. Perkin and R. Atkin, Long range electrostatic forces in ionic liquids, *Chemical Communications* **53**, 1214–1224 (2017)

[54] P. Debye and E. Hückel, Zur Theorie der Elektrolyte. I. Gefrierpunktserniedrigung und verwandte Erscheinungen, *Physikalische Zeitschrift* **24**, 185–206 (1923)

[55] M. Gouy, Sur la constitution de la charge électrique à la surface d'un électrolyte, *Journal de Physique Théorique et Appliquée* **9**, 457 (1910)

[56] D. L. Chapman, A contribution to the theory of electrocapillarity, *Philosophical Magazine* **25**, 475–481 (1913)

[57] P. Attard, Asymptotic analysis of primitive model electrolytes and the electrical double layer, *Physical Review E* **48**, 3604–3621 (1993)

[58] R. Evans, R. J. F. Leote de Carvalho, J. R. Henderson and D. C. Hoyle, Asymptotic decay of correlations in liquids and their mixtures, *The Journal of Chemical Physics* **100**, 591–603 (1994)

[59] R. J. F. Leote de Carvalho and R. Evans, The decay of correlations in ionic fluids, *Molecular Physics* **83**, 619–654 (1994)

[60] L. M. Varela, M. García and V. Mosquera, Exact mean-field theory of ionic solutions: non-Debye screening, *Physics Reports* **382**, 1–111 (2003)

[61] A. A. Kornyshev, Double-Layer in Ionic Liquids: Paradigm Change?, *The Journal of Physical Chemistry B* **111**, 5545–5557 (2007)

[62] M. A. Brown, G. V. Bossa and S. May, Emergence of a Stern Layer from the Incorporation of Hydration Interactions into the Gouy-Chapman Model of the Electrical Double Layer, *Langmuir* **31**, 11477–11483 (2015)

[63] Z. A. H. Goodwin, G. Feng and A. A. Kornyshev, Mean-Field Theory of Electrical Double Layer In Ionic Liquids with Account of Short-Range Correlations, *Electrochimica Acta* **225**, 190–197 (2017)

[64] F. Coupette, A. A. Lee and A. Härtel, Screening Lengths in Ionic Fluids, *Physical Review Letters* **121**, 075501 (2018)

[65] N. Gavish, D. Elad and A. Yochelis, From Solvent-Free to Dilute Electrolytes: Essential Components for a Continuum Theory, *The Journal of Physical Chemistry Letters* **9**, 36–42 (2018)

[66] R. Kjellander, Focus Article: Oscillatory and long-range monotonic exponential decays of electrostatic interactions in ionic liquids and other electrolytes: The significance of dielectric permittivity and renormalized charges, *The Journal of Chemical Physics* **148**, 193701 (2018)

[67] B. Rotenberg, O. Bernard and J.-P. Hansen, Underscreening in ionic liquids: a first principles analysis, *Journal of Physics: Condensed Matter* **30**, 054005 (2018)

[68] R. Kjellander, The intimate relationship between the dielectric response and the decay of intermolecular correlations and surface forces in electrolytes, *Soft Matter* **15**, 5866–5895 (2019)

[69] R. Kjellander, A multiple decay-length extension of the Debye-Hückel theory: to achieve high accuracy also for concentrated solutions and explain under-screening in dilute symmetric electrolytes, *Physical Chemistry Chemical Physics* **22**, 23952–23985 (2020)

[70] M. B. Hahn, T. Solomun, R. Wellhausen, S. Hermann, H. Seitz, S. Meyer, H.-J. Kunte, J. Zeman, F. Uhlig, J. Smiatek and H. Sturm, Influence of the Compatible Solute Ectoine on the Local Water Structure: Implications for the Binding of the Protein G5P to DNA, *The Journal of Physical Chemistry B* **119**, 15212–15220 (2015)

[71] J. Zeman, F. Uhlig, J. Smiatek and C. Holm, A coarse-grained polarizable force field for the ionic liquid 1-butyl-3-methylimidazolium hexafluorophosphate, *Journal of Physics: Condensed Matter* **29**, 504004 (2017)

[72] F. Uhlig, J. Zeman, J. Smiatek and C. Holm, First-Principles Parametrization of Polarizable Coarse-Grained Force Fields for Ionic Liquids, *Journal of Chemical Theory and Computation* **14**, 1471–1486 (2018)

[73] M. P. Schlaile, J. Zeman and M. Mueller, It's a match! Simulating compatibility-based learning in a network of networks, *Journal of Evolutionary Economics* **28**, 1111–1150 (2018)

[74] J. Michalowsky, J. Zeman, C. Holm and J. Smiatek, A polarizable MARTINI model for monovalent ions in aqueous solution, *The Journal of Chemical Physics* **149**, 163319 (2018)

[75] M. P. Schlaile, T. Knausberg, M. Mueller and J. Zeman, Viral ice buckets: A memetic perspective on the ALS Ice Bucket Challenge's diffusion, *Cognitive Systems Research* **52**, 947–969 (2018)

[76] J. Zeman, C. Holm and J. Smiatek, The Effect of Small Organic Cosolutes on Water Structure and Dynamics, *Journal of Chemical & Engineering Data* **65**, 1197–1210 (2020)

[77] J. Zeman, S. Kondrat and C. Holm, Bulk ionic screening lengths from extremely large-scale molecular dynamics simulations, *Chemical Communications* **56**, 15635–15638 (2020)

[78] J. Zeman, S. Kondrat and C. Holm, Ionic screening in bulk and under confinement, *The Journal of Chemical Physics* **155**, 204501 (2021)

[79] R. Kubo, The fluctuation-dissipation theorem, *Reports on Progress in Physics* **29**, 255–284 (1966)

[80] V. Balakrishnan, Nonequilibrium Statistical Mechanics, `https://nptel.ac.in/courses/115/106/115106091`, [online; accessed 2020-02-03], 2016

[81] H. J. C. Berendsen, Simulating the Physical World: Hierarchical Modeling from Quantum Mechanics to Fluid Dynamics (Cambridge University Press, 2007)

[82] D. Frenkel and B. Smit, Understanding Molecular Simulation, From Algorithms to Applications, 2nd ed. (Academic Press, San Diego, 2002)

[83] J. E. Lennard-Jones, Cohesion, *Proceedings of the Physical Society* **43 pt. 5**, 461 (1931)

[84] L. Verlet, Computer Experiments on Classical Fluids. I. Thermodynamical Properties of Lennard-Jones Molecules, *Physical Review* **159**, 98 (1967)

[85] R. W. Hockney, S. P. Goel and J. W. Eastwood, Quiet high-resolution computer models of a plasma, *Journal of Computational Physics* **14**, 148–158 (1974)

[86] T. Darden, D. York and L. Pedersen, Particle Mesh Ewald: An $N \log(N)$ method for Ewald sums in large systems, *The Journal of Chemical Physics* **98**, 10089–10092 (1993)

[87] U. Essmann, L. Perera, M. L. Berkowitz, T. Darden, H. Lee and L. G. Pedersen, A smooth Particle Mesh Ewald method, *The Journal of Chemical Physics* **103**, 8577–8593 (1995)

[88] J. W. Eastwood, R. W. Hockney and D. N. Lawrence, P3M3DP – The three-dimensional periodic particle-particle/particle-mesh program, *Computer Physics Communications* **19**, 215–261 (1980)

[89] P. P. Ewald, Die Berechnung optischer und elektrostatischer Gitterpotentiale, *Annalen der Physik* **369**, 253–287 (1921)

[90] R. W. Hockney and J. W. Eastwood, Computer Simulation Using Particles (IOP, London, 1988)

[91] M. Deserno and C. Holm, How to mesh up Ewald sums. I. A theoretical and numerical comparison of various particle mesh routines, *The Journal of Chemical Physics* **109**, 7678 (1998)

[92] M. Deserno and C. Holm, How to mesh up Ewald sums. II. An accurate error estimate for the Particle-Particle-Particle-Mesh algorithm, *The Journal of Chemical Physics* **109**, 7694 (1998)

[93] H. C. Andersen, Molecular dynamics simulations at constant pressure and/or temperature, *The Journal of Chemical Physics* **72**, 2384–2393 (1980)

[94] S. Nosé, A molecular dynamics method for simulations in the canonical ensemble, *Molecular Physics* **52**, 255–268 (1984)

[95] W. G. Hoover, Canonical dynamics: Equilibrium phase-space distributions, *Physical Review A* **31**, 1695–1697 (1985)

[96] M. Parrinello and A. Rahman, Polymorphic transitions in single crystals: A new molecular dynamics method, *Journal of Applied Physics* **52**, 7182–7190 (1981)

[97] H. J. C. Berendsen, J. P. M. Postma, W. F. van Gunsteren, A. DiNola and J. R. Haak, Molecular dynamics with coupling to an external bath, *The Journal of Chemical Physics* **81**, 3684–3690 (1984)

[98] M. Sega, S. S. Kantorovich, A. Arnold and C. Holm, "On the Calculation of the Dielectric Properties of Liquid Ionic Systems", in *Recent Advances in Broadband Dielectric Spectroscopy*, edited by Y. P. Kalmykov, NATO Science for Peace and Security Series B: Physics and Biophysics (Springer Netherlands, 2013), pp. 103–122

[99] M. Neumann and O. Steinhauser, On the calculation of the frequency-dependent dielectric constant in computer simulations, *Chemical Physics Letters* **102**, 508 (1983)

[100] B. U. Felderhof, Fluctuation theorems for dielectrics, *Physica A: Statistical Mechanics and its Applications* **95**, 572–580 (1979)

[101] J. Zeman and C. Holm, Statistical Error Analysis, Lecture Notes of "Simulation Methods in Physics I", `https://www.icp.uni-stuttgart.de/~icp/html//teaching/2019-ws-sim_methods/lecture09_notes.pdf`, [online; accessed 2021-07-31], 2019

[102] W. Janke, Statistical Analysis of Simulations: Data Correlations and Error Estimation, *Quantum Simulations of Complex Many-Body Systems: from Theory to Algorithms*, 423–445 (2002), https://juser.fz-juelich.de/record/24560/files/NIC-Band-10.pdf

[103] J. W. Cooley and J. W. Tukey, An algorithm for the machine calculation of complex Fourier series, *Mathematics of Computation* **19**, 297–301 (1965)

[104] M. Frigo and S. G. Johnson, "The Design and Implementation of FFTW3", in Proceedings of the IEEE, Vol. 93, 2, Special issue on "Program Generation, Optimization, and Platform Adaptation" (2005), pp. 216–231

[105] M. J. Abraham, T. Murtola, R. Schulz, S. Páll, J. C. Smith, B. Hess and E. Lindahl, GROMACS: High performance molecular simulations through multi-level parallelism from laptops to supercomputers, *SoftwareX* **1–2**, 19–25 (2015)

[106] S. Páll, M. J. Abraham, C. Kutzner, B. Hess and E. Lindahl, "Tackling Exascale Software Challenges in Molecular Dynamics Simulations with GROMACS", in Solving Software Challenges for Exascale: International Conference on Exascale Applications and Software, EASC 2014, Stockholm, Sweden, April 2-3, 2014, Revised Selected Papers, edited by S. Markidis and E. Laure (2015), pp. 3–27

[107] S. Pronk, S. Páll, R. Schulz, P. Larsson, P. Bjelkmar, R. Apostolov, M. R. Shirts, J. C. Smith, P. M. Kasson, D. van der Spoel, B. Hess and E. Lindahl, GROMACS 4.5: a high-throughput and highly parallel open source molecular simulation toolkit, *Bioinformatics* **29**, 845–854 (2013)

[108] B. Hess, C. Kutzner, D. van der Spoel and E. Lindahl, GROMACS 4: Algorithms for Highly Efficient, Load-Balanced, and Scalable Molecular Simulation, *Journal of Chemical Theory and Computation* **4**, 435–447 (2008)

[109] D. van der Spoel, E. Lindahl, B. Hess, G. Groenhof, A. E. Mark and H. J. C. Berendsen, GROMACS: Fast, flexible, and free, *Journal of Computational Chemistry* **26**, 1701–1718 (2005)

[110] E. Lindahl, B. Hess and D. van der Spoel, GROMACS 3.0: A package for molecular simulation and trajectory analysis, *Journal of Molecular Modeling* **7**, 306–317 (2001)

[111] H. J. C. Berendsen, D. van der Spoel and R. van Drunen, GROMACS: A message-passing parallel molecular dynamics implementation, *Computer Physics Communications* **91**, 43–56 (1995)

[112] H. J. C. Berendsen, J. R. Grigera and T. P. Straatsma, The missing term in effective pair potentials, *The Journal of Physical Chemistry* **91**, 6269–6271 (1987)

[113] M. R. Reddy and M. Berkowitz, The dielectric constant of SPC/E water, *Chemical Physics Letters* **155**, 173–176 (1989)

[114] W. L. Jorgensen, J. Chandrasekhar, J. D. Madura, R. W. Impey and M. L. Klein, Comparison of simple potential functions for simulating liquid water, *The Journal of Chemical Physics* **79**, 926–935 (1983)

[115] J. L. Abascal and C. Vega, A general purpose model for the condensed phases of water: TIP4P/2005, *The Journal of Chemical Physics* **123**, 234505 (2005)

[116] S. Izadi, R. Anandakrishnan and A. V. Onufriev, Building Water Models: A Different Approach, *The Journal of Physical Chemistry Letters* **5**, 3863–3871 (2014)

[117] J. Hunger, N. Ottosson, K. Mazur, M. Bonn and H. J. Bakker, Water-mediated interactions between trimethylamine-N-oxide and urea, *Physical Chemistry Chemical Physics* **17**, 298–306 (2015)

[118] M. Sega and C. Schröder, Dielectric and Terahertz Spectroscopy of Polarizable and Nonpolarizable Water Models: A Comparative Study, *The Journal of Physical Chemistry A* **119**, 1539–1547 (2015)

[119] J. Zeman, S. Kondrat and C. Holm, Ionic Screening in Bulk and under Confinement, *The Journal of Chemical Physics* (accepted)

[120] M. Neumann, Dipole moment fluctuation formulas in computer simulations of polar systems, *Molecular Physics* **50**, 841–858 (1983)

[121] C. Schröder, M. Haberler and O. Steinhauser, On the computation and contribution of conductivity in molecular ionic liquids, *The Journal of Chemical Physics* **128**, 134501, 134501 (2008)

[122] P. M. Oger and M. Jebbar, The many ways of coping with pressure, *Research in Microbiology* **161**, 799–809 (2010)

[123] I. Baskakov, A. Wang and D. W. Bolen, Trimethylamine-N-oxide counteracts urea effects on rabbit muscle lactate dehydrogenase function: a test of the counteraction hypothesis, *Biophysical Journal* **74**, 2666–2673 (1998)

[124] P. Venkatesu, M.-J. Lee and H.-m. Lin, Trimethylamine N-oxide counteracts the denaturing effects of urea or GdnHCl on protein denatured state, *Archives of Biochemistry and Biophysics* **466**, 106–115 (2007)

[125] F. Meersman, D. Bowron, A. K. Soper and M. H. J. Koch, Counteraction of urea by trimethylamine N-oxide is due to direct interaction, *Biophysical Journal* **97**, 2559–2566 (2009)

[126] F. Meersman, D. Bowron, A. K. Soper and M. H. J. Koch, Correction to "Counteraction of urea by trimethylamine N-oxide is due to direct interaction (2009)", *Biophysical Journal* **98**, 174 (2010)

[127] F. Meersman, D. Bowron, A. K. Soper and M. H. J. Koch, An X-ray and neutron scattering study of the equilibrium between trimethylamine N-oxide and urea in aqueous solution, *Physical Chemistry Chemical Physics* **13**, 13765–13771 (2011)

[128] P. Ganguly, T. Hajari, J.-E. Shea and N. F. A. van der Vegt, Mutual Exclusion of Urea and Trimethylamine N-Oxide from Amino Acids in Mixed Solvent Environment, *The Journal of Physical Chemistry Letters* **6**, 581–585 (2015)

[129] E. A. Oprzeska-Zingrebe and J. Smiatek, Aqueous Mixtures of Urea and Trimethylamine-N-oxide: Evidence for Kosmotropic or Chaotropic Behavior?, *The Journal of Physical Chemistry B* **123**, 4415–4424 (2019)

[130] B. J. Bennion and V. Daggett, The molecular basis for the chemical denaturation of proteins by urea, *Proceedings of the National Academy of Sciences of the United States of America* **100**, 5142–5147 (2003)

[131] R. Zangi, R. Zhou and B. J. Berne, Urea's Action on Hydrophobic Interactions, *Journal of the American Chemical Society* **131**, 1535–1541 (2009)

[132] D. A. C. Beck, B. J. Bennion, D. O. V. Alonso and V. Daggett, Simulations of Macromolecules in Protective and Denaturing Osmolytes: Properties of Mixed Solvent Systems and Their Effects on Water and Protein Structure and Dynamics, *Methods in Enzymology* **428**, 373–396 (2007)

[133] A. M. Bhattacharyya and P. Horowitz, Alteration Around the Active Site of Rhodanese during Urea-induced Denaturation and Its Implications for Folding, *The Journal of Biological Chemistry* **275**, 14860–14864 (2000)

[134] A. K. Bhuyan, Protein Stabilization by Urea and Guanidine Hydrochloride, *Biochemistry* **41**, 13386–13394 (2002)

[135] L. Hua, R. Zhoua, D. Thirumalaic and B. J. Berne, Urea denaturation by stronger dispersion interactions with proteins than water implies a 2-stage unfolding, *Proceedings of the National academy of Sciences of the United States of America* **105**, 16928–16933 (2008)

[136] S. N. Timasheff, Water as ligand: Preferential binding and exclusion of denaturants in protein unfolding, *Biochemistry* **31**, 9857–9864 (1992)

[137] E. A. Oprzeska-Zingrebe and J. Smiatek, Aqueous ionic liquids in comparison with standard co-solutes, *Biophysical Reviews* **10**, 809–824 (2018)

[138] E. A. Oprzeska-Zingrebe, M. Kohagen, J. Kästner and J. Smiatek, Unfolding of DNA by co-solutes: insights from Kirkwood-Buff integrals and transfer free energies, *European Physical Journal Special Topics* **227**, 1665–1679 (2019)

[139] P. Lo Nostro and B. W. Ninham, Hofmeister Phenomena: An Update on Ion Specificity in Biology, *Chemical Reviews* **112**, 2286–2322 (2012)

[140] L. M. Mayr and F. X. Schmid, Stabilization of a protein by guanidinium chloride, *Biochemistry* **32**, 7994–7998 (1993)

[141] J. Smiatek, Osmolyte Effects: Impact on the Aqueous Solution around Charged and Neutral Spheres, *The Journal of Physical Chemistry B* **118**, 771–782 (2014)

[142] J. Heyda and J. Dzubiella, Thermodynamic Description of Hofmeister Effects on the LCST of Thermosensitive Polymers, *The Journal of Physical Chemistry B* **118**, 10979–10988 (2014)

[143] S. Micciulla, J. Michalowsky, M. A. Schroer, C. Holm, R. von Klitzing and J. Smiatek, Concentration dependent effects of urea binding to poly(N-isopropylacrylamide) brushes: a combined experimental and numerical study, *Physical Chemistry Chemical Physics* **18**, 5324–5335 (2016)

[144] T. Solomun, H. Sturm, R. Wellhausen and H. Seitz, Interaction of a single-stranded DNA-binding protein G5P with DNA oligonucleotides immobilised on a gold surface, *Chemical Physics Letters* **553**, 92–94 (2012)

[145] E. A. Oprzeska-Zingrebe, S. Meyer, A. Roloff, H.-J. Kunte and J. Smiatek, Influence of compatible solute ectoine on distinct DNA structures: thermodynamic insights into molecular binding mechanisms and destabilization effects, *Physical Chemistry Chemical Physics* **20**, 25861–25874 (2018)

[146] V. Pierce, M. Kang, M. Aburi, S. Weerasinghe and P. E. Smith, Recent applications of Kirkwood-Buff theory to biological systems, *Cell Biochemistry and Biophysics* **50**, 1–22 (2008)

[147] E. A. Oprzeska-Zingrebe and J. Smiatek, Preferential Binding of Urea to Single-Stranded DNA Structures: A Molecular Dynamics Study, *Biophysical Journal* **114**, 1551–1562 (2018)

[148] A. Narayanan Krishnamoorthy, C. Holm and J. Smiatek, Influence of Cosolutes on Chemical Equilibrium: a Kirkwood-Buff Theory for Ion Pair Association-Dissociation Processes in Ternary Electrolyte Solutions, *The Journal of Physical Chemistry C* **122**, 10293–10302 (2018)

[149] J. Smiatek, Aqueous ionic liquids and their effects on protein structures: an overview on recent theoretical and experimental results, *Journal of Physics: Condensed Matter* **29**, 233001 (2017)

[150] D. Harries and J. Rösgen, A Practical Guide on How Osmolytes Modulate Macromolecular Properties, *Methods in Cell Biology* **84**, 679–735 (2008)

[151] R. Politi and D. Harries, Enthalpically driven peptide stabilization by protective osmolytes, *Chemical Communications* **46**, 6449–6451 (2010)

[152] V. Lesch, A. Heuer, V. A. Tatsis, C. Holm and J. Smiatek, Peptides in the presence of aqueous ionic liquids: tunable co-solutes as denaturants or protectants?, *Physical Chemistry Chemical Physics* **17**, 26049–26053 (2015)

[153] M. A. Schroer, J. Michalowsky, B. Fischer, J. Smiatek and G. Grübel, Stabilizing Effect of TMAO on Globular PNIPAM States: Preferential Attraction Induces Preferential Hydration, *Physical Chemistry Chemical Physics* **18**, 31459–31470 (2016)

[154] D. Diddens, V. Lesch, A. Heuer and J. Smiatek, Aqueous Ionic Liquids and Their Influence on Peptide Conformations: Denaturation and Dehydration Mechanisms, *Physical Chemistry Chemical Physics* **19**, 20430–20440 (2017)

[155] A. Panuszko, P. Bruździak, J. Zielkiewicz, D. Wyrzykowski and J. Stangret, Effects of Urea and Trimethylamine-N-oxide on the Properties of Water and the Secondary Structure of Hen Egg White Lysozyme, *The Journal of Physical Chemistry B* **113**, 14797–14809 (2009)

[156] P. Bruździak, A. Panuszko and J. Stangret, Influence of Osmolytes on Protein and Water Structure: A Step To Understanding the Mechanism of Protein Stabilization, *The Journal of Physical Chemistry B* **117**, 11502–11508 (2013)

[157] A. Panuszko, P. Bruździak, E. Kaczkowska and J. Stangret, General Mechanism of Osmolytes' Influence on Protein Stability Irrespective of the Type of Osmolyte Cosolvent, *The Journal of Physical Chemistry B* **120**, 11159–11169 (2016)

[158] B. Bagchi, Water Dynamics in the Hydration Layer around Proteins and Micelles, *Chemical Reviews* **105**, 3197–3219 (2005)

[159] C. J. Sahle, M. A. Schroer, I. Juurinen and J. Niskanen, Influence of TMAO and urea on the structure of water studied by inelastic X-ray scattering, *Physical Chemistry Chemical Physics* **18**, 16518–16526 (2016)

[160] M. B. Hahn, F. Uhlig, T. Solomun, J. Smiatek and H. Sturm, Combined influence of ectoine and salt: spectroscopic and numerical evidence for compensating effects on aqueous solutions, *Physical Chemistry Chemical Physics* **18**, 28398–28402 (2016)

[161] S. Funkner, M. Havenith and G. Schwaab, Urea, a Structure Breaker? Answers from THz Absorption Spectroscopy, *The Journal of Physical Chemistry B* **116**, 13374–13380 (2012)

[162] R. Buchner and J. Barthel, Dielectric relaxation in solutions, *Annual Reports on the Progress of Chemistry Section C: Physical Chemistry* **97**, 349–382 (2001)

[163] J. Morgan and B. E. Warren, X-Ray Analysis of the Structure of Water, *The Journal of Chemical Physics* **6**, 666–673 (1938)

[164] P. Wernet, D. Nordlund, U. Bergmann, M. Cavalleri, M. Odelius, H. Ogasawara, L. Å. Näslund, T. K. Hirsch, L. Ojamäe, P. Glatzel, L. G. M. Pettersson and A. Nilsson, The Structure of the First Coordination Shell in Liquid Water, *Science* **304**, 995–999 (2004)

[165] A. Lapini, M. Pagliai, S. Fanetti, M. Citroni, S. Scandolo, R. Bini and R. Righini, Pressure Dependence of Hydrogen-Bond Dynamics in Liquid Water Probed by Ultrafast Infrared Spectroscopy, *The Journal of Physical Chemistry Letters* **7**, 3579–3584 (2016)

[166] C. Huang, K. T. Wikfeldt, T. Tokushima, D. Nordlund, Y. Harada, U. Bergmann, M. Niebuhr, T. M. Weiss, Y. Horikawa, M. Leetmaa, M. P. Ljungberg, O. Takahashi, A. Lenz, L. Ojamäe, A. P. Lyubartsev, S. Shin, L. G. M. Pettersson and A. Nilsson, The inhomogeneous structure of water at ambient conditions, *Proceedings of the National academy of Sciences of the United States of America* **106**, 15214–15218 (2009)

[167] P. E. Mason and J. W. Brady, "Tetrahedrality" and the Relationship between Collective Structure and Radial Distribution Functions in Liquid Water, *The Journal of Physical Chemistry B* **111**, 5669–5679 (2007)

[168] E. Duboué-Dijon and D. Laage, Characterization of the Local Structure in Liquid Water by Various Order Parameters, *The Journal of Physical Chemistry B* **119**, 8406–8418 (2015)

[169] P.-L. Chau and A. J. Hardwick, A new order parameter for tetrahedral configurations, *Molecular Physics* **93**, 511–518 (1998)

[170] J. R. Errington and P. G. Debenedetti, Relationship between structural order and the anomalies of liquid water, *Nature* **409**, 318–321 (2001)

[171] D. Bandyopadhyay, S. Mohan, S. K. Ghosh and N. Choudhury, Molecular Dynamics Simulation of Aqueous Urea Solution: Is Urea a Structure Breaker?, *The Journal of Physical Chemistry B* **118**, 11757–11768 (2014)

[172] A. Einstein, Über die von der molekularkinetischen Theorie der Wärme geforderte Bewegung von in ruhenden Flüssigkeiten suspendierten Teilchen, *Annalen der Physik* **322**, 549–560 (1905)

[173] D. van der Spoel, P. J. van Maaren, P. Larsson and N. Tîmneanu, Thermodynamics of Hydrogen Bonding in Hydrophilic and Hydrophobic Media, *The Journal of Physical Chemistry B* **110**, 4393–4398 (2006)

[174] A. Y. Zasetsky and R. Buchner, Quasi-linear least squares and computer code for numerical evaluation of relaxation time distribution from broadband dielectric spectra, *Journal of Physics: Condensed Matter* **23**, 025903 (2011)

[175] V. Agieienko and R. Buchner, Urea hydration from dielectric relaxation spectroscopy: old findings confirmed, new insights gained, *Physical Chemistry Chemical Physics* **18**, 2597–2607 (2016)

[176] U. Kaatze, H. Gerke and R. Pottel, Dielectric relaxation in aqueous solutions of urea and some of its derivatives, *The Journal of Physical Chemistry* **90**, 5464–5469 (1986)

[177] R. Buchner, What can be learnt from dielectric relaxation spectroscopy about ion solvation and association?, *Pure and Applied Chemistry* **80**, 1239–1252 (2008)

[178] R. Buchner and G. Hefter, Interactions and dynamics in electrolyte solutions by dielectric spectroscopy, *Physical Chemistry Chemical Physics* **11**, 8984–8999 (2009)

[179] J. Hunger, S. Niedermayer, R. Buchner and G. Hefter, Are Nanoscale Ion Aggregates Present in Aqueous Solutions of Guanidinium Salts?, *The Journal of Physical Chemistry B* **114**, 13617–13627 (2010)

[180] M. Sega, S. S. Kantorovich, C. Holm and A. Arnold, Communication: Kinetic and pairing contributions in the dielectric spectra of electrolyte solutions, *The Journal of Chemical Physics* **140**, 211101 (2014)

[181] C. Hölzl, P. Kibies, S. Imoto, R. Frach, S. Suladze, R. Winter, D. Marx, D. Horinek and S. M. Kast, Design principles for high-pressure force fields: Aqueous TMAO solutions from ambient to kilobar pressures, *The Journal of Chemical Physics* **144**, 144104 (2016)

[182] S. Weerasinghe and P. E. Smith, A Kirkwood-Buff derived force field for mixtures of urea and water, *The Journal of Physical Chemistry B* **107**, 3891–3898 (2003)

[183] E. Wernersson, J. Heyda, M. Vazdar, M. Lund, P. E. Mason and P. Jungwirth, Orientational Dependence of the Affinity of Guanidinium Ions to the Water Surface, *The Journal of Physical Chemistry B* **115**, 12521–12526 (2011)

[184] B. Hess, H. Bekker, H. J. C. Berendsen and J. G. E. M. Fraaije, LINCS: A linear constraint solver for molecular simulations, *Journal of Computational Chemistry* **18**, 1463–1472 (1997)

[185] S. Miyamoto and P. A. Kollman, Settle: An analytical version of the SHAKE and RATTLE algorithm for rigid water models, *Journal of Computational Chemistry* **13**, 952–962 (1992)

[186] N. Michaud-Agrawal, E. J. Denning, T. B. Woolf and O. Beckstein, MDAnalysis: A toolkit for the analysis of molecular dynamics simulations, *Journal of Computational Chemistry* **32**, 2319–2327 (2011)

[187] R. J. Gowers, M. Linke, J. Barnoud, T. J. E. Reddy, M. N. Melo, S. L. Seyler, J. Domański, D. L. Dotson, S. Buchoux, I. M. Kenney and O. Beckstein, "MDAnalysis: A Python Package for the Rapid Analysis of Molecular Dynamics Simulations", in Proceedings of the 15th Python in Science Conference, edited by S. Benthall and S. Rostrup (2016), pp. 98–105

[188] F. Merzel and J. C. Smith, Is the first hydration shell of lysozyme of higher density than bulk water?, *Proceedings of the National Academy of Sciences of the United States of America* **99**, 5378–5383 (2002)

[189] J. C. Smith, F. Merzel, C. S. Verma and S. Fischer, Protein hydration water: Structure and thermodynamics, *Journal of Molecular Liquids* **101**, 27–33 (2002)

[190] R. Abseher, H. Schreiber and O. Steinhauser, The influence of a protein on water dynamics in its vicinity investigated by molecular dynamics simulation, *Proteins: Structure, Function, and Genetics* **25**, 366–378 (1996)

[191] D. Vitkup, D. Ringe, G. A. Petsko and M. Karplus, Solvent mobility and the protein 'glass' transition, *Nature Structural Biology* **7**, 34–38 (2000)

[192] M. Tarek and D. J. Tobias, The Dynamics of Protein Hydration Water: A Quantitative Comparison of Molecular Dynamics Simulations and Neutron-scattering Experiments, *Biophysical Journal* **79**, 3244–3257 (2000)

[193] A. C. Fogarty and D. Laage, Water Dynamics in Protein Hydration Shells: The Molecular Origins of the Dynamical Perturbation, *The Journal of Physical Chemistry B* **118**, 7715–7729 (2014)

[194] R. Singh, I. Haque and F. Ahmad, Counteracting Osmolyte Trimethylamine N-Oxide Destabilizes Proteins at pH below its pK_a: Measurements of Thermodynamic Parameters of Proteins in the Presence and Absence of Trimethylamine N-Oxide, *The Journal of Biological Chemistry* **280**, 11035–11042 (2005)

[195] I. Yu and M. Nagaoka, Slowdown of water diffusion around protein in aqueous solution with ectoine, *Chemical Physics Letters* **388**, 316–321 (2004)

[196] J. D. Batchelor, A. Olteanu, A. Tripathy and G. J. Pielak, Impact of Protein Denaturants and Stabilizers on Water Structure, *Journal of the American Chemical Society* **126**, 1958–1961 (2004)

[197] A. Rani, A. Jayaraj, B. Jayaram and V. Pannuru, Trimethylamine-N-oxide switches from stabilizing nature: A mechanistic outlook through experimental techniques and molecular dynamics simulation, *Scientific Reports* **6**, 23656 (2016)

[198] A. N. Krishnamoorthy, C. Holm and J. Smiatek, Specific ion effects for polyelectrolytes in aqueous and non-aqueous media: the importance of the ion solvation behavior, *Soft Matter* **14**, 6243–6255 (2018)

[199] J. Smiatek, A. Heuer and M. Winter, Properties of Ion Complexes and Their Impact on Charge Transport in Organic Solvent-Based Electrolyte Solutions for Lithium Batteries: Insights from a Theoretical Perspective, *Batteries* **4**, 62 (2018)

[200] J. Smiatek, Enthalpic contributions to solvent-solute and solvent-ion interactions: Electronic perturbation as key to the understanding of molecular attraction, *The Journal of Chemical Physics* **150**, 174112 (2019)

[201] A. Nandy and J. Smiatek, Mixtures of LiTFSI and urea: ideal thermodynamic behavior as key to the formation of deep eutectic solvents?, *Physical Chemistry Chemical Physics* **21**, 12279–12287 (2019)

[202] T. Kobayashi, A. Kemna, M. Fyta, B. Braunschweig and J. Smiatek, Aqueous Mixtures of Room-Temperature Ionic Liquids: Entropy-Driven Accumulation of Water Molecules at Interfaces, *The Journal of Physical Chemistry C* **123**, 13795–13803 (2019)

[203] Y. Hayashi, Y. Katsumoto, S. Omori, N. Kishii and A. Yasuda, Liquid Structure of the Urea-Water System Studied by Dielectric Spectroscopy, *The Journal of Physical Chemistry B* **111**, 1076–1080 (2007)

[204] Y. Hayashi, Y. Katsumoto, I. Oshige, S. Omori and A. Yasuda, Comparative Study of Urea and Betaine Solutions by Dielectric Spectroscopy: Liquid Structures of a Protein Denaturant and Stabilizer, *The Journal of Physical Chemistry B* **111**, 11858–11863 (2007)

[205] Y.-T. Liao, A. C. Manson, M. R. DeLyser, W. G. Noid and P. S. Cremer, Trimethylamine N-oxide stabilizes proteins via a distinct mechanism compared with betaine and glycine, *Proceedings of the National Academy of Sciences of the United States of America* **114**, 2479–2484 (2017)

[206] C. Held, T. Neuhaus and G. Sadowski, Compatible solutes: Thermodynamic properties and biological impact of ectoines and prolines, *Biophysical Chemistry* **152**, 28–39 (2010)

[207] D. M. Makarov, G. I. Egorov and A. M. Kolker, Density and Volumetric Properties of Aqueous Solutions of Trimethylamine N-Oxide in the Temperature Range from (278.15 to 323.15) K and at Pressures up to 100 MPa, *Journal of Chemical & Engineering Data* **60**, 1291–1299 (2015)

[208] F. T. Gucker, F. W. Gage and C. E. Moser, The Densities of Aqueous Solutions of Urea at 25 and 30° and the Apparent Molal Volume of Urea, *Journal of the American Chemical Society* **60**, 2582–2588 (1938)

[209] K. Kawahara and C. Tanford, Viscosity and Density of Aqueous Solutions of Urea and Guanidine Hydrochloride, *The Journal of Biological Chemistry* **241**, 3228–3232 (1966)

[210] M. Tanaka, G. Girard, R. Davis, A. Peuto and N. Bignell, Recommended table for the density of water between 0 °C and 40 °C based on recent experimental reports, *Metrologia* **38**, 301–309 (2001)

[211] P. Walden, Über die Molekulargröße und elektrische Leitfähigkeit einiger geschmolzener Salze, *Bulletin de l'Académie Impériale des Sciences de Saint-Pétersbourg* **8**, 405–422 (1914)

[212] R. Hayes, G. G. Warr and R. Atkin, Structure and Nanostructure in Ionic Liquids, *Chemical Reviews* **115**, 6357–6426 (2015)

[213] Z. Lei, B. Chen, Y.-M. Koo and D. R. MacFarlane, Introduction: Ionic Liquids, *Chemical Reviews* **117**, 6633–6635 (2017)

[214] R. D. Rogers and K. R. Seddon, Ionic Liquids–Solvents of the Future?, *Science* **302**, 792–793 (2003)

[215] S. V. Sambasivarao and O. Acevedo, Development of OPLS-AA Force Field Parameters for 68 Unique Ionic Liquids, *Journal of Chemical Theory and Computation* **5**, 1038–1050 (2009)

[216] F. Dommert and C. Holm, Refining classical force fields for ionic liquids: theory and application to [MMIm][Cl], *Physical Chemistry Chemical Physics* **15**, 2037–2049 (2013)

[217] F. Dommert, K. Wendler, B. Qiao, L. Delle Site and C. Holm, Generic force fields for ionic liquids, *Journal of Molecular Liquids* **192**, 32–37 (2014)

[218] J. N. Canongia Lopes, J. Deschamps and A. A. H. Pádua, Modeling Ionic Liquids Using a Systematic All-Atom Force Field, *The Journal of Physical Chemistry B* **108**, 2038–2047 (2004)

[219] J. N. Canongia Lopes, J. Deschamps and A. A. H. Pádua, Addtitions and corrections to "Modeling Ionic Liquids Using a Systematic All-Atom Force Field", *The Journal of Physical Chemistry B* **108**, 11250–11250 (2004)

[220] J. N. Canongia Lopes and A. A. H. Pádua, Molecular Force Field for Ionic Liquids Composed of Triflate or Bistriflylimide Anions, *The Journal of Physical Chemistry B* **108**, 16893–16898 (2004)

[221] J. N. Canongia Lopes and A. A. H. Pádua, Molecular Force Field for Ionic Liquids III: Imidazolium, Pyridinium, and Phosphonium Cations; Chloride, Bromide, and Dicyanamide Anions, *The Journal of Physical Chemistry B* **110**, 19586–19592 (2006)

[222] J. N. Canongia Lopes, A. A. H. Pádua and K. Shimizu, Molecular Force Field for Ionic Liquids IV: Trialkylimidazolium and Alkoxycarbonyl-Imidazolium Cations; Alkylsulfonate and Alkylsulfate Anions, *The Journal of Physical Chemistry B* **112**, 5039–5046 (2008)

[223] J. N. Canongia Lopes and A. A. H. Pádua, CL&P: A generic and systematic force field for ionic liquids modeling, *Theoretical Chemistry Accounts* **131**, 1129 (2012)

[224] X. Zhong, Z. Liu and D. Cao, Improved Classical United-Atom Force Field for Imidazolium-Based Ionic Liquids: Tetrafluoroborate, Hexafluorophosphate, Methylsulfate, Trifluoromethylsulfonate, Acetate, Trifluoroacetate, and Bis(trifluoromethylsulfonyl)amide, *The Journal of Physical Chemistry B* **115**, 10027–10040 (2011)

[225] T. Köddermann, D. Paschek and R. Ludwig, Molecular Dynamic Simulations of Ionic Liquids: A Reliable Description of Structure, Thermodynamics and Dynamics, *ChemPhysChem* **8**, 2464–2470 (2007)

[226] N. M. Micaelo, A. M. Baptista and C. M. Soares, Parametrization of 1-Butyl-3-methylimidazolium Hexafluorophosphate/Nitrate Ionic Liquid for the GROMOS Force Field, *The Journal of Physical Chemistry B* **110**, 14444–14451 (2006)

[227] T. Yan, C. J. Burnham, M. G. DelPopolo and G. A. Voth, Molecular Dynamics Simulation of Ionic Liquids: The Effect of Electronic Polarizability, *The Journal of Physical Chemistry B* **108**, 11877–11881 (2004)

[228] O. Borodin, Polarizable Force Field Development and Molecular Dynamics Simulations of Ionic Liquids, *The Journal of Physical Chemistry B* **113**, 11463–11478 (2009)

[229] M. Salanne, L. J. A. Siqueira, A. P. Seitsonen, P. A. Madden and B. Kirchner, From molten salts to room temperature ionic liquids: Simulation studies on chloroaluminate systems, *Faraday Discussions* **154**, 171–188 (2012)

[230] J. G. McDaniel, E. Choi, C. Y. Son, J. R. Schmidt and A. Yethiraj, Ab Initio Force Fields for Imidazolium-Based Ionic Liquids, *The Journal of Physical Chemistry B* **120**, 7024–7036 (2016)

[231] F. Dommert, K. Wendler, R. Berger, L. D. Site and C. Holm, Force Fields for Studying the Structure and Dynamics of Ionic Liquids: A Critical Review of Recent Developments, *ChemPhysChem* **13**, 1625–1637 (2012)

[232] M. Salanne, Simulations of room temperature ionic liquids: from polarizable to coarse-grained force fields, *Physical Chemistry Chemical Physics* **17**, 14270–14279 (2015)

[233] C. Schröder, Comparing reduced partial charge models with polarizable simulations of ionic liquids, *Physical Chemistry Chemical Physics* **14**, 3089–3102 (2012)

[234] V. Lesch, H. Montes-Campos, T. Méndez-Morales, L. J. Gallego, A. Heuer, C. Schröder and L. M. Varela, Molecular dynamics analysis of the effect of electronic polarization on the structure and single-particle dynamics of mixtures of ionic liquids and lithium salts, *The Journal of Chemical Physics* **145**, 204507 (2016)

[235] I. Leontyev and A. Stuchebrukhov, Accounting for electronic polarization in non-polarizable force fields, *Physical Chemistry Chemical Physics* **13**, 2613–2626 (2011)

[236] J. Schmidt, C. Krekeler, F. Dommert, Y. Zhao, R. Berger, L. Delle Site and C. Holm, Ionic Charge Reduction and Atomic Partial Charges from First-Principles Calculations of 1,3-Dimethylimidazolium Chloride, *The Journal of Physical Chemistry B* **114**, 6150–6155 (2010)

[237] K. Wendler, S. Zahn, F. Dommert, R. Berger, C. Holm, B. Kirchner and L. D. Site, Locality and Fluctuations: Trends in Imidazolium-Based Ionic Liquids and Beyond, *Journal of Chemical Theory and Computation* **7**, 3040–3044 (2011)

[238] K. Wendler, F. Dommert, Y. Y. Zhao, R. Berger, C. Holm and L. Delle Site, Ionic liquids studied across different scales: A computational perspective, *Faraday Discussions* **154**, 111–132 (2012)

[239] C. E. S. Bernardes, K. Shimizu, J. N. Canongia Lopes, P. Marquetand, E. Heid, O. Steinhauser and C. Schröder, Additive polarizabilities in ionic liquids, *Physical Chemistry Chemical Physics* **18**, 1665–1670 (2016)

[240] D. Roy and M. Maroncelli, An Improved Four-Site Ionic Liquid Model, *The Journal of Physical Chemistry B* **114**, 12629–12631 (2010)

[241] C. Péan, B. Rotenberg, P. Simon and M. Salanne, Multi-scale modelling of supercapacitors: From molecular simulations to a transmission line model, *Journal of Power Sources* **326**, 680–685 (2016)

[242] O. Y. Fajardo, F. Bresme, A. A. Kornyshev and M. Urbakh, Electrotunable Friction with Ionic Liquid Lubricants: How Important Is the Molecular Structure of the Ions?, *The Journal of Physical Chemistry Letters* **6**, 3998–4004 (2015)

[243] K. Breitsprecher, K. Szuttor and C. Holm, Electrode Models for Ionic Liquid-Based Capacitors, *The Journal of Chemical Physics C* **119**, 22445–22451 (2015)

[244] X. Jiang, J. Huang, B. G. Sumpter and R. Qiao, Electro-Induced Dewetting and Concomitant Ionic Current Avalanche in Nanopores, *The Journal of Physical Chemistry Letters* **4**, 3120–3126 (2013)

[245] X. Jiang and R. Qiao, Electrokinetic Transport in Room-Temperature Ionic Liquids: Amplification by Short-Wavelength Hydrodynamics, *The Journal of Physical Chemistry C* **116**, 1133–1138 (2012)

[246] M. Maroncelli, X.-X. Zhang, M. Liang, D. Roy and N. P. Ernsting, Measurements of the complete solvation response of coumarin 153 in ionic liquids and the accuracy of simple dielectric continuum predictions, *Faraday Discussions* **154**, 409–424 (2012)

[247] C. Merlet, C. Péan, B. Rotenberg, P. A. Madden, P. Simon and M. Salanne, Simulating Supercapacitors: Can We Model Electrodes As Constant Charge Surfaces?, *The Journal of Physical Chemistry Letters* **4**, 264–268 (2013)

[248] C. Merlet, B. Rotenberg, P. A. Madden, P.-L. Taberna, P. Simon, Y. Gogotsi and M. Salanne, On the molecular origin of supercapacitance in nanoporous carbon electrodes, English, *Nature Materials* **11**, 306–310 (2012)

[249] C. Merlet, M. Salanne, B. Rotenberg and P. A. Madden, Imidazolium Ionic Liquid Interfaces with Vapor and Graphite: Interfacial Tension and Capacitance from Coarse-Grained Molecular Simulations, *The Journal of Physical Chemistry C* **115**, 16613–16618 (2011)

[250] E. I. Izgorodina, Towards large-scale, fully ab initio calculations of ionic liquids, *Physical Chemistry Chemical Physics* **13**, 4189–4207 (2011)

[251] M. Kohagen, M. Brehm, J. Thar, W. Zhao, F. Müller-Plathe and B. Kirchner, Performance of Quantum Chemically Derived Charges and Persistence of Ion Cages in Ionic Liquids. A Molecular Dynamics Simulations Study of 1-n-Butyl-3-methylimidazolium Bromide, *The Journal of Physical Chemistry B* **115**, 693–702 (2011)

[252] A. Putrino, D. Sebastiani and M. Parrinello, Generalized variational density functional perturbation theory, *The Journal of Chemical Physics* **113**, 7102–7109 (2000)

[253] S. Luber, M. Iannuzzi and J. Hutter, Raman spectra from ab initio molecular dynamics and its application to liquid S-methyloxirane, *The Journal of Chemical Physics* **141**, 094503 (2014)

[254] S. A. Blair and A. J. Thakkar, Relating polarizability to volume, ionization energy, electronegativity, hardness, moments of momentum, and other molecular properties, *The Journal of Chemical Physics* **141**, 074306 (2014)

[255] K. E. Laidig and R. F. W. Bader, Properties of atoms in molecules: Atomic polarizabilities, *The Journal of Chemical Physics* **93**, 7213–7224 (1990)

[256] H. Yu and W. F. van Gunsteren, Accounting for polarization in molecular simulation, *Computer Physics Communications* **172**, 69–85 (2005)

[257] G. Lamoureux and B. Roux, Modeling induced polarization with classical drude oscillators: Theory and molecular dynamics simulation algorithm, *The Journal of Chemical Physics* **119**, 3025–3039 (2003)

[258] G. Lamoureux, A. D. MacKerell Jr. and B. Roux, A simple polarizable model of water based on classical drude oscillators, *The Journal of Chemical Physics* **119**, 5185–5197 (2003)

[259] J. A. Lemkul, J. Huang, B. Roux and A. D. MacKerell Jr., An Empirical Polarizable Force Field Based on the Classical Drude Oscillator Model: Development History and Recent Applications, *Chemical Reviews* **116**, 4983–5013 (2016)

[260] B. T. Thole, Molecular polarizabilities calculated with a modified dipole interaction, *Chemical Physics* **59**, 341–350 (1981)

[261] P. Cieplak, F. Dupradeau, Y. Duan and J. Wang, Polarization effects in molecular mechanical force fields, *Journal of Physics: Condensed Matter* **21**, 333102 (2009)

[262] S. Y. Noskov, G. Lamoureux and B. Roux, Molecular Dynamics Study of Hydration in Ethanol-Water Mixtures Using a Polarizable Force Field, *The Journal of Physical Chemistry B* **109**, 6705–6713 (2005)

[263] T. M. Becker, D. Dubbeldam, L.-C. Lin and T. J. H. Vlugt, Investigating polarization effects of CO_2 adsorption in MgMOF-74, *Journal of Computational Science* **15**, 86–94 (2016)

[264] J. Hutter, M. Iannuzzi, F. Schiffmann and J. VandeVondele, CP2K: atomistic simulations of condensed matter systems, *Wiley Interdisciplinary Reviews: Computational Molecular Science* **4**, 15–25 (2014)

[265] J. VandeVondele and J. Hutter, Gaussian basis sets for accurate calculations on molecular systems in gas and condensed phases, *The Journal of Chemical Physics* **127**, 114105 (2007)

[266] Y. Zhang and W. Yang, Comment on "Generalized Gradient Approximation Made Simple", *Physical Review Letters* **80**, 890 (1998)

[267] P. E. Blöchl, Electrostatic decoupling of periodic images of plane-wave-expanded densities and derived atomic point charges, *The Journal of Chemical Physics* **103**, 7422–7428 (1995)

[268] W. Smith and T. R. Forester, The DL_POLY_2 User Manual, version 2.13, *CCLRC, Daresbury Laboratory, Daresbury, Warrington WA4 4AD, England* (2001), `http://www.cse.stfc.ac.uk/ccg/software/DL_MULTI/MANUALS/USERMAN2.13.pdf`

[269] B. Hess, P–LINCS: A Parallel Linear Constraint Solver for Molecular Simulation, *Journal of Chemical Theory and Computation* **4**, 116–122 (2008)

[270] S. Nosé and M. L. Klein, Constant pressure molecular dynamics for molecular systems, *Molecular Physics* **50**, 1055–1076 (1983)

[271] S. Páll and B. Hess, A flexible algorithm for calculating pair interactions on SIMD architectures, *Computer Physics Communications* **184**, 2641–2650 (2013)

[272] H. Tokuda, K. Hayamizu, I. Kunikazu, A. B. H. Susan and M. Watanabe, Physicochemical Properties and Structures of Room Temperature Ionic Liquids. 1. Variation of Anionic Species, *The Journal of Physical Chemistry B* **108**, 16593–16600 (2004)

[273] H. Machida, Y. Sato and R. L. Smith Jr., Pressure-volume-temperature (PVT) measurements of ionic liquids ([bmim$^+$][PF_6^-], [bmim$^+$][BF4−], [bmim$^+$][$OcSO_4^-$]) and analysis with the Sanchez-Lacombe equation of state, *Fluid Phase Equilibria* **264**, 147–155 (2008)

[274] M. P. Allen and D. J. Tildesley, Computer Simulation of Liquids, 1st ed., Oxford Science Publications (Clarendon Press, Oxford, 1987)

[275] J. a. P. Leal, J. M. S. S. Esperança, M. E. Minas da Piedade, J. N. Canongia Lopes, L. P. N. Rebelo and K. R. Seddon, The Nature of Ionic Liquids in the Gas Phase, *The Journal of Physical Chemistry A* **111**, 6176–6182 (2007)

[276] G. Bussi, D. Donadio and M. Parrinello, Canonical sampling through velocity rescaling, *The Journal of Chemical Physics* **126**, 014101 (2007)

[277] P. K. Patra and B. Bhattacharya, Nonergodicity of the Nose-Hoover chain thermostat in computationally achievable time, *Physical Review E* **90**, 043304 (2014)

[278] F. Legoll, M. Luskin and R. Moeckel, Non-Ergodicity of the Nosé-Hoover Thermostatted Harmonic Oscillator, *Archive for Rational Mechanics and Analysis* **184**, 449–463 (2007)

[279] D. H. Zaitsau, G. J. Kabo, A. A. Strechan, Y. U. Paulechka, A. Tschersich, S. P. Verevkin and A. Heintz, Experimental Vapor Pressures of 1-Alkyl-3-methylimidazolium Bis(trifluoromethylsulfonyl)imides and a Correlation Scheme for Estimation of Vaporization Enthalpies of Ionic Liquids, *The Journal of Physical Chemistry A* **110**, 7303–7306 (2006)

[280] Y. U. Paulechka, G. J. Kabo, A. V. Blokhin, O. A. Vydrov, J. W. Magee and M. Frenkel, Thermodynamic properties of 1-butyl-3-methylimidazolium hexafluorophosphate in the ideal gas state, *Journal of Chemical & Engineering Data* **48**, 457–462 (2003)

[281] C. Krekeler, F. Dommert, J. Schmidt, Y. Zhao, C. Holm, R. Berger and L. Delle Site, Electrostatic properties of liquid 1,3-dimethylimidazolium chloride: role of local polarization and effect of the bulk. *Physical Chemistry Chemical Physics* **12**, 1817–1821 (2010)

[282] D. H. Vogel, Das Temperaturabhängigkeitsgesetz der Viskosität von Flüssigkeiten, *Zeitschrift für Physik* **22**, 645 (1921)

[283] G. S. Fulcher, Analysis of recent measurements of the viscosity of glasses, *Journal of the American Ceramic Society* **8**, 339–355 (1925)

[284] G. Tammann and W. Hesse, Die Abhängigkeit der Viskosität von der Temperatur bei unterkühlten Flüssigkeiten, *Zeitschrift für anorganische und allgemeine Chemie* **156**, 245–257 (1926)

[285] D. Jeong, M. Y. Choi, H. J. Kim and Y. Jung, Fragility, Stokes-Einstein violation, and correlated local excitations in a coarse-grained model of an ionic liquid, *Physical Chemistry Chemical Physics* **12**, 2001–2010 (2010)

[286] C. Merlet, M. Salanne and B. Rotenberg, New Coarse-Grained Models of Imidazolium Ionic Liquids for Bulk and Interfacial Molecular Simulations, *The Journal of Physical Chemistry C* **116**, 7687–7693 (2012)

[287] C. Merlet, M. Salanne, B. Rotenberg and P. A. Madden, Influence of solvation on the structural and capacitive properties of electrical double layer capacitors, *Electrochimica Acta* **101**, 262–271 (2013)

[288] Y. Wang, S. Feng and G. A. Voth, Transferable Coarse-Grained Models for Ionic Liquids, *Journal of Chemical Theory and Computation* **5**, 1091–1098 (2009)

[289] C. Schröder and O. Steinhauser, On the dielectric conductivity of molecular ionic liquids, *The Journal of Chemical Physics* **131**, 114504 (2009)

[290] S. Pandey, Analytical applications of room-temperature ionic liquids: A review of recent efforts, *Analytica Chimica Acta* **556**, 38–45 (2006)

[291] A. E. Visser, R. P. Swatloski, W. M. Reichert, R. Mayton, S. Sheff, A. Wierzbicki, J. H. Davis Jr. and R. D. Rogers, Task-specific ionic liquids for the extraction of metal ions from aqueous solutions, *Chemical Communications*, 135–136 (2001)

[292] T. L. Greaves, A. Weerawardena, C. Fong, I. Krodkiewska and C. J. Drummond, Protic Ionic Liquids: Solvents with Tunable Phase Behavior and Physicochemical Properties, *The Journal of Physical Chemistry B* **110**, 22479–22487 (2006)

[293] T. L. Greaves, A. Weerawardena, C. Fong, I. Krodkiewska and C. J. Drummond, Correction of "Protic Ionic Liquids: Solvents with Tunable Phase Behavior and Physicochemical Properties", *The Journal of Physical Chemistry B* **110**, 26506 (2006)

[294] P. Gaddam and W. Ducker, Electrostatic Screening Length in Concentrated Salt Solutions, *Langmuir* **35**, 5719–5727 (2019)

[295] N. Hjalmarsson, R. Atkin and M. W. Rutland, Switchable long-range double layer force observed in a protic ionic liquid, *Chemical Communications* **53**, 647–650 (2017)

[296] M. Han and R. M. Espinosa-Marzal, Electroviscous Retardation of the Squeeze Out of Nanoconfined Ionic Liquids, *The Journal of Physical Chemistry C* **122**, 21344–21355 (2018)

[297] M. Han and R. M. Espinosa-Marzal, Influence of Water on Structure, Dynamics, and Electrostatics of Hydrophilic and Hydrophobic Ionic Liquids in Charged and Hydrophilic Confinement between Mica Surfaces, *ACS Applied Materials & Interfaces* **11**, 33465–33477 (2019)

[298] A. A. Lee, C. S. Perez-Martinez, A. M. Smith and S. Perkin, Scaling Analysis of the Screening Length in Concentrated Electrolytes, *Physical Review Letters* **119**, 026002 (2017)

[299] R. M. Adar, S. A. Safran, H. Diamant and D. Andelman, Screening length for finite-size ions in concentrated electrolytes, *Physical Review E* **100**, 042615 (2019)

[300] A. Ciach and O. Patsahan, Correct scaling of the correlation length from a theory for concentrated electrolytes, *Journal of Physics: Condensed Matter* **33**, 37LT01 (2021)

[301] J. R. Rumble, ed., CRC Handbook of Chemistry and Physics, 100 (Internet Version 2019), CRC Handbook of Chemistry and Physics (CRC Press / Taylor & Francis, Boca Raton, Florida, 2019), `http://hbcponline.com`

[302] R. Kjellander and D. J. Mitchell, An exact but linear and Poisson-Boltzmann-like theory for electrolytes and colloid dispersions in the primitive model, *Chemical Physics Letters* **200**, 76–82 (1992)

[303] R. Kjellander and D. J. Mitchell, Dressed-ion theory for electrolyte solutions: A Debye-Hückel-like reformulation of the exact theory for the primitive model, *The Journal of Chemical Physics* **101**, 603–626 (1994)

[304] W. Humphrey, A. Dalke and K. Schulten, VMD: Visual Molecular Dynamics, *Journal of Molecular Graphics* **14**, 33–38 (1996)

[305] C. L. Wennberg, T. Murtola, B. Hess and E. Lindahl, Lennard-Jones Lattice Summation in Bilayer Simulations Has Critical Effects on Surface Tension and Lipid Properties, *Journal of Chemical Theory and Computation* **9**, 3527–3537 (2013)

[306] I.-C. Yeh and M. L. Berkowitz, Ewald summation for systems with slab geometry, *The Journal of Chemical Physics* **111**, 3155–3162 (1999)

[307] B. Doherty, X. Zhong, S. Gathiaka, B. Li and O. Acevedo, Revisiting OPLS Force Field Parameters for Ionic Liquid Simulations, *Journal of Chemical Theory and Computation* **13**, 6131–6145 (2017)

[308] J. Rigby and E. I. Izgorodina, Assessment of atomic partial charge schemes for polarisation and charge transfer effects in ionic liquids, *Physical Chemistry Chemical Physics* **15**, 1632–1646 (2013)

[309] I. V. Leontyev and A. A. Stuchebrukhov, Electronic continuum model for molecular dynamics simulations, *The Journal of Chemical Physics* **130**, 085102 (2009)

[310] F. Dommert, J. Schmidt, C. Krekeler, Y. Y. Zhao, R. Berger, L. Delle Site and C. Holm, Towards multiscale modeling of ionic liquids: From electronic structure to bulk properties, *Journal of Molecular Liquids* **152**, 2–8 (2010)

[311] S. Weerasinghe and P. E. Smith, A Kirkwood–Buff derived force field for sodium chloride in water, *The Journal of Chemical Physics* **119**, 11342–11349 (2003)

[312] M. Takeuchi, Y. Kameda, Y. Umebayashi, S. Ogawa, T. Sonoda, S.-i. Ishiguro, M. Fujita and M. Sano, Ion-ion interactions of $LiPF_6$ and $LiBF_4$ in propylene carbonate solutions, *Journal of Molecular Liquids* **148**, 99–108 (2009)

[313] L. D. Dalcín, R. R. Paz and M. Storti, MPI for Python, *Journal of Parallel and Distributed Computing* **65**, 1108–1115 (2005)

[314] L. D. Dalcín, R. R. Paz, M. Storti and J. D'Elía, MPI for Python: Performance improvements and MPI-2 extensions, *Journal of Parallel and Distributed Computing* **68**, 655–662 (2008)

[315] L. D. Dalcín, R. R. Paz, P. A. Kler and A. Cosimo, Parallel distributed computing using Python, *Advances in Water Resources* **34**, 1124–1139 (2011)

[316] S. Gabl, C. Schröder and O. Steinhauser, Computational studies of ionic liquids: Size does matter and time too, *The Journal of Chemical Physics* **137**, 094501 (2012)

[317] J.-F. Côté, D. Brouillette, J. E. Desnoyers, J.-F. Rouleau, J.-M. St-Arnaud and G. Perron, Dielectric constants of acetonitrile, γ-butyrolactone, propylene carbonate, and 1,2-dimethoxyethane as a function of pressure and temperature, *Journal of Solution Chemistry* **25**, 1163–1173 (1996)

[318] C. Daguenet, P. J. Dyson, I. Krossing, A. Oleinikova, J. Slattery, C. Wakai and H. Weingärtner, Dielectric Response of Imidazolium-based Room-temperature Ionic Liquids, *The Journal of Physical Chemistry B* **110**, 12682–12688 (2006)

[319] E. Krucker-Velasquez and J. W. Swan, Underscreening and hidden ion structures in large scale simulations of concentrated electrolytes, *The Journal of Chemical Physics* **155**, 134903 (2021)

[320] V. Lockett, M. Horne, R. Sedev, T. Rodopoulos and J. Ralston, Differential capacitance of the double layer at the electrode/ionic liquids interface, *Physical Chemistry Chemical Physics* **12**, 12499–12512 (2010)

[321] D. J. Bozym, B. Uralcan, D. T. Limmer, M. A. Pope, N. J. Szamreta, P. G. Debenedetti and I. A. Aksay, Anomalous Capacitance Maximum of the Glassy Carbon-Ionic Liquid Interface through Dilution with Organic Solvents, *The Journal of Physical Chemistry Letters* **6**, 2644–2648 (2015)

[322] W. J. Hamer and Y.-C. Wu, Osmotic Coefficients and Mean Activity Coefficients of Uni-univalent Electrolytes in Water at 25°C, *Journal of Physical and Chemical Reference Data* **1**, 1047–1100 (1972)

[323] S. W. Coles, C. Park, R. Nikam, M. Kanduč, J. Dzubiella and B. Rotenberg, Correlation Length in Concentrated Electrolytes: Insights from All-Atom Molecular Dynamics Simulations, *The Journal of Physical Chemistry B* **124**, 1778–1786 (2020)

[324] P. Cats, R. Evans, A. Härtel and R. van Roij, Primitive model electrolytes in the near and far field: Decay lengths from DFT and simulations, *The Journal of Chemical Physics* **154**, 124504 (2021)

[325] N. Anousheh, F. J. Solis and V. Jadhao, Ionic structure and decay length in highly concentrated confined electrolytes, *AIP Advances* **10**, 125312 (2020)

[326] R. Kjellander, Decay behavior of screened electrostatic surface forces in ionic liquids: the vital role of non-local electrostatics, *Physical Chemistry Chemical Physics* **18**, 18985–19000 (2016)

[327] J. Ulander and R. Kjellander, The decay of pair correlation functions in ionic fluids: a dressed ion theory analysis of Monte Carlo simulations, *The Journal of Chemical Physics* **114**, 4893–4904 (2001)

[328] R. Lhermerout and S. Perkin, Nanoconfined ionic liquids: Disentangling electrostatic and viscous forces, *Physical Review Fluids* **3**, 014201 (2018)

[329] M. Vraneš, N. Zec, A. Tot, S. Papović, S. Dožić and S. Gadžurić, Density, electrical conductivity, viscosity and excess properties of 1-butyl-3-methylimidazolium bis(trifluoromethylsulfonyl)imide + propylene carbonate binary mixtures, *The Journal of Chemical Thermodynamics* **68**, 98–108 (2014)